High speed reactive RTM with on-line mixing in dualscale fibrous reinforcements : Experimental and numerical developments and investigations

Mathieu Imbert

UNIVERSITE BRETAGNE LOIRE

CENTRALE NANTES

Thèse de Doctorat

Mathieu IMBERT

Mémoire présenté en vue de l'obtention
du grade de Docteur de l'École Centrale de Nantes
sous le sceau de l'Université Bretagne Loire

École doctorale : Science pour l'Ingénieur, Géoscience, Architecture

Discipline : *Mécanique des solides, des matériaux, des structures et des surfaces*
Unité de recherche : Institut de Recherche en Génie Civil et Mécanique, UMR 6183 CNRS

Soutenue le 13 Juillet 2017

High speed reactive RTM with on-line mixing in dual-scale fibrous reinforcements: Experimental and numerical developments and investigations

RTM réactif haute cadence avec mélange en tête dans les renforts fibreux à double-échelle de porosité : Développements et investigations expérimentaux et numériques

JURY

Président :	**Saouab Abdelghani**, Professeur d'Université, Université du Havre Normandie
Rapporteurs :	**Arquis Eric**, Professeur d'Université, École Nationale Supérieure de Chimie, Biologie et Physique de Bordeaux **Schmidt Fabrice**, Professeur de l'Institut Mines-Télécom, Ecole des Mines d'Albi
Invité:	**Prono David**, Ingénieur, ESI Group
Directeur de thèse :	**Comas-Cardona Sébastien**, Professeur d'Université, École Centrale de Nantes
Co-directeur de thèse :	**Abisset-Chavanne Emmanuelle**, Maitre de Conférences (HDR), École Centrale de Nantes

Remerciements

Cette thèse est l'aboutissement de ma formation de docteur-ingénieur et je tiens donc à remercier en premier lieu tous les professeurs qui m'ont inspiré et accompagné vers la recherche. Mes pensées vont tout particulièrement à Messieurs Xavier Defrance pour le gout qu'il m'a donné pour la physique, Erwan Jahier pour le raisonnement scientifique qu'il m'a fait développer, Bertrand Huneau pour m'avoir donné l'envie de me lancer dans une thèse et Francisco Chinesta pour son grain de folie et son amour de la belle physique.

J'adresse mes plus sincères remerciements aux membres du jury Abdelghani Saouab, Eric Arquis et Fabrice Schmidt pour l'intérêt qu'ils ont porté à mes travaux et pour les discussions qu'ont ouvertes leurs questions constructives.

Je tiens également à remercier du fond du coeur mon directeur de thèse Sébastien Comas-Cardona ainsi que ma co-directrice de thèse Emmanuelle Abisset-Chavanne pour la confiance qu'ils m'ont manifesté, ainsi que pour le juste équilibre entre encadrement et autonomie dans lequel il m'ont permis d'évoluer durant ces 3 belles années.

J'exprime également toute ma gratitude à l'entreprise ESI Group qui a financé cette thèse et en particulier à David Prono mon encadrant au sein de l'entreprise ainsi qu'à Mathilde Chabin. Merci pour la vision que vous m'avez donné de l'Entreprise et de ses besoins. Merci également pour la confiance que vous m'avez démontré.

Je souhaite également remercier ici les professeurs de l'équipe du GeM : Christophe Binetruy, Michel Coret, Adrien Leygue, Erwan Verron, Christian Burtin,... qui m'ont apporté de l'aide ou des idées quand j'en avais besoin et qui contribuent à rendre agréable la vie du laboratoire. J'adresse également un immense merci aux techniciens du laboratoire qui m'ont apporté un soutien indispensable pour la réalisation de mes expériences : Jean-Michel Lebrun, François Bertrand et Yannick Benoit. Merci également aux doctorants du laboratoire pour les bons moments que nous avons partagés : Julie Hemmer, Thomas Corre, Arthur Babeau, Adrien Molinier,...

Je souhaite enfin remercier ma famille et tout particulièrement mon grand-père Jean Hameurt. Merci de m'avoir accompagné et encouragé au cours de mon parcours et de mes expériences de recherche avec ta bienveillance et ton exigence. Merci aussi du fond du coeur à mes parents et à mes soeurs pour la structure familiale dans laquelle j'ai pu m'épanouir. Merci enfin à toi, Juliette, de m'avoir accompagné et encouragé durant cette aventure.

Contents

Introduction **2**

I Literature review **3**

1 RTM process **3**

2 Isothermal fluid flow in the RTM process **4**
2.1 Fibrous materials 4
2.1.1 Fibers 4
2.1.2 Types of textiles 4
2.1.3 Single-scale or dual-scale porous materials 5
2.1.4 Textile property: Permeability 6
2.2 Introduction to single-scale and dual-scale flow 8
2.3 Theory of isothermal fluid flow in single-scale porous materials 9
2.3.1 Mass balance 9
2.3.2 Flow regimes 9
2.3.3 Single-scale fluid flow modeling: Darcy law 10
2.4 Theory of isothermal fluid flow in dual-scale porous materials 10
2.4.1 Analytical treatment 10
2.4.2 Characteristic numbers of dual-scale flow 12

3 Thermo-chemo-mechanical coupling during the RTM process **13**
3.1 Resins used in RTM processes 13
3.1.1 Cure kinetics 14
3.1.2 Rheological models 14
3.2 Advection equation for the degree of cure 15
3.3 Governing equation for the temperature: heat equation 15

4 Experimental studies **16**
4.1 Non-reactive experiments 16
4.1.1 Study of single-scale porosity flow 16
4.1.2 Study of dual-scale porosity flow 17
4.2 Reactive experiments 22
4.2.1 Study of single-scale porosity flow 22
4.2.2 Study of dual-scale porosity flow 24

5 Numerical simulations **26**
5.1 Non-reactive simulations 26
5.1.1 Study of single-scale porosity flow 26
5.1.2 Study of dual-scale porosity flow 26
5.2 Reactive simulations 29
5.2.1 Study of single-scale porosity flow 29
5.2.2 Study of dual-scale porosity flow 31

6 Conclusion and research program **31**
6.1 Conclusion 31
6.2 Research program 32

II Numerical simulation of the reactive RTM process 33

1 Developed numerical methods 33
1.1 General concept . . . 33
1.1.1 Notion of single-scale and dual-scale materials . . . 33
1.1.2 Numerical technique . . . 34
1.1.3 Notation conventions . . . 35
1.2 Non-reactive single-scale model . . . 35
1.2.1 Introduction of the variables . . . 35
1.2.2 General algorithm . . . 36
1.3 Non-reactive dual-scale model . . . 38
1.3.1 Dual-scale flow related sink term . . . 38
1.3.2 Macro-micro volume distribution . . . 38
1.3.3 Microscopic tow discretization . . . 39
1.3.4 Dual-scale filling algorithm . . . 42
1.3.5 Convergence study . . . 44
1.4 Reactive single-scale model . . . 50
1.4.1 Introduction of the variables . . . 50
1.4.2 Algorithm for reactive flow . . . 52
1.5 Reactive dual-scale model . . . 54
1.5.1 Dual-scale flow related sink and source terms . . . 54
1.5.2 Algorithm for reactive flow . . . 55
1.5.3 Validation of the numerical model and convergence . . . 56
1.6 Conclusion on the developed numerical method . . . 64

2 Numerical results 65
2.1 Non-reactive simulations: Parameters influencing the size of the unsaturated area . . . 65
2.1.1 Influence of the injection parameters . . . 65
2.1.2 Influence of the channel/tow permeability ratio . . . 66
2.1.3 Influence of channel/overall volume ratio . . . 68
2.1.4 Influence of the length of the unsaturated area on the injection pressure 69
2.2 Reactive simulations . . . 70
2.2.1 Gel and curing time in stationary conditions . . . 70
2.2.2 Process understanding . . . 70
2.2.3 Influence of the injection/curing time ratio . . . 85
2.2.4 Influence of the length of the unsaturated area on the injection pressure and the quantities of interest distribution . . . 88
2.2.5 Influence of the injection time on the curing time . . . 92
2.3 Process optimization on a part with complex geometry . . . 95

3 Conclusions 103

III Experimental determination of the mechanisms influencing reactive RTM 105

1 Introduction 105

2 Materials **106**
2.1 Textiles . . . 107
2.1.1 Presentation of the textiles . . . 107
2.1.2 Textile properties characterization . . . 109
2.2 Model fluids (non-reactive) . . . 109
2.2.1 Presentation of the fluids . . . 109
2.2.2 Model fluid properties characterization . . . 111
2.3 Curing resin . . . 111
2.3.1 Presentation of the curing fluid . . . 111
2.3.2 Curing fluid properties characterization . . . 111
2.4 Colorants . . . 112

3 Macroscopic trends investigation: Setup and methods **112**
3.1 Principle of the experiment . . . 112
3.2 Setup and equipment . . . 113
3.2.1 Mold . . . 113
3.2.2 Injection equipment . . . 114
3.2.3 Lighting system . . . 114
3.3 Measurement and monitoring equipment . . . 115
3.3.1 Camera, lenses and acquisition system . . . 115
3.3.2 Weighing scale . . . 115
3.4 Post-treatment tools . . . 115
3.4.1 Software: Matlab . . . 115
3.4.2 Software: ImageJ . . . 115
3.5 Experiment calibration . . . 115
3.5.1 Setup thickness calibration . . . 115
3.5.2 Selection of fluid viscosities . . . 116
3.5.3 Lighting, camera and concentration selection . . . 116
3.5.4 Grey level/Concentration calibration curve . . . 117
3.6 Experimental protocol . . . 120
3.7 Post treatment . . . 121
3.8 Designs of experiment . . . 126

4 Macroscopic trends investigation: Results **127**
4.1 Validity of the macroscopic intra-tow investigation technique and repeatability 127
4.1.1 Validity of the technique . . . 127
4.1.2 Repeatability . . . 129
4.1.3 Influence of viscosity and duration of the injection . . . 133
4.2 Intra-tow storage: Macroscopic trends investigation . . . 134
4.2.1 Influence of FVF . . . 134
4.2.2 Influence of textile architecture . . . 135
4.2.3 Influence of tow orientation . . . 136
4.2.4 Investigation of concentration variations inside of the sample . . . 138
4.3 Conclusions on macroscopic trends investigation . . . 141

5 Microscopic mechanisms investigation: Setup and methods **142**
5.1 Principle of the experiment . . . 142
5.2 Setup and equipment . . . 143
5.2.1 Mold and injection system . . . 143
5.2.2 UV-curing equipment . . . 143
5.3 Measurement and monitoring equipment . . . 143
5.3.1 Camera, lenses and acquisition system . . . 143

5.3.2 Weighing scale . . . 143
5.3.3 Scanning Electronic Microscope . . . 144
5.3.4 Micro-tomograph . . . 144
5.4 Post-treatment tools . . . 144
5.5 Experiment calibration . . . 144
5.5.1 Selection of fluid viscosity . . . 144
5.5.2 Resin curing characterization . . . 144
5.6 Experimental protocol . . . 144
5.6.1 Injection and curing . . . 144
5.6.2 Sample preparation . . . 145
5.6.3 Imaging the samples . . . 145
5.7 Post-treatment: Image analysis methods . . . 146
5.7.1 Determination of the storage location . . . 146
5.7.2 Channel/tow volume distribution . . . 146
5.7.3 Microscopic local FVF measurement methods . . . 147
5.8 Design of experiment . . . 149

6 Microscopic mechanisms investigation: Results 150
6.1 Validation of the macroscopic trends . . . 150
6.2 Microstructure evolution versus FVF . . . 153
6.2.1 Channel/tow volume distribution versus FVF . . . 153
6.2.2 Intra-tow FVF versus macroscopic FVF . . . 156
6.3 Identification of micro-scale flow mechanisms . . . 158
6.3.1 Correlation between violet resin location and local intra-tow FVF . 158
6.3.2 Evolution of the intra-tow violet colorant content with distance from entry . . . 161
6.4 Conclusions on micro-scale mechanisms investigation . . . 163

7 Macro and micro-scale analysis 164
7.1 Average FVF calculated from micro-scale analysis . . . 164
7.2 Dual-scale character of the samples . . . 165
7.3 Local intra-tow FVF and longitudinal intra-tow front propagation . . . 165

8 Conclusions 170

Conclusion and Perspectives 172

Appendix 175

Appendix 177

Introduction

The interest for introducing composite materials in the automotive industry is growing fast. This trend initiated by environmental regulations on green house gas emission reduction lead automotive manufacturer to investigate the use of new materials to reduce the structural weight of the cars. In this context, composites, with their high mechanical properties and low density appear as promising solutions. However, a major challenge in introducing composites in the automotive industry is the cycle time. As a matter of fact, historical metal stamping and welding processes are still the reference so that composite manufacturing processes must be optimized in order to reach at least 2- to 4-minutes cycle time. This range of duration is accessible for processes as pultrusion (where parts are produced continuously) or thermoforming. However, these processes are not suited for large, 3D-shaped structural parts or for parts containing inserts. For these types of parts, Resin Transfer Molding (RTM) is an appropriate process. It consists in injecting in-plane a curing resin in the cavity of a mold where a fibrous reinforcement has been placed. This process has been initially developed for long cycle times (more than 20 minutes), therefore major optimizations are required to reach the desired 2- to 4-minute cycle time. The challenges lay both the curing time of the resin mixed on-line and the possibility of injecting quickly the resin without reaching too high pressures. Therefore, low viscosity, fast curing resins have been developed recently. However, due to their high reactivity and on-line mixing, these resins are very sensitive to the processing conditions, making experimental optimization of complex shaped parts very difficult and expensive. Numerical simulations of the process appear therefore of great interest in order to determine numerically the best injection strategy and process parameters.

ESI Group already proposes a simulation software called ESI PAM-COMPOSITES that includes a PAM-RTM module for classical RTM injections.

However, recent works have revealed that phenomena related to the flow of the resin in the structure of reinforcements such as woven textiles or NCF (Non-crimp fabrics), that exhibit dual-scale flow, become very important when injection and curing times are close to each other. As PAM-RTM does actually not take the dual-scale flow into account, it is expected that the numerical predictions may be inaccurate. For this reason, it has been decided to launch this research program. Its aim is to investigate, identify and quantify the mechanisms involved in the RTM process and that are likely to play a significant role in short cycle time applications. Once identified, these mechanisms should be transposed into simulation in order to propose a numerical tool suited for the industrial simulation of the short cycle time RTM process with on-line mixing and flow in dual-scale fibrous media.

In a first part, a literature review will highlight the knowledge and the lacks in the numerical and experimental works presented in the literature. The second part will be dedicated to the introduction of the developed numerical model and the presentation of the obtained results. Part III will deal with the experimental methods and results. Finally, obtained results will be summarized and perspectives will be proposed.

Part I
Literature review

1 RTM process

The resin transfer molding (RTM) process has been developed and implemented in the seventies and eighties to produce diverse composite parts [8]. Due to the long cycle times (more than 20 minutes for the classical RTM technologies), its use was limited to small series production. However, in the recent years, the interest for this process is growing, especially in the automotive industry, as progresses have been made to reduce the cycle time. It allows the RTM to become a mass production process. RTM features a good ability to produce parts with:

- Complex shapes (inserts can be used)
- Good mechanical properties (using continuous fiber textiles)
- Good surface quality

The RTM process consists in three steps (Figure 1):

- Placement of a fibrous preform in the cavity of the mold
  During this step, a fibrous reinforcement is positioned in the cavity of the mold. For parts with complex geometries, the 2D textiles may have been formed in the 3D shape of the final part in a previous step called preforming.
- Mold closing, injection and curing or solidification of the resin
  During this step, the cavity of the mold is closed and a thermosetting or thermoplastic resin is injected in the fibrous reinforcement. Flow occurs mainly in-plane in the fibrous material until the end of injection. During the injection time, multiple physics as fluid flow, heat transfers, viscosity evolution and polymerization (for reactive injections) occur inside the cavity. If the process parameters are appropriate, the reinforcement is fully saturated with the resin at the end of injection. Then solidification begins with curing and/or cooling.
- Mold opening and evacuation of the part for final trimming
  Once the resin has fully cured or solidified the part is removed.

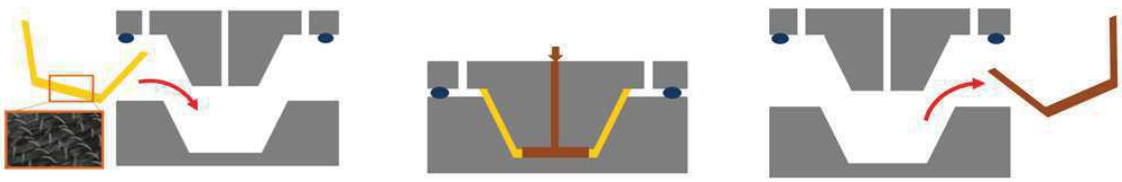

Figure 1: Three steps of the RTM process

The duration of the cycle time is mainly driven by the injection and the curing step. For small series applications, cycle time is often close to 20-30 minutes. Injection is conducted within some minutes during which cure evolution is negligible and injection conditions can be considered isothermal. Significant resin properties evolutions only occur when the injection is finished. However, for short cycle time applications as in the automotive industry, high speed RTM will target 2-4 min cycle time using on-line mixing. This technique consists in mixing the resin and its curing agents right at the mold inlet during

injection allowing a fine control, automation and cleanliness of the process. In order to reduce cycle time, fast curing resins are used. Additionally, injection time is wished to be close to curing time in order to reduce the duration of final curing after the end of injection. This induces that the effects of curing (exothermy, viscosity evolution,...) become significant during the injection stage. Couplings that could be neglected before will have to be taken into account. Additionally, fast injections will generate high pressures and potential flow induced deformations of the preform.

Reduction of the cycle time in the RTM process introduces new challenges that require a fine understanding of the mechanisms involved in the process (high pressures, potential fiber washing, temperature and viscosity evolutions during injection) and their couplings. Aspects related to resin distribution coupled to property evolution during the injection and curing steps should be further investigated.

2 Isothermal fluid flow in the RTM process

2.1 Fibrous materials

2.1.1 Fibers

A wide variety of fibers can be used for RTM applications. Commonly used fibers are glass or carbon fibers but aramide or natural fibers (hemp, flax,...) can also be processed. For performance, density or economical reasons, carbon and glass fibers are the most used types of reinforcing fibers. Commonly, carbon fiber of 5-6 μm in diameter are obtained from the carbonization of precursors (that may have several origins) while glass fibers of 12-20 μm are obtained from extruded molten glass composed of oxides blends.

2.1.2 Types of textiles

Several types of textiles can be used as reinforcements in the RTM process:

- Randomly oriented fiber materials
  They are made of continuous or chopped fibers oriented randomly. These types of fibrous materials are quite easy to preform and feature high permeability. However, they do not allow achieving high Fiber Volume Fractions (FVF) and do not feature high mechanical properties due to the random orientation of the fibers. There use is therefore limited to non-structural parts. Figure 2 present the typical aspect of a random mat.

Figure 2: Example of a chopped fiber random mat

- Continuous fiber textiles
  These textiles are made of continuous fibers aligned in specific directions. This family can be divided into two types of materials:

  – Non crimp fabrics (NCF)
    These textiles are made of one (unidirectional material) or multiple layers (multidirectional materials) of tows stitched together to form a fibrous bed where the fibers are oriented in different orientations depending on the ply. Figure 3 presents the principle of the structure and production of a NCF.

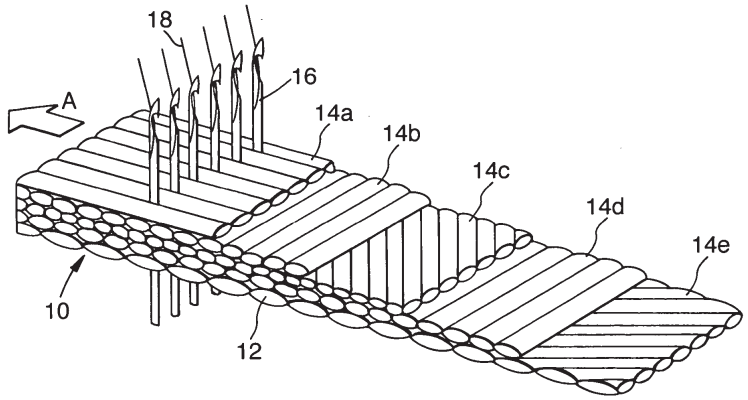

Figure 3: Principle of the structure and production of a multidirectional NCF material ([28])

  – Woven or braided textiles
    These textiles are made of tows that are woven or braided together. Many different architectures can be obtained depending on the weaving or braiding machine settings. Some examples of woven and braided textiles are given in Figure 4.

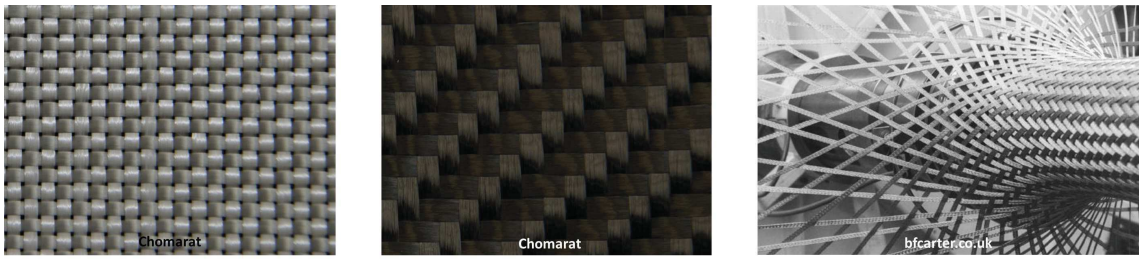

Figure 4: Examples of woven textiles. Left: plain weave glass . Center: Twill-weave carbon. Right: Braided.

2.1.3 Single-scale or dual-scale porous materials

It can be observed from the different types of textiles presented in section 2.1.2 that a major difference exists in terms of structure between the randomly oriented fiber materials and the continuous fiber textiles. In fact, for the latter, the presence of fiber tows and gaps between the tows engenders two types of pore sizes in the reinforcement. The property characterizing the two regions of the dual-scale porous materials is the porosity ϵ. The porosity represents the ratio of volume that can be filled by a fluid during impregnation

per unit volume. It is directly related to the fiber volume fraction: $\epsilon = 1 - FVF$. Because they feature fiber dense intra-tow regions and channels (also called gaps) without fibers, these types of material are called dual-scale porous materials. On the contrary, randomly oriented fiber materials that only exhibit one single type of pores, are called single-scale porous materials. Figure 5 presents the micrograph of a unidirectional material where the two different pore sizes can be observed.

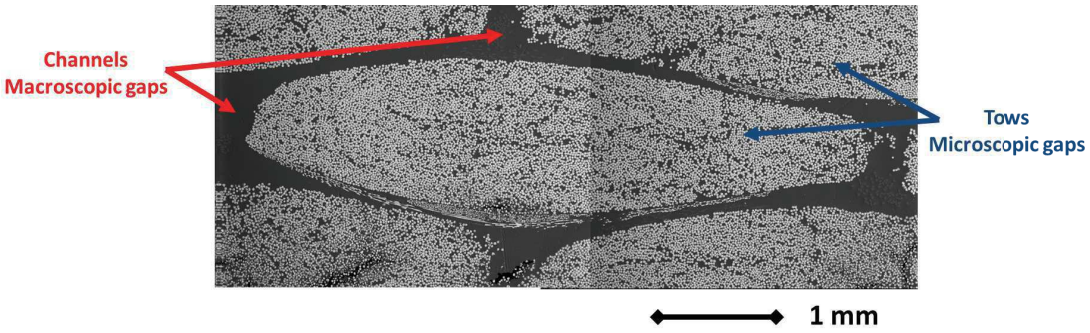

Figure 5: Micrograph of a undirectional material exhibiting the two different porosity scales (in white the fibers and in black the porosity)

2.1.4 Textile property: Permeability

Permeability is an intrinsic property of a porous material that characterizes the ability for a fluid to flow through it. Textiles exhibit very complex and to some extent random microstructures, therefore, the classical way to access their permeability is to conduct experimental measurements ([78], [30], [16]). A good experimental measurement of permeability review has been written by Sharma and Siginer ([61]). Some publications ([42],[45] and [55]) propose analytical technique for the determination of the textile permeability but require experimental measurement to be calibrated. The requirement of experimental measurements is due to the complexity of the fiber arrangement at the macroscopic level. However, some local regions (channels or intra-tow domains) feature simpler morphologies that allow a simpler analytical description.

Channel permeability

As introduced in section 2.1.2, continuous woven or stitched fibrous material feature a dual-scale porosity structure made of fiber densely filled tows and gaps containing no fibers. These gaps can be simplified, especially in NCF materials as rectilinear domains with specific (rectangular, cylindrical or hyperbolic quadrilateral) cross sections ([52], [42], [45]) as presented in Figure 6.

The permeability associated to the gaps are treated in two different ways in the literature. Its value can calculated analytically, for example from the equation of pressure drop for a Stokes flow between two infinite plates($K_c = h^2/12$ ([41]), with h the distance between the plates. Other geometries as elliptical pipes: $K_c = \dfrac{a^2 b^2}{4(a^2 + b^2)}$ ([18] with a and b the major and minor semi-axes can be also used). Finally, an other approach consist in taking K_c equal to the measured bulk permeability assuming that intra-tow flow is negligible.

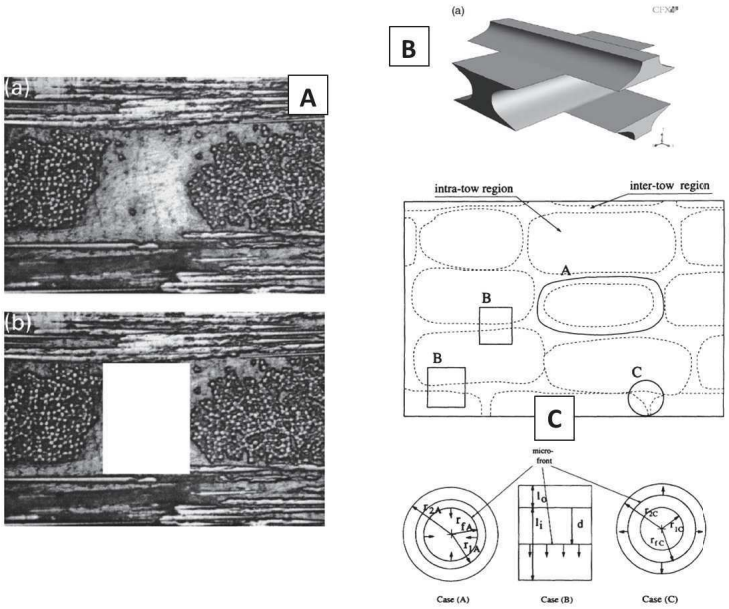

Figure 6: Idealized channel geometries. A: rectangular cross section ([42]) , B: hyperbolic quadrilateral ([45]), C: cylindrical and rectangular cross sections ([52])

Intra-tow permeability

Analytical models have also been developed to determine the permeability in idealized media (fiber tows with homogeneously dispersed fibers). It is the case for the Kozeny-Carman model ([12]) that predicts an isotropic permeability for porous beds made of spherical or ellipsoidal particles. The Kozeny-Carman relationship is given in Equation 1.

$$K = r_f^2 \frac{(1 - V_f)^3}{4 k_{KC} V_f^2} \tag{1}$$

where r_f is the fiber radius, V_f the fiber volume fraction and k_{KC} the Kozeny-Carman constant. However this model has two limits:

- This expression cannot model orthotropic permeabilities
- The characteristics of the fiber arrangement are lumped into the Kozeny-Carman constant.

Therefore, two other models have been proposed. One by Gutowski ([27]) who proposed a specific expression for the transverse permeability of fiber bundles (Kozeny-Carman model is further used for the permeability in the direction of the fibers):

$$K_{ii} = r_f^2 \frac{\left(\sqrt{\frac{V_\alpha}{V_f}} - 1\right)^3}{4 k_{ii} \left(\sqrt{\frac{V_\alpha}{V_f}} + 1\right)} \tag{2}$$

where k_{ii} and V_α are empirically determined parameters and $i = y$ or z are the directions transverse to the fibers. However, in Gutowski's model, the geometrical arrangement of the fibers is still lumped into the empirical parameters. Therefore, Gebart proposed in 1992 an analytical expression based on the flow of a Newtonian fluid through a quadratic

or hexagonal arrangement of fibers ([24]). He obtained the following expressions (Equations 3 and 4) respectively for the permeability in the direction parallel to the tows and perpendicular to the fibers.

$$K_{\parallel} = \frac{8r_f^2}{c}\frac{(1-V_f)^3}{V_f^2} \tag{3}$$

$$K_{\perp} = C_I r_f^2 \left(\sqrt{\frac{V_{fmax}}{V_f}} - 1\right)^{5/2} \tag{4}$$

where V_{fmax} is the maximal fiber volume fraction (closed packing), and c and C_I are constants depending of the fiber arrangement. Gebart's equations are therefore very interesting to calculate intra-tow permeability from intra-tow FVF values that can be obtained from micrographs for example.

2.2 Introduction to single-scale and dual-scale flow

Finally, it is expected that, due to the difference of their properties, the saturation behavior of the two regions of a dual-scale porous material will be very different. Figure 7 presents the characteristic impregnation behaviors of single and dual-scale porous materials widely reported in the literature ([49], [72], and [45]). This impregnation behavior is characterized, for dual-scale porous materials, by the existence of an unsaturated area behind the macroscopic flow front. In this region, inter-tow channels are saturated while intra-tow domains are still not impregnated due to the high FVF that slows down flow front propagation. This phenomenon is not observed in single-scale porous materials as all pores are in the same range of sizes and are thus saturated at the same speed. Intra-tow resin storage in the saturated area has also been reported in [62] and [56]. Details on the experimental methods, physics and modeling proposed in the literature to study and describe dual-scale flow will be given in the following sections.

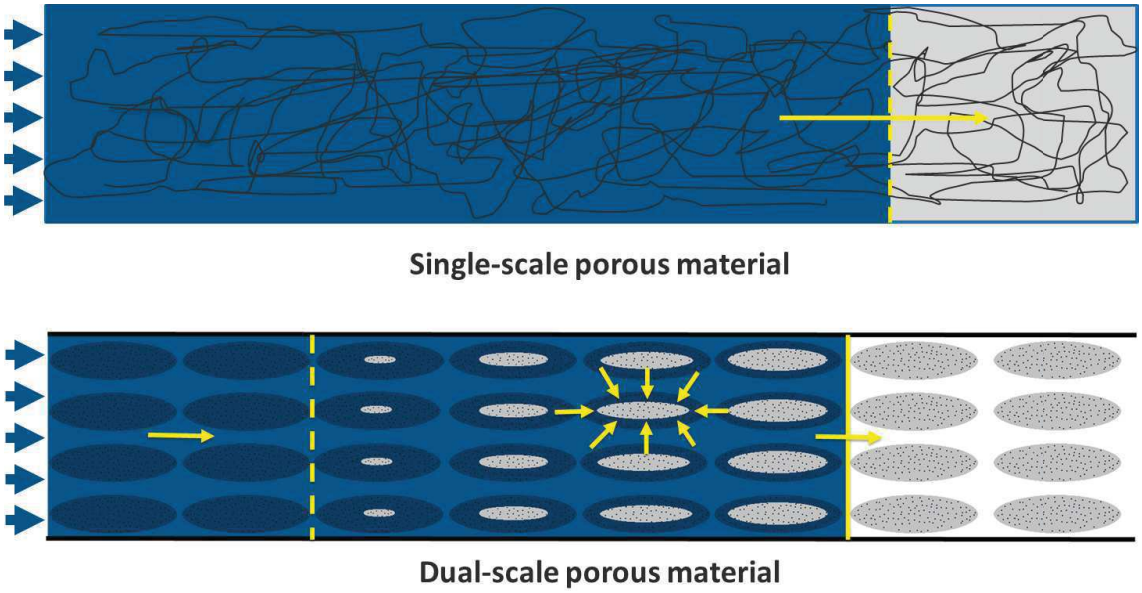

Figure 7: Schematic representation of the saturation of single-scale and dual-scale porous microstructures

Due to their good mechanical properties, continuous fiber textiles are likely to be used in short cycle time RTM processes for structural applications. Therefore, the effects induced by their dual-scale porous characteristics on the process (unsaturated area, intra-tow resin storage,...) are interesting to be investigated. Thus, focus will be placed on the consequences of this dual-scale structure.

2.3 Theory of isothermal fluid flow in single-scale porous materials

2.3.1 Mass balance

The governing equation of fluid flow in the RTM process is the mass balance equation. It states in its general form:

$$\frac{d\rho}{dt} + \nabla \cdot (\rho \mathbf{v}) = 0 \tag{5}$$

If they contain no air bubbles, resins used for RTM applications can be considered incompressible, therefore, Equation 5 can be simplified to Equation 6 in the case of a flow in a single-scale porous material.

$$\nabla \cdot \mathbf{v} = 0 \tag{6}$$

2.3.2 Flow regimes

As presented in section 1, the principle of the RTM process consists in injecting a resin in a reinforcement placed in the cavity of a mold. Depending on the flow velocity, several flow regimes can be achieved. To characterize these flow regimes in single-scale porous materials, the Reynolds number is introduced.

Reynolds number

The Reynolds number is a dimensionless number defined as the ratio of the inertial forces over the viscous forces in the fluid flow. When the inertial force becomes higher than the viscous forces, the ratio becomes bigger than 1 and the flow is no more laminar. On the other hand, when viscous forces become predominant, the ratio becomes lower than 1 and the flow is considered laminar. The Reynolds number is defined in a porous material by the Equation 7:

$$R_e = \frac{\rho_r v_{pore} l_\epsilon}{\mu} \tag{7}$$

where v_{pore} is the velocity of the fluid in the pores of the porous material, l_ϵ is the characteristic dimension of the pores inside the porous material. It is widely accepted that l_ϵ can be well approximated by the square root of the permeability [9]. For classical RTM injections, resin density is in the range of 1200 kg/m^3, preform permeability in the range of 10^{-10} m^2 and viscosity in the range of 0.05 Pa.s. Under these conditions, Reynolds number remains below the value of 1 if the flow velocity remains below 4 m/s. This condition is always verified for RTM injections as flow velocity is classically in the range of some centimeters per second for high speed injections. It is thus verified that RTM injections are conducted in laminar conditions.

2.3.3 Single-scale fluid flow modeling: Darcy law

Flow of a Newtonian fluid in a porous material has been investigated in many fields in the past as in soils, rocks or filters. The most widely used equation treating this phenomenon is Darcy's law (8).

$$Q = \frac{K\Delta P}{\mu A \Delta z} \tag{8}$$

where Q is the volumic flow rate, K the permeability of the porous medium, μ the dynamic viscosity of the fluid, A the cross section of the flow domain, ΔP the pressure difference between oulet and inlet of the flow domain and Δz the length of the flow domain. It has been determined empirically from observations conducted on the flow of water through a sand column. This equation initially developed to describe the unidirectional flow of a newtonian fluid in as single-scale porous material can in fact be also obtained from volume averaging of Navier-Stokes equation under, among others, the following conditions [74]:

- The fluid is incompressible
- Inertia effects in the flow are negligible (Flow occurs at small Reynolds numbers)
- The volumic forces (gravity,...) and the forces at the domain interfaces are small compared to the other forces.

Under these assumptions, Navier-Stokes equation can be rewritten in the 3D form of Darcy's equation:

$$\mathbf{v} = \frac{-\mathbf{K}}{\mu}\nabla P \tag{9}$$

where, $\mathbf{v}$ is the Darcy's velocity, $\mathbf{v} = \epsilon \mathbf{v}_{pore}$ with ϵ the porosity of the medium and v_{pore} the true pore flow velocity. $\mathbf{K}$ is the permeability tensor of the porous material. It can be thus noticed that Darcy's law links the flow velocity and the pressure gradient through the permeability which depends on the microstructural characteristics of the porous medium and the viscosity which is a property of the fluid.

2.4 Theory of isothermal fluid flow in dual-scale porous materials

2.4.1 Analytical treatment

Dual-scale porous materials are composed of two domains characterized by different properties: channels with no fiber content and tows densely filled with fibers. Additionally, as introduced in section 2.2, the dual-scale structure generates a complex flow pattern, especially at the flow front. In order to reproduce this phenomenon and its consequences on the pressure field, two approaches have been proposed in the literature.

Single-scale model including unsaturated permeability

This first approach consists in reproducing the effects of dual-scale flow by applying an unsaturated permeability to the flow front domain where the material is not fully saturated ([48]). The permeability is calculated as a function of the saturation and the saturation as a function of the distance to the flow front (Figure 8). This approach presents the advantage of allowing treating dual-scale flow in an analytic way. However, the method has been developed for simple flow cases (1D linear flow and radial flow) in isothermal conditions. Its extension to more complex flow patterns and with varying viscosity values

would be very complex as the saturation would be much more difficult to predict.

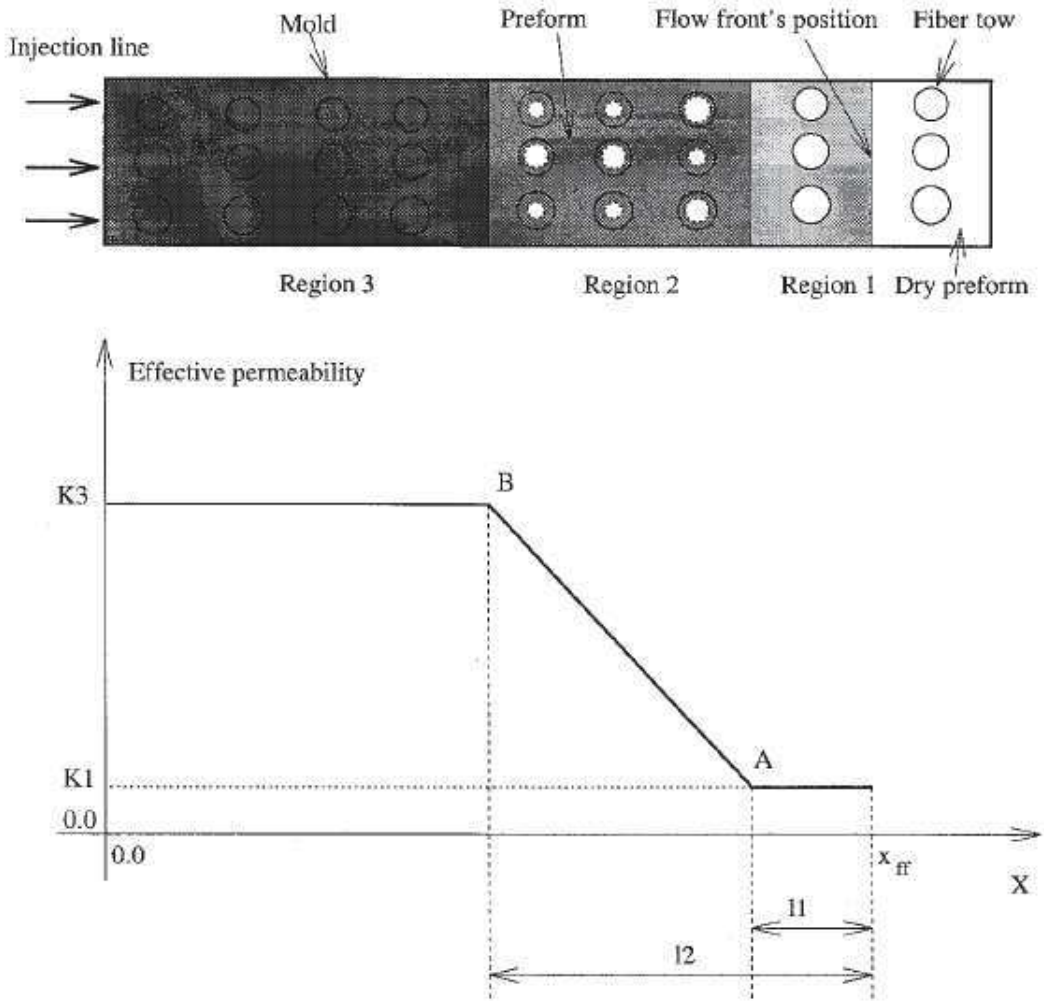

Figure 8: Distribution of the unsaturated permeability along the unsaturated area taken from ([48])

Dual-scale model including a modification of the equation of mass balance In this context, a second approach, that is more suited for simulation purposes, has been developed. It consists in treating separately the channel and tow regions of the reinforcement (Figure 9). Channel and tows are assumed to be single-scale porous media in which Darcy's law is satisfied. Flow occurs in the channels in the saturated area and occurs both in the channel and from the channel to the tows in the unsaturated area ([52], [63] and [70]).

Therefore, the equation of mass balance in the form of Equation 6 is not satisfied in the channels in the unsaturated area as resin is removed to saturate the tows. The equation of mass balance requires thus the introduction of a sink term q that takes the absorption of fluid by the tows into account. Finally, Equation 10 is the mass balance governing equation in the channels of a dual-scale porous material during resin injection.

$$\nabla \cdot \mathbf{v} = q \tag{10}$$

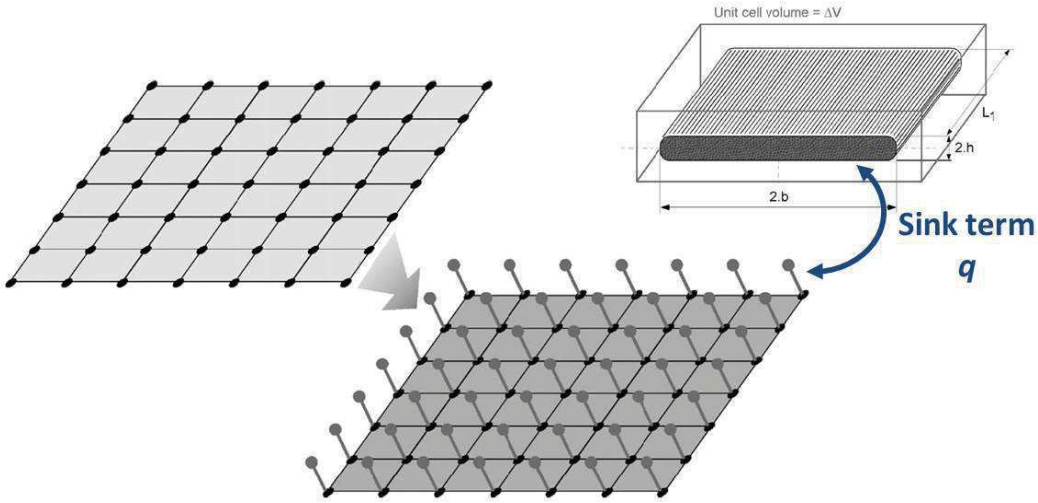

Figure 9: Representation of a dual-scale model separating channels and tows([63])

On the other hand, the intra-tow domain can be assumed as a single-scale porosity domain and Equation 6 governs its saturation. This approach based on a two-level simulation of dual-scale flow has been massively used for dual-scale simulations (Section 4.1.2).

2.4.2 Characteristic numbers of dual-scale flow

In order to quantify the dual-scale flow mechanism, several ratios have been introduced.

Pore volume ratio

Pillai proposed in 1998 ([51]) the pore volume ratio expressed as:

$$\gamma = \frac{\epsilon A_i}{\epsilon 0 A_0} \tag{11}$$

where the subscripts i and 0 correspond respectively to the intra-tow and channel regions. A_x is the cross section area of each region. This ratio is interesting to quantify the tow/channel distribution. However it provides no information on the tow filling kinetic that is related to the channel/tow permeability ratio. Therefore, the permeability ratio is also considered as a parameter in [51].

Sink effect index

Dual-scale effect have also been characterized by the sink effect index ψ proposed by Slade et al. [66].

$$\psi = \frac{K_t}{K_c}\left(\frac{L}{b}\right)^2 \frac{A_t}{A_{tot}} \tag{12}$$

where K_t is the transverse tow permeability, K_c is the channel permeability, L is the characteristic length of the part, b is the semi minor axis of the representative tow in the model and A_t and A_{tot} are respectively the area of the cross section occupied by the tows and the total cross section. This index couples the microstrucural and permeability parameters, however, it is based on a representation of the microstructure made of elliptical tows.

Capillary number

In dual-scale flow, the respective velocities of viscous flow and capillary driven flows have a huge influence on potential residual air entrapment. Therefore, the Capillary number has been introduced. The Capillary number provides information on the ratio of viscous versus capillary forces. It has been formulated in two sightly different forms: the Capillary number proposed in Equation 13 and the modified Capillary number proposed in Equation 14.

$$C_a = \frac{\mu v}{\gamma_{st}} \tag{13}$$

In Equation 13, γ_{st} is the surface tension of the fluid.

$$C_a^* = \frac{\mu v}{\gamma_{st} \cos(\theta)} \tag{14}$$

In Equation 14, θ is the contact angle between the fluid and the fiber. This number has been shown to play a significant role on air entrapment mechanisms in dual-scale porous materials. At low C_a, air entrapment occurs in the channels due to fingering, while at high C_a, air entrapment occurs in the tows (Figure 11). Details on the experimental methods used to characterize the porosity content will be given in section 4.1.2.

Equations governing singe-scale and dual-scale isothermal flows have been established and verified in the literature. They will be used in simulation to reproduce fluid flow during the process.

3 Thermo-chemo-mechanical coupling during the RTM process

Multiple physics are coupled in the reactive RTM injections. In addition to the fluid flow, polymerization occurs as well as heat transfers and rheological evolutions. The physical description of the isothermal flow has been treated in the previous section. In this section the equations governing transport and evolution of the degree of cure and temperature will be detailed in this section as well as the rheological evolution.

3.1 Resins used in RTM processes

Five major families of thermosetting resins are used for the production of structural parts:

- Polyester/Vinylester
- Epoxy
- Acrylic
- Polyamide
- Polyurethane

The chemical polymerization mechanisms (radical polymerization, ionic polymerization,...) differ from a resin type to the other however the chemical aspects will not be considered in this work. Focus will be placed on macroscopic quantities of interest: degree of cure and viscosity. In this sense, as soon as the curing and viscosity model are appropriate for the considered resin, the nature of the resin does not matter. Cure and viscosity models are presented in the following sections.

3.1.1 Cure kinetics

In the frame of this work, the process is considered from a macroscopic point of view so that the precise knowledge of the chemical composition of the resin during curing is not required. Therefore, only a macroscopic quantity of interest called degree of cure (α) or fractional conversion will be considered to follow the evolution of the cure. Its rate $\frac{d\alpha}{dt}$ is defined as:

$$\frac{d\alpha}{dt} = \frac{1}{H_t}\frac{dH}{dt} \tag{15}$$

where H is the enthalpy and H_t is the total heat generated by the reaction. Thus the degree of cure represents the relative amount of heat generated at a certain time to the total heat that the resin will generate until the end of the reaction. It is a macroscopic indicator and therefore do not allow to access the morphology of the macromolecules in the resin. However, it gives direct information on the amount of heat generated by the reaction. Furthermore, kinetic models have been proposed in the literature to predict the evolution of this degree of cure with time and temperature. The degree of cure is therefore an appropriate macroscopic indicator of the evolution of the polymerization. Some of these models are presented below.

Nth-order kinetic models with the generic form presented in Equation 16 are commonly used. Peyser [50] used a first order kinetic model to model the kinetic of epoxy resin, and Pusatcioglu [54] used the model below for polyester thermosets.

$$\frac{d\alpha}{dt} = De^{\frac{-E_a}{RT}}\alpha^x(1-\alpha)^y \tag{16}$$

In Equation 16, D is a constant, E_a is the energy of activation of the reaction, R is the constant of ideal gases and x and y are coefficients. $k = Ae^{\frac{-E_a}{RT}}$ is commonly called an Arrhenius rate coefficient.

Kamal proposed in [32] a more complex model (Equation 17) that can be used to describe, among others, epoxy and polyester curing.

$$\frac{d\alpha}{dt} = (k_1 + k_2\alpha^m)(1-\alpha)^n \tag{17}$$

In Equation 17, k_1 and k_2 are Arrhenius rate coefficients and m and n parameters determined experimentally.

Even more complex models have been presented in the literature. Cuadrado proposed in [19] a couple of kinetic models to fit experimental polyester curing results in two different ranges of temperatures. A first-order model was used at low temperature and a second-order model at high temperature.

It can be observed in these models that the temperature plays a significant role on the evolution of the degree of cure. Indeed, the value of the rate coefficients increase when the temperature increases: the reaction is accelerated by an increase of the resins temperature.

3.1.2 Rheological models

During the High speed reactive RTM, curing is wished to begin during the injection in order to reduce the cycle time. This curing induces an evolution of the composition of the resin and has a direct influence on the viscosity of the fluid. As for the cure kinetics, several models relating the viscosity, the degree of cure and the temperature have been

proposed in the literature.
Williams, Landel and Ferry [79] proposed in 1955 a model relating viscosity and temperature of an uncured resin (Equation 18).

$$\mu(T) = \mu_g \exp\left[\frac{C_1(T - T_{g0})}{C_2 + T - T_{g0}}\right] \tag{18}$$

where μ_g is the viscosity at the glass transition, T_{g0} is the glass transition temperature of the uncured system and C_1 and C_2 are constants. This model has been widely used and modified, including also the influence of the degree of cure to treat epoxy systems ([34], [44]).
Castro and Macoscko ([13]) proposed another law in 1982 initially for polyurethane systems for Resin Injection Molding (RIM).

$$\mu(T, \alpha) = K_\mu \exp\left(\frac{E_\mu}{RT}\right)\left(\frac{\alpha_g}{\alpha_g - \alpha}\right)^{E+F_\alpha} \tag{19}$$

where K_μ is a pre-exponential factor, E_μ is an activation energy, E and F are constants and α_g the degree of cure at the gel point. This equation was also adapted and coupled with a modified Williams Landel and Ferry's equation to fit the behavior of an epoxy resin ([31]).

$$\mu(T, \alpha) = \mu_g \exp\left[\frac{C_1(T - T_{g0})}{C_2 + T - T_{g0}}\right]\left(\frac{\alpha_g}{\alpha_g - \alpha}\right)^{n} \tag{20}$$

It can be observed from these models that the effects of the temperature and the degree of cure are antagonist on the evolution of the viscosity. When the temperature increases, the viscosity decreases while an increase in degree of cure increases the viscosity. Thus using high injection temperatures, the viscosity of the resin could be decreased, reducing the injection pressure. Caution should however be paid to the induced accelerated curing that could affect the injection.

3.2 Advection equation for the degree of cure

As introduced previously, resin property evolution is likely to be significant during the injection stage of the High speed-RTM process. For this reason, degree of cure evolutions must be tracked in space and time. The advection equation that governs the degree of cure is introduced in Equation 21.

$$\frac{\partial \alpha}{\partial t} + \mathbf{v} \cdot \nabla \alpha = \dot{\alpha} \tag{21}$$

In Equation 21, $\mathbf{v}$ is the fluid flow velocity and the right hand side term $\dot{\alpha} = \frac{d\alpha}{dt}$ the curing rate for which several expressions have been given in section 3.1.1.

3.3 Governing equation for the temperature: heat equation

The equation of heat that governs temperature evolution in the part is obtained from the energy balance and is given in Equation 22 ([39]).

$$(\rho Cp)^* \left(\frac{\partial T}{\partial t} + \mathbf{v} \cdot \nabla T\right) = S^{T_{cond}} + S^{T_{polym}} + Bc^{Resin-Fiber} \tag{22}$$

T the temperature of the media composed of fibers and resin and characterized by its porosity ϵ. $(\rho Cp)^* = \epsilon \rho_r Cp_r + (1 - \epsilon)\rho_f Cp_f$ is the homogenized product of density by heat capacity (subscripts r stand for resin and f for fiber). The expression of the source

terms S^x and flow front heat exchange Bc^x are given below: $S^{T_{cond}}$ are the source or sink term relative to the conductive thermal exchanges inside of the media or with the mold and are generically defined in Equation 23.

$$S^{T_{cond}} = k\Delta T \tag{23}$$

where$k$ is the thermal conductivity of the saturated material and ΔT the laplacian of the temperature. $S_{ss}^{T_{polym}}$ is a source term relative to the generation of heat of the exothermic curing reaction. It defined in Equation 24.

$$S^{T_{polym}} = \rho\epsilon\Delta H\frac{\partial\alpha}{\partial t} \tag{24}$$

where ΔH is the heat generated by the curing reaction.

Finally, $Bc_{ss}^{Resin-Fiber}$ is the heat transfer at the flow front corresponding to the thermal exchanges between the resin and the fibers, leading to the resin-fiber temperature homogenization. Due to the small diameter of the fibers, temperature equilibrium is supposed to be achieved instantaneously. Its expression is given in Equation 25.

$$Bc_{ss}^{Resin-Fiber} = \frac{dI}{dt}(1-\epsilon_{ss})\rho_f Cp_f(T_f - T_r) \tag{25}$$

In Equation 25,I is the fluid filling factor, T_f is the temperature of the fibers and T_r the temperature of the incoming resin.

Also on reactive aspects, RTM has been deeply investigated, providing governing and constitutive laws. The numerical methods presented in the literature implementing these equations and their couplings with flow equations will be presented in section 5. But first, the developed techniques in the literature to study experimentally the phenomenon implied in reactive injections and the obtained results will be reported.

4 Experimental studies

4.1 Non-reactive experiments

4.1.1 Study of single-scale porosity flow

As introduced previously, the fluid flow in single-scale porosity materials is classically described by Darcy's equation. Furthermore, this type of material does not exhibit an unsaturated area nor intra-tow resin storage. This has been illustrated by Roy et al. [56] in 2005. The so-called "two-color" experiment has been conducted: green and then blue resin have been injected in a random mat. Colorant distribution at the end of injection can be observed in Figure 10.

It can be clearly seen in Figure 10 that the first (green) injected resin has been pushed forward by the following (blue) resin. This proves that negligible resin storage occurs in the material. Additionally, the flow front is clearly defined, which is a particularity of resin flow in a single-scale porous material.

Thus, the only flow characteristic that requires a tracking is the flow front position to avoid macroscopic dry spots. In order to ensure an accurate description of the flow, Darcy's law validity has been confirmed for fibrous materials in many publications. This validity is confirmed both at a very local scale inside of fiber tows [36] as at the macroscopic scale for random mats ([48] and [72]). This equation is then a starting point for simulations

Figure 10: Colorant distribution at the end of the "two-color" central injection experiment in a single-scale porous material ([56])

(section 5) or injection optimization tools as the mold filling optimization tools proposed in [43] and [7].

The typical single-scale flow characteristics have been identified to be the absence of unsaturated area at the flow front as well as the absence of resin storage within the microstructure.

4.1.2 Study of dual-scale porosity flow

As introduced in section 2.2, dual-scale flow occurs in materials that exhibit two characteristic sizes of pores. Typically for stitched NCF or woven continuous fiber materials, intra-tow gap sizes are in the range of some dozens of micrometers while between the tows, gaps are in the range of one millimeter. This induces several phenomena: presence of an unsaturated area that generates both a non-linearity in the macroscopic pressure field and potential residual porosities as well as intra-tow resin storage that are likely to affect degree of cure and temperature distribution in the part during reactive injection.

Unsaturated area and void formation
Patel et al. ([49]) studied intensively in 1995 the micro-scale mechanisms involved in air entrapment during low injection speed RTM injection. Thanks to image analysis, macroscopic (channel) void proportion was determined and related to the modified Capillary number C_a^* (Equation 14). It was concluded from this work that macroscopic channel void content was minimal for the considered materials (stitched biaxial materials) for modified Capillary number larger than 6.00×10^{-4} to 3.43×10^{-3}. A typical void content versus Capillary number curve is presented in Figure 11 taken from [38].

Using other characterization methods (Standard ASTM-D3171-06 based on density measurement [38]), it has been later demonstrated ([38]) that void content is increasing above a certain value of modified Capillary number due to intra-tow air bubble formation and finally decreasing at higher Capillary number when pressure overcomes a critical pressure leading to air bubble evacuation ([25]). Therefore, void content is not only dependent on the capillary number but also on the distance to the flow front. Several techniques

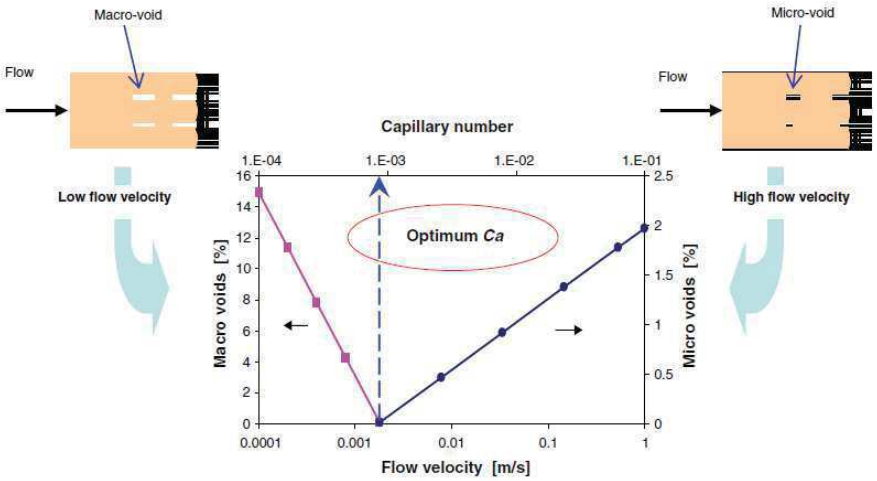

Figure 11: Influence of the Capillary number on the void content generated during RTM process ([38])

based on electrical conductivity ([10]) or optical observations and image analysis ([35], [65] and [23]) highlighted this result. Figure 12 presents the concept of the experience presented by Gascon et al [23].

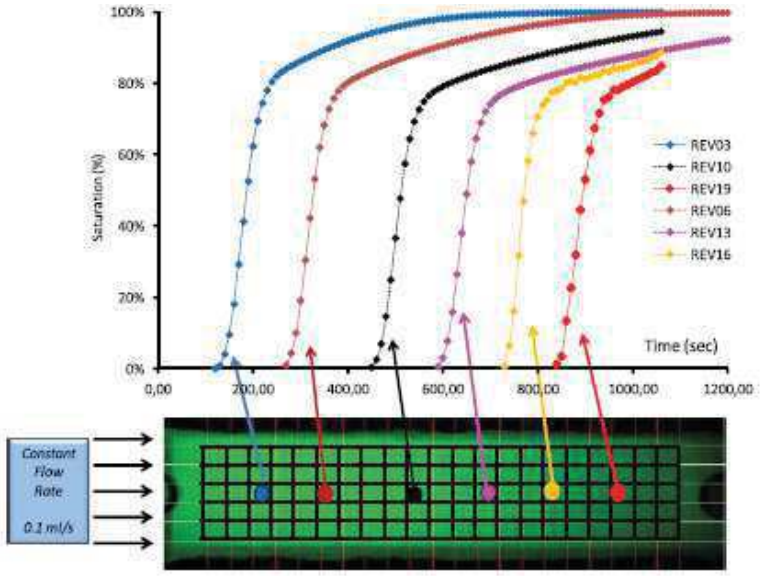

Figure 12: Principle of porosity content tracking using the transparency of glass fibers textiles ([23])

In [35], [65] and [23] the principle of the technique consists in lighting on one side and making pictures on the other side of the part made of glass fiber reinforcements during injection of a transparent fluid. It is assumed that, when the textile is dry, it is opaque and when it is saturated it is fully transparent and appears therefore white or green depending on the color of the injected fluid. The grey or color scale of the pictures is then related to the saturation of the sample through calibration relationships (detailed in [35], [65] and [23]). Other methods have also been proposed to quantify porosity: in [45], the part is photographed during injection and the flow front progression is caught by image difference. The saturation at the flow front is then calculated for each line of pixel using

an equivalent method as in [65]. The details of the method used by Norlund are presented in Figure 13.

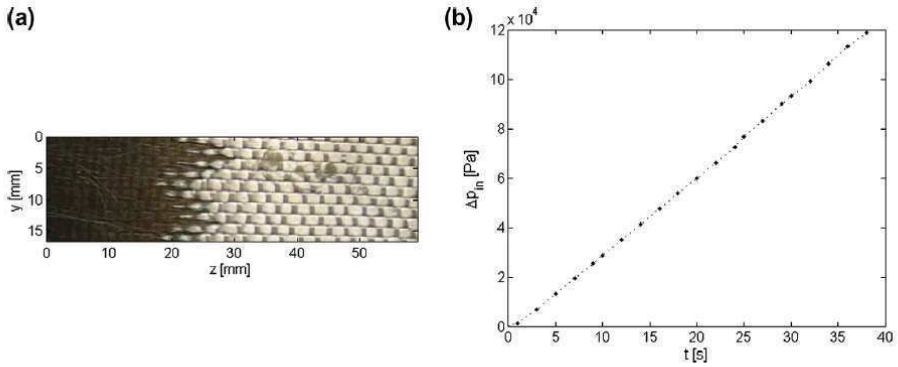

Fig. 6. Experimental data from (a) the video acquisition at $t = 10$ s and (b) the inlet pressure measurement. The resin flows in the positive z-direction. (For interpretation of the references to colour in this figure legend, the reader is referred to the web version of this article.)

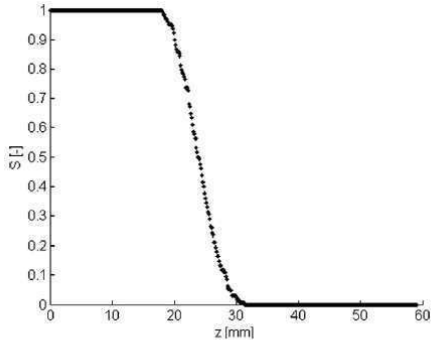

Fig. 7. $S(z)$ calculated by image analysis from the video frame at $t_i = 10$ s.

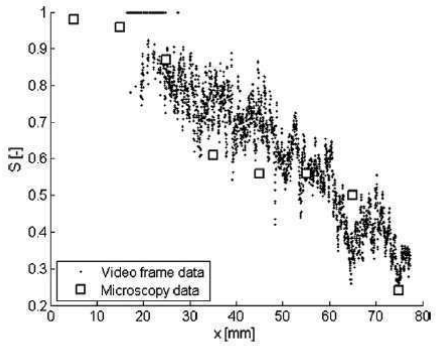

Fig. 8. Measurements of the saturation performed by two analysis methods: video frame analysis and microscopy analysis.

Figure 13: Principle of the measurements realized by Norlund ([45])

Finally, in [60], the porosity content is determined through microtomography analysis.

Two mechanisms of residual porosity formation in dual-scale porous materials have been identified in the literature. At low injection speeds, macroscopic voids are generated in the channels and at higher injection speeds, micro-scale voids are generated in the tows. The micro-scale voids are the more likely to be observed in automotive processes. However experimental investigation quantify their content in the range of some percents that would be acceptable for automotive applications. Additionally, air bubble evacuation has been reported to occur under high pressures. In this context, decision has been made not to further investigate the aspects related to air entrapment

Unsaturated area and pressure profile non-linearity

The dual-scale flow has been reported in some works to induce non-linearities in the inlet pressure during injections at constant injection flow rates. Typical pressure increase during this type of injection is presented in Figure 14 ([25]).

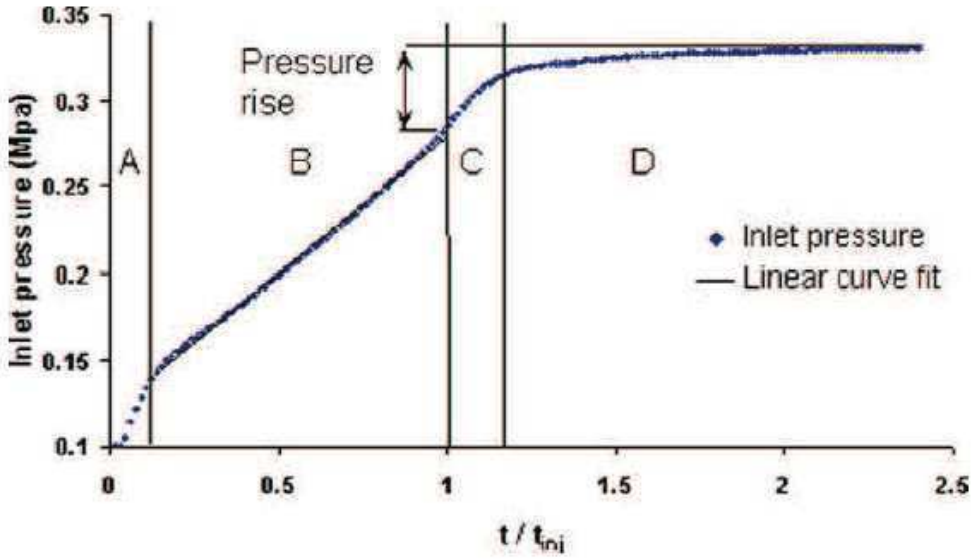

Figure 14: Inlet pressure for an injection at constant injection flow rate ([25])

Four flow phases had been identified ([25] and[47]): phase A, fluid fills the entry cavity and the unsaturated area is generated, B: linear pressure increase as in single-scale porous materials, C: macroscopic flow front has reached the end of the sample, pressure continues rising, D: final stationary state is achieved. It has been determined by Gourichon et al. that the pressure rise in phase C corresponds to the resorption of the unsaturated area and the evacuation of air trapped in the tows during saturation. In some other works, this pressure rise has been observed but in a much higher extent. This is the case for the experiments conducted on the same setup presented in [72], [6], [48], and [80]. In these publications, injections of parts measuring about 1 m are conducted within 10 to 25 s inducing flow velocities of 4 to 10 cm/s. Additionally, injection pressures are in the range of 1 to 5 bar and injections are conducted in a mold with thin transparent top wall. Two typical injection pressure evolutions for injections conducted on a unidirectional material are presented in Figure 15 taken from [72].

As in Figure 14, a pressure rise can be observed on these curves after the end of the theoretical mold filling. However, the value of the pressure rise is very high: almost one half of the final pressure. This significant pressure rise is explained in these works as a consequence of dual-scale flow and of the channel-tow sink effect. However, due to the high flow velocities and high flow pressures, it can be questioned if the observed effects are not due to air bubble formation and delayed evacuations due to the short injection time or to mold deformation.

It has thus been established that injections in dual-scale porous materials induce injection pressure non-linearities compared to theoretical saturated Darcean flow (even in isothermal conditions). Further investigations should be conducted to evaluate the range of maximal pressure rise that can be expected.

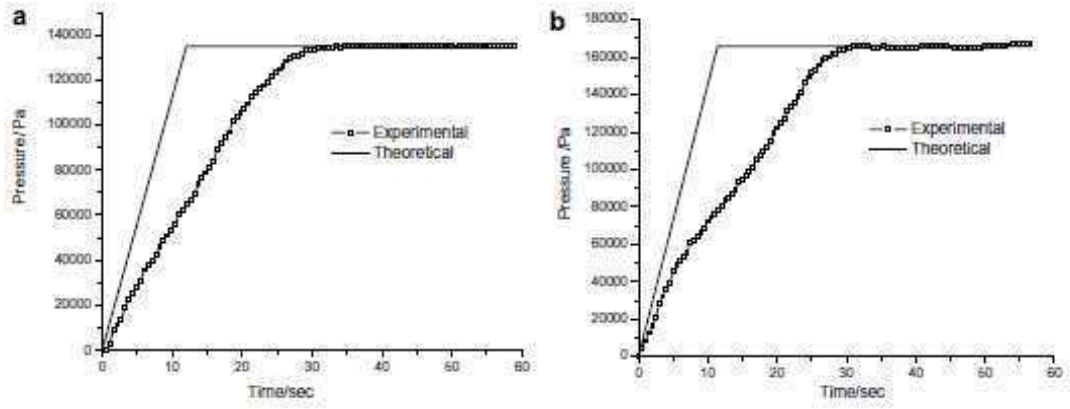

Figure 15: Inlet pressure observed for two unidirectional injection conducted at constant flow rate in a UD material ([72])

Intra-tow resin storage

Another phenomena that has been reported to be linked with the dual-scale porous character of the reinforcement is intra-tow resin storage. In 1998, Shih et al. [62] conducted injections of colored fluids in bidirectional materials. Light colored fluid was first injected in the reinforcement followed by red fluid and it was observed that the secondly injected fluid was mainly flowing in the channels (between the tows) and reached quickly the flow front (Figure 16).

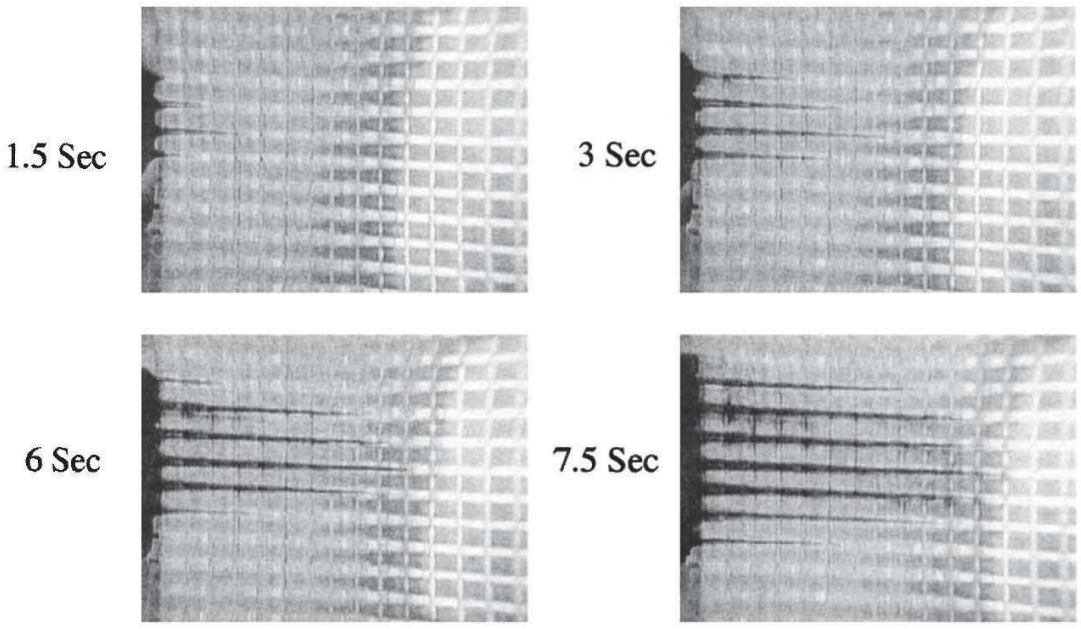

Figure 16: Distribution of a dark colorant during injection in a saturated unidirectional material ([62])

Similar experiments were conducted and reported by Roy et al. in 2005 ([56] and [71]). In this case, the "two-color" experiment presented in section 4.1.1 was conducted in a biaxial NCF. After curing, cuts were made of the parts to investigate colorant distribution within the microstructure and it was established that resin storage did occur inside of the tows (Figure 17). However, these investigations were only conducted in a qualitative manner so that storage evolution with time or volume of injected fluid was not investigated.

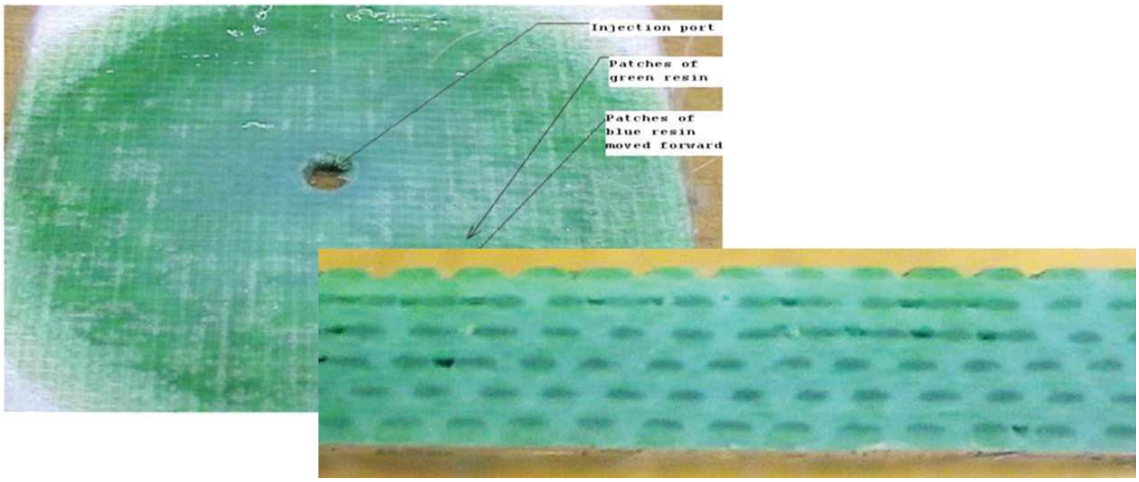

Figure 17: Final aspect of the part after the "two-color" experiment in a biaxial NCF ([56]) and micrograph highlighting the green patches of firstly injected resin stored in the tows ([71])

It has thus been established in the literature that resin storage occurs in the tows of dual-scale porous materials. However, the investigations were conducted only in a qualitative manner such that the evolution of the storage along injection or the influence of textile architecture, fiber orientation or fiber volume fraction was not investigated.

Other dual-scale flow related issues

Additionally, some other work were conducted on the topic of dual-scale porous flow as dynamic response during injection ([29]) or filtration problematics([15] and [4]). A deeper investigation of the micro-scale mechanisms could allow to better understand and predict the observed phenomena related to these topics.

4.2 Reactive experiments

4.2.1 Study of single-scale porosity flow

During the late nineties, several works have been published on the topic of Reaction Injection molding (RIM) and especially on Structural RIM (SRIM). This process is very similar to the reactive RTM process as curing resin is injected in a reinforcement placed in the cavity of a mold. However, the used materials were often random mats for the reinforcements and thermosetting polyurethane for the resins, compared to woven or NCF textiles and Polyester/Vinylester or Epoxy resins for the reactive RTM used nowadays. Kendall et al. [33] and Lebrun et al. [37] studied experimentally as well the filling as the curing stages of the process. Figure 18 presents the mold cavity as well as the injection pressure and the mold temperature during central injection and curing of a polyurethane resin in a continuous strand mat at the fiber volume fraction FVF=0.22 ([33]). In this experiment, resin is injected at 25°C in a fibrous material and a cavity at 74°C. Temperature decreases can be observed at locations 2, 3 and 5 at the very first moments when the resin reaches the sensors but the temperature begins already to increase due to polymerization after 8 s. This highlight that during very reactive injections, significant resin exothermy can occur. Therefore, a fine tracking of the resin and its curing must be realized to control the process.

On the other hand, Lee et al. [39] proposed to simulate the process and correlated it with experimental thermal investigations. Comas-cardona [17] worked on the topic of

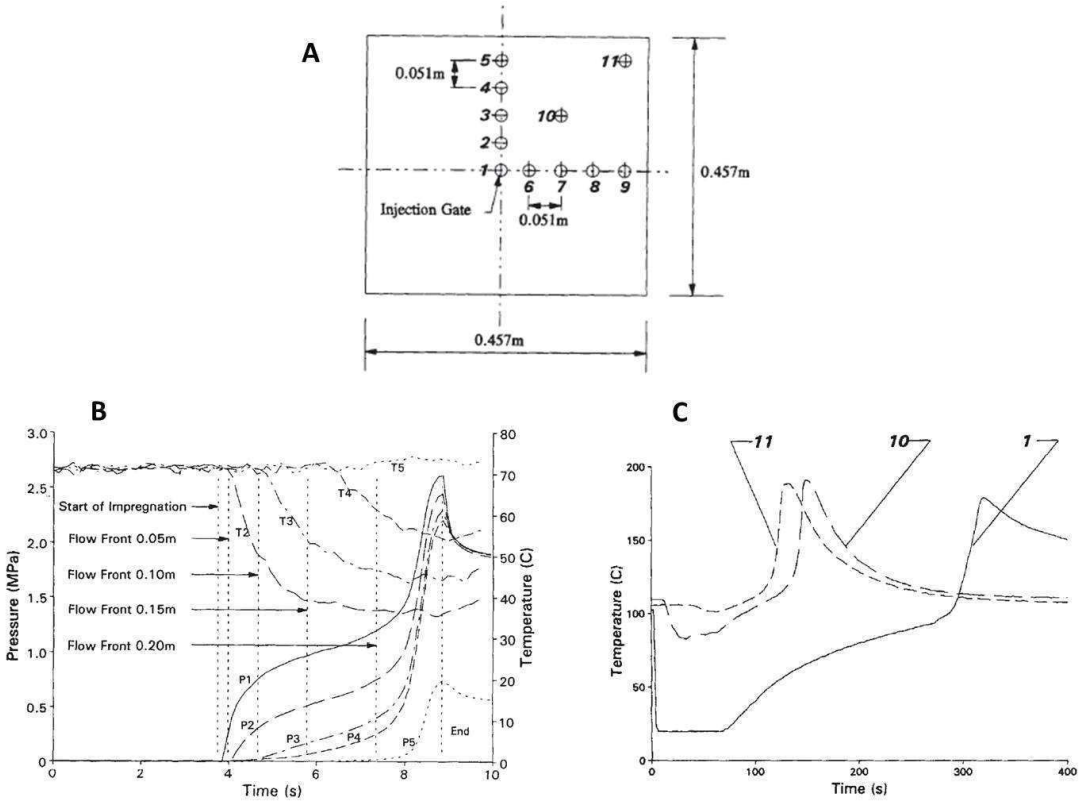

Figure 18: A: Mold cavity with position of the sensors, B: Pressure, temperature and flow front evolution during injection, C: Temperature evolution during injection and curing ([33])

on-line mixing and the optimization of the curing agents proportions during injection to reduce curing duration and to generate spatially homogenized curing. Finally, Antonucci et al. [3] proposed a technique to reduce temperature gradients in the part during curing.

Experimental investigations of SRIM conducted on random mats highlighted significant exothermy of the resin during injection due to curing. This warns about the necessity of tracking accurately temperature and degree of cure distribution in the part in order to control the process. In this context, resin storage reported in 4.1.2 is likely to play a role on the temperature distribution in the part during reactive injections.

4.2.2 Study of dual-scale porosity flow

No publication could be found in the literature specifically dedicated to the experimental investigation of the coupling between dual-scale flow and reactivity. However, Devillard [21] conducted a Vacuum assisted RTM (VARTM) experiment with on-line mixing consisting of a stack of low permeability reinforcements on the top of which was placed a distribution media. This architecture can be considered as a reproduction at a large scale of a dual-scale porous material composed of the low permeability reinforcement playing the role of a tow and the distribution media the role of the channel (Figure 19).

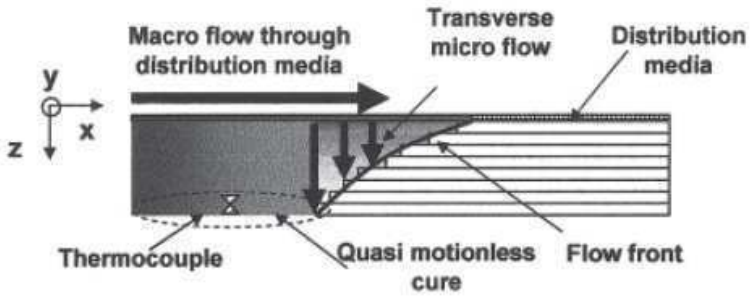

Figure 19: Setup used by Devillard et al. in [21]

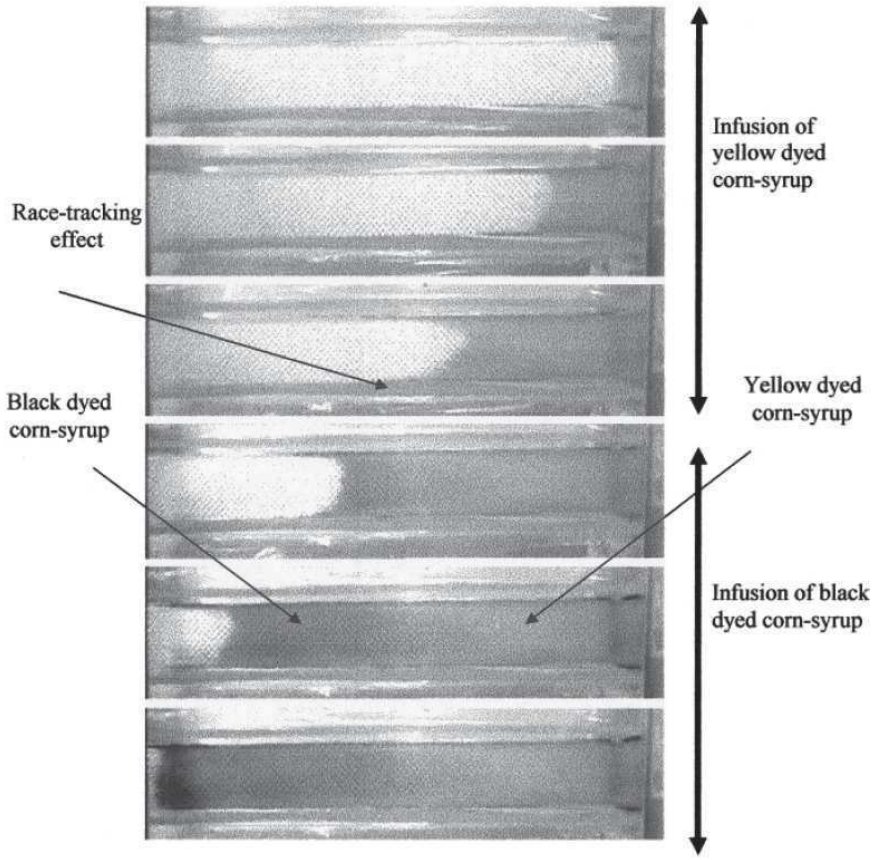

Figure 20: "Tow-color" experiment conducted by Devillard et al. on the stack presented in Figure 19 ([21])

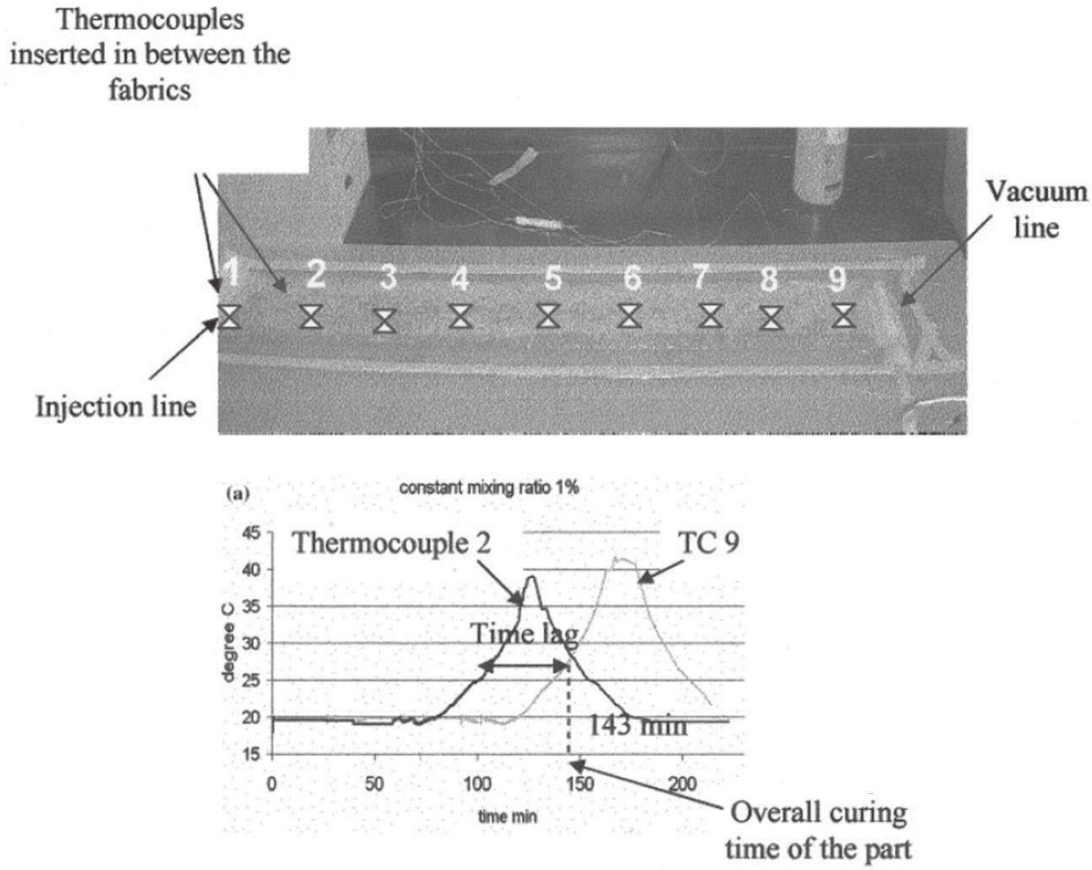

Figure 21: Location of the thermocouples in the part and temperature evolution in thermocouples 2 and 9 ([21])

In this study, Devillard et al. investigated the possibility of changing the proportions of curing agents in the injected resin to ensure homogeneous gelation and curing of the part. The effects of dual-scale flow pattern (resin storage in the low permeability stack) was clearly observed as for a constant mixed resin composition, the latest curing time was observed next to the vents: The resin injected at last (i.e. the youngest resin) flowed in the distribution media to saturate the reinforcement at the end of the part (Figure 20 presents the resin flow pattern and Figure 21 the temperature evolution reported by a thermocouple located at the entry (2) and a thermocouple located at the end of the part (9)). Due to its shorter life time since mixing, curing occurs later than for the first injected resin. Additionally, no particular interaction in terms of temperature exchanges or degree of cure was reported between "channel" and "tow". This might be due to the location of the thermocouples, close to the bottom of the stack (and thus away from the distribution media).

Experimental investigations at a large scale of dual-scale flow conducted by Devillard ([21]) proved the existence of storage effects under reactive conditions. However, no study was found to be conducted on the very local mechanisms involved in tow-channel thermal exchanges expected in dual-scale porous materials. This highlights the difficulty of conducting experiments at such small scales. For this reason, numerical simulation could be profitable to study these local phenomena.

5 Numerical simulations

5.1 Non-reactive simulations

5.1.1 Study of single-scale porosity flow

Several methods as Finite Element Method/Control volume (FEM/CV)([11]), finite difference method ([75]), boundary element method ([82]) or FEM with level set [67] have been proposed in the past to simulate the filling of a part made of a single scale porous material. The FEM/CV method with fixed mesh is nowadays the most used technique. This technique consists in computing the pressure field over the mesh in the saturated domain using mass balance (Equation 6) and Darcy's law (Equation 9). The fluid volume distribution is then computed using the Volume of Fluid (VOF) technique in the Control Volumes associated to each node ([11], [64]) or element ([73], [58]) of the domain. Figure 22 presents the domain discretized for a FEM/CV calculation where Control Volumes are associated to the nodes of the mesh. The wide majority of commercial software for LCM process simulation is based on the FEM/CV technique. LIMS (based on the work of Simacek et al. [64]) uses control volumes associated with the nodes of the mesh while PAM-RTM (based o the work of Trochu et al. [73]) uses directly the volume of the elements as controle volumes.

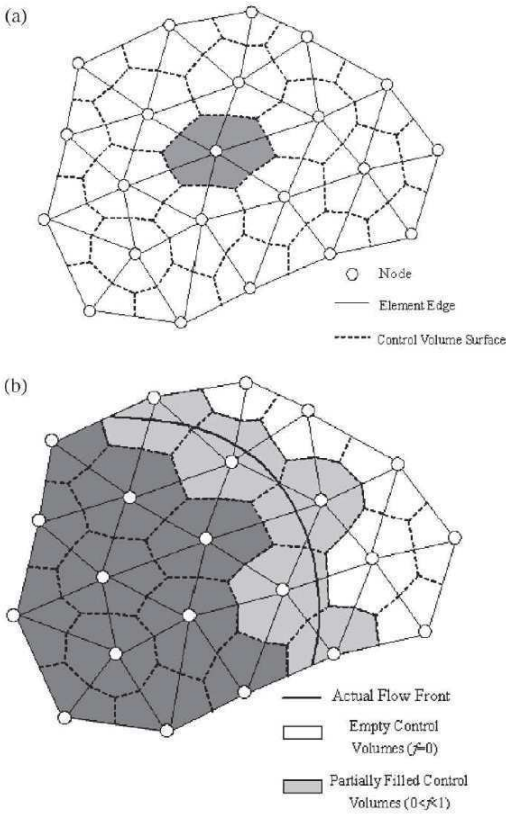

Figure 22: Principle of the CV method with Control Volumes associated with the nodes of the mesh ([69])

5.1.2 Study of dual-scale porosity flow

In order to take the effects of the dual-scale flow into account, new simulation approaches based on the FEM/CV technique have been developed. A first approach called "Two-layer model" has been proposed by Pillai in 2007 ([53]). The principle of this simulation is to

reproduce finely in a 2D model the saturation of a channel and a single-tow. Figure 23 presents the concept of the approach based on finite difference calculations for the transport of the quantities of interest. This model has been used for reactive simulations, the reactive-related results will be discussed in section 5.2.2.

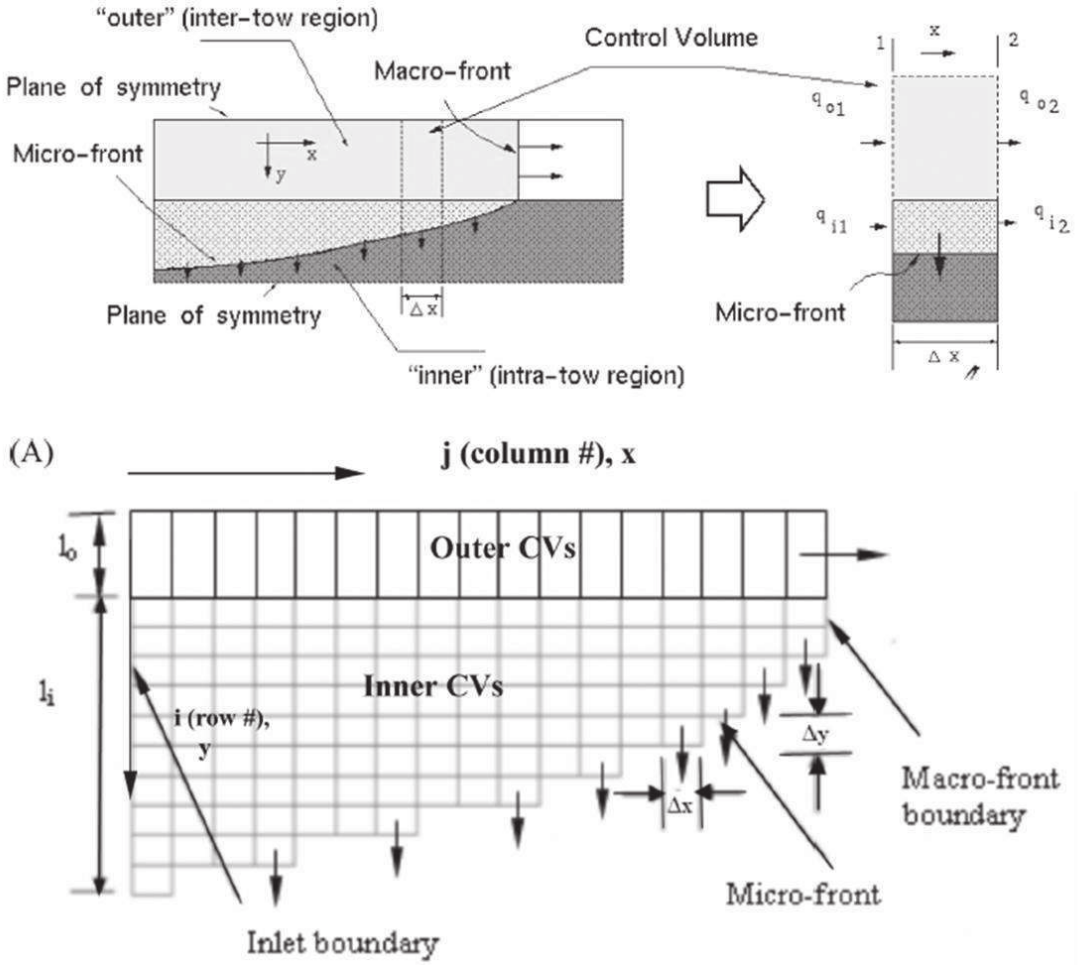

Figure 23: Principle of the "Two-layer model" presented by Pillai et al. in [53]

However, this approach is limited to fluid flow in the direction of the channels and can therefore not be used for 2D or 3D part injection simulations. For this reason, another approach based on the single-scale FEM/CV technique has been proposed. The principle of this new development consists in dividing the volume to be filled in the dual-scale porous material into two domains: a channel domain treated as a single-scale porous medium and a tow domain in which the resin stays stored after saturation. This is numerically done by associating to each control volume of the mesh treating the macroscopic flow an additional volume representative of the microstructure of the material. The general principle of this technique is presented in Figure 24 taken from [70].

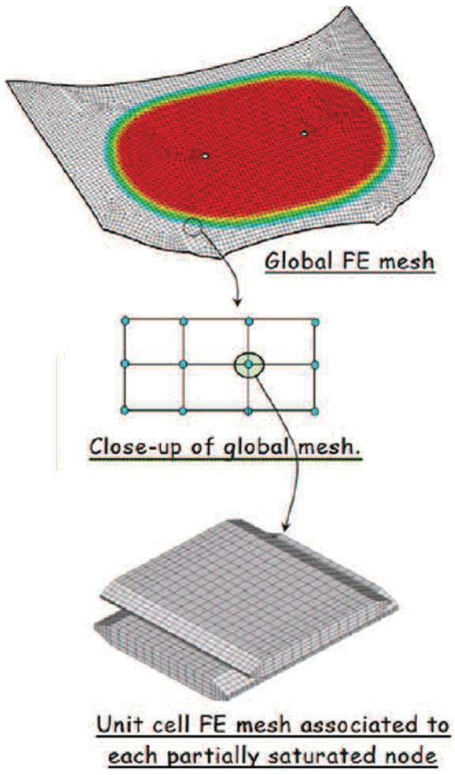

Figure 24: Principle of the FEM/CV dual-scale simulation ([70])

Fluid transfer kinetic between the channel and the tows depends on the model chosen for the microstructure. This technique has been initially proposed by Pillai et al. ([52]) and then further developed by Simacek et al. ([63]). In these approaches, tows have been considered respectively as cylinders or parallelepipeds on the outer boundary of which was applied a pressure boundary condition. Babeau et al. ([5]) proposed also, in the context of the pulltrusion process, to modify the outer boundary condition along the progress of the material through the dye. More complex microstructures have been later proposed: Wang et al. ([77]) proposed a 2D model reproducing a tow cross section, while Tan ([68]) and Lee ([40]) proposed 3D modelisation of tow crossings for UD, biaxial, triaxial or woven textiles. Figure 25 presents examples of microstructures proposed in the literature.

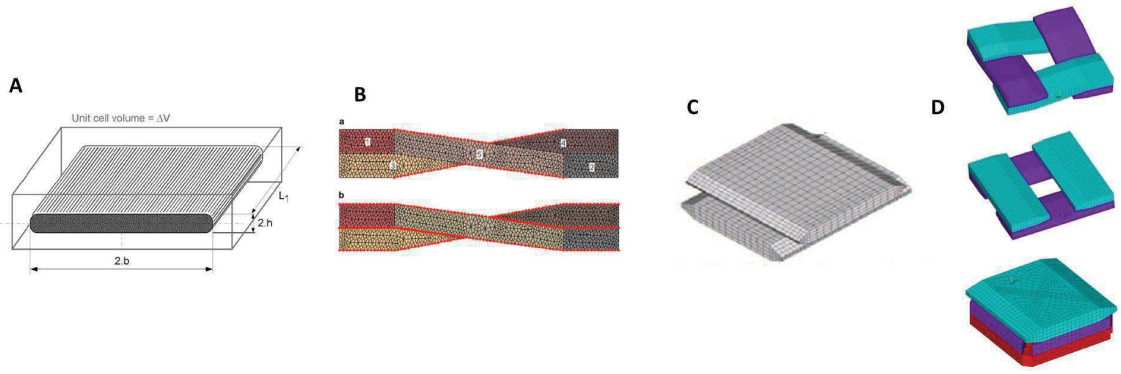

Figure 25: Examples of microstructures used in the literature. A: tow with rectangular cross section ([63]), B: 2D model of tow crossing ([77]), C: 3D model of two superposed tows ([68]), D: Three 3D models of woven, biaxial and triaxial textiles ([40])

This dual-scale simulation approach has then been used for the study of several phenomena. Intra-tow air entrapment has been studied through simulation in [57], [22], [23] and [26]. Additionally, the influence of tow saturation regarding textile and tow shearing has been studied by Walther ([76]). Finally, the influence of dual-scale flow on reactive injections has been investigated and will be detailed in section 5.2.2.

However and despite its advantages and its proven ability to treat accurately the dual-scale flow, the dual-scale FEM/CV technique presents two major disadvantages:

- The association of a specific microstructure to each node of the mesh imposes the size of the elements of the macroscopic mesh.
  This might be a significant meshing constraint and may lead to very heavy calculations as representative cells presented in the literature are in the range of some mm^2 while parts may measure more than 1 m^2.

- The use of 2D or 3D micro-scale models associated to each macroscopic element leads to a huge number of elements and therefore an significant expected CPU time.

Several numerical techniques have been developed to simulate isothermal dual-scale flow. The method featuring the best combination of accuracy, simplicity of use and modification and accuracy should be used in this work to quantify the influence of the different parameters in the process. The choice of a more efficient method for the industrial applications should then be investigated.

5.2 Reactive simulations

5.2.1 Study of single-scale porosity flow

The effects of reactivity on single-scale RTM injections have been experimentally investigated as presented in section 4.2.1, but also numerically. Several numerical approaches have been proposed. Deleglise proposed in 2011 ([20]) to take the viscosity evolution during reactive injection into account. Viscosity evolution with time was first recorded at constant temperature. Then, the ratio K/μ was updated at each time step and at each node depending on the age of the resin that it contained. This technique presented the advantage of being usable with an isothermal simulation approach. However, exact thermal history of the resin could not be tracked. Other methods have thus been proposed to transport and update the various quantities of interest during injection and enable their tracking during injection. Finite element methods have been proposed by Chan et al. ([14]) and Tan et al. with the Flux corrected Transport (FCT) ([69]). While implicit and explicit finite difference techniques have been used respectively by Lee et al.l ([39]) and Abisset-Chavanne et al. ([1]). Qualitative validation of the numerical technique has been conducted in [14], [69] and [1] highlighting interesting results on temperature and degree of cure distribution. Figure 26 presents the results of injection presented in [69]. In this simulation, resin at 20°C is injected in a cavity at 75°C containing fiber at mold temperature. It can be seen that the most cured an hottest resin is located at the flow front, confirming that the numerical method reproduces accurately the non-storage flow observed experimentally.

Additionally, the experimental and numerical results presented by Lee et al. in [39] showed very good agreement.

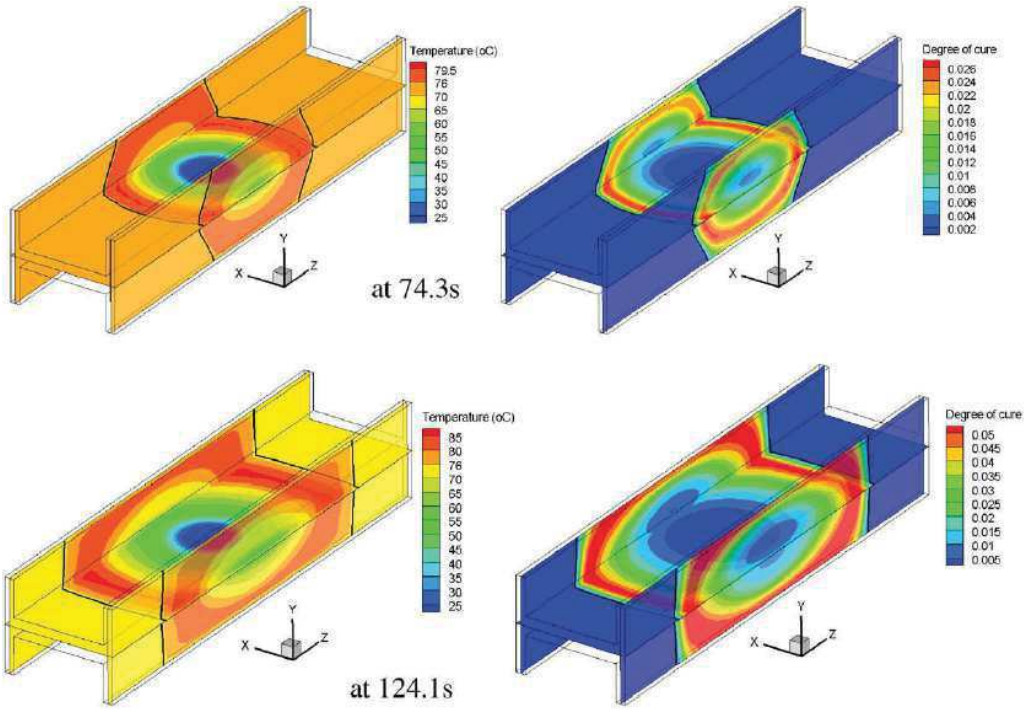

Figure 26: Temperature and degree of cure distribution during reactive resin injection conducted in [69]

Various numerical techniques have been proposed in the literature to simulate the reactive flow of resin in single-scale porous materials. They exhibited good abilities to reproduce the process. The most accurate, efficient and simple to handle approach should be used first to investigate the process and define the requirements for the industrial software.

5.2.2 Study of dual-scale porosity flow

Finally, except the article treating the two layer model ([53]), only one article has been found treating both dual-scale flow and reactive aspects in a manner allowing industrial part manufacturing simulation. In this article proposed by Tan et al. ([71]), the flow aspects of the dual-scale simulation are based on a macroscopic mapping of the channels and the association of a 3D microscopic cell to each node taken from [70]. The thermo-chemo-rheological couplings are treated using the FCT technique introduced in [69]. In this publication, process understanding investigations were conducted by tracking gap and tow temperature evolution during the early stage of a reactive 1D injection of a cold resin in a hot textile. The influence of the pore volume ratio with varying FVF was also investigated revealing an accelerated temperature increase in the tows due to a higher filling speed.

One single article was found dealing with the simulation of a reactive injection in a dual-scale porous material. However, the sensibility study was limited to the influence of the pore volume ratio on the process. Further investigations should therefore be conducted in order to investigate deeper the parameters influencing the reactive injections in single and dual-scale porous materials (differences between single-scale and dual-scale simulations, influence of the injection time/curing time ratio on the property evolution in the part...)

6 Conclusion and research program

6.1 Conclusion

In this chapter, a review of the mechanisms involved in the short cycle time RTM process with on-line mixing have been conducted, as well on the analytical as experimental and numerical aspects. The typical types of textiles used in high speed RTM have been first introduced and identified as dual-scale porous materials made of tows and channels. The isothermal physics of the flow of Newtonian fluids in single-scale and in dual-scale porous materials have been then introduced, followed by the thermo-chemo-rheological physics involved in resin cure. It has been concluded from these investigations that all physical phenomena involved in the process have been mathematically described and can be coupled to produce a simulation tool allowing to reproduce the process. A review of the experimental works conducted on the topic of resin injections in isothermal or reactive conditions and in single-scale as in dual-scale porous materials has been conducted. It has been concluded from these investigations that the dual-scale flow is characterized by the presence of an unsaturated area at the flow front generated by the difference in permeability of the channel and tow regions. Intra-tow resin storage has also been identified as a significant mechanism likely to affect in an important manner temperature and degree of cure distribution during reactive injections. Finally, injection pressure non-linearities compared to theoretical Darcean flows have been reported in various extents that required further investigations. However, only few experimental investigations have been conducted on reactive injections in dual-scale porous materials and especially on intra-tow storage and its influence on the process. Finally, the review of the numerical methods developed to reproduce the RTM process revealed that techniques had been already proposed to simulate both single and dual-scale flows in isothermal and reactive conditions. The dual-scale FEM/CV method has been identified as interesting to treat the isothermal injection. Additionally, the numerical method proposed by Abisset-Chavanne in [1] based on the use of the advection equation of the quantities of interest was found to feature a good mix of

accuracy, simplicity of use and modification and flexibility for a further implementation in a dual-scale model. Results obtained from the simulations in the literature were interesting in terms of isothermal investigation of injection pressure non-linearities but weak on the topic of reactive dual-scale flow.

6.2 Research program

It has been established from the literature review that the high speed reactive RTM process with on-line mixing is coupling multiple physics as dual-scale resin flow, curing and heat exchanges. The understanding and accurate reproduction of these coupled physics is essential to propose an accurate simulation tool. Therefore, a reseach programm has been established. It follows two objectives:

- Investigate numerically and experimentally the reactive RTM process to extract the influencing parameters and phenomena
- Develop an accurate and efficient numerical method integrating the observed significant mechanisms to allow further industrial applications of this research

To achieve these goals, numerical and experimental works have been conducted.

Numerical work

Numerical work, will be focused on:

- Isothermal investigations:
  - Determine the parameters influencing the size of the unsaturated area
  - Determine the parameters influencing the injection pressure non-linearity and its range of values
- Reactive investigations:
  - Study the differences between single-scale and dual-scale reactive simulations
  - Study the influence of the ratio injection time/curing time on the quantities of interest in the part
  - Study the influence of the length of the unsaturated area on reactive injections

In addition to these scientific investigations on the influencing parameters of the reactive RTM process, development work has been conducted to propose an accurate, flexible and efficient simulation technique.

Experimental work

Experimental work focused on investigating intra-tow storage mechanisms. The main goals were to:

- Study quantitatively resin storage along injection for:
  - various textile architectures
  - various fiber volume fractions
  - various fiber orientations
- Identify and quantify the mechanisms involved in storage or release of the intra-tow resin

Part II
Numerical simulation of the reactive RTM process

1 Developed numerical methods

As introduced in the previous section, the aim of the study is to identify and quantify the mechanisms involved in the reactive RTM process with on-line mixing. However, very local mechanisms are difficult to study experimentally, therefore, a numerical simulation approach has been developed. The aim of this simulation tool is to describe finely the resin flow and curing during the reactive RTM process with on-line mixing within single or dual-scale porous reinforcements. As introduced in the previous section, the technique of Finite Element Method/Control Volumes (FEM/CV) used in [58] and [1] has been worked with and further developed to treat also dual-scale flow. Within this section, single-scale and dual-scale simulations will be introduced first for non-reactive and then for reactive injection conditions.

1.1 General concept

1.1.1 Notion of single-scale and dual-scale materials

In the frame of this chapter, a reinforcement will be called "single-scale porous material" if it is defined by an homogeneous microstructure characterized by a single value of Fiber Volume Fraction (FVF) (and thus a single value of porosity ϵ_{ss}) and a single permeability tensor $\mathbf{K}_{ss}$. It is thus important to notice that the notion of single-scale porous material can be used both for reinforcements that feature physically a single-scale pore size or for a dual-scale porous material whose characteristics are homogenized macroscopically. Tables 1 and 2 summarizes the values of the reinforcements properties required for the single-scale and dual-scale simulations as well as the equations used for the homogenization of the dual-scale properties.

Single-scale material		**Dual-scale material**	
		Single-scale simulation	
Average permeability	$\mathbf{K}_{ss}$	Average permeability	$\mathbf{K}_{ss} = \mathbf{K}_c$
Macroscopic porosity	ϵ_{ss}	Macroscopic porosity	$\epsilon_{ss} = (1 - \varphi_c)\epsilon_t$
Average thermal conductivity	$\mathbf{k}_{ss}$	Average thermal conductivity	$\mathbf{k}_{ss} = \mathbf{k}_r(1 - \varphi_c)\epsilon_t$ $+\mathbf{k}_f\varphi_c\epsilon_t$
Average heat capacity	Cp_{ss}	Average heat capacity	$Cp_{ss} =$ $Cp_r(1 - \varphi_c)\epsilon_t$ $+Cp_f\varphi_c\epsilon_t)$
Average density	ρ_{ss}	Average density	$\rho_{ss} = \rho_r(1 - \varphi_c)\epsilon_t$ $+\rho_f\varphi_c\epsilon_t$

Table 1: Material parameters required for the simulations

Dual-scale material		**Dual-scale material**	
Dual-scale simulation		Single-scale simulation	
Tow geometry	$\circ$ or $\square$		
Tow dimensions	Radius or thickness		
Channel/Overall volume ratio	$\varphi_c = V_c/V_{tot}$		
Channel permeability	$\mathbf{K}_c$	Average permeability	$\mathbf{K}_{ss} = \mathbf{K}_c$
Tow transverse permeability	K_t		
Channel porosity	$\epsilon_c = 1$	Macroscopic porosity	$\epsilon_{ss} = (1 - \varphi_c)\epsilon_t$
Intra-tow porosity	ϵ_t		
Channel thermal conductivity	$\mathbf{k}_c = \mathbf{k}_r$	Average thermal conductivity	$\mathbf{k}_{ss} = \mathbf{k}_r(1 - \varphi_c)\epsilon_t + \mathbf{k}_f\varphi_c\epsilon_t$
Intra-tow thermal conductivity	$\mathbf{k}_t = \mathbf{k}_r(1 - \epsilon_t) + \mathbf{k}_f\epsilon_t$		
Channel heat capacity	$Cp_c = Cp_r$	Average heat capacity	$Cp_{ss} = Cp_r(1 - \varphi_c)\epsilon_t + Cp_f\varphi_c\epsilon_t)$
Intra-tow heat capacity	$Cp_t = Cp_r(1 - \epsilon_t) + Cp_f\epsilon_t$		
Channel density	$\rho_c = \rho_r$	Average density	$\rho_{ss} = \rho_r(1 - \varphi_c)\epsilon_t + \rho_f\varphi_c\epsilon_t$
Intra-tow density	$\rho_t = \rho_r(1 - \epsilon_t) + \rho_f\epsilon_t$		

Table 2: Material parameters required for the simulations

In Tables 1 and 2 $\mathbf{k}_r$ and $\mathbf{k}_f$, Cp_r and Cp_f, ρ_f and ρ_t respectively the resin and fiber thermal conductivity tensors, heat capacities and densities.

It will be thus possible to conduct, for a material exhibiting a dual-scale microstructure, a classical single-scale (with homogenized properties) or a dual-scale (with detailed microstructure) simulation. Such comparisons will especially highlight the enrichment provided by the dual-scale simulation.

1.1.2 Numerical technique

As presented in the literature review, the chosen model for the dual-scale simulation tool is based on the FEM/CV. A macroscopic mesh is used to deal with the flow in the channels while a microstructure is associated to each macroscopic element to allow reproducing both the unsaturated area and the intra-tow resin storage. As conducted in other works, the simulation strategy will consist in treating both macroscopic (channel) and microscopic (intra-tow) levels as two single-scale media governed by Darcy flows. Additionally, the evolution of the quantities of interest at both scales are related through sink or source

terms is added in the advection equations. Therefore and as introduced in the previous section, presenting separately the single-scale and dual-scale simulations is motivated both by the fact that single-scale simulation is the ground algorithm of the dual-scale simulation; but also by the utility of a single-scale simulation to compare its results with the ones of dual-scale simulation. For this reason, the numerical strategy for the simulation of a single-scale porosity material will be first introduced before the introduction of the additional features related to the dual-scale simulation.

1.1.3 Notation conventions

In order to differentiate the several models, time steps and elements, subscripts, superscripts and element names will be used. They are summarized below:

Subscripts

- ss: Single-scale
  The subscript ss will be used for the variables describing the quantities of interest in the single-scale simulations.
- c and t or x: Dual-scale
  The subscript c will be used for the channel level in the dual-scale simulation and the subscript t for the tows. For generic expressions valid at both scales in the dual-scale simulation, the subscript x will be used.

Superscripts

- $n-1$: Previous time step
- n: Current time step
- $n+1$: Next time step

Element name

- e: Considered element
- e^-: Upstream element(s)
  Finally, notation e will be used for the currently considered element while e^- will be used for the single or multiple upstream element(s).

1.2 Non-reactive single-scale model

In this section, the variables and ground algorithm necessary to compute the non-reactive resin flow in a single-scale porous material will be introduced.

1.2.1 Introduction of the variables

The pressure field P_{ss} is defined using pressures values P_i at the nodes of the mesh and linear shape functions ϵ_i associated with each node i of the model. The expression of P_{ss} is given in Equation 26.

$$P_{ss} = \sum_i \epsilon_i P_i \tag{26}$$

Furthermore, the following variables are defined and feature constant values in each element that has begun to be filled. It is assumed that, on the inflow boundary of each element, the physical value is equal to the value in the upstream element.

- $\mathbf{v}_{ss}$: Darcy's velocity of the fluid in the element e governed by Darcy's law (Equation 27):

$$\mathbf{v}_{ss} = \frac{-\mathbf{K}_{ss}}{\mu_{ss}} \nabla P_{ss} \tag{27}$$

- I_{ss}: Fluid fraction in the control volumes
  The fluid fraction function I_{ss} indicates the ratio of the volume of fluid present in an element, to the overall volume of this element. It is also the ratio of saturated exchange surface between two elements to the overall exchange surface. The fluid fraction is governed by the advection Equation 28 in the whole impregnated domain.

$$\frac{\partial I_{ss}}{\partial t} + \mathbf{v}_{ss} \cdot \nabla I_{ss} = 0 \tag{28}$$

1.2.2 General algorithm

Overview
Computation of the single-scale cavity filling follows a four step explicit incremental algorithm with constant time step inspired from [1]. The different steps are listed bellow.

1. Computation of the macroscopic pressure field using a FEM/CV method
2. Computation of the fluid velocity in the elements
3. Calculation of time step duration
4. Updating of the fluid-fraction

Detailed Algorithm
Details on the different steps of the algorithm are given hereafter.

1. Pressure field calculation
   The first step of the numerical strategy consists in computing the macroscopic pressure field in the impregnated area. Darcy law (Equation 27) and mass balance equations are combined to obtain Equation 29.

$$\nabla \cdot \left(-\frac{\mathbf{K}_{ss}}{\mu_{ss}} \nabla P_{ss} \right) = 0 \tag{29}$$

   Using the variational formulation, Equation 29 is rewritten as Equation 30, over the saturated domain, which states that for a linear shape function φ^*:

$$\iiint \nabla \varphi^* \cdot \left(-\frac{\mathbf{K}_{ss}}{\mu_{ss}} \right) dV = \oint \varphi^* \frac{-\mathbf{K}_{ss}}{\mu_{ss}} \nabla P_{ss} \cdot \mathbf{n} dS \tag{30}$$

   This equation is used in matricial form to calculate the pressure in the impregnated area. The left hand side term is transformed into the product of a "stiffness matrix" and a vector containing the pressure values at the different nodes using the shape functions while the right hand side terms correspond to the boundary conditions. It is also used to impose velocity boundary conditions on the model.

2. Fluid flow velocity
   From the pressure field, upstream and downstream elements are determined for each element of the impregnated area. Then, using Darcy's law (Equation 27) and the pressure at the nodes of each element, the velocity of the fluid is computed in each element of the impregnated area.

3. Time step determination
   Once the flow velocity has been calculated in each element, the time step must be determined in order to compute the volume of fluid entering and exiting each element during the time step. In order to avoid element overfilling the condition presented in Equation 31 is applied.

$$I_{ss}^{n+1} - I_{ss}^{n} \leqslant (1 - I_{th}) \tag{31}$$

   In Equation 31, I_{th} is a number close to one (in the case of this study I_{th}=0.95). I_{th} corresponds to the level of element filling above which an element is considered as filled. In order to reduce the computational cost of the time step determination, the current time step is computed by adjusting the previous time step using the filling conditions obtained from the previous time step. The minimal value of Δt^n obtained over all elements from Equation 32 is used for the current calculation.

$$\Delta t^n = \Delta t^{n-1} \times \left(\frac{1 - I_{th}}{I_{ss}^{n} - I_{ss}^{n-1}} \right) \tag{32}$$

4. Fluid fraction calculation

   General Principle
   From the flow velocities, the list of upstream and downstream elements (based on the average node pressure) and the duration of the time step, the exchanged volume of fluids and fluid fractions are computed. The weak form of Equation 28 is integrated and expressed using a first order explicit approximation of the time derivative. Moreover, as proposed in [58], the test function δ_x is introduced in the equation in order to avoid diffusion of the macroscopic flow front (δ_x=1 if the element e is numerically considered as filled, δ_x=0 in the other cases). Equation 33 is obtained.

$$I_{ss}^{n+1}(e) = I_{ss}^{n}(e) - \delta_{ss}^{n}(e) I_{ss}^{n}(e) \frac{V_{out}^{n+1}(e)}{V_{ss}(e)} + \delta_{ss}^{n}(e^{-}) I_{ss}^{n}(e^{-}) \frac{V_{out}^{n+1}(e^{-})}{V_{ss}(e)} \tag{33}$$

   In this equation, $V_{out}^{n+1}(e)$ is the volume flowing out of the element e at time step $n+1$ calculated from fluid velocity in e through the edges of the element. e^{-} is the upstream element of element e thus, $V_{out}^{(n+1)}(e^{-})$ is the overall volume coming in the element e at time step $n+1$. Finally, $V_{ss}(e)$ is the volume of fluid that can contain the element e.

   Mass conservation
   In order to avoid any element over-filling and thus to ensure mass conservation, the fluid fraction calculation is conducted from the upstream to the downstream elements. Elements are sorted from the maximal average pressure to the minimal average pressure (average is made on the values of pressure at the three nodes of the elements). Thus, if for numerical reasons, the computed fluid fraction in an element is greater than 1, the extra volume is automatically added to the volume flowing out of the element. This extra volume is distributed to the single or two downstream elements proportionally to the transferred amount of fluid computed with Darcy's equation. Thus, when Equation 33 is used to compute the fluid fraction in the downstream element(s), the volume of fluid coming from the element e includes the fraction of extra volume. To conclude the fluid factor in the element e is equal to 1 and the extra fluid volume is not lost but transferred to the downstream elements according to the physics of the flow.

Once the fluid fraction has been updated in each element, the new nodes that belong to the saturated area are included in the calculation of the new pressure profile and a new loop begins.

1.3 Non-reactive dual-scale model

1.3.1 Dual-scale flow related sink term

As introduced in part I, the dual-scale simulation allows reproducing the unsaturated area. In this region, fluid flowing in the channels is absorbed in the tows. Therefore, the condition of mass balance at the macroscopic scale must be adjusted using a sink term. This affects, thus, the computation of the pressure field but also the advection equation for flow at the macroscopic level. The new equation (Equation 34) for the computation of the pressure includes a sink term S_I.

$$\nabla \cdot \left(-\frac{\mathbf{K}_{ss}}{\mu_{ss}} \nabla P_{ss} \right) = S_I \tag{34}$$

The sink term S_I is relative to the absorption of fluid in the tows. The generic expression of S_I is given in equation 35 with Q_{abs} the absorption flow rate in the tows and V_c the volume of the macroscopic element.

$$S_I = \frac{Q_{abs}}{V_c} \tag{35}$$

S_I is not equal to zero at the macroscopic scale when the tows are being filled and is equal to zero when the tows are saturated. S_I is also equal to zero at the micro-scale as the flow in the tows is single-scale. The new numerical technique developed in this work to compute S_I in the unsaturated area will be introduced in the following section.

It can be additionally noticed that the sink term introduced in the calculation of the fluid factor features the same expression as S_I. With this sink term, Equation 28 becomes:

$$\frac{\partial I_{ss.}}{\partial t} + \mathbf{v}_{ss} \cdot \nabla I_{ss} = S_I \tag{36}$$

1.3.2 Macro-micro volume distribution

The dual-scale simulation, based on a macroscopic mesh, made of triangular elements covering the whole part, allows dealing with the flow in the channels of the material while a representative microstructure is associated to each macroscopic element to treat the flow in the tows. In the frame of this work, decision has been taken to adapt the microstructure associated to each macroscopic element to the size, shape and textile shearing of the considered element. This approach allows indeed to be more flexible in terms of meshing. A convergence study in section 1.3.5 will demonstrate the robustness of the developed method.

Starting from a given macroscopic mesh, the method used in this study allows defining an equivalent microstructure associated to each element. This macro-micro association is based on purely geometrical considerations. Tow geometry (cylindrical or rectangular cross section), tow radius or thickness, inter-tow gap sizes in weft and warp directions for biaxial textiles as well as fiber orientations (obtained from former draping simulations for example) are considered. Then using the size and shape of the triangular elements of the mesh and the shearing in the element, the number of tows in both directions, as well as the average length of tows in both directions is determined in order to maintain the appropriate overall porosity in the element. The principle of the volume distribution technique is presented in Figure 27 and the detailed calculations are presented in Appendix 8.

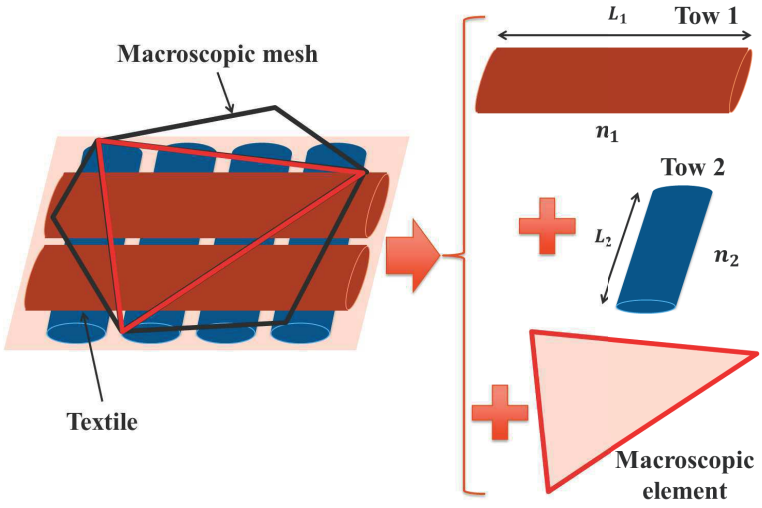

Figure 27: Principle of the microstructure determination method for the dual-scale simulation

Thanks to this technique, it is therefore possible to determine the number and average length of the tows in both directions of the textile whatever size or shape the element may have, the only limitation being the necessity for the element to be larger in both directions than half the width of one tow. During the simulation, all tows in warp and all tows in weft direction will be supposed to fill simultaneously within the same element so that the injection problems will be reduced to two tows: one in each direction. The volumes of fluid absorbed, computed for these two tows, will then be multiplied by the number of tows in both directions in each element and removed from the macroscopic (channel) level.

1.3.3 Microscopic tow discretization

As the tows are considered as single-scale porous media, the classical FEM/CV approach is used to compute the pressure and the filling of the microscopic elements. This approach is based on a meshing of the tows. Three assumptions are made regarding tow filling which helps defining the microscopic tow meshing:

- In each element, the ratio of tow impregnated surface to the overall tow surface is assumed equal to the fluid fraction (Figure 28).
  This assumption neglects the influence of the flow front orientation relatively to the tows on the impregnation. However, more complex law relating the ratio of volume and the ratio of impregnated surfaces could be introduced to deal with this aspect without introducing difficulties. Additionally, as the location of the resin in the element is not known, and for sake of simplicity, in the following representations, tow filling will be conducted from one end of the tow. However, it would give identical results starting from any location on the tow. In Figure 28, I_c is, as defined, the ratio of impregnated volume V_{imp} to the volume of the macroscopic element V_c. It is equal to the ratio of tow impregnated surface S_{imp} to the total tow surface S_{tot} and also to the impregnated length L_{imp} to the total length of the tow L.

- Tow filling is assumed to occur exclusively transversely in the tows
  For fast injections (less than a few minutes for parts whose dimensions are in the range of 1 m^2) and high pressures (5-30 bar), calculations made on simple cases highlighted that the ratio of longitudinal intra-tow permeability to channel permeability induces a major difference in flow velocities. Therefore longitudinal intra-tow

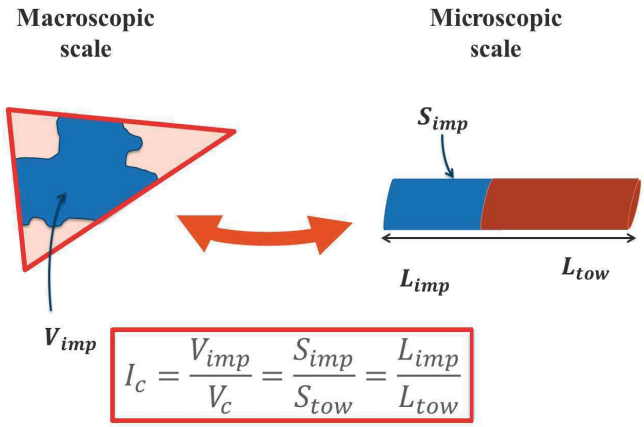

Figure 28: Equivalence between macroscopic fluid fraction and saturated/total macroscopic volume, tow surface area and tow length

flow is assumed negligible in the developed simulations during and after saturation. Therefore the major phenomena generating the impregnation of the tow is the transverse tow filling. Channel permeability to transverse tow permeability ratio has been reported to be in the range of 50 to 2000 ([59], [70]), for this reason, channels are expected to be filled much faster than the tows so that the tows being impregnated are considered to be surrounded with fluid over their whole periphery. Thus, tow filling problems are reduced to simple 1D filling problems with imposed inlet pressure on the surface of the tow. This pressure is the addition of the channel pressure and the capillary pressure. In the case of cylindrical tows, a radial flow problem is solved, in the case of a rectangular cross section, the flow problem is solved in the half thickness of the tow with a 1D Cartesian formulation.

- The tow radius or half thickness cannot be discretized in elements smaller than 10 times the radius of a glass fiber (0.15 mm) in the transverse direction.
  With this condition, it is assumed that the flow occurs in an homogeneous medium. Therefore Darcy's equation can be used.

Additionally, as explained in the previous section, the microscopic filling problem in each element can be reduced to two tow filling problems treated separately, one for the warp and one for the weft direction. The tow filling problem is illustrated in Figure 29.

As presented in Figure 29, the discretization of the tow is made both in the transverse (A) and the longitudinal (B) directions. The mesh in the transverse direction is fixed and used for the FEM computation of the pressure field. Furthermore, a longitudinal mesh is built along the filling of the macroscopic element (figure 4B) using a numerical method presented in the following section. This longitudinal mesh defines "columns" that will be treated as separated 1D filling problems. These "columns" will allow representing finely the unsaturated area even in macro elements bigger than this unsaturated area. The only limitation of this approach is the condition that in each "column", the fluid should not fill more than the neighbor element of an element containing fluid. This condition is imposed by the VOF method used to compute the values of the quantities of interest in the tows. This microscopic tow discretization presents the following advantages:

- The evolution of the fluid in the longitudinal direction is not limited by any pre-positioned mesh.
  This makes the approach more flexible in terms of time step definition as there is no additional limitation of the flow front longitudinal progress within a time step (the same criteria as for the single-scale model is used to avoid macroscopic over-filling).

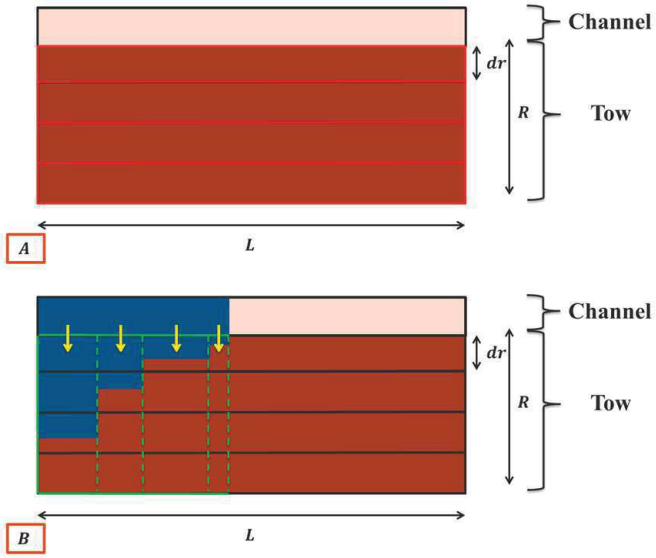

Figure 29: General principle of microscopic tow discretization, (A) transverse fixed discretization and (B) longitudinal discretization built along element filling

- The longitudinal discretization and the purely transverse flow assumption reduce the filling problem to a sum of 1D filling problems in each of the "columns".
  This approach is less CPU time consuming than a 2D or 3D approach as the maximal number of 1D pressure field computations to solve is equal to $2N - 1$ with N the number of microscopic elements in the thickness of the tow (micro transverse flow front can be initially located at N positions and can progress of 1 thickness element for all positions except for the central element, leading to a maximal number of pressure calculations equal to $2N - 1$).

- The method is applicable whether the elements of the mesh are smaller (Figure 30 A) or bigger (Figure 30 B) than the unsaturated area.
  This is a major advantage as the method can be applied to any mesh without caring about the size of the unsaturated area as it would be done for a classical single-scale simulation.

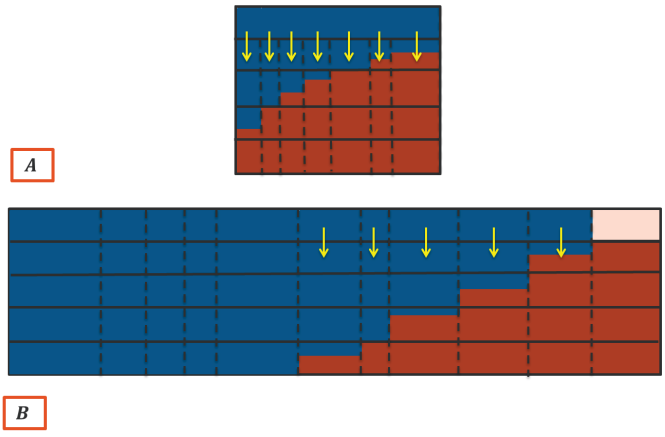

Figure 30: Examples of configurations in which the unsaturated area is smaller or larger than the equivalent length of the tow in the considered element

1.3.4 Dual-scale filling algorithm

The dual-scale filling algorithm follows the same steps as the single-scale simulation. However some additional features are required. The general algorithm is detailed (calculations that require an adaptation are listed in bold) and the new features are listed and detailed below.

Overview

1. **Computation of the macroscopic pressure field using a FEM/CV method**
   The macroscopic pressure computation must be modified in unsaturated area as mass conservation is not ensured in the channels due to intra-tow absorption.

2. Computation of the macroscopic fluid velocity in the elements
   Darcy's law is used as for the single-scale simulation.

3. **Calculation of time step duration**
   At the macroscopic level, the same criteria is used as in the single-scale simulation to avoid any element over-filling. Additionally, a criteria is added on the time step to ensure that no more than one transverse element will be filled at the microscopic scale during 1 time step.

4. **Update of the macro and micro fluid-fraction including micro-scale pressure field calculation**
   A new technique is used to compute the macro and micro fluid fraction to satisfy both intra-tow transverse Darcy equation and macro-micro mass conservation.

Specificities of the dual-scale simulation will be precised below.

Detailed algorithm

1. Macroscopic pressure field computation
   It is made with the same technique as for the single-scale simulation but using Equation 34. Its variational formulation is:

$$\iiint \nabla\varphi^* \cdot \left(-\frac{\mathbf{K}_{ss}}{\mu_{ss}}\right) dV = \oint \varphi^* \frac{-\mathbf{K}_{ss}}{\mu_{ss}} \nabla P_{ss} \cdot \mathbf{n} dS - \iiint \varphi^* S_I dV \qquad (37)$$

   Due to the presence of the sink term, the pressure field is modified in the region of the unsaturated area. Additionaly, as for the single-scale simulation, upstream and downstream elements are then determined for each element of the impregnated area.

2. Flow velocity calculation
   Using Darcy's law and the pressure at the nodes of each element, the channel flow velocity is computed in each element of the impregnated area.

3. Calculation of time step duration
   The macroscopic criteria used to avoid element overfilling is the same as for the single-scale simulation. Additionally, a criteria is added to ensure that not more than one element is filled in the transverse tow direction. The expression of Δt to satisfy this criteria is given in Equation 38.

$$\Delta t \leqslant \frac{\Delta z^2 \mu_c}{P_{av} K_t} \qquad (38)$$

where Δz is the tow transverse discretization size and P_{av} is the average pressure over the three nodes of the macroscopic element that is used as boundary condition for the tow filling problem. The minimum value between the macroscopic and microscopic computed time steps duration is retained. As for the single-scale simulation, the volumes exchanged between the elements is computed.

4. Macroscopic and Microscopic filling
Considering the element e_{macro} with n_1 tows in direction 1 and n_2 tows in direction 2. Tows in direction 1 have the average length L_1 and tows in direction 2 the average length L_2.
As explained in the previous section, a result of the macroscopic pressure and flow velocity determination is the amount of fluid V_{in} coming in the considered element during a considered time step. This volume needs to be shared between the macroscopic and the microscopic scales. In fact, a position of equilibrium for the macroscopic flow front can be determined analytically so that both Darcy's flow in the tow and mass balance for the distribution of V_{in} between the two scales can be satisfied.

First time step of the elements filling

When fluid arrives for the first time in an element, the distribution of the volume V_{in} between the macroscopic and microscopic levels requires determining:

- The position in the thickness of the tow that will be reached by the microscopic flow front during the time step due to Darcy's flow.
- The increase in impregnated tow surface (corresponding to the longitudinal propagation of the flow front) during this time step.

These two problems are solved analytically using the following processes:

Flow front position in the thickness of the tow
A simple 1D filling problem is solved to determine the position reached in the thickness of the tow during the purely transverse filling. The average pressure over the three nodes of the macroscopic element added to the capillary pressure computed from the expression given by Ahn [2] is used as boundary condition. Using the transverse discretization of the tow, the pressure field is computed using Equation 29 applied to the case of the 1D transverse tow problem. Flow velocity is additionally calculated using Darcy'law (Equation 27). The duration of the time step allows determining the volumes V_1 and V_2 of fluid that would be absorbed through the entire surface of one tow in directions 1 (S_{tot1}) and 2 (S_{tot2}). Thus the volumes of fluid really absorbed in tows 1 and 2 during the time step are respectively $V_1 \frac{S_{imp1}}{S_{tot1}} n_1$ and $V_2 \frac{S_{imp2}}{S_{tot2}} n_2$ with S_{imp1} and S_{imp2} the exchange, impregnated, surfaces between channel and tows 1 and 2. S_{imp1} and S_{imp2} need to be determined.

Impregnated tow surface determination
The volume injected in the element, V_{in}, needs to be shared between the channel and the tow satisfying mass balance. Its distribution satisfies Equation 39.

$$V_{in} = V_1 \frac{S_{imp1}}{S_{tot1}} n_1 + V_2 \frac{S_{imp2}}{S_{tot2}} n_2 + V_{imp} \tag{39}$$

In Equation 39, V_{imp} is the volume remaining in the channel.

Assuming that $I_c = \frac{S_{imp1}}{S_{tot1}} = \frac{S_{imp2}}{S_{tot2}}$ and $V_{imp} = \frac{V_{imp}}{V_c} V_c = I_c V_c$, Equation 39 can be rewritten as Equation 40

$$V_{in} = V_1 I_c n_1 + V_2 I_c n_2 + I_c V_c \tag{40}$$

Therefore, the new fluid fraction I_c^{n+1} can be computed using:

$$I_c^{n+1} = \frac{V_{in}}{V_1 n_1 + V_2 n_2 + V_c} \tag{41}$$

It allows accessing the new exchange surface $S_{imp}^{n+1} = I_c^{n+1} S_{tot}$ and the longitudinal length of the first column: $I_c^{n+1} L_1$ in the tow 1 and $I_c^{n+1} L_2$ in the tow 2. These lengths are saved to be used at the following time step.

In the newly generated column, the filling state of the microscopic elements is updated using Equation 33. The flow front position in the column is saved for the future pressure field computation as well as the filling factor of the element where the flow front is located for the future update of the filling. Additionally, the volume absorbed in the tows is saved to compute S_I using Equation 35. Finally, the volumes exchanged between the longitudinal elements are computed from the volumes exchanged in each column. Furthermore, the filling state of the longitudinal elements is calculated using Equation 33. Exchanged volumes and filling factor will be used later to update the curing related quantities of interest.

Following time steps
Once the first column has been generated, the approach is the same for two or more columns. The longitudinal length of each existing column is known. Thus, in these columns, the volume absorbed is computed directly using Darcy's law and removed from the volume V_{in} introduced in the element. Once the contribution of all columns has been taken into account, the remaining volume of fluid is shared between the channel and the tow using the same procedure as for the first column. In this case, longitudinal length of the microscopic "column" i created during the time step $n+1$ in each tow is expressed as follows: $(I_c^{n+1} - I_c^n) L_i$. The same information as for the first filling time step are saved regarding flow front position and filling state in the columns as well as their overall values in the longitudinal elements. Once the level of filling at the macroscopic scale has reached I_{th}, macroscopic flow is allowed in the downstream elements, the tows continue being filled using the same microscopic approach to compute S_I and the filling state I_c is updated using Equation 42 obtained from Equation 36 in a similar way as Equation 33

$$I_{ss}^{n+1}(e) = I_{ss}^n(e) - \delta_{ss}^n(e) I_{ss}^n(e) \frac{V_{out}^{n+1}(e)}{V_{ss}(e)} + \delta_{ss}^n(e^-) I_{ss}^n(e^-) \frac{V_{out}^{n+1}(e^-)}{V_{ss}(e)} - S_I^{n+1} \Delta t^n \tag{42}$$

1.3.5 Convergence study

One of the claims of the developed technique is that it is able to treat dual-scale flow with the same degree of precision with various element sizes. Therefore, isothermal 1D filling simulations with constant inlet pressure have been conducted using meshes with element sizes from 2 mm to 20 mm. Different values of material properties have also

been considered in order to determine the sensitivity of the method to the relative size of the channels to the overall volume of the part (φ_c) or the channel to transverse tow permeability ratio (K_c/K_t). The tows are considered cylindrical and exhibit a constant geometry and a constant intra-tow porosity equal to 0.4. Therefore, the evolutions of φ_c and the average porosity are only due to the increase of the size of the channels. The characteristics of the textile and the processing conditions are described in Table 3.

Material parameters	**Values**		
Length of the cavity	20 cm		
Diameter of the tows in direction 1	0.812 mm		
Diameter of the tows in direction 2	0.812 mm		
Channel to overall volume ratio (φ_c)	0.13	0.26	0.40
Average porosity (ϵ_{ss})	0.48	0.55	0.64
Channel isotropic permeability	10^{-10} m^2		
Tow radial permeability	1×10^{-13} m^2	5×10^{-13} m^2	5×10^{-12} m^2
Injection parameters	**Values**		
Injection pressure	10^5 Pa		
Injection viscosity	8.2×10^{-3} Pa.s		

Table 3: Material parameters and processing conditions used for the different pressure imposed isothermal filling simulations

Additionally, as presented in section 3.1, the size and length of the tows associated to each macroscopic element depend on the characteristics of the considered material and the size of the element itself. The values and average length of tows in the elements depending on the size of the elements and φ_c are presented in Table 4.

Two types of results will be presented: first, the injected volume versus time will be compared for the different scenarios. This result is a direct representation of the flow front propagation and tow impregnation as they both influence the flow velocity in the part and thus the injected volume. Second, the length of the unsaturated area will be compared for the reference case ($K_c/K_t = 200$, $\varphi_c = 0.26$) in order to highlight the ability for the model to reproduce the unsaturated area in the same way for different mesh sizes. Unidirectional injections with constant pressure equal to 10×10^5 Pa (10 bar) are conducted. The reference time to compare the different simulations is the time necessary to fill one half of the volume of the cavity (1D flow over 10 cm). For the considered injection pressure and channel permeability, the average flow velocity during impregnation is in the range of 4 cm/s and the smallest flow velocity at the end of injection is 1.2 cm/s. Thus the flow regime is in the range of the ones observed in high pressure RTM. Figure **??** presents results obtained for mesh sizes between 2 and 20 mm, with $K_c/K_t = 200$, $\epsilon_c = 0.26$. The reference volume for the volume normalization in Figure 31 is one half the volume of the cavity. It can be observed that the plots of injected volume versus time are very close to each other for the 4 elements sizes. Table 5 gives the numerical values of injection times for the different scenarios. In each cases, the injection time is compared to the time obtained from the most refined 2 mm mesh simulation.

It can be noticed from Table 5 , that with increasing mesh size, the error on the injection time is increasing. However, even when dividing the number of macroscopic elements in the model by a factor 10, this error remains below 6%. This demonstrates the flexibility of the proposed approach and its ability to treat equivalently an isothermal injection case for several element sizes. Additionally, the size of the unsaturated area has been compared for the different mesh sizes for the reference case ($K_c/K_t = 200$, $\epsilon_c = 0.26$). Figure 32

	φ_c=0.13			
Macroscopic mesh	2 mm	5 mm	10 mm	20 mm
Number of tows in dir.1	0.5	1.5	3	6
Tow average length dir.1	1.2 mm	2.6 mm	5.1 mm	10.3 mm
Number of tows in dir.2	1	3	6	12.5
Tow average length dir.2	0.6 mm	1.3 mm	2.6 mm	4.9 mm
	φ_c=0.26			
Macroscopic mesh	2 mm	5 mm	10 mm	20 mm
Number of tows in dir.1	0.5	1.5	3	6
Tow average length dir.1	1.2 mm	2.4 mm	4.8 mm	9.7 mm
Number of tows in dir.2	1	3	6	11.5
Tow average length dir.2	0.6 mm	1.2 mm	2.4 mm	5 mm
	φ_c=0.4			
Macroscopic mesh	2 mm	5 mm	10 mm	20 mm
Number of tows in dir.1	0.5	1.5	2.5	4.5
Tow average length dir.1	1.2 mm	2.9 mm	4.7 mm	10.5 mm
Number of tows in dir.2	1	2.5	4.5	9.5
Tow average length dir.2	0.6 mm	1.2 mm	2.6 mm	5 mm

Table 4: Number and dimensions of tows for various macroscopic mesh size and channel properties

presents the filling state of the part after 2 seconds of injection for the reference case. I_c represents the level of filling at the macroscopic scale while I_t presents the level of filling of the tows. It can be noticed that with the 2 mm mesh, the unsaturated area can be well observed as the elements are smaller than the unsaturated area. Its length is estimated to 9 mm. The bigger the elements of the mesh, the more difficult it is to notice the unsaturated area as it is spread over a smaller number of elements or is even smaller than the element itself. However its size can be determined using the microscopic model. In the case of the 20 mm large mesh, the average length of unsaturated area during injection is 9.25 mm. This value is very close to the length of unsaturated area that can be measured from the more discretized 2 mm mesh simulation.

This highlights the capacity for the approach to track finely the unsaturated area even with large macro elements. Mesh convergence is achieved.

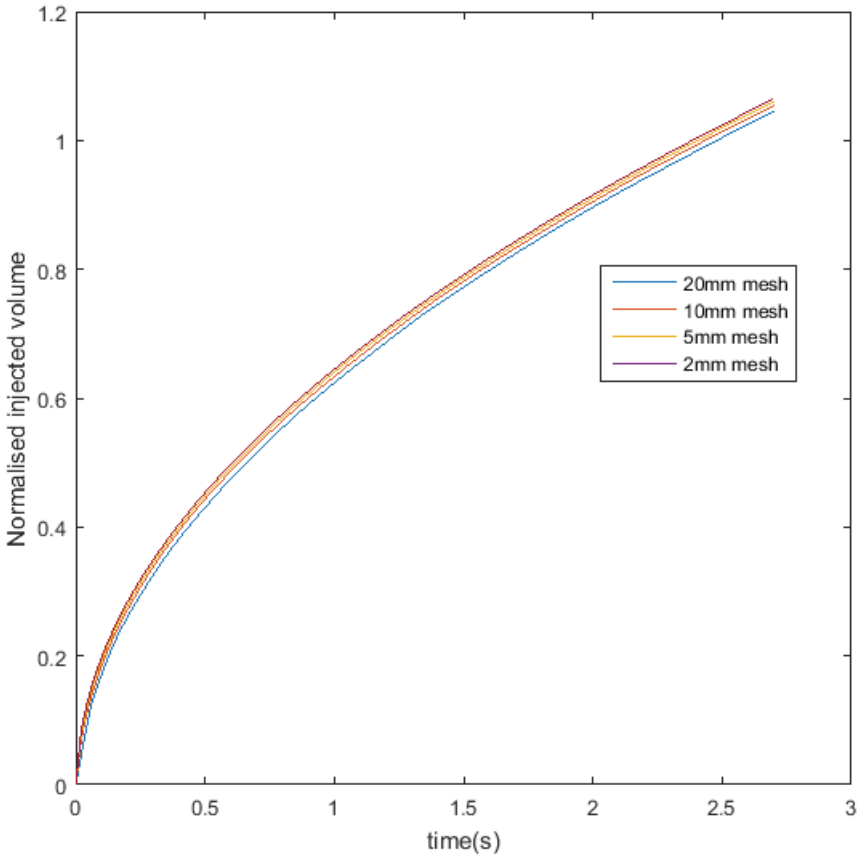

Figure 31: Influence of mesh size on the normalized injected volume versus time for an isothermal injection with constant injection pressure

Finally, Table 6 presents the advantages of the numerical method in terms of CPU time reduction for the reference calculation. In the case of the 20 mm mesh, the computation time is reduced by a factor 124 while the error on the filling time stays smaller than 5% compared to the 2 mm mesh.

These results highlight therefore that the approach can be run with the same degree of accuracy with various element sizes. This may enable time savings both at the meshing step, as elements with sizes between 2 and 20 mm generate equivalent results, and at the calculation step, as larger elements allow reducing the number of elements in the model and thus the CPU time.

K_c/K_t=1000		φ_c=0.26	K_c/K_t=200		φ_c=0.13
Mesh size	Time to fill 1/2 of the cavity	Error to the 2 mm mesh	Mesh size	Time to fill 1/2 of the cavity	Error to the 2 mm mesh
2 mm	2.41 s	-	2 mm	2.06 s	-
5 mm	2.44 s	1.2%	5 mm	2.06 s	0%
10 mm	2.48 s	2.9%	10 mm	2.08 s	0.9%
20 mm	2.53 s	5.0%	20 mm	2.1 s	1.9%
K_c/K_t=200		φ_c=0.26	K_c/K_t=200		φ_c=0.26
Mesh size	Time to fill 1/2 of the cavity	Error to the 2 mm mesh	Mesh size	Time to fill 1/2 of the cavity	Error to the 2 mm mesh
2 mm	2.38 s	-	2 mm	2.38 s	-
5 mm	2.40 s	0.8%	4 mm	2.40 s	0.8%
10 mm	2.43 s	2.1%	10 mm	2.43 s	2.1%
20 mm	2.47 s	3.8%	20 mm	2.47 s	3.8%
K_c/K_t=20		φ_c=0.26	K_c/K_t=200		φ_c=0.40
Mesh size	Time to fill 1/2 of the cavity	Error to the 2 mm mesh	Mesh size	Time to fill 1/2 of the cavity	Error to the 2 mm mesh
2 mm	2.38 s	-	2 mm	2.72 s	-
5 mm	2.38 s	0%	4 mm	2.76 s	1.5%
10 mm	2.42 s	1.68%	10 mm	2.80 s	2.9%
20 mm	2.47 s	3.8%	20 mm	2.88 s	5.9%

Table 5: Computed injection times for the different scenarios and errors to the results obtained from the 2 mm mesh calculations

Macroscopic element size	2 mm	5 mm	10 mm	20 mm
Number of macroscopic elements in the model	2000	800	400	200
Ratio of computational time compared to the 2 mm mesh calculation for the reference calculation ($K_c/K_t = 200$ and $\varphi_c = 0.26$)	1/1	1/6.5	1/30	1/124

Table 6: Number of elements and relative computational cost for the reference case treated with different element sizes

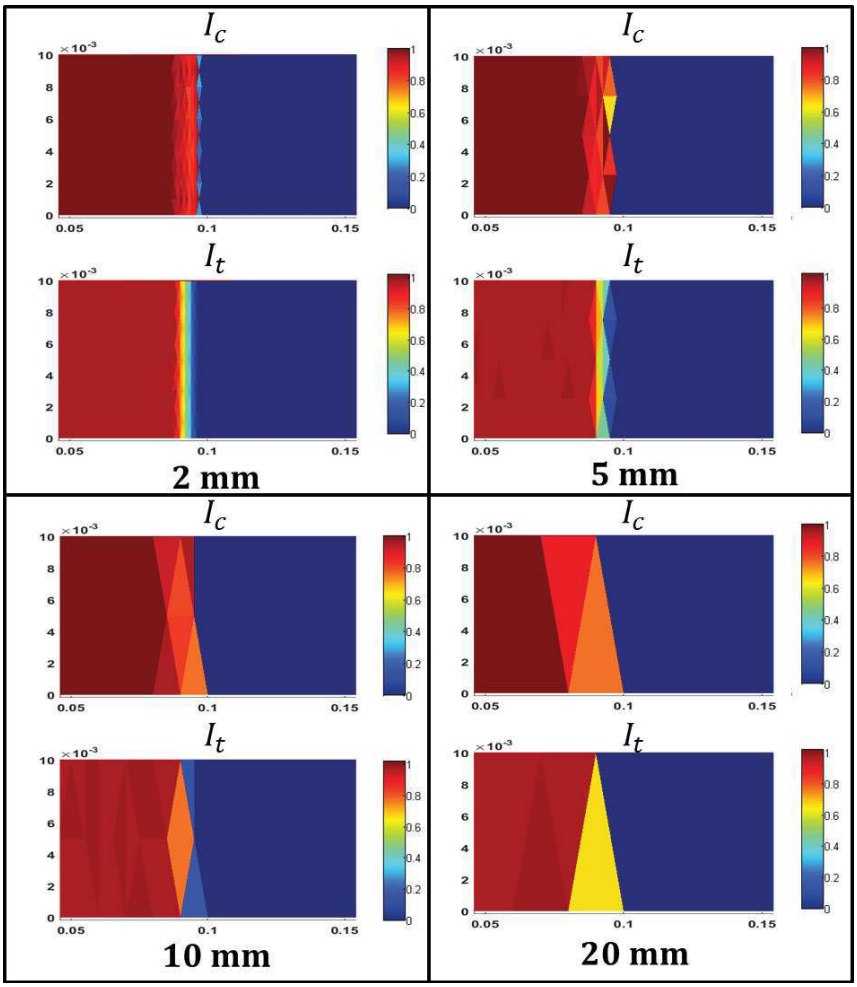

Figure 32: Isothermal 1D filling simulation under the same conditions with varying mesh sizes. Filling state at the macroscopic (I_c) and microscopic (I_t) levels

1.4 Reactive single-scale model

1.4.1 Introduction of the variables

In order to simulate the exothermic curing reaction which induces temperature, degree of cure and viscosity evolutions, these three quantities of interest must be considered.

- α_{ss}: Degree of cure in the elements governed by the advection Equation 43 adapted from [1].

$$\frac{\partial \alpha_{ss}}{\partial t} + \mathbf{v}_{ss} \cdot \nabla \alpha_{ss} = S_{ss}^{\alpha_{polym}} \tag{43}$$

This equation features the source term $S_{ss}^{\alpha_{polym}}$ relative to the polymerization of the resin. Among the many models of polymerization presented in the literature, the modified Kamal et al model [31] has been chosen in the frame of this work. The expression of $S_{ss}^{\alpha_{polym}}$ is detailed in Equation 44.

$$S_{ss}^{\alpha_{polym}} = \left[K_{i1} \exp\left(\frac{-E_{a1}}{RT_{ss}}\right) + K_{i2} \exp\left(\frac{-E_{a2}}{RT_{ss}}\right) * \alpha_{ss}^{m} \right] (\alpha_{max} - \alpha_x)^p \tag{44}$$

K_{i1} and K_{i2} are polymerization kinetics parameters, E_{a1} and E_{a2} are activation energies of the reaction, R is the constant of ideal gases, T_x the temperature of the resin in the channel and m and p experimentally determined reaction orders. Values for these parameters, taken from [31], are given in Table 7.

- T_{ss}: Temperature in the elements governed by the advection equation also called equation of heat.

$$\rho_{ss} Cp_{ss} \left(\frac{\partial T_{ss}}{\partial t} + \mathbf{v}_{ss} \cdot \nabla T_{ss} \right) = S_{ss}^{T_{cond}} + S_{ss}^{T_{mold}} + S_{ss}^{T_{polym}} + Bc_{ss}^{Resin-Fiber} \tag{45}$$

In this equation, ρ_{ss} is the average density and Cp_{ss} the average heat capacity. These two values are assumed constant (however the introduction of their dependency to the temperature would not present difficulties). The equations to calculate the values of ρ_{ss} and Cp_{ss} from the resin and reinforcement properties are given in Table 7.
$S_{ss}^{T_{cond}}$ is a source or sink term relative to the conductive thermal exchanges between one element and its neighbors and is defined as:

$$S_{ss}^{T_{cond}} = k_{ss} \Delta T_{ss} \tag{46}$$

$S_{ss}^{T_{mold}}$ is a source or sink term relative to the conductive thermal exchanges between the element and the mold and is calculated using:

$$S_{ss}^{T_{cond}} = k_{mold} \Delta T_{ss} \tag{47}$$

In this case the temperature laplacian is calculated in the thickness direction of the elements. k_{mold} is a parameter added to tune the behavior of the mold in order to allow more or less mold-part conductive exchanges.

$S_{ss}^{T_{polym}}$ is a source term relative to the generation of heat of the exothermic curing reaction. It is defined as:

$$S_{ss}^{T_{polym}} = \rho_{ss}\epsilon_{ss}\Delta H\frac{\partial \alpha_{ss}}{\partial t} \tag{48}$$

where ΔH is the heat generated by the curing reaction (Table 7).

Finally, $Bc_{ss}^{Resin-Fiber}$ is the heat transfer at the flow front corresponding to the thermal exchanges between the resin and the fibers leading to the resin-fiber temperature homogenization. As introduced in part I temperature equilibrium is supposed to be achieved instantaneously when resin comes in contact with the fibers. Its expression is:

$$Bc_{ss}^{Resin-Fiber} = \frac{dI}{dt}(1-\epsilon_{ss})\rho_f Cp_f(T_f - T_r) \tag{49}$$

In Equation 49, T_f is the temperature of the fibers and T_r the temperature of the incoming resin. This term is only active in the elements being saturated and vanishes after full filling of the element.

It can be noted that both temperature and degree of cure follow an advection equation form (Equation 50) where J_{ss} is a generic quantity of interest. Therefore, to simplify the following explanations regarding reactive aspects, Equation 50 will be used to explain how the evolution of temperature and degree of cure are treated numerically. Sj_{ss} and Bc_{ss} are respectively a generic expression for sink or source term(s) relative to the considered quantity of interest and a flow front exchange (only for the advection equation of temperature). C is the coefficient multiplying the left hand side term.

$$C\left(\frac{\partial J_{ss}}{\partial t} + \mathbf{v}_{ss}\cdot\nabla J_{ss}\right) = Sj_{ss} + Bc_{ss} \tag{50}$$

- μ_{ss} : Viscosity of the fluid governed by the chemo-thermo-rheological law taken as in [31]:

$$\mu_{ss} = \mu_g \exp\left[\frac{C_1(T_{ss}-T_{g0})}{C_2 + T_{ss} - T_{g0}}\right]\left(\frac{\alpha_{ss}}{\alpha_g - \alpha_{ss}}\right)^{n_\mu} \tag{51}$$

In Equation 51, T_{g0} is the glass transition temperature of the uncured resin, μ_g is the viscosity at T_{g0} and α_g the degree of cure at the gelation point. C_1, C_2 and n_μ are constants. Values of these parameters are given in Table 7.

Parameters	Values
K_{i1}	$e^{10.7}$ s^{-1}
E_{a1}	61.4 kJ/mol
K_{i2}	$e^{12.6}$ s^{-1}
E_{a2}	62.1 kJ/mol
m	0.64
p	1.36
R	8.314 J/mol/K
α_{max}	-1.43+0.00591×T
ΔH	365×10^3 J/kg
ρ_r	1028 kg/m^3
ρ_f	2575 kg/m^3
ϵ_c	1
ϵ_t	0.4
Cp_r	1500 J/K/kg
k_r	0.24 W/m/K
Cp_f (Glass fiber)	670 J/K/kg
k_f (Glass fiber)	0.0335 W/m/K
μ_g	10^{12} Pa.s
C_1	36.5
C_2	19.6
T_{g0}	235.4 K
α_g	0.331
n_μ	2.7

Table 7: Values of the parameters used in the model [20]

1.4.2 Algorithm for reactive flow

The transport and update of the various quantities of interest is treated in a different way for the viscosity, the degree of cure and the temperature. Viscosity is calculated directly for each element depending on the temperature and degree of cure in this element, while degree of cure and temperature are advected and require therefore a special treatment. The single-scale simulation algorithm including reactive treatment is presented briefly below and detailed afterward

Overview

1. **Viscosity update**
2. Computation of the macroscopic pressure field using a FEM/CV method
   The macroscopic pressure computation is conducted by taking into account the viscosity field in the part.
3. Computation of the macroscopic fluid velocity in the elements
4. Calculation of time step duration
5. Updating of the fluid fraction
6. **Transport and update of the quantities of interest (Degree of cure and Temperature)**

Detailed Algorithm

1. **Viscosity update**
   The first step of the algorithm consists in updating the viscosity in each element using the values of temperature and degree of cure computed at the previous time step and Equation 51.

2. Computation of the macroscopic pressure field using a FEM/CV method
   The values of viscosity are included in the "stiffness" matrix for the calculation of the pressure field and calculations are conducted as in isothermal conditions.

3. Computation of the macroscopic fluid velocity in the elements
   As Darcy's equation depends on the viscosity, flow velocities will be affected by the viscosity distribution in the part, however, the same approach as in the isothermal conditions is used.

4. Calculation of time step duration
   No modification is conducted on the time step duration calculation.

5. Fluid fraction update

6. **Transport and update of the quantities of interest (Degree of cure and Temperature)**
   As highlighted in the previous section, degree of cure and temperature are governed by the same type of advection (Equation 50). This type of equation is very similar to Equation 36 and is therefore treated with the same explicit approximation of the time derivative introduced in [1]. The Equation 52 is obtained:

$$J_{ss}^{n+1}(e) = \frac{1}{I_{ss}^{n+1}(e)}[I_{ss}^{n}(e)\tilde{J}_{ss}^{n+1}(e) - \delta_{ss}^{n}(e)\tilde{J}_{ss}^{n+1}(e)\frac{V_{out}^{n+1}(e)}{V_c(e)} + \delta_{ss}^{n}(e^-)\tilde{J}_{ss}^{n+1}(e^-)\frac{V_{out}^{n+1}(e^-)}{V_c(e)} + \frac{Bc_{ss}^{n+1}\Delta t}{C}] \tag{52}$$

   $\tilde{J}_{ss}^{n+1}(e)$ takes the non-convective source terms of Equation 52 into account. It is defined in Equation 53.

$$\tilde{J}_{ss}^{n+1}(e) = J_{ss}^{n}(e) + \frac{Sj_{ss}^{n+1}\Delta t}{C} \tag{53}$$

   where $Sj_{ss}^{n+1} = \frac{1}{V_{ss}} \iiint Sj_{ss} dv$ for volumic source terms as polymerization or $Sj_{ss}^{n+1} = \frac{1}{V_{ss}} \oint Sj_{ss} ds$ for surfacic source terms as conduction source terms. Using Equations 52 and 53, with the appropriate sink and source terms, the degree of cure and then the temperature are updated in each element.

The new values of quantities of interest will be used at the beginning of the next time step to compute the viscosity.

1.5 Reactive dual-scale model

1.5.1 Dual-scale flow related sink and source terms

Additional sink and source terms need to be added to the equations presented in section 1.4. These sink and source terms are listed below:

- Degree of cure
  It is assumed from the assumptions made on the flow that once entered in the tows, the fluid is stored in a permanent manner. Thus the only sink term relative to the dual-scale flow that affects the degree of cure is a convective term during tow saturation expressed in Equation 54:

$$S_c^{\alpha_{micro}} = S_I \alpha_c \tag{54}$$

  Therefore, at the macroscopic scale the advection equation for the degree of cure in a dual-scale simulation is expressed in Equation 55.

$$\frac{\partial \alpha_c}{\partial t} + \mathbf{v}_c \cdot \nabla \alpha_c = S_c^{\alpha_{polym}} - S_c^{\alpha_{micro}} \tag{55}$$

  On the other hand, Equation 43 is used directly at the microscopic scale with the channel as upstream element of the outer longitudinal tow element.

- Temperature
  Thermal exchanges between the tows and the channel are of two types: Convective exchanges during tow saturation and conductive exchanges once the tow is saturated. Equation 56 presents the convective sink term.

$$S_c^{T_{micro}} = \rho_c C p_c S_I T_c \tag{56}$$

  $S_c^{T_{micro}}$ is not equal to zero during the tow saturation phase and equal to zero when the tows are saturated. Furthermore, Equation 57 give the expression of the conductive thermal source received by the channel from the tow and Equation 58 the heat received by the tow from the channel. These two quantities must be equal to ensure energy conservation.

$$S_c^{T_{MicroCond}} = \mathbf{k}_c \Delta T \tag{57}$$

$$S_t^{T_{MacroCond}} = \mathbf{k}_t \Delta T \tag{58}$$

  These terms are computed as the conductive exchanges of the cylindrical or parallelepipedic tow surrounded by fluid flowing in the channel.

  Additionally, conductive mold thermal exchanges are treated in a particular manner in the dual-scale simulation. Indeed, it cannot be assumed that only channel is in contact with the mold as the reinforcement is also in contact with it. Thus, the macro-scale sink/source term is modified and a sink/source term is calculated for the mold-tow conductive thermal exchanges. These two terms are weighted with the channel/overall volume ratio in order to feature a thermal conduction behavior equivalent to the single-scale simulation. Additionally, as no thermal variations are considered in the thickness of the part, the contribution of the mold to the temperature of the tows is distributed homogeneously in the whole volume of tows in each element. The expressions of these two terms are given in Equation 59 and 60.

$$S_c^{T_{mold}} = k_{mold}\varphi_c \mathbf{k}_c \Delta T \tag{59}$$

$$S_c^{T_{mold}} = k_{mold}(1-\varphi_c) \mathbf{k}_t \Delta T \tag{60}$$

In the same way, in-plane conductive exchanges are weighted using φ_c for the channel and $(1-\varphi_c)$ for the tows to feature a conductive thermal behavior similar to the single-scale model.
Finally, regarding flow front thermal exchanges, it must be precised that as channels contain no fibers, the flow front thermal exchange Bc is equal to zero at the macro-scale but must be taken into account at the micro-scale. $Bc_t^{Resin-Fiber}$ features the same expression as in Equation 49.

Thus the advection equation for temperature at the macroscopic scale becomes:

$$\rho_c Cp_c \left(\frac{\partial T_c}{\partial t} + \mathbf{v}_c \cdot \nabla T_c \right) = S_c^{T_{cond}} + S_c^{T_{mold}} + S_c^{T_{polym}} - S_c^{T_{micro}} + S_t^{T_{MicroCond}} \tag{61}$$

At the micro-scale the temperature is governed by Equation 62 for the outer longitudinal tow element considering the channel as upstream element and Equation 45 for the other longitudinal tow elements. The source term $S_t^{T_{cond}}$ takes into account both the conductive thermal exchanges between the longitudinal elements of the tows and the in-plane conductive exchanges.

$$\rho_t Cp_t \left(\frac{\partial T_t}{\partial t} + \mathbf{v}_t \cdot \nabla T_t \right) = S_t^{T_{cond}} + S_t^{T_{polym}} + S_c^{T_{MacroCond}} + S_t^{T_{mold}} + Bc_t^{Resin-Fiber} \tag{62}$$

1.5.2 Algorithm for reactive flow

The previously presented additional sink and source terms need to be integrated in the calculation of the transport and update of the quantities of interest at the macroscopic scale. Additionally, the treatment of the quantities of interest at the micro-scale needs to be detailed.

Overview

1. Viscosity update
   Viscosity is updated both at the macroscopic and microscopic scales
2. Computation of the macroscopic pressure field using a FEM/CV method
3. Computation of the macroscopic fluid velocity in the elements
4. Calculation of time step duration
5. Fluid fraction update
6. **Transport and update of the quantities of interest at the macro and micro scales**
   Additional sink terms are added at the macro-scale to take the effects of intra-tow resin storage into account. Additionally a specific treatment is implemented for the quantities of interest at the micro-scale.

Detailed Algorithm

1. Viscosity update
   Using Equation 51, the viscosity is computed in all saturated elements at the macro and micro-scales.

2. Computation of the macroscopic pressure field using a FEM/CV method

3. Computation of the macroscopic fluid velocity in the elements

4. Calculation of time step duration

5. Fluid fraction update

6. **Transport and update of the quantities of interest at the macro and micro scales**
   Temperature and degree of cure are updated at the macroscopic scale using the adapted Equation 52 (including the appropriate sink and source terms). However, considering micro-scale, specific attention must be paid. In fact, when the tow finishes being filled, fully filled columns (Region A) and partially filled columns (Region B) cohabit in the element. Therefore, treatment of the advection Equation 52 must be adapted. Figure 33 illustrates the problem.

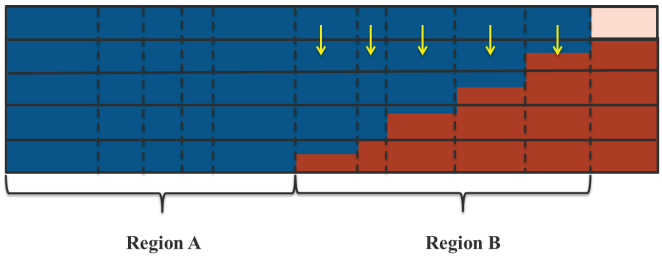

Figure 33: Presentation of the two regions that cohabit in the tows at the end of filling

In the calculation of Equation 52, the values of source terms must be adjusted regarding the respective volumes of Regions A and B. Indeed, region A is saturated, therefore, for this region, only the conductive and polymerization terms must be considered. On the other hand, in Region B, flow still occurs and convection terms need to be considered. In order to tackle this issue, the source terms associated with each region is weighted by the respective volume of each region. Finally, a unique value of temperature and degree of cure is obtained in each longitudinal micro-scale element. Once the quantities of interest relative to the reactive character of the injection have been computed, viscosity is computed in each element using Equation 51 and a new time step can be started.

1.5.3 Validation of the numerical model and convergence

In this section, energy balance will be verified for the various sink and source terms used in the reactive single-scale and dual-scale simulations. Sensibility study to the mesh size as well as to the time step duration will also be conducted.
As introduced in section 1.4, the advection equation for the degree of cure is affected by the flow velocity and a source term $S_{ss}^{\alpha_{polym}}$ that depends on the temperature. The accurate reproduction of the flow has been demonstrated in section 1.3.5. Thus, if thermal exchanges are treated well, advection and update of the degree of cure will be conducted

in the appropriate way. Therefore the choice has been made to focus the convergence and sensitivity study on the equation of heat.

Therefore, and before conducting fully coupled simulations, the influence of each source term in the equation of heat will be investigated regarding energy balance, mesh size and time step duration. The aim here is to confirm that the simulation technique is as less sensitive as possible to the size of the mesh and the duration of the time step and that the simulation approach conserves energy.

In order to conduct the convergence study, three configurations featuring equal overall FVF will be compared. The aim is to evaluate the behavior of several microstructure exhibiting equal homogenized thermal properties. The three microstructures are described below and numerical values are given in Table 8.

- Single-scale
  Single-scale simulation based on the techniques presented in section 1.4 will be conducted. The volume of the cavity is filled with an homogeneous permeable material with a porosity of 0.53 in which flows the resin. There is no storage.

- DS1: Dual-scale simulation with a small amount of channels (φ_c=8.85%)
  Dual-scale simulations are based on the techniques presented in sections 1.4 and 1.5 The material is a biaxial made of elliptical tows characterized by an equivalent radius $r_t = \sqrt{ab}$ (where a and b are the semi-major and semi-minor axes of the tows). The equivalent radius is equal to 0.81 mm. The channels represent 8.85% of the volume of the cavity, the other 91.15% are occupied by the tows with an average porosity equal to 0.48 ensuring the same overall FVF as for the single-scale simulation. Tows are discretized in 5 radial elements. Flow occurs only in the channels and once filled, the tows store the fluid in a permanent manner.

- DS2: Dual-scale simulation with a large amount of channels (φ_c=32.7%)
  Dual-scale simulation DS2 is also conducted for a biaxial material. However the channels represent 32.7% of the volume of the material. The equivalent tow radius is reduced to 0.6 mm and the intra-tow porosity is reduced to 0.3 ensuring an overall FVF equal to 0.53. Tows are discretized in 4 radial elements.

Single-scale									
			K_c (m^2)			ϵ_{av}	$\rho_s s C p_{ss}$ (J/K/m^3)		
			1×10^{-10}			0.53	1.62×10^{6}		
DS1									
Tow eq. radius (mm)	φ_c	ϵ_c	K_c (m^2)	ϵ_t	$K_{t\perp}$ (m^2)	ϵ_{av}	$\rho_t Cp_t$ (J/K/m^3)	$\rho_c Cp_c$ (J/K/m^3)	Intra-tow elements
0.812	8.85%	1	1×10^{-10}	0.48	5×10^{-13}	0.53	1.63×10^{6}	1.54×10^{6}	5
DS2									
Tow eq. radius (mm)	φ_c	ϵ_c	K_c (m^2)	ϵ_t	$K_{t\perp}$ (m^2)	ϵ_{av}	$\rho_t Cp_t$ (J/K/m^3)	$\rho_c Cp_c$ (J/K/m^3)	Intra-tow elements
0.6	32.7%	1	1×10^{-10}	0.3	5×10^{-13}	0.53	1.66×10^{6}	1.54×10^{6}	4

Table 8: Material properties used for the convergence and sensitivity study

In Table 8, the product $\rho_x Cp_x$ are computed using Equation 63.

$$\rho_x Cp_x = \epsilon_x \rho_r Cp_r + (1-\epsilon_x)\rho_f Cp_f \tag{63}$$

Simulations will be conducted on a domain measuring 5 cm × 5 cm× 2.8 mm. Element size are either 1 cm, 5 mm or 2 mm. The initial temperature is 140°C and the curing model is based on the one presented by Ivankivoc et al in [31]. As the model is not suited for short injections, it has been adjusted to enable a gel time of approximately 80 s and a full curing time of 159 s under adiabatic conditions at an initial temperature of 140°C. Initial degree of cure value has been fixed to α_{inj}=0.085 and the heat generation of the curing reaction to ΔH=300×10^3 J/kg to reduce exothermy.

Source term: Polymerization

The effects and sensitivity of the polymerization source term are investigated in this section. Starting from equation 61 and after discretization, Equation 64 that only take into account the polymerization is obtained.

$$T_x^{n+1}(e) = T_x^{n+1}(e) + \Delta H * \frac{\rho_r}{\rho_x Cp_x}(\alpha_x^{n+1}(e) - \alpha_x^n(e)) \tag{64}$$

Table 9 summarizes the numerical values of the coefficient $\frac{\rho_r}{\rho_x Cp_x}$ for the different domains.

Single-scale	Dual-scale		
	Channel	Tow DS1	Tow DS2
$\frac{\rho_r}{\rho_{ss} Cp_{ss}}$ (K.kg/J)	$\frac{\rho_r}{\rho_c Cp_c}$ (K.kg/J)	$\frac{\rho_r}{\rho_t Cp_t}$ (K.kg/J)	$\frac{\rho_r}{\rho_t Cp_t}$ (K.kg/J)
6.33 ×10^{-4}	6.67 ×10^{-4}	6.30 ×10^{-4}	6.18 ×10^{-4}

Table 9: Material properties used for the convergence and sensitivity study

Simulations are first conducted for element sizes equal to 1 cm. In Figure 34, temperature elevations is plotted versus time (0°C on the curve correspond to the initial temperature of the elements (140°C)). At first, channels and tows are supposed to have no thermal interaction in order to study temperature evolution independently in the various material configurations.

It can be seen in Figure 34 that as well the temperature increase rate as the asymptotic values are different due to different values of coefficient $\frac{\rho_r}{\rho_x Cp_x}$ but also to different porosity (and thus resin volumic contents). The dual-scale simulations DS1 and DS2 are then conducted including intra-tow and tow-channel thermal conductive exchanges. Figure 35 presents the temperature elevations in the channel and the 4 radial elements of the tows for simulation DS2.

It can be observed on these curves that the temperature elevation occurs at similar rates for tow and channel elements. When considering in details the curves, it can be however observed (as expected) that the channel temperature elevation is slightly steeper than the one of the central element of the tow. This difference stays nevertheless small as the temperatures reach their maximal value within an interval of 1 s. This highlights the fact that, in the considered configuration, conductive effects tending to homogenize the temperature compete with the curing effects that would generate higher temperature elevation in the channel. The exothermic curing mechanism is well reproduced. The same trend of close temperatures in channel and tows are observed for simulation DS1 even if the channel volume is much smaller.
Additionally, temperature elevations in the single-scale simulation and in the channels

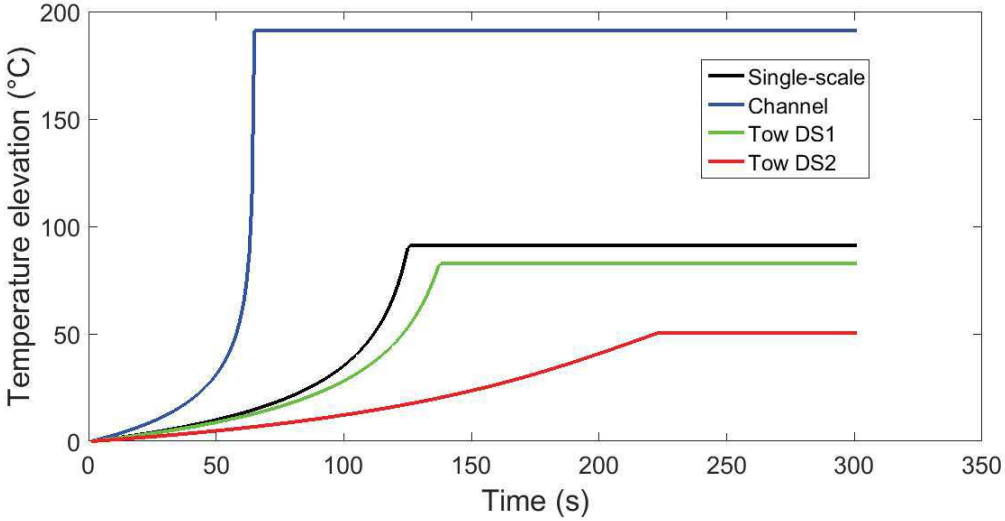

Figure 34: Temperature elevation in the different domains with only polymerization as thermal source term. Channel and tows have no thermal interaction.

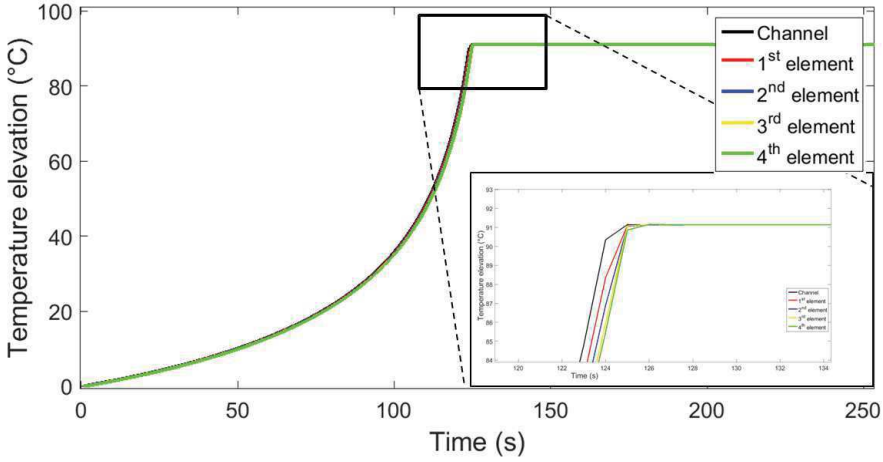

Figure 35: Temperature elevation in the different channel and tow elements of the dual-scale simulation DS2

of simulations DS1 and DS2 (including conductive intra-tow and tow-channel thermal exchanges) are plotted in Figure 36.

It can be noticed in Figure 36 that the three curves follow the same temperature elevation rates and asymptotic values. This results provide several pieces of information. First of all, the channel/tow distribution has no influence on the temperature evolution. As explained previously, conductive effects homogenize the temperature between tows and channels which leads to a temperature elevation equivalent with large channels, small channels or no channels (at the same overall FVF). Additionally, the fact that asymptotic values are equivalent ensure that energy is conserved during simulation. Indeed, as the average porosity is equal for all simulation, the elements in each simulation contain the same amount of resin and feature the same average thermal capacity. Thus, the same amount of heat is produced in all cases with the same heat capacity. This leads therefore to the same final temperature as no other thermal exchanges are considered. A brief calculation of the expected temperature increase for the single-scale simulation can be made:

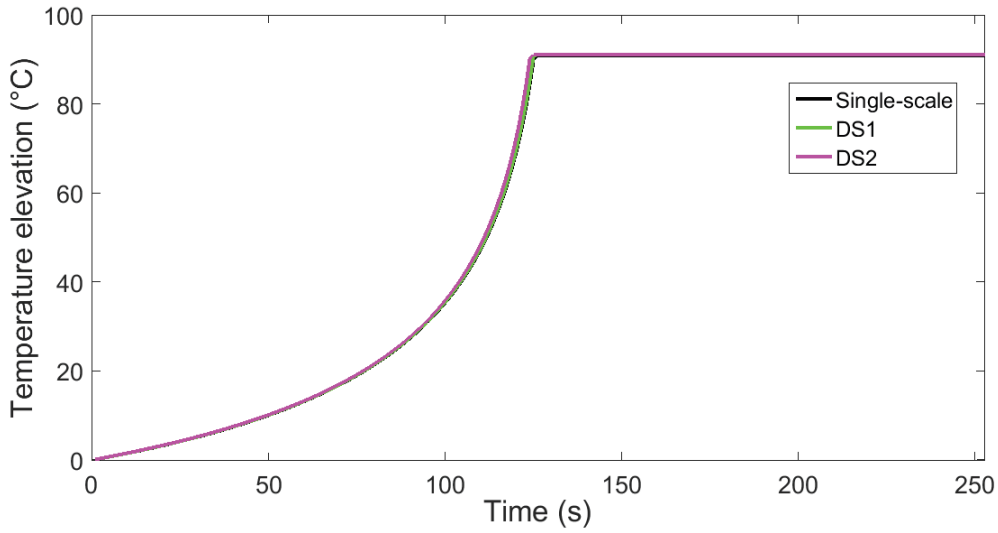

Figure 36: Temperature elevation due to polymerization for the three simulations. In simulations DS1 and DS2, channel and tows feature thermal conductive interactions

$\Delta T = \frac{\Delta H(1-\alpha_{inj})\epsilon_{av}\rho_r}{Cp_{ss}\rho_{ss}}$=91.9°. The numerically obtained value of the asymptote is 91.1° confirming energy conservation of the curing and heat conduction simulation procedures.

Finally, as the same procedure is used to compute conductive sink and source terms at the micro-scale as at the macro-scale, it is considered that energy conservation is also verified for conductive thermal exchanges between the macroscopic elements.

On the other hand, in order to study the influence of mesh size, simulations have been conducted with element sizes equal to 2 mm. The same results have been obtained as for the 1 cm mesh as well for the single as the dual-scale simulations. Curing is therefore not sensitive to mesh size.

It has been thus verified, that:

- Temperature elevation due to polymerization is independent from the mesh size.
- Temperature elevation due to polymerization is independent from the channel/overall volume ratio in a dual-scale simulations including intra-tow and channel-tow conductive thermal exchanges.
- Energy is conserved during simulations treating the exothermy due to polymerization
- Energy is conserved during simulations including conduction, as well inside of the tows level as at the tow-channel interface and by extension at the macroscopic level (same procedure for the macro-scale conductive thermal exchanges as for intra-tow)

Source-term: Thermal conduction

It has been previously verified that the numerical treatment of the conduction conserves energy. Now, it will be verified that the three microstructures behave the same under conductive exchanges with the mold.

- Conduction with the mold
  Single-scale and dual-scale simulations treating the thermal conductive exchange between the part and the mold have been conducted for various element sizes. Mold temperature is fixed at 160°C and initial part temperature is 140°C. The thermal coefficient for the mold is equal to 0.7 and the element size is 1 cm. Temperature elevation for the three simulations are plotted versus time in Figure 37.

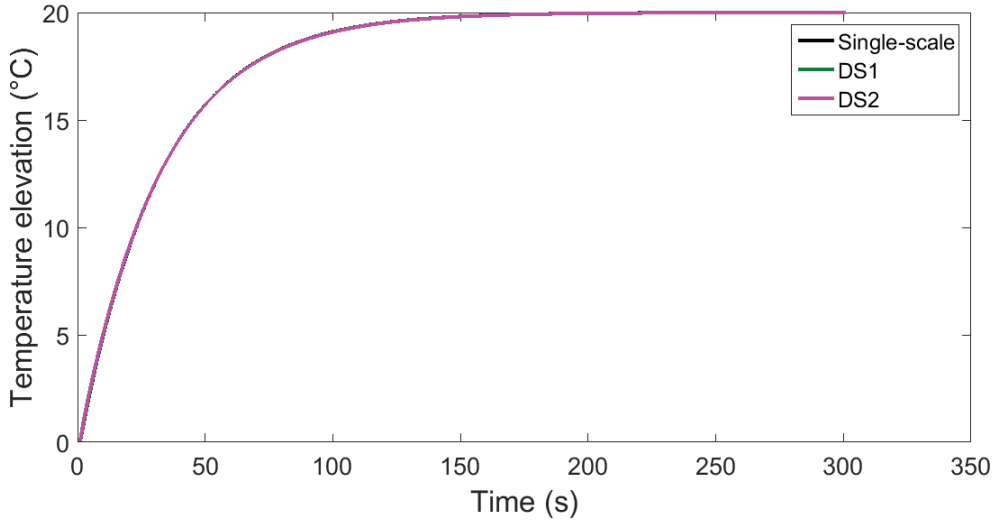

Figure 37: Temperature elevation of the part (initial temperature 140°C) due to conductive heat transfer with the mold (temperature 160°C) for the three configurations

It can be clearly seen in Figure 37 that the curves obtained from the three simulations are superposed. This is a consequence of the choice made to distribute the conductive thermal exchanges both in tows and channels. This provides a major advantage for the fully coupled simulations. Indeed, microstructure has been shown to have no influence on static curing nor on part-mold thermal exchanges. This result will enable to study the influence of the microstructure (storage,...) on the process as external thermal effects will be similar for all configurations.

Finally, the same simulation has been run for element sizes of 2 mm. Similar results have been obtained confirming that .

Conductive thermal exchanges between the mold and the part have been proven to be independant from the mesh size. Moreover, the three tested configurations exhibited similar heating kinetics. This induces that, observed differences in the temperature distribution during the reactive injection simulations will only be due to the effects of the microstructure (storage,...).

- In-plane macroscopic conduction
  Energy conservation during conductive thermal exchanges has been previously verified as well as equivalence of the micro-structures in static conditions. Now the influence of mesh size on macroscopic thermal conduction will be investigated. For the three configurations, simulations of a cavity filled with fluid with initial temperature 160° on the half left cavity side and 140° on the half right cavity side.

Figure 38 presents the initial temperature distribution and the temperature distribution after 300 s. Temperature evolution in the elements of the initial interface are plotted versus time in Figure 39. For the 5 mm mesh, the average temperature of four neighbour elements (featuring together the volume of a 1 cm element) is plotted in Figure 39.

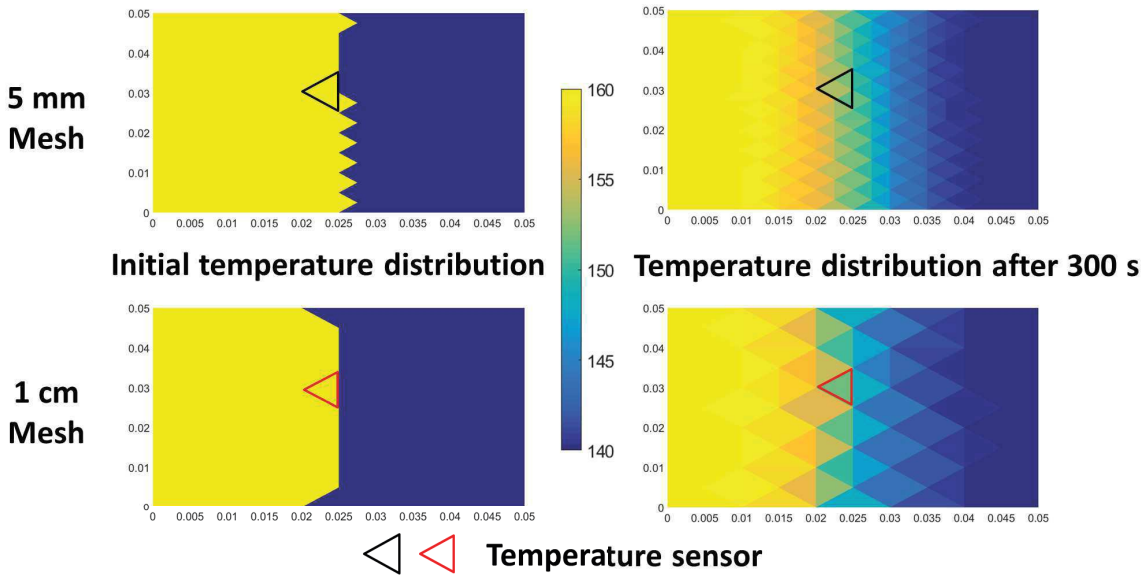

Figure 38: Mappings of the initial temperature (left) and temperature after 300 s (right) for the 5 mm and 1 cm meshes

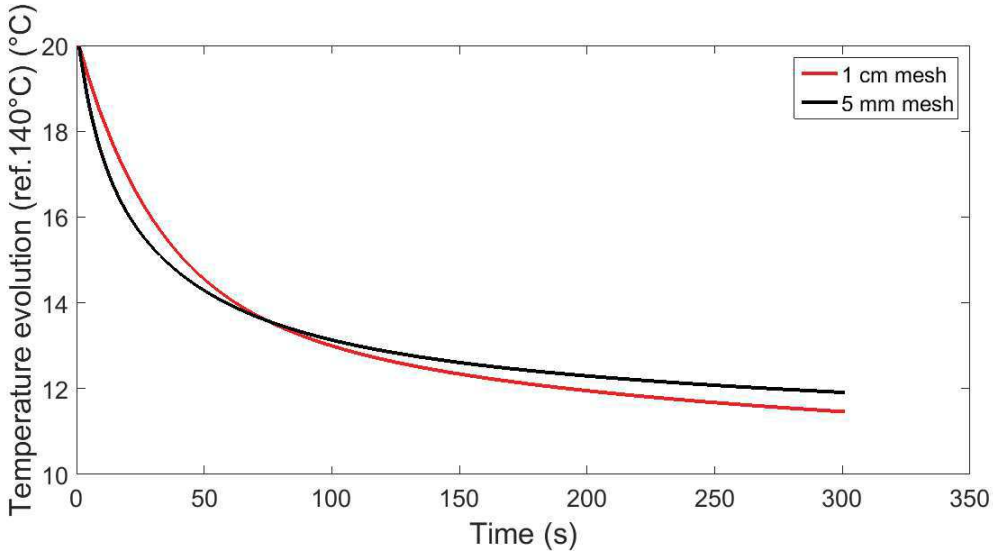

Figure 39: Temperature evolution of elements located at the initial interface between the area at temperatures 160° and 140° for mesh sizes equal to 1 cm and 5 mm

It can be seen in Figure 38 that temperature distribution are similar for the two mesh sizes. This result is confirmed by the plots of Figure 39. This provides confidence about the reduced sensitivity of the method regarding conduction for reasonable element size variations.

It has been verified that dual-scale and single-scale simulations with equivalent average FVF contents feature similar conductive properties. Furthermore, it has been proven that reasonable mesh size variations generate only limited variations in terms of numerical results. Therefore, no differences are expected due to conduction between single-scale and dual-scale simulations at the same average FVF and with the same mesh size. An limited differences are expected for reasonable mesh size variations.

Flow front heat exchange

The flow front heat exchange depends both on flow front progression and temperature difference between resin and fibers. It is thus expected that if a fluid is injected with a constant temperature in an element filled with tows at a different temperature, a equilibrium temperature should be achieved. This equilibrium is expected to be reached when the temperature evolution due to the entry of fluid at a certain temperature is balanced by the temperature evolution due to flow front heat exchange. This temperature of equilibrium T_eq can be expressed as:

$$T_{eq}\Delta I = T_{inj}\Delta I + \frac{\rho_f Cp_f(1-\epsilon)(T_t - T_{eq}}{\rho_{ss}Cp_{ss}} \tag{65}$$

which leads to:

$$T_{eq} = \frac{T_{inj}\rho_{ss}Cp_{ss} + T_f\rho_f Cp_f(1-\epsilon)}{\rho_{ss}Cp_{ss} - (1-\epsilon)\rho_f Cp_f} \tag{66}$$

where T_{inj} is the temperature of the injected resin and T_f the initial temperature of the fibers. It is considered that fibers temperature (T_f) is initially 160° while the temperature of the injected fluid (T_{inj}) is 140°C. Using the values of thermal properties presented in Table 8, the temperature of equilibrium should be 143.3°C. To verify the validity of the model, a single-scale simulation including the flow front heat exchange is conducted. The filling simulation of an entry element containing fibers at 160° with a non-reactive fluid at 140°C is realized. No mold conductive exchanges are considered for this simulation. Figure 40 presents the temperature evolution of the element.

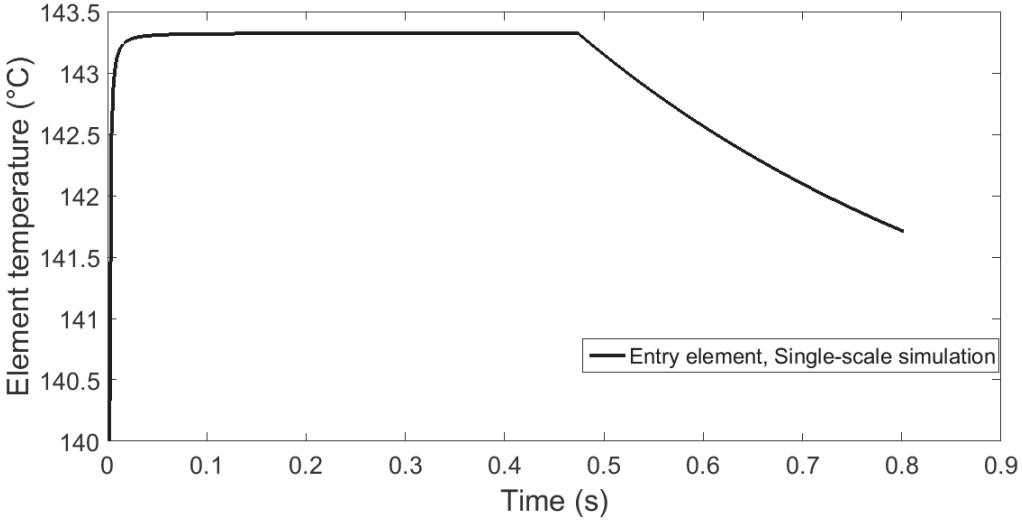

Figure 40: Temperature evolution in the entry element containing fibers at 160° during saturation with a fluid at 140° due to flow front fiber-resin heat exchange

It can be clearly observed in Figure 40 that the temperature reaches a equilibrium value after approximately 0.06 s. The value of this equilibrium temperature is 143.3°C

which is in agreement with the value calculated analytically. This verifies that energy is conserved when treating numerically the flow front heat exchange. Once the element is filled (after 0.47 s) the flow front heat exchange vanishes. The temperature begins to decrease because fluid at 140°C continues being injected in the element and no source term contributes to maintain the temperature.
The simulation has been only conducted on a single-scale model to verify energy balance. The same approach is used at the micro-scale in the dual-scale simulation. It is therefore assumed that energy is also conserved in this type of simulation.

It has been thus demonstrated that energy is conserved when treating numerically the flow front heat exchange between fibers and resin.

1.6 Conclusion on the developed numerical method

In this section, a new simulation technique has been introduced to simulate in an accurate and efficient way the injection of a reactive resin both in single and dual-scale porous materials.
The numerical technique is based on the technique of the FEM/CV for the transport of the fluid. Quantities of interest are transported and updated using an explicit first order approximation of the time derivative. Several novelties have been proposed compared to the current content of the literature:

- Microstructure is fitted to the macroscopic elements of the mesh
  This technique associate automatically, based on geometrical considerations, the appropriate number of tows with the equivalent length to ensure the appropriate FVF in each element. Therefore, association of a microstructure required for a dual-scale simulation does not require specific meshing constraints

- The micro-scale tow filling is treated in simplified an efficient way
  In the literature, micro-scale models used for dual-scale simulations can be 2D or 3D meshed micro-cells inducing large CPU costs. In this work, and under the assumption of fast injections (inducing assumed purely transverse tow filling), tow-filling is reduced to a sum of 1D transverse filling problems reducing significantly the computational cost.

Convergence studies have been run as well on the non-reactive as on the reactive numerical aspects.
Considering non-reactive (filling) aspects, is has been demonstrated that similar results in terms of length of unsaturated area and injected volume versus time (for injections at constant injection pressure) have been obtained for element sizes from 2 to 20 mm. Significant computation time reduction has additionally been observed when increasing the size of the elements.
Considering reactive aspects, energy balance has been verified for the treatment of all thermal exchanges. It has also been demonstrated that single and dual-scale simulations feature similar behaviors to pure curing and pure conduction (with the mold or in-plane in the part). This highlights that the observed differences during fully coupled simulations will only be due to the microstructure and the associated storage effects. In the following section, a sensitivity study will be conducted to determine the influence of the microstructure on the non-reactive and reactive simulations.

2 Numerical results

2.1 Non-reactive simulations: Parameters influencing the size of the unsaturated area

2.1.1 Influence of the injection parameters

The first goal of this sensitivity study is to investigate the evolution of the size of the unsaturated area with the injection parameters. Therefore, the length of the unsaturated area will be measured at fixed material properties for various injection pressures and flow rates, at increasing distances from the inlet and with and without capillary pressure.
1D injections of a non reactive fluid featuring a viscosity of 11.8 mPa.s are conducted in a cavity measuring 55 cm. The length of the unsaturated area will be measured at flow front arrival at 10, 20, 30, 40 and 50 cm from the inlet.

Constant injection pressure

Two injections at constant injection pressure (1 bar and 10 bar) are conducted in the configuration DS2 envisaged in Table 8. Comparisons are made with and without capillary pressure. Capillary pressure is taken equal to 10^4 Pa which is in the range of the highest capillary pressures encountered in RTM injections. Figure 41 plots the length of the unsaturated area versus distance from the inlet

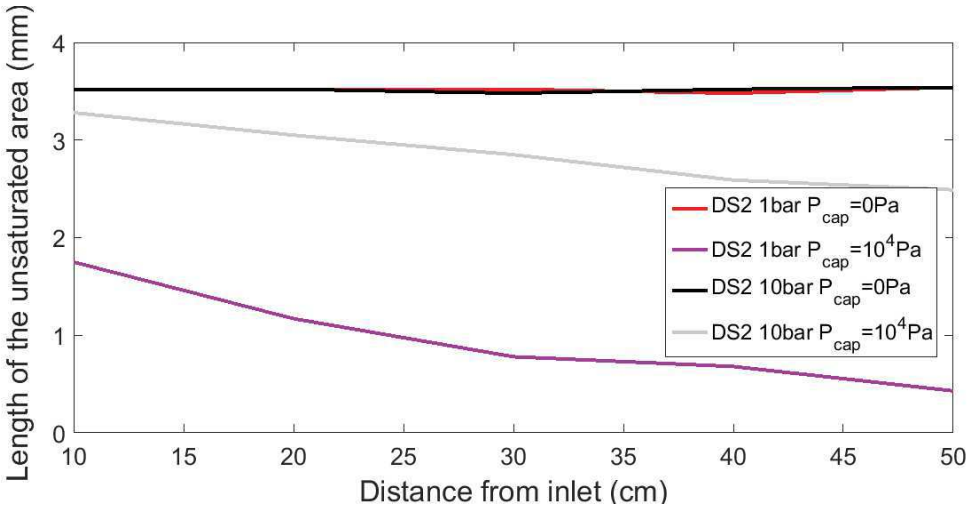

Figure 41: Length of the unsaturated area for injections at imposed pressure (1 and 10 bar) with or without capillary pressure

It can be seen in Figure 41 that when capillarity effects are not taken into account, the length of the unsaturated area is independent from the macroscopic pressure gradient. Indeed, the unsaturated area is of same length along the part for both injection pressures. However, when capillary effects are taken into account, the macroscopic pressure gradient plays a significant role. Indeed, the length of the unsaturated area is maximal at the beginning of injection when the macroscopic pressure gradients are the largest. It is in these conditions that the contribution of the capillary pressure to the tow saturation is the smallest compared to the transverse Darcy flow induced by the channel pressure. It has been therefore demonstrated that in presence of capillary forces the length of the unsaturated area increases with the macroscopic pressure gradient to reach a maximal value imposed by the channel-intra-tow Darcy-Darcy flow.

Constant injection flow rate

Three injections at constant injection flow velocities (0.25, 1 and 4 cm/s) are conducted

in the two dual-scale configurations to confirm the observed trends on the injections at constant injection pressure. Results are reported in Figure 42.

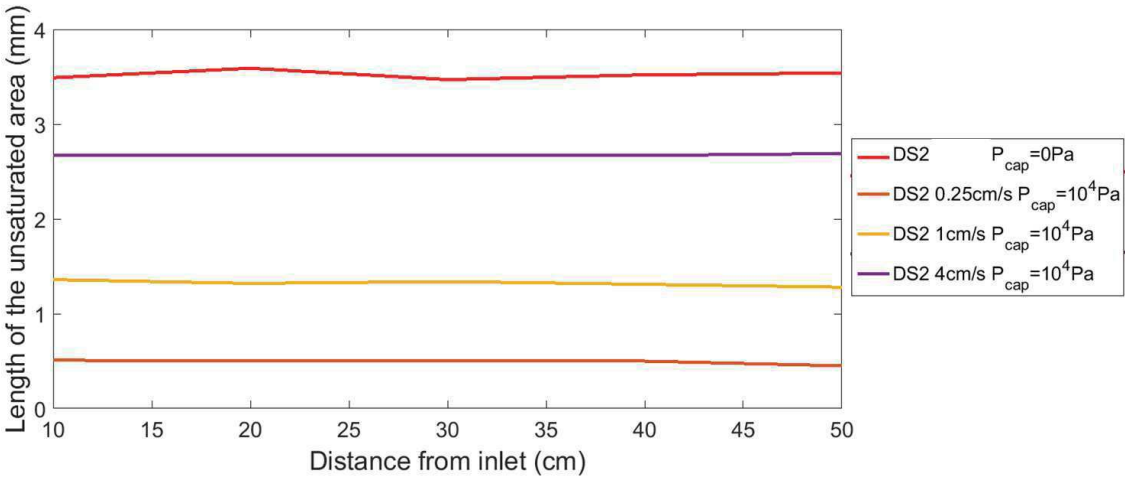

Figure 42: Length of the unsaturated area for injections at imposed velocities (0.25, 1 and 4 cm/s) with or without capillary pressure

When capillary pressure is not taken into account, the length of the unsaturated area has been reported to be independent from the flow velocity (and thus the pressure gradient) and from the distance from inlet. Its value is even equal to the one obtained from the injections at constant injection pressure (3.5 mm). Therefore one single curve has been plotted in Figure 42. Additionally, when capillary pressure is taken into account, the length of the unsaturated area is constant over the whole part as injection velocity (and thus pressure gradient) are constant. Its size increases with increasing injection velocity (and thus pressure gradient). This confirms the results reported previously.

Therefore, it has been demonstrated that when the capillary pressure is not considered, the length of the unsaturated area is independent from the macroscopic pressure gradient. However, when the capillary pressure is included in the calculations, the length of the unsaturated area increases with increasing macroscopic pressure gradient.

2.1.2 Influence of the channel/tow permeability ratio

The channel/tow permeability ratio is expected to play a significant role on the length of the unsaturated area. Therefore, the influence of the ratio K_c/K_t will be investigated. Investigations are conducted with a constant flow velocity of 1 cm/s and with a capillary pressure equal to 10^4 Pa. At first, fixed channel and varying intra-tow permeability will be investigated, then varying channel and fixed intra-tow permeability. As channel permeability influences the macroscopic pressure gradient, the length of the unsaturated area is expected to be different for the same K_c/K_t ratio but for higher or lower K_c values.

Variation of the intra-tow permeability

Figure 43 presents the aspect of the unsaturated area for the permeability ratios K_c/K_t=30, 500, 1000 and 2000 for configurations DS1 and DS2. K_c is constant and equal to 10^{-10} m^2.

It can be seen in Figure 43 that as expected, the length of the unsaturated area increases with increasing K_c/K_t ratio. Additionally, it is observed that the unsaturated areas obtained for configuration DS1 are larger than for configuration DS2. These results

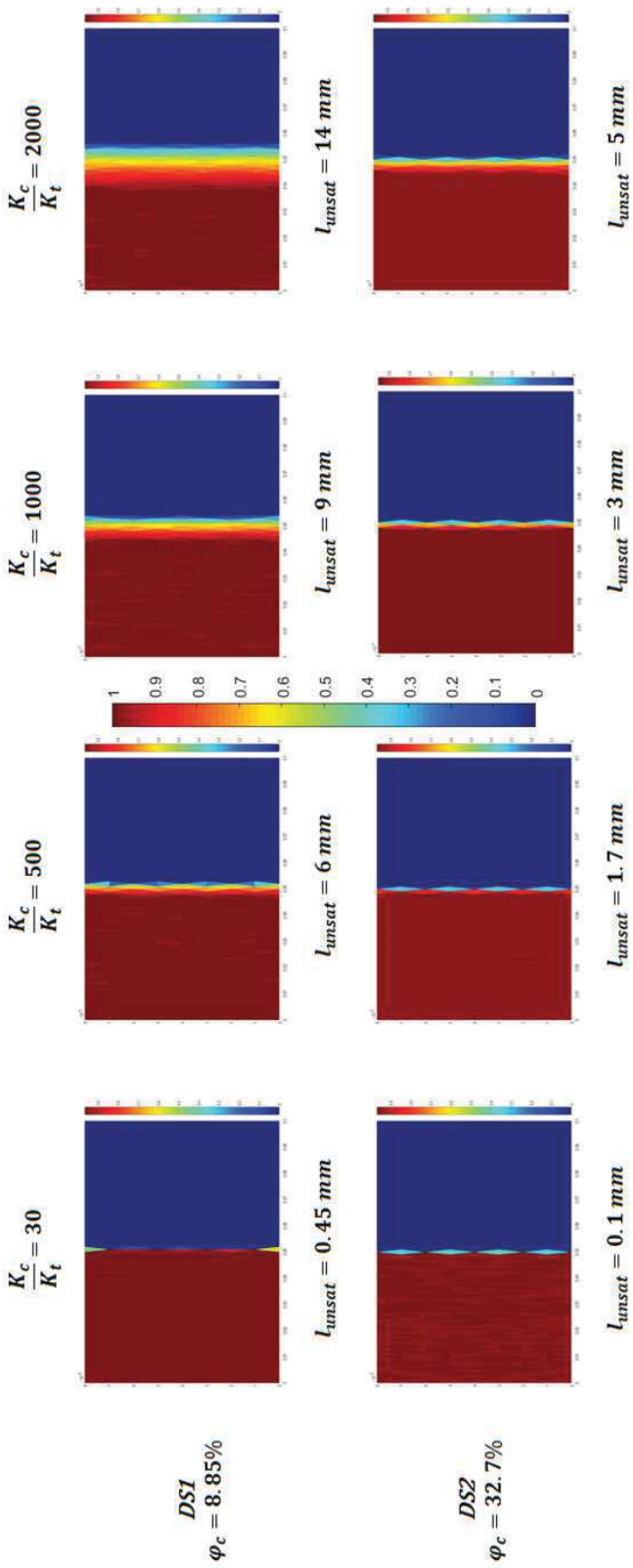

Figure 43: Mappings of the unsaturated area for various values of φ_c and K_c/K_t ratios with constant K_c=10^{-10} m^2

will be investigated in the following section.

Variation of the channel permeability

Figure 44 presents the mappings and measured lengths of the unsaturated areas for two different K_c/K_t ratios (30 and 1000). The two upper images compare the unsaturated area for K_c/K_t equal to 30 and 1000 with K_t being reduced. The two lower images compare the unsaturated area for K_c/K_t equal to 30 and 1000 with K_c being increased. It can be clearly seen, as noticed previously that increasing the permeability ratio increases the size of the unsaturated area. It can be additionally noticed that at constant K_c/K_t ratio, the length of unsaturated areas are different. It is always larger for the simulations featuring the lowest channel permeability. This is an interesting result proving that the ratio K_c/K_t alone is not sufficient to predict the length of the unsaturated area. This result is also in agreement with the trend noticed earlier: as lower channel permeability induce higher pressure gradients, in this case, it is verified again that the size of the unsaturated area increases with increasing macroscopic pressure gradient.

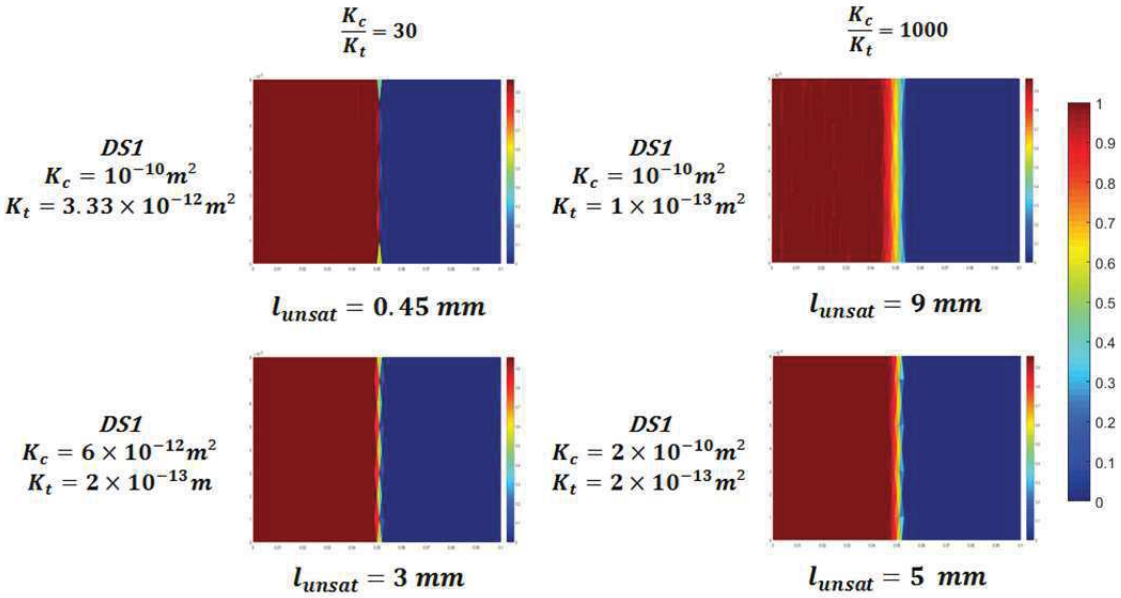

Figure 44: Mappings of the unsaturated area for configuration DS1 with various values of K_c/K_t ratios and varying K_c

It has been therefore shown again that the length of the unsaturated area is increasing with the pressure gradient. This has for consequence that for equal K_c/K_t ratios, the unsaturated area can feature different lengths depending on the value of K_c.

2.1.3 Influence of channel/overall volume ratio

In the previous sections, the results of simulations conducted on configurations DS1 and DS2 have been presented. It has been observed that for all permeability ratios, the length of the unsaturated area obtained in configuration DS2 were smaller than the ones obtained from configuration DS1. This result is due to the differences in terms of microstructure between the two configurations at constant overall FVF. In DS1, tow radius is 1.34 times larger than in configuration DS2. Additionally, due to higher intra-tow porosity, the volume of fluid that they can contain is almost three times larger. It is therefore expected that for equivalent K_c/K_t ratios the tows in configuration DS2 will saturate faster.
This result highlight thanks to the decoupling allowed by the simulation that the geome-

try of the microstructure plays a significant role on the length of the unsaturated area. It must be however precised that the only knowledge of φ_c is not sufficient to characterize the microstructure. Indeed, φ_c is only a ratio of volume and the same value of φ_c could be obtained with a few big tows generating a large unsaturated area or a lot of small tows that would saturate very fast. Therefore a parameter describing the geometry of the reinforcement would be required to characterize accurately the dual-scale character of the material.

It has been demonstrated in this section (in which channel and tow geometries have been decoupled from the values of permeability) that φ_c provides some information on the expectable unsaturated area. However, this ratio is an average value. It has been therefore highlighted that a parameter describing more finely the microstructure of the reinforcement (shape and size of the tows) would be of interest to characterize accurately the dual-scale character of the material.

2.1.4 Influence of the length of the unsaturated area on the injection pressure

Dual-scale flow has been reported in the literature to generate a drooping effect during injections at constant flow rate ([35], [72]). In order to quantify this effect, 1D injections are conducted at a flow velocity of 1 cm/s in a 10 cm long cavity. K_c/K_t ratios are chosen to generate artificially different lengths of unsaturated areas. Figure 45 plots the evolution of the injection pressure versus time for the configuration DS1 with various lengths of unsaturated areas.

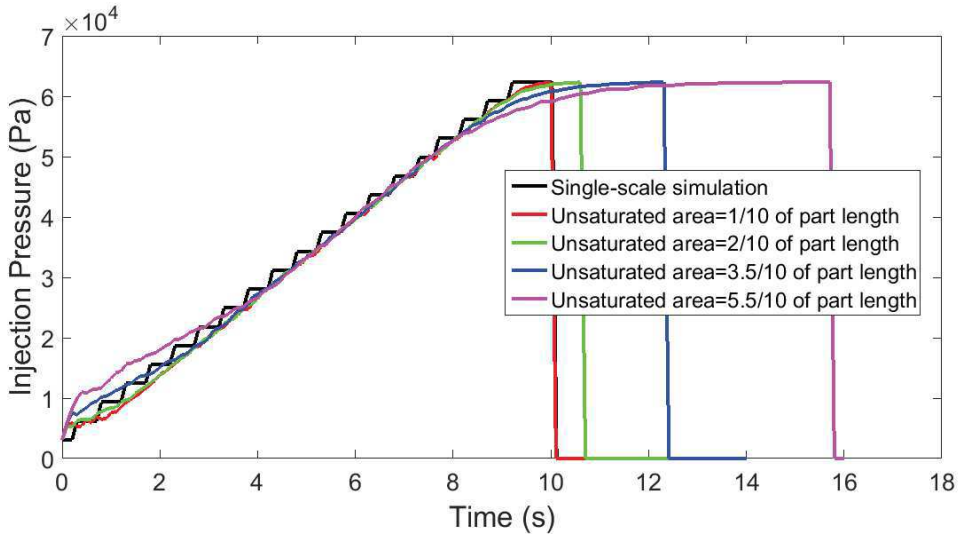

Figure 45: Injection pressures for injections at constant injection flow rate in a 10 cm long part and for various lengths of unsaturated areas

It can be observed in Figure 45 that injection pressures in the dual-scale configuration are exhibiting non-linearities at the beginning and at the end of injection (generation and resorbtion of the unsaturated area).This results is in excellent agreement with the experimental results presented in [25] It can be additionally, observed that non-linearities increase with the ratio length of unsaturated area/length of the part. Thus, it can be seen that pressure evolutions for ratios of unsaturated area versus length of the part smaller that 1/5 are very close to the theoretical pressure evolutions. Table 10 reports the ratio of time required to saturate the sample for the different lengths of unsaturated areas compared to theoretical time (10 s).

Ratio length of unsaturated area/ length of the part	0/10 Single-scale	1/10	2/10	3.5/10	5.5/10
Ratio time to saturate the part/ theoretical time	1	1	1.06	1.23	1.57

Table 10: Ratio of time required to saturate the part versus theoretical time for single-scale case and dual-scale cases featuring various lengths of unsaturated area

It can be noticed from Table 10 that under isothermal conditions, when the length of the unsaturated area is smaller than 1/5 of the length of the part, the time required to fully saturate the part is very close to the single-scale time. When the unsaturated area is larger, the extra-time required to fully saturate the part become non-negligible. These results indicate that pressure non-linearities due to channel-tow flow should become negligible for large parts. Indeed, unsaturated areas are not expected to measure more than some centimeters, therefore, ratio of length of unsaturated area to length of the part should be under 1/10 for parts measuring in the range of 1 m. This leads to reconsider the assumption or conclusions made in some publications dealing with the drooping effect ([72], [48]). In these publications, large pressure non-linearities were observed and pressure drooping was explained to be due to the sink effect of tows regarding fluid flow in the channels. The present result shows however that this effect is very limited for long parts. It can be therefore expected that the observed effects (as in Figure 15 in Part I) were due to other effects as air entrapement (discussed by Gourichon et al ([25])) or mold deformation.

Pressure non-linearities due to the sink effect of fluid in the tows have been shown to be significant for lengths on unsaturated areas large compared to the length of the part. However, for length of unsaturated areas smaller that 1/5 of the length of the part, sink effects can be neglected.

2.2 Reactive simulations

2.2.1 Gel and curing time in stationary conditions

Figure 46 plots the evolution of temperature, degree of cure and viscosity of the resin during a curing experiment in a mold at 140°C in stationary conditions.

It can be thus observed in Figure 46 that gel occurs approximately 80-90 s after components mixing (begin of the simulation) and that the end of curing occurs 160 s after mixing inducing an exothermic peak of 68°C bringing the resin to a temperature of 208°C.

2.2.2 Process understanding

Unidirectional fully coupled reactive injections with on-line mixing are conducted in a cavity measuring 90 cm. The thermo-chemo-rheological values of the parameters has been described in section 1.5.3. The maximal numerical value for the viscosity is set to 10 Pa.s. Figures 47, 48 and 49 present the mappings of degree of cure for the configurations Single-scale, DS1 and DS2 for a constant injection flow rate ensuring cavity filling within 90 s. Figures 50, 51 and 52 present the mappings of temperature and Figures 53, 54 and 55 the mappings of viscosity.

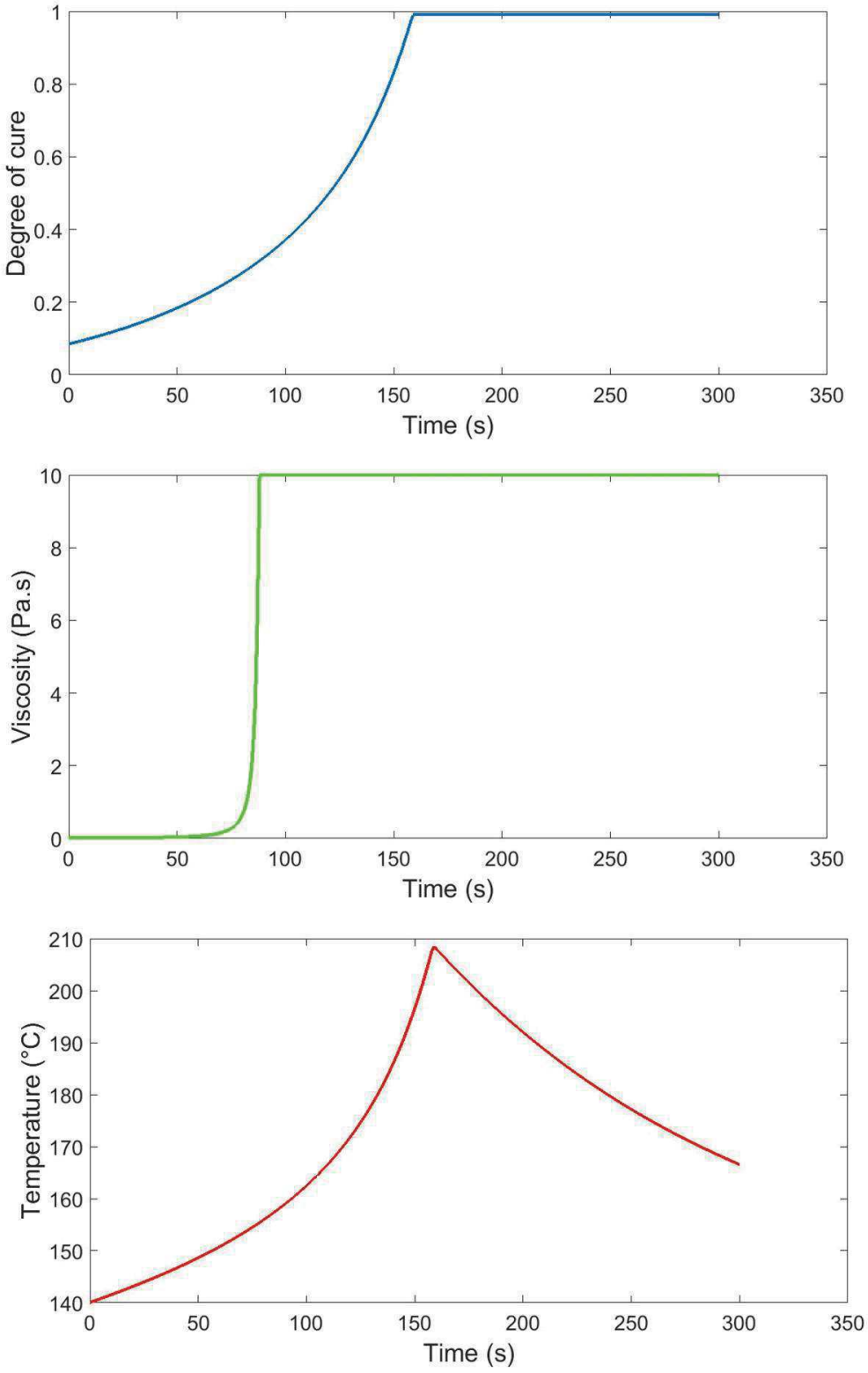

Figure 46: Degree of cure, viscosity and temperature evolution during stationary curing in a cavity at 140° C

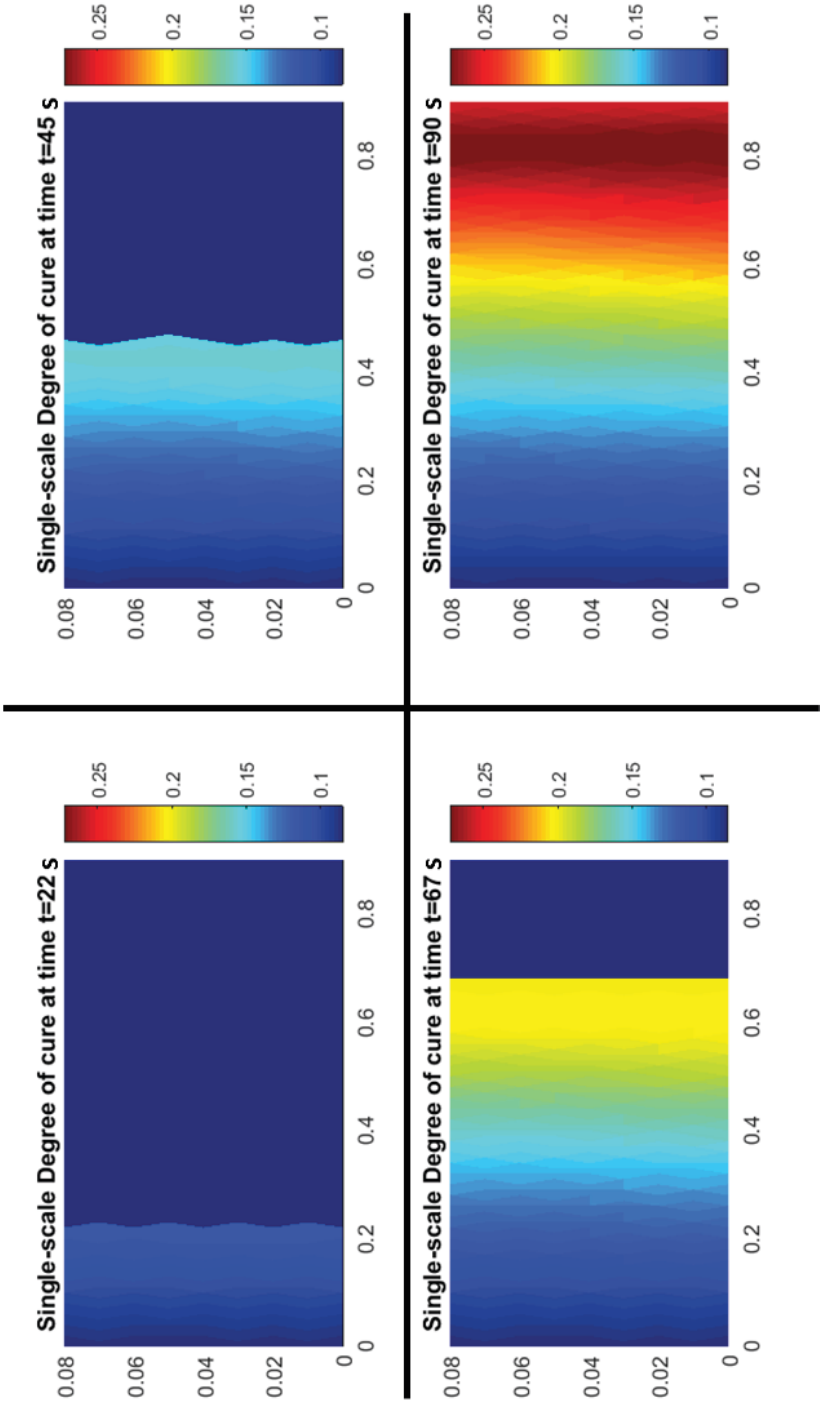

Figure 47: Mappings of the degree of cure in the Single-scale simulation

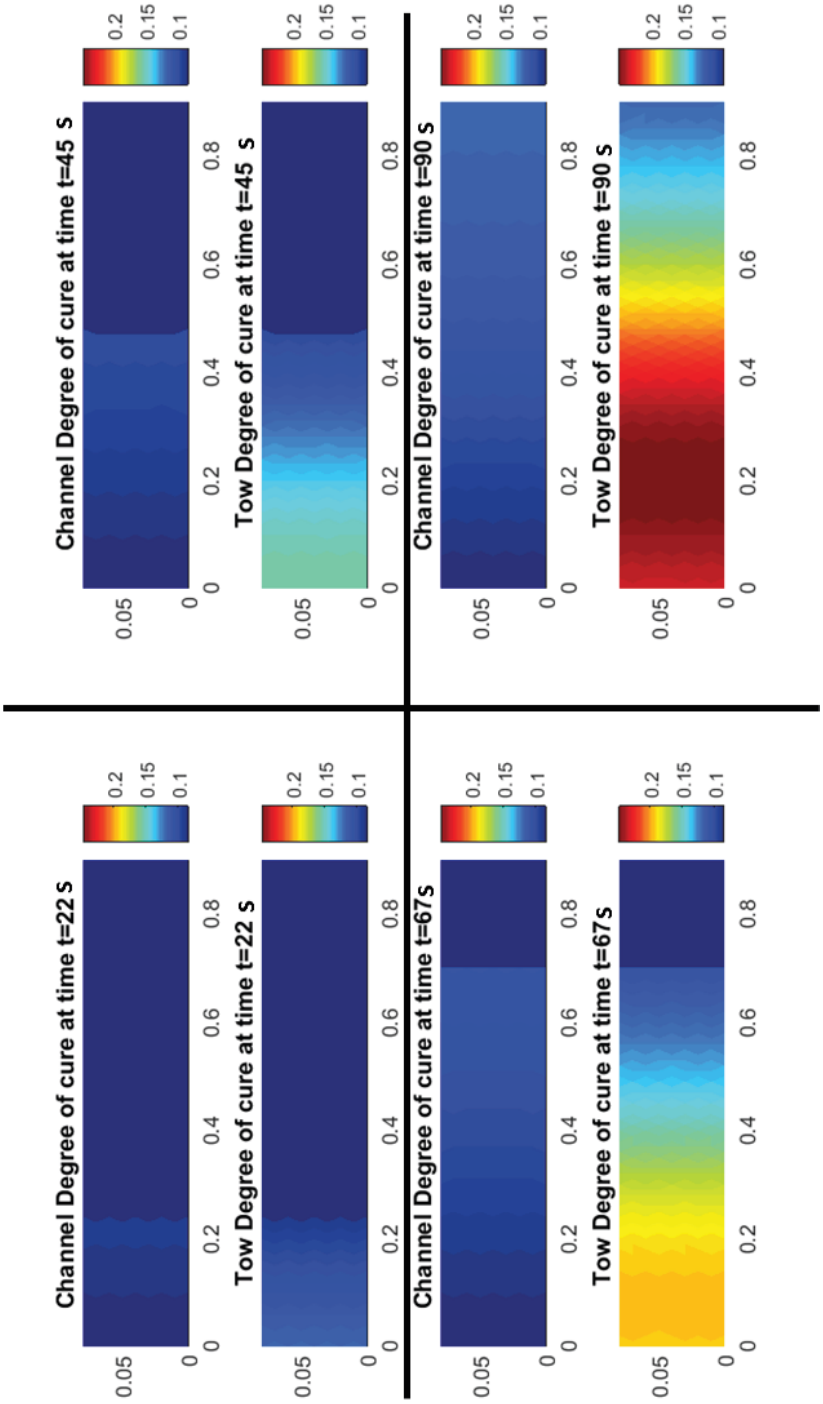

Figure 48: Mappings of the degree of cure in the DS1 simulation

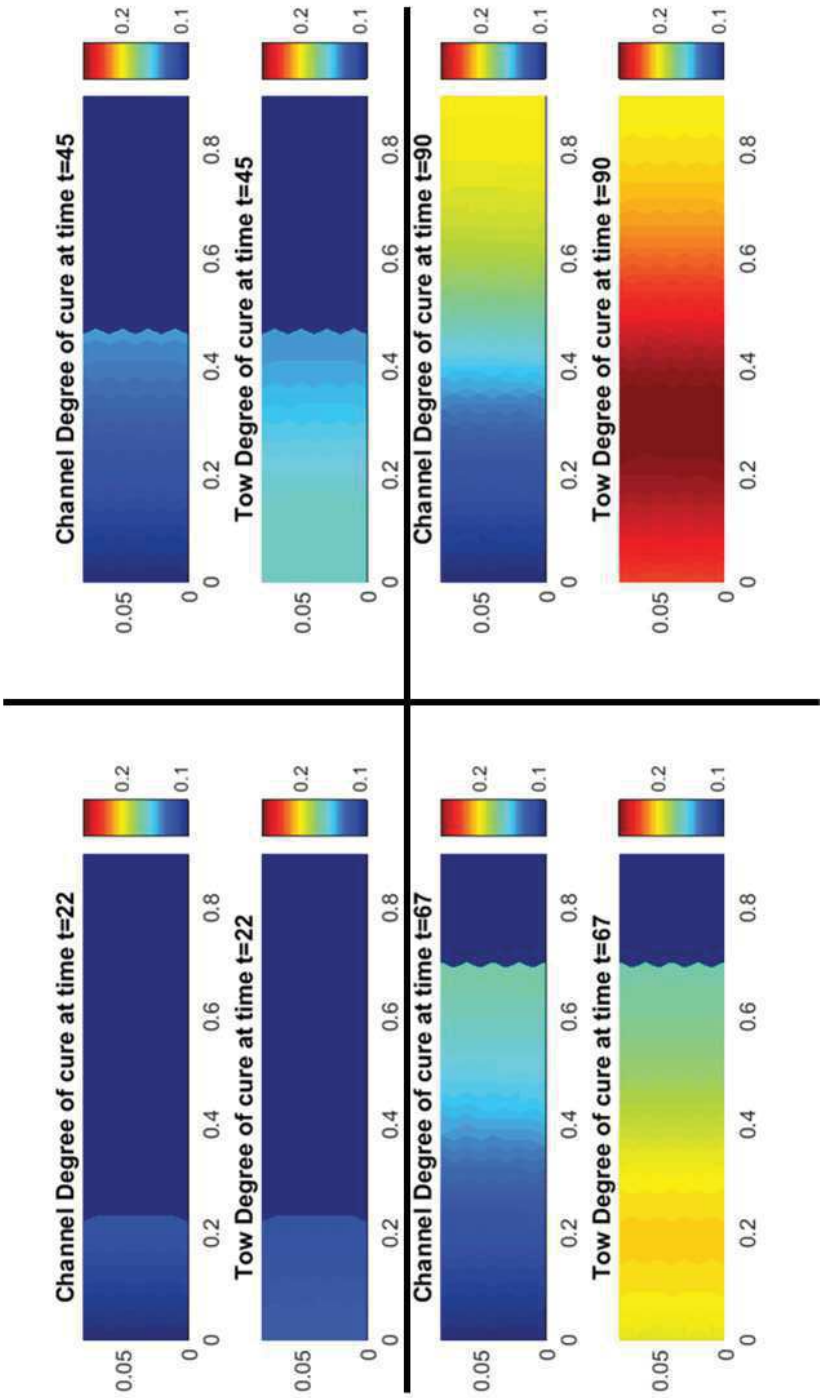

Figure 49: Mappings of the degree of cure in the DS2 simulation

Several observations can be made from these mappings:

- Distribution of degree of cure
  - Single-scale simulation

    It can be observed from Figure 47 that the highest degree of cure is always located slightly behind the flow front. This is in good agreement with the qualitative experiments presented by Roy et al in [56]. The oldest, most cured resin is located at the flow front. The fact that a small area at the flow front is less cured is due to the resin-fiber thermal exchanges. Indeed, the resin located at the flow front is all along injection meeting fibers at the temperature of the mold. Therefore, the flow front resin is maintained at a temperature close to the mold temperature (as can be seen in Figure 50). Due to a smaller temperature, kinetic is not so fast as upstream locations in the saturated area.
  - Dual-scale simulation

    Significant differences can be observed between the dual-scale and the single-scale simulations. Indeed, in the dual-scale simulations, the most cured resin is not located at the flow front in the channels but in the tows near the entry. This is also in good agreement with the qualitative observations ([56] and the assumption made of permanent intra-tow storage. Indeed, the resin injected in the early times of injection have been stored in the tows near the entry. It has therefore the longest time of residence and are expected to exhibit a high degree of cure. However, it can be noticed that the highest values of degree of cure in the tows are not located directly at the inlet but some centimeters away. This can be explained by the fact that the first centimeters of the part are crossed by resin at injection temperature that is smaller than the temperature in the part (due to polymerization). Therefore, resin stored in the tows near the entry is maintained at a temperature close to the injection temperature, which reduces the curing kinetics compared to locations further where channel resin has already been heated. On the other side, at the flow front, degree of cure in the tows is also low, due, as for the single-scale simulation, to the thermal exchanges with the fibers.

    Regarding channels, the degree of cure is increasing with increasing distance from the entry. However, the values remain below 0.15 for configuration DS1 and below 0.2 for configuration DS2. These values are small compared to the values obtained at the flow front for the single-scale simulation (in the range of 0.27). This is due to intra-tow resin storage. Indeed, all along filling the resin located at the flow front is removed from the channels to be stored in the tows. For this reason, the degree of cure of the resin located in the channels remains relatively low compared to the single-scale simulation where the most cured resin remains at the flow front.

    Finally, differences between configurations DS1 and DS2 can be observed. These differences are smaller than between single and dual-scale simulations however, they are noticeable. For configuration DS1, the value of degree of cure in the channels after 90s (end of injection) is in the range of 0.12, while in configuration DS2, it is in the range of 0.2. This is due to the size of the channel. Indeed, in configuration DS2, channels are larger and tows smaller. Therefore, the resin spends more time in the channel before flowing into the tows.

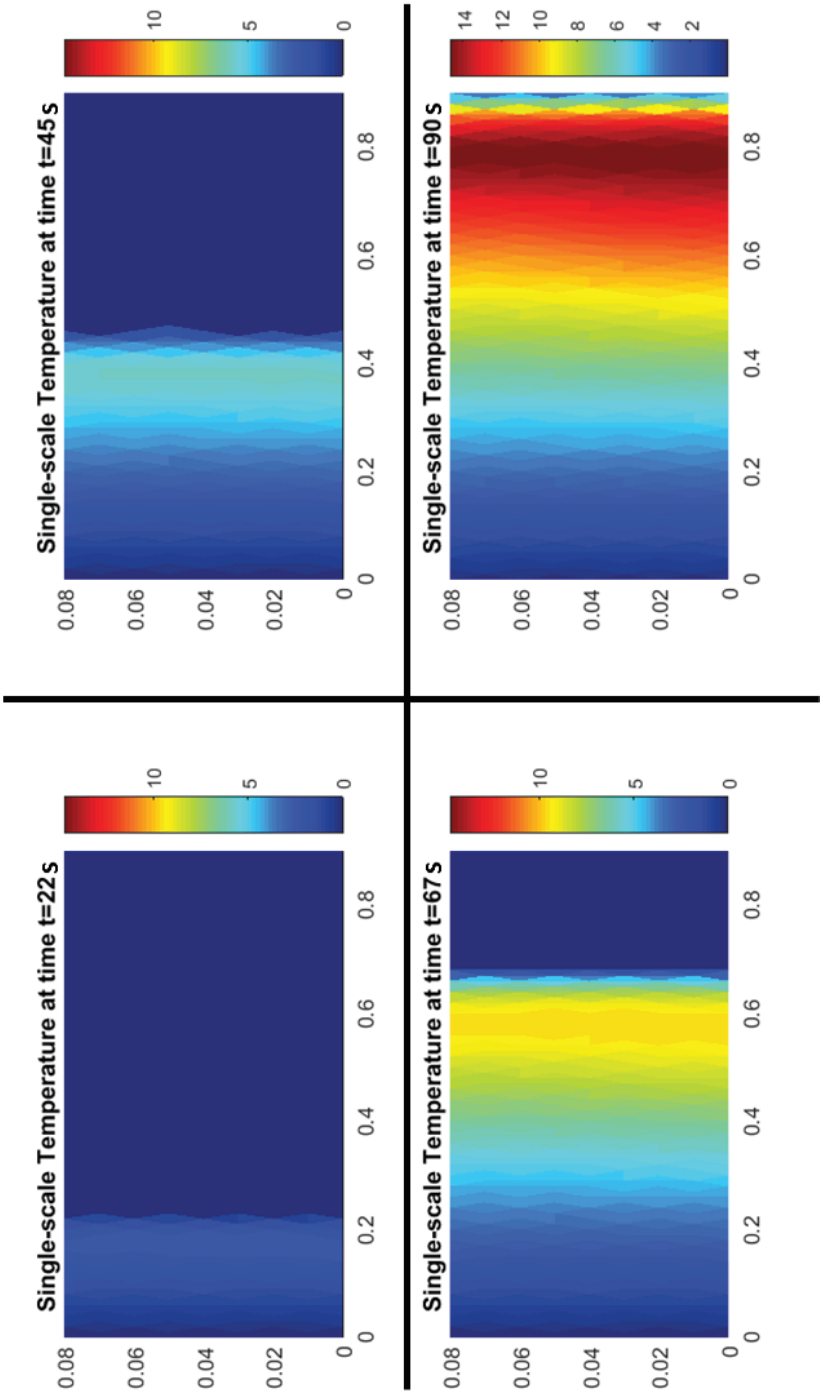

Figure 50: Mappings of the resin temperature elevation in the Single-scale simulation (°C)

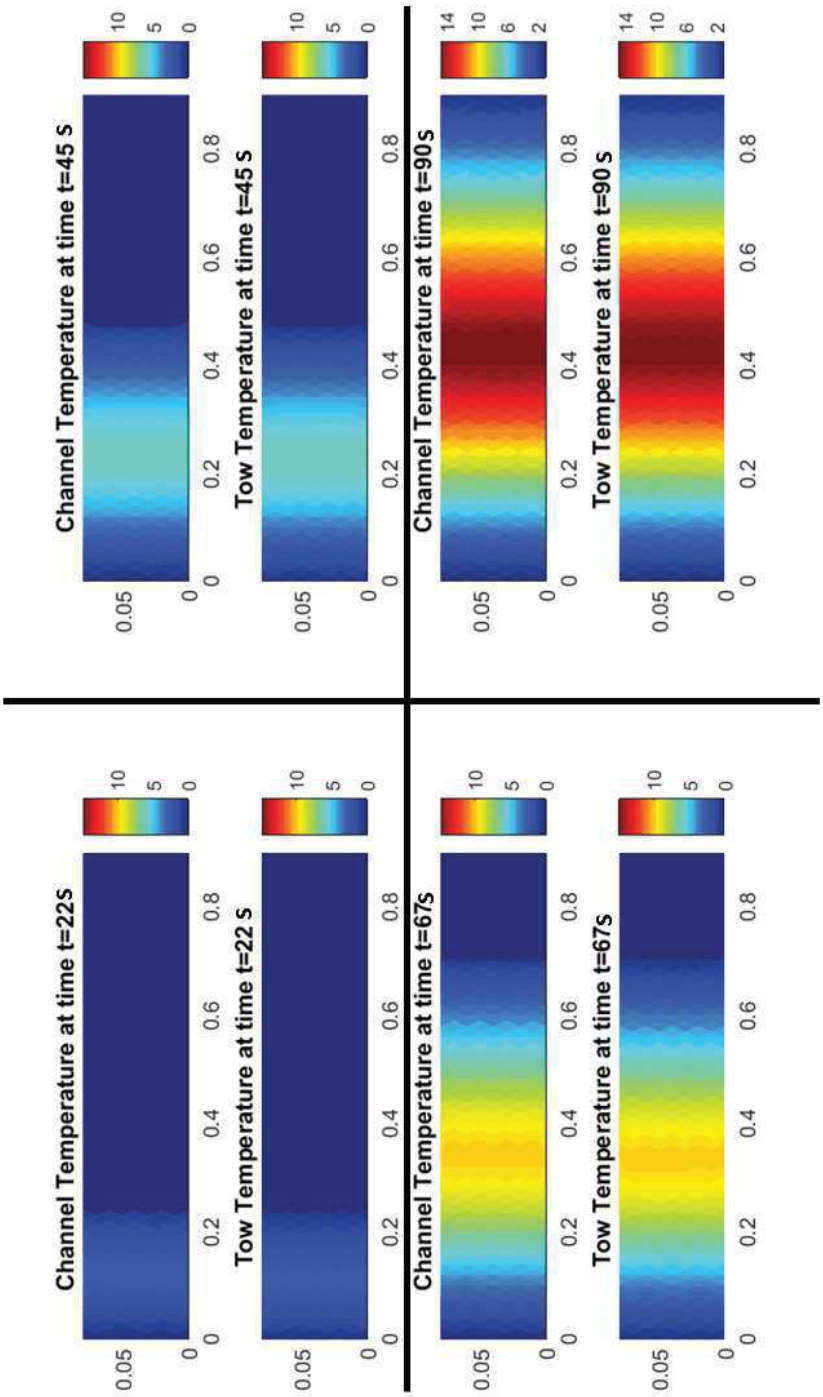

Figure 51: Mappings of the resin temperature elevation in the DS1 simulation (°C)

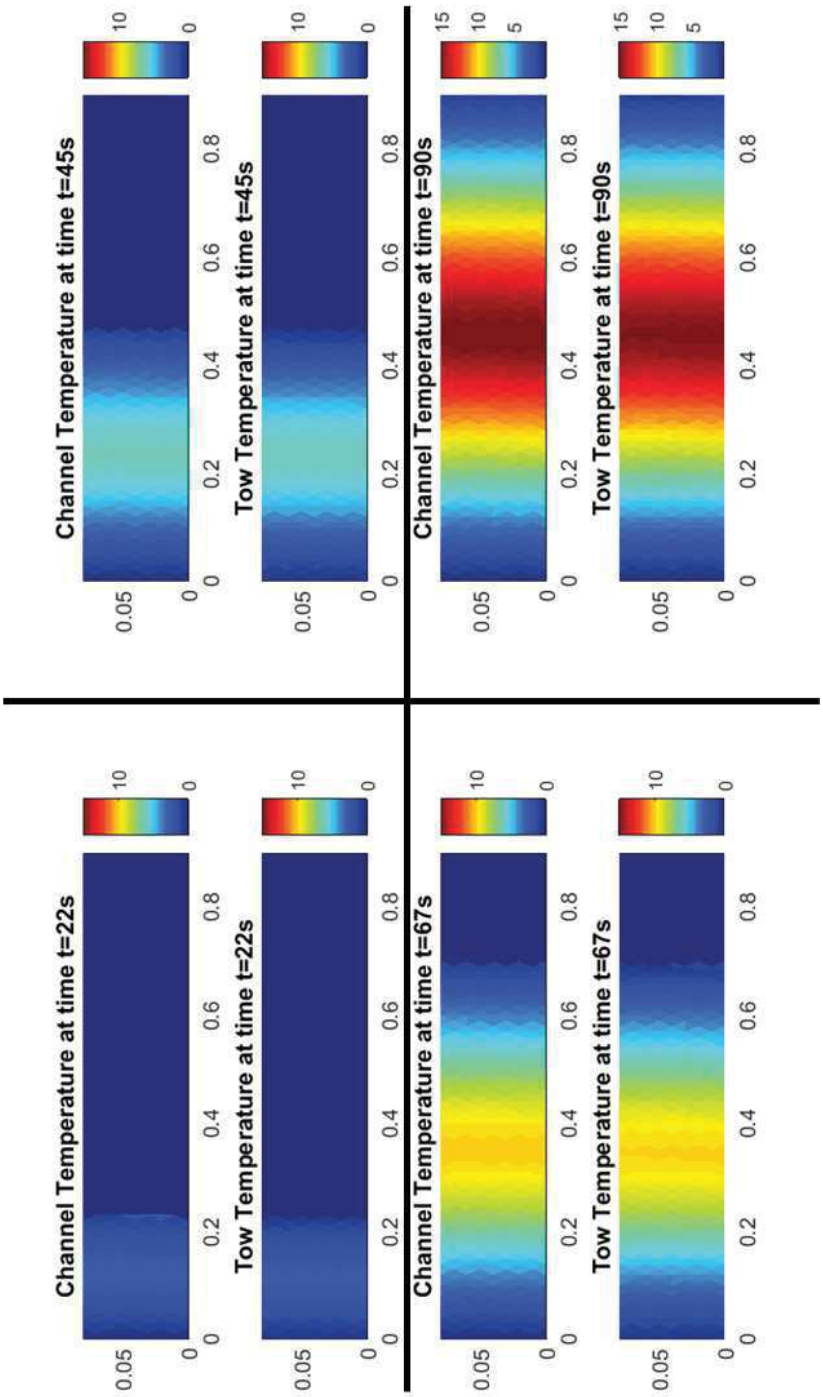

Figure 52: Mappings of the resin temperature elevation in the DS2 simulation (°C)

- Temperature distribution
  - Single-scale simulation

    High temperature distribution are similar to the high degree of cure distribution: the hottest regions are located just behind the flow front. This indicates that temperature is convected with the curing resin. The heat generated by the first injected resin induces a temperature elevation of the resin that is transported along injection. As discussed in the previous paragraph, a short region at the flow front features smaller temperatures tending to the mold and fiber temperature at the very flow front. This is due to the heat exchange between the fibers and the resin. However, this area measures only a few centimeters. Temperature transition is quick because in the single-scale porous material, the resin that has just impregnated the reinforcement is quickly replaced by hotter resin located upstream and pushed by the resin constantly injected. On the other side of the mold, temperature remains low during the whole injection. Indeed, as the reinforcement is single-scale, the resin crossing the first centimeters of the mold have always the same time of residence. In this region, a steady state is achieved and the degree of cure is constant.
  - Dual-scale simulations

    First of all, it can be observed that channel and average tow temperatures are always very close, highlighting the fact that thermal conductive effects homogenize the temperature quickly. It can then be observed that the hottest temperatures are located in the center of the saturated area. This temperature distribution is different from the one observed in the single-scale simulations. Indeed, the region with smaller temperature near the flow front is much longer than in the single-scale simulation. This is due to the flow front fiber-resin heat exchange and the geometry of the microstructure. In the dual-scale materials, fiber-resin heat exchange only occurs in the tows and the temperature of the resin tends therefore to the temperature of the fiber. Once saturated, resin is only flowing in the channels that represent a small volume of the material (8.87% in DS1 and 32.7% in DS2). Therefore, the heat that can be provided by the resin in the channels to increase the temperature in the tows is small and channel temperature is quickly homogenized. Additionally, on the other hand, due to the lower temperature and the low intra-tow porosity, curing kinetic in the tow is reduced. For these reasons, the lower temperature area behind the flow front is much larger in the dual-scale simulation than in the single-scale simulation. The tendency that channels are transporting heat to the colder regions closer to the flow front can be noticed in the simulations: the hotter region is indeed slightly translated in the direction of the flow front compared to the intra-tow hot region.
    Finally, only small differences can be observed in terms of temperature between the configurations DS1 and DS2. The only observable difference is a slightly higher maximal temperature at the end of injection in configuration DS1. This confirms the fact that curing is occuring faster (as more heat is generated) when channels are larger (configuration DS2).

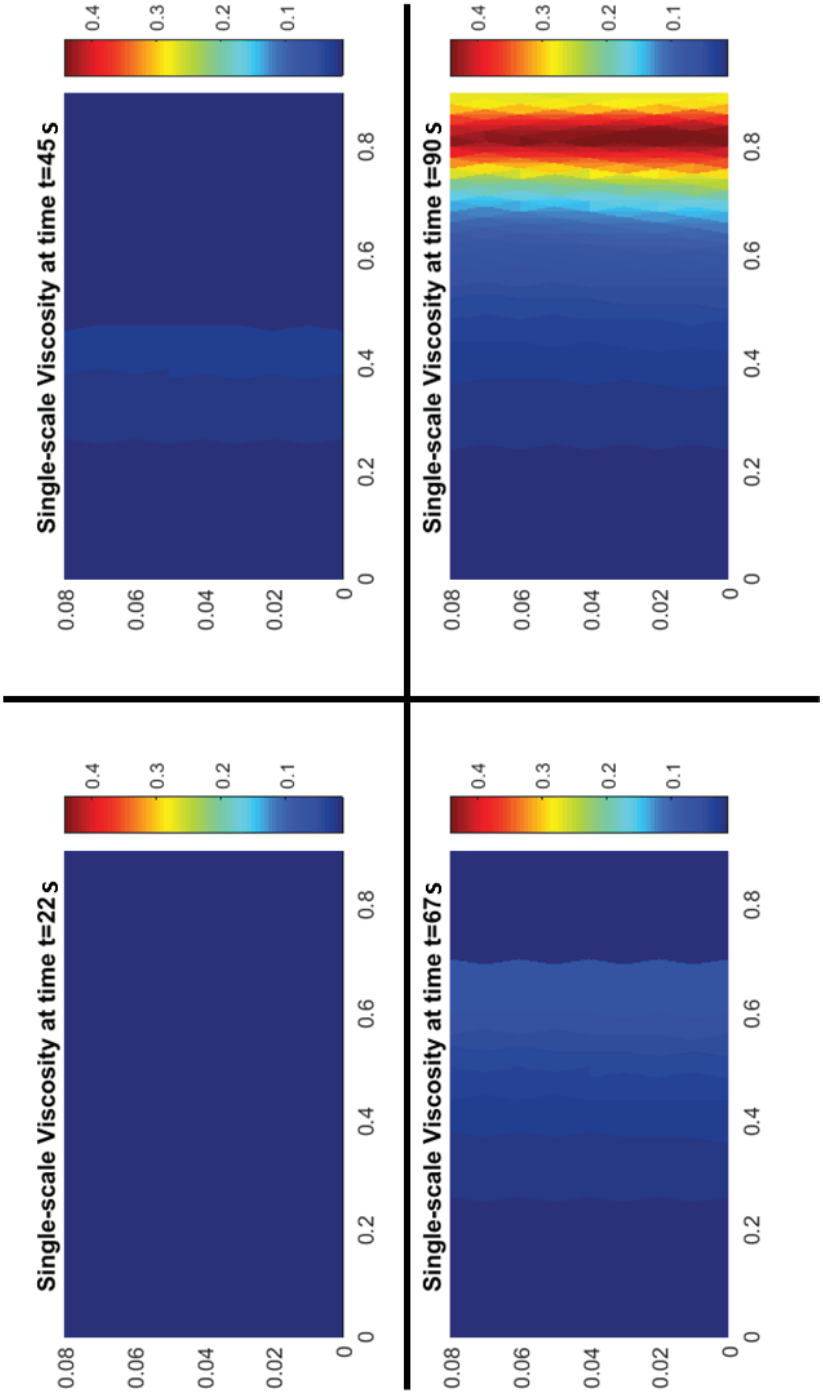

Figure 53: Mappings of the viscosity in the Single-scale simulation (Pa.s)

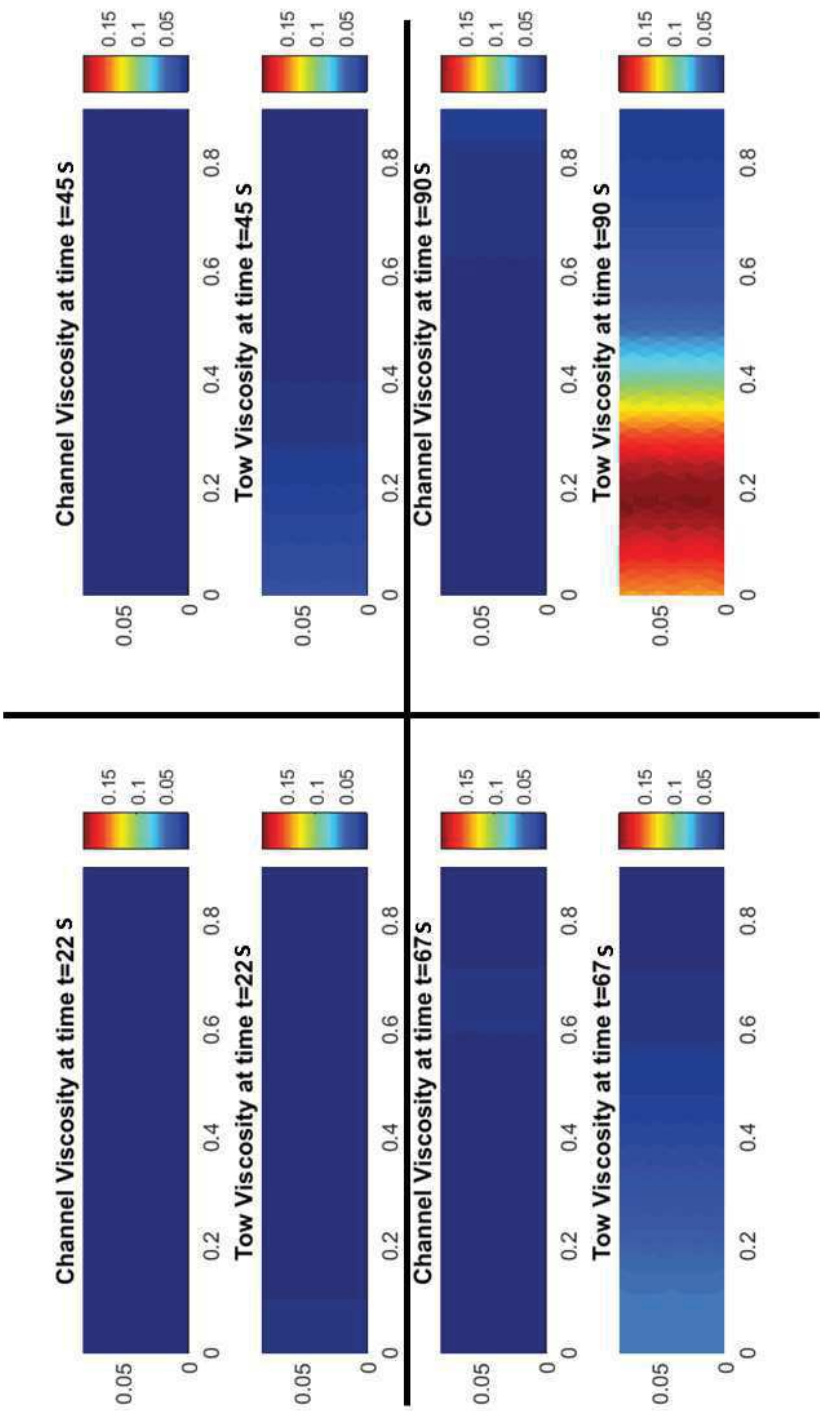

Figure 54: Mappings of the viscosity in the DS1 simulation (Pa.s)

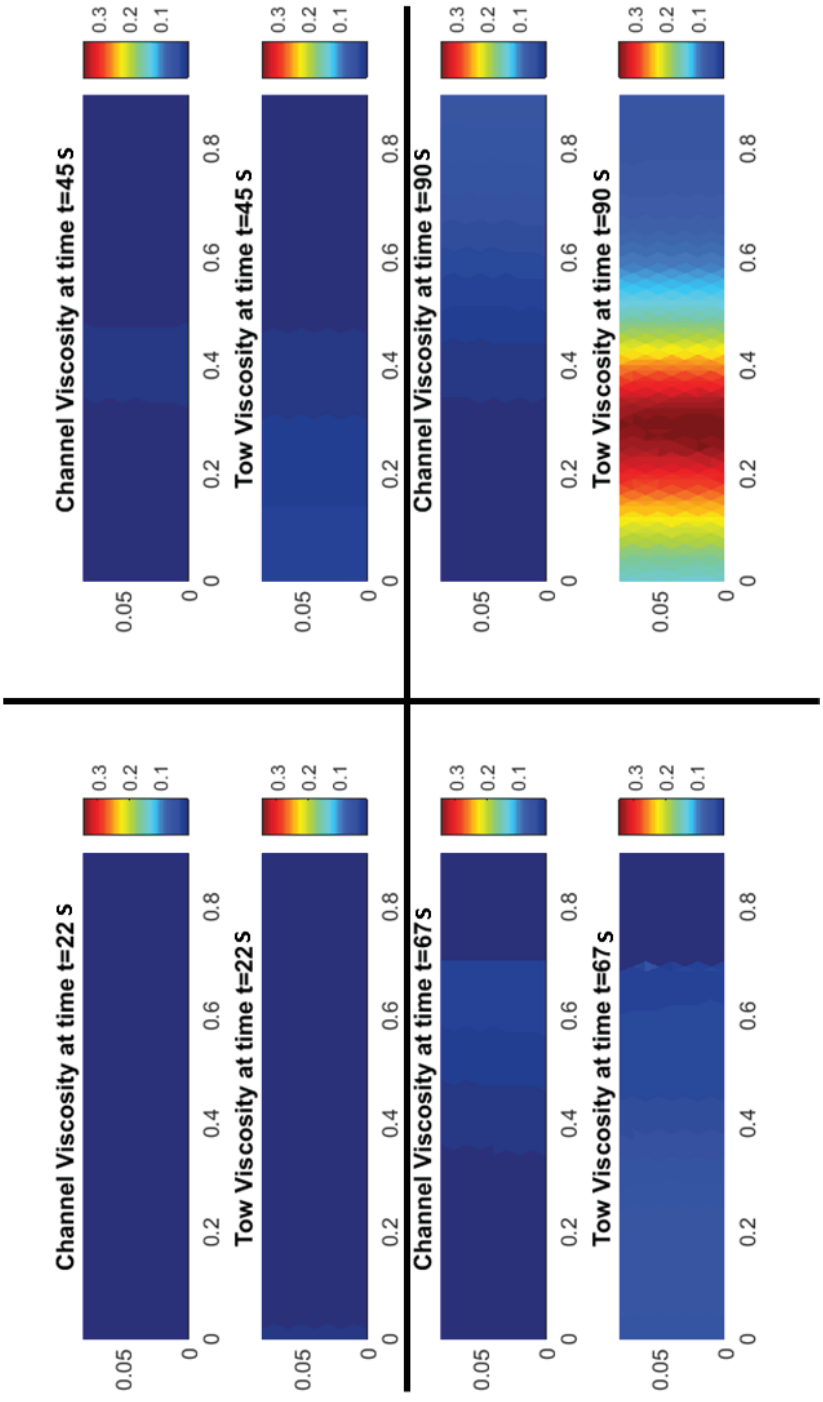

Figure 55: Mappings of the viscosity in the DS2 simulation (Pa.s)

- Viscosity
  - Single-scale simulation

    As introduced in section 3.1.2 of part I, viscosity is increasing with increasing degree of cure and decreasing for increasing temperature. It can also be noticed from Figure 46 that viscosity increase is very sharp about 80-90 s after mixing in stationary conditions. In this context, the viscosity mappings of Figures 53-55 can be interpreted. It can indeed be observed that viscosity increase is small at 22, 45 and 67 s after injection. However, a significant viscosity increase can be observed at 90 s near the flow front. This region corresponds to the hottest region but also where degree of cure is the highest.
  - Dual-scale simulation

    As for degree of cure and temperature, viscosity distribution is very different for the dual-scale simulations from the single-scale simulation. And as for degree of cure, the most cured resin is located in the tows near the inlet. The discrepancy between channel and tow viscosity is very significant. In simulations DS1, viscosity increase in the channel is almost not noticeable while in DS2, a slight increase can be observed. This must be once again coupled with the higher degree of cure in the channels due to longer time of residence. Finally, the antagonist effects of degree of cure and temperature on viscosity can be observed in the tows. The hottest region at the end of injection in both configuration is roughly located between 40 and 60 cm. In this region, degree of cure is also relatively high (between 0.18 and 0.25), however, viscosity is low (between injection viscosity and 0.1 Pa.s). This highlights the interest of conducting fully coupled simulations.
    Additionally, as described in Darcy's law, viscosity distribution and values are supposed to affect injection pressure. It can be observed from the mappings that the highest viscosity values at the end of injection are obtained for the single-scale simulation. Injection pressure is therefore expected to be the highest for this simulations. On the other hand, for dual-scale simulations, flow is assumed to occur only in the channels and that intra-tow storage is permanent. The viscosity values recorded in the channels of the two dual-scale simulations are significantly lower than in the single-scale simulation and slightly higher in configuration DS2 than DS1. Injection pressures are therefore expected to be higher in configuration DS2 than DS1. Figure 56 plots the injection pressures of the three simulations.

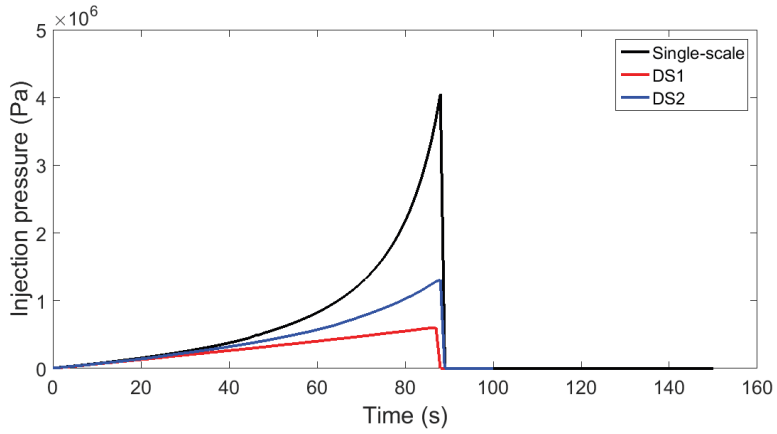

Figure 56: Injection pressure for the three configurations for the injections at constant injection flow rate ensuring cavity filling within 90 s

Several mechanisms differentiating single-scale and dual-scale flows in reactive injections with on-line mixing have been identified:

- For the tested dual-scale simulations, temperature of tows and channels are close to each other.
- The fiber-resin heat exchange at the flow front has been shown to play a major role in the temperature, degree of cure and viscosity distribution especially in the dual-scale simulations. This heat exchange generate a region where the temperature is lower and cure therefore slower than upstream where resin arrived heated by polymerization (and heat exchanges with the tows in the dual-scale simulations).
- In single-scale simulation, the hottest, more cured and more viscous region is located just behind the flow front. On the other hand, in dual-scale simulations, the hottest region is located in the middle of the saturated area and the most viscous and most cured regions in the tows near the inlet.
- For a given injection flow rate, the smaller the channels are in the materials, the faster resin flows in these channels and therefore the shorter the time of residence. Evolutions of degree of cure or viscosity are very limited for small channels.

2.2.3 Influence of the injection/curing time ratio

In the previous section, the mechanisms involved in the reactive RTM process with on-line mixing have been identified. The influence of the injection/curing time ratio will now be investigated.

For the three configurations, reactive injections at constant injection flow rate ensuring various injection times have been simulated. Figure 57, 58 and 59 presents the injection pressure evolution respectively for the Single-scale simulation, for the configuration DS1 and the configuration DS2.

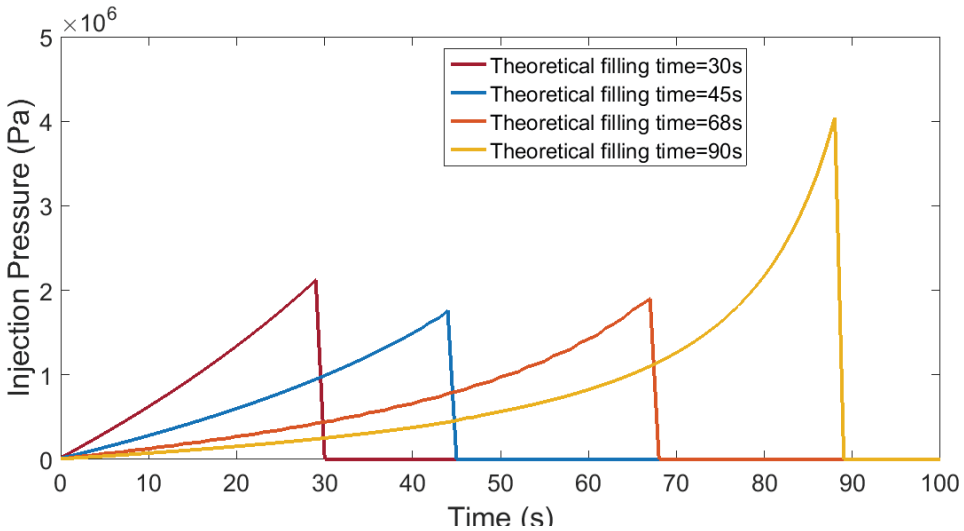

Figure 57: Injection pressure for the configuration Single-scale under reactive conditions for various injection flow rates

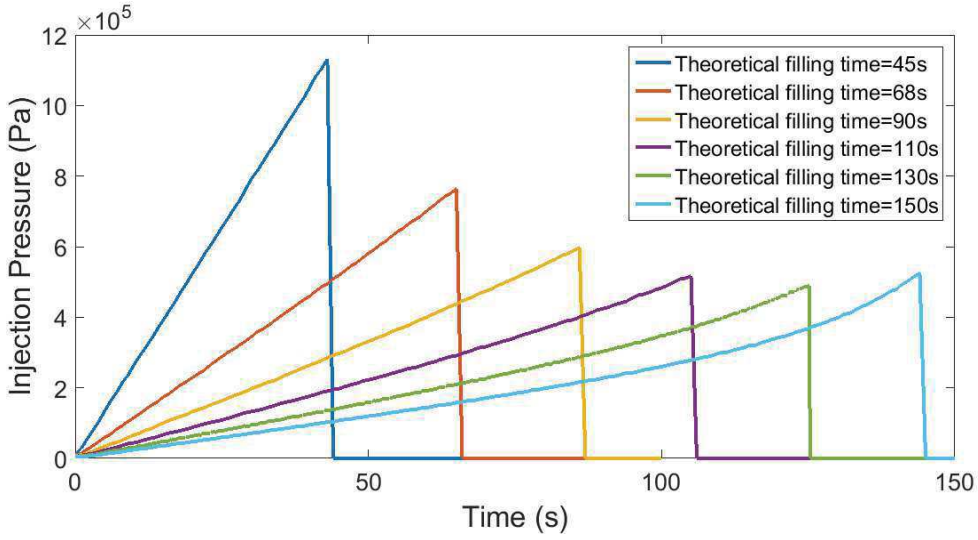

Figure 58: Injection pressure for the configuration DS1 under reactive conditions for various injection flow rates

It can be observed in these curves that for all configurations, an injection flow rate can be found that induce a minimal pressure at the end of injection (for a sake of simplicity the discussions will be further made on theoretical filling times -the injection flow rates are constant). The origin of this minimal value can be deducted from the curves. Indeed, the pressure evolution for injection times shorter than the one of the minimal final pressure

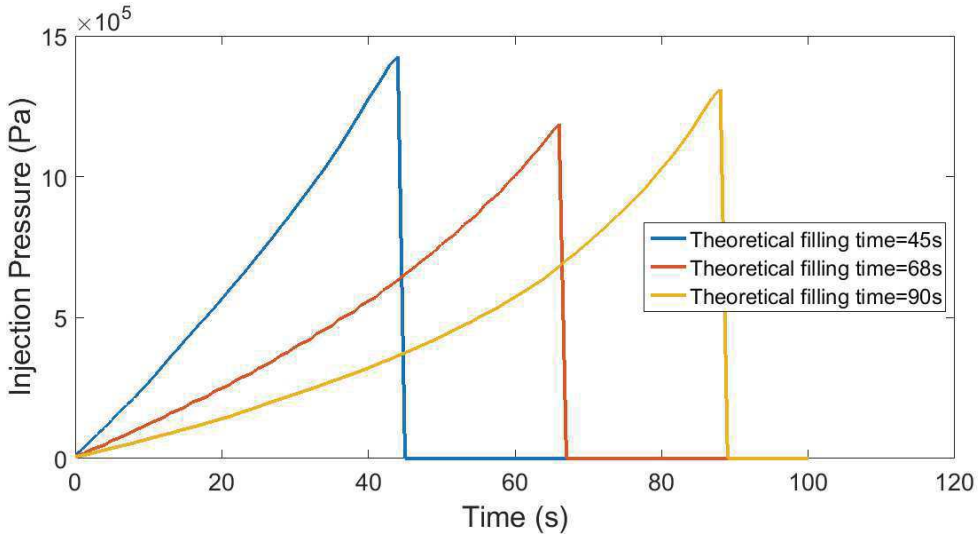

Figure 59: Injection pressure for the configuration DS2 under reactive conditions for various injection flow rates

are linear while the pressure evolutions for longer injection times exhibit significant non linearities. This can be therefore explained by the fact that for short injection times, injection conditions are quasi isothermal and pressure evolution are mainly governed by Darcy flow with constant viscosity in the part. However, for large injection times, viscosity increase becomes significant inducing the observed pressure evolution non-linearities.
Additionally, it can be noticed that the optimum injection time to minimize the final injection pressure is not the same for all configurations. Its value is in the range of 50-60 seconds for the Single-scale simulation but in the range of 70 seconds for configuration DS2 and about 130 seconds for configuration DS1. For the Single-scale simulation and configuration DS2, the optimum injection time to minimize final injection pressure is below the limit of 90 seconds corresponding to the gel of the resin in stationary conditions. Additionally, it has been shown in Figures 53-55 that gel was not achieved in any location in the part for these two configurations for an injection time of 90 s. Therefore, these injection times allow part manufacturing without major defects. However, the injection time to minimize final injection pressure in configuration DS1 is far longer than the gel time in stationary conditions reported in section 2.2.1. It would be therefore surprising that gel did not already occur in some locations in the part. As no significant viscosity increase is noticed in the channels, gel is very likely to have occurred in the tows. Figures 60, 61 and 62 shows mappings of temperature, degree of cure and viscosity in configuration DS1 at the end of the 130 s lasting injection.

As expected, it can be noticed that resin has gelled in the tows in the first 50 cm of the part at the end of the 130 s injection. This is not acceptable for an industrial process as it generates huge gradients of degree of cure and may lead to significant residual stresses in the material. This result highlights that the only injection pressure is not sufficient in dual-scale simulations to ensure the good quality of the injection. Degree of cure and viscosity distribution in the part must also be considered carefully. After study of these distributions for the simulation with a theoretical injection time of 110 s, it appears that gel is about to occur in the tows at the end of injection. For this reason and in order to conduct a safe injection, injection time of the resin should always be kept under the gel time of the resin in stationary conditions.

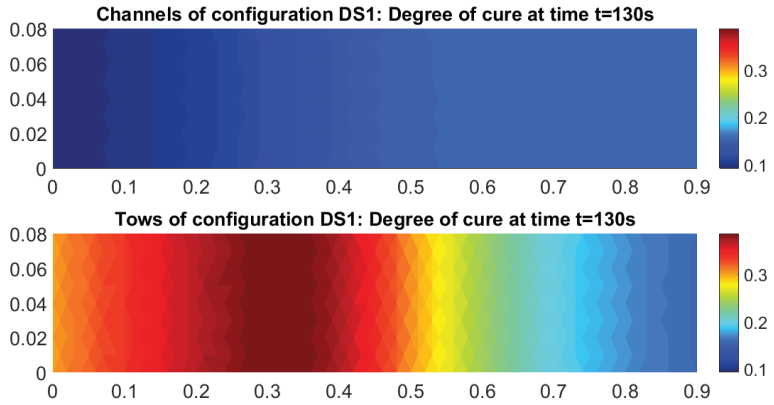

Figure 60: Mappings of degree of cure at the end of injection for configuration DS1 and a theoretical filling time of 130 s

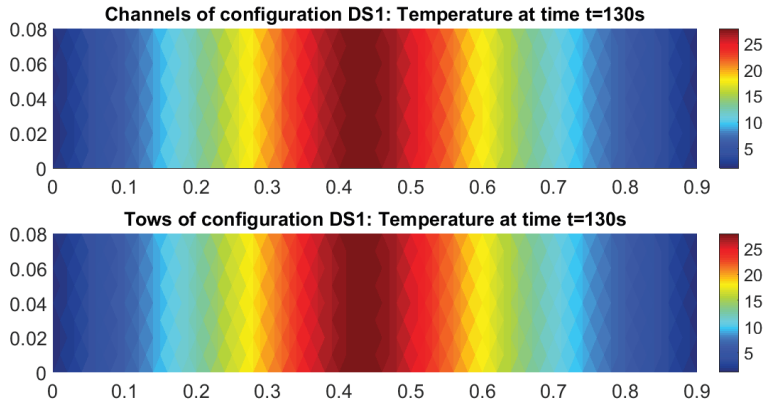

Figure 61: Mappings of temperature at the end of injection for configuration DS1 and a theoretical filling time of 130 s

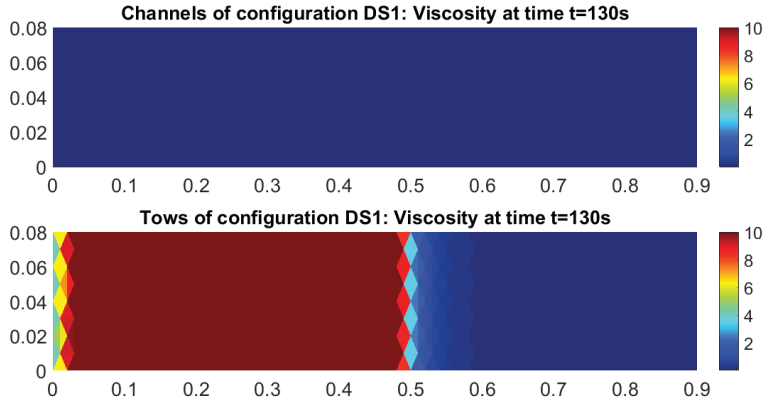

Figure 62: Mappings of viscosity at the end of injection for configuration DS1 and a theoretical filling time of 130 s

The influence of the injection/curing time has been investigated on the reactive process in the case of equal temperatures for mold, fibers and injected resins. The following conclusions have been established:

- It exists a flow rate (i.e. an injection time) that minimizes the final injection pressure. This injection time is a compromise between fast injection inducing high pressure due to Darcy flow in quasi-isothermal conditions and slow injections in which the effects of curing induce viscosity increases and therefore injection pressure increases.
- The injection time minimizing the final injection pressure is not the same for all materials at a given FVF. The larger the flow region are in the microstructure, the shorter this time will be.
- In configurations with small channels and for injection times longer than the gel time in stationary conditions, gel can occur in the tows. And this phenomenon is not especially noticeable on the injection pressure.
- If the criteria of process optimization is the reduction of the injection pressure, the configuration of the microstructure of the material should be investigated. Additionally, in any case, injection times longer than the gel time should be avoided, and if conducted, the values of degree of cure and viscosity in the tows should be carefully observed.

2.2.4 Influence of the length of the unsaturated area on the injection pressure and the quantities of interest distribution

Intra-tow resin storage has been demonstrated to play an increasing role in temperature, degree of cure and viscosity distribution during reactive injections when injection time come close to curing time. However, the effects of the the unsaturated area has not been considered. This aspect will therefore be investigated in this section. Figure 63 presents the injection pressure evolution for configuration DS1 for different lengths of unsaturated areas (1 cm, 2 cm, 3.5 cm) (ratio K_c/K_t is modified by reducing K_t). These length of unsaturated areas are in the range of the values observed experimentally ([70], [46]).

It can be observed from Figure 63 that slight injection pressure differences can be observed between the curves. In particular, the time to reach full saturation is 4 seconds longer for the 3.5 cm unsaturated area. This increase is in the range of values observed in isothermal conditions in section 2.2.1. In a more general manner, no differential pressure non-linearities that would be related to values of viscosity evolving differently are observed for the various lengths of unsaturated areas. The same observations are made for configuration DS2, even if the effects of curing are more observable. In order to ensure that property evolution in the part are similar for the different lengths of unsaturated areas, degree of cure, temperature and viscosity mappings of the channels and tows of configuration DS1 are presented respectively in Figures 64 and 65.

It can be clearly observed in Figures 64 and 65 that degree of cure, temperature and viscosity values and distributions are very similar in the channels (Figures 64) for the three different lengths of unsaturated area. Clear similarities are also noticed in the tows (Figures 65. These mappings confirm therefore that the length of the unsaturated area has only a very limited influence in the process during reactive injections with initially equal temperature of mold, fibers and injection resin. This phenomenon can be explained by the fact that for dual-scale simulations, the temperature at the flow front is very close to the mold temperature. Therefore, curing occurs slowly compared to other hotter regions

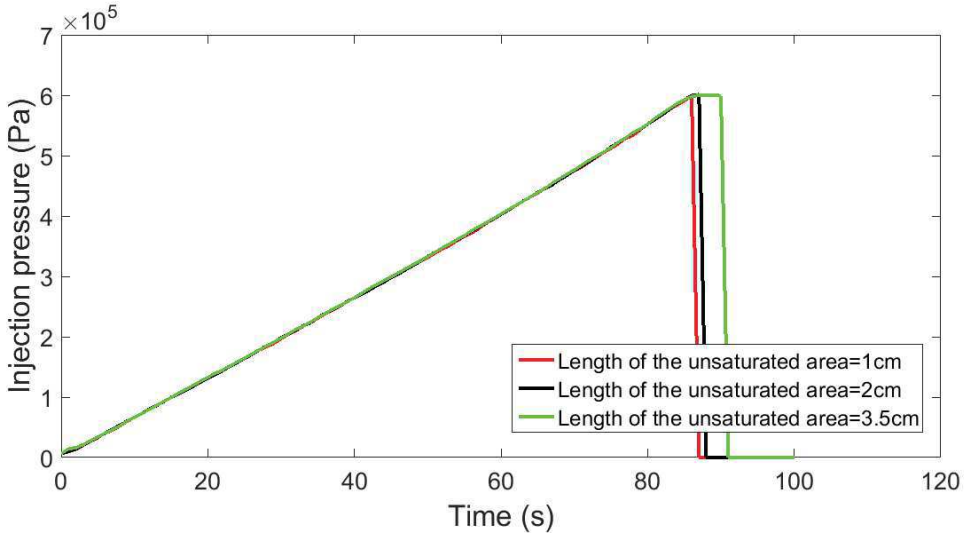

Figure 63: Injection pressure for three different length of unsaturated areas for configuration DS1 and for the injections at constant injection flow rate ensuring cavity filling within 90 s

in the mold. Thus, the evolution of resin properties during the extra-time spent by the resin in the channels for longer unsaturated areas is negligible.

It is thus demonstrated that for a reactive injection with online mixing with the same initial temperatures for the mold, the fibers and the injected resin, and for an injection time equivalent to the gel time, the presence of an unsaturated area featuring a reasonable size has a negligible influence on the values and distribution of the quantities of interest in the part. Additionally, the only difference induced by the length of the unsaturated area was found to be an increase of the injection time equivalent to the one observed in isothermal conditions. For these reasons, and as in isothermal conditions, it can be assumed that in the considered reactive conditions, the length of the unsaturated area has a negligible influence on the process.

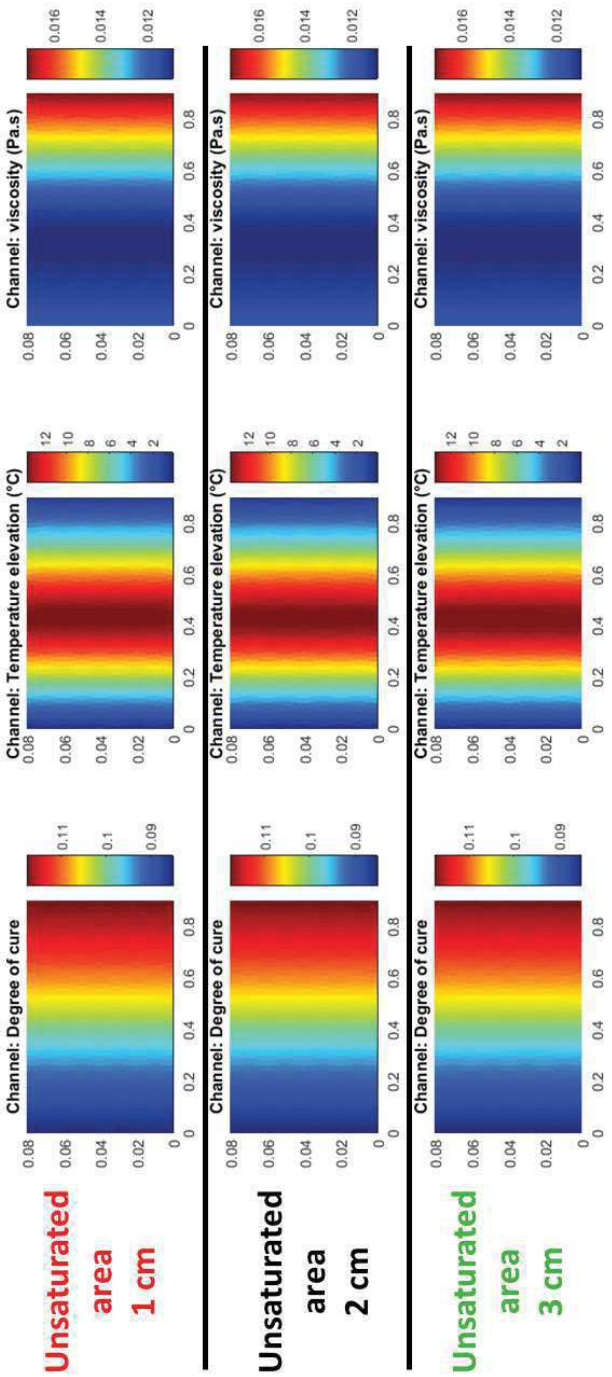

Figure 64: Mappings of degree of cure, temperature and viscosity in the channels of the configuration DS1 for several lengths of unsaturated areas at time t=87 s

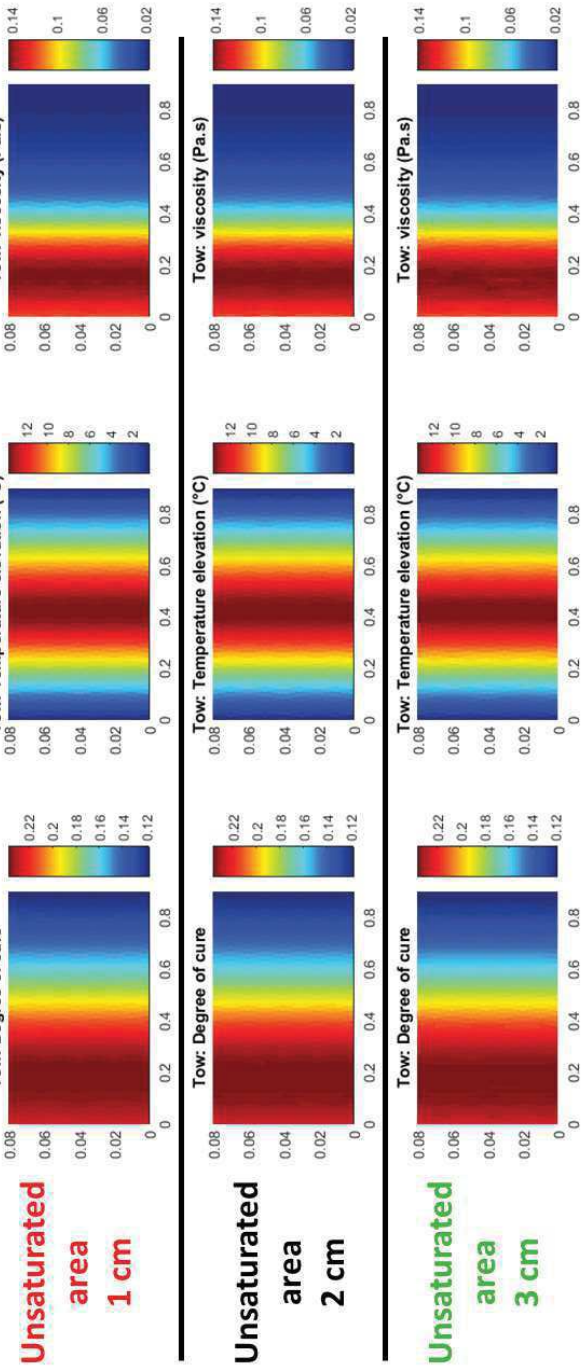

Figure 65: Mappings of degree of cure, temperature and viscosity in the tows of the configuration DS1 for several lengths of unsaturated areas at time t=87 s

2.2.5 Influence of the injection time on the curing time

In the previous sections, the influence of the microstructure and the process parameters have been evaluated during injection only. In this section, the influence of these parameters will be investigated regarding time to reach full cure in the part. Configuration DS1 and DS2 are compared. It is expected (and verified on the mappings) that the latest location to cure in all simulations is the location near the entry. Indeed, it is the location where the latest drops of resins are injected. For this reason, the evolution of the degree of cure in the entry elements are plotted for various injection times and two configurations (Single-scale and DS1). Figure 66 presents the evolution of degree of cure in the Single-scale configuration.

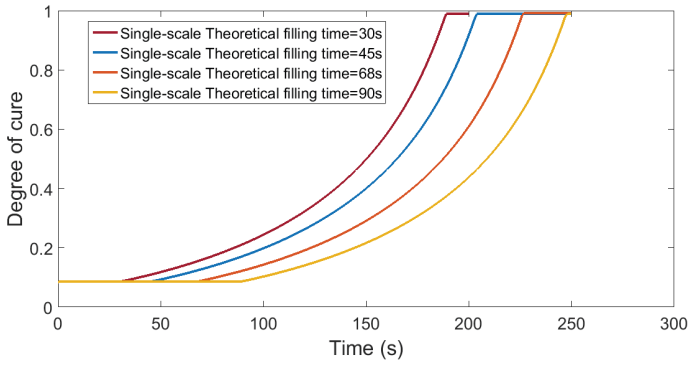

Figure 66: Evolution of the degree of cure in the entry elements of the Single-scale simulation for various injection times

Figures 67 and 68 presents the evolution of the degree of cure in the channels and in the tows of configuration DS1 separately and Figure 69 compares the evolutions of degree of cure in the channels of configuration DS1 with the degree of cure in the elements of the Single-scale simulation.

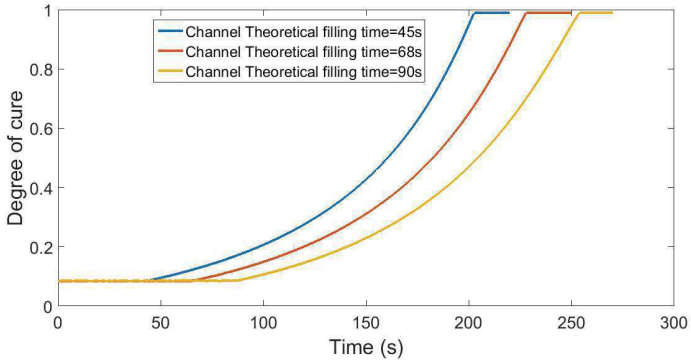

Figure 67: Evolution of the degree of cure in the channels of the entry elements of the configuration DS1 for various injection times

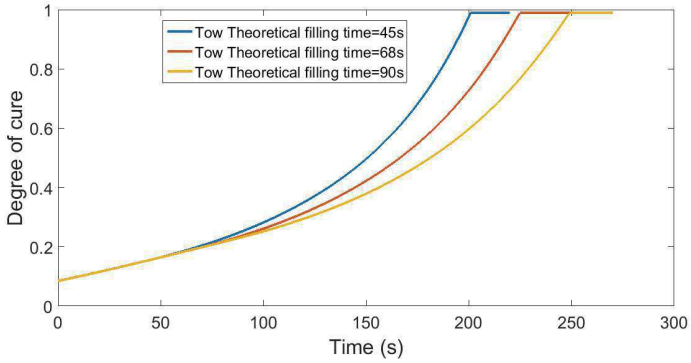

Figure 68: Evolution of the degree of cure in the tows of the entry elements of configuration DS1 for various injection times

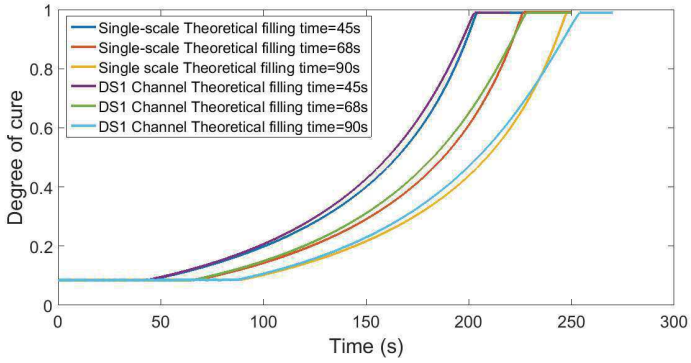

Figure 69: Comparison of the degree of cure evolution in one entry element in configuration Single-scale and DS1 for three different filling times

Several observations can be made from these curves. Considering Figure 66, two phases can be noticed in the evolution of the degree of cure. Until the end of injection, the degree of cure in the entry element remains constant. Indeed, an equilibrium is established between the cure occurring within the entry element during the time required for the injected resin to flow through it and the constant replacement of the resin flowing out of the element and replaced by resin at injection degree of cure. After the end of injection, significant increase in the degree of cure can be observed. When the resin is no more replaced in the element by young resin, the degree of cure rises. Due to the various filling times, degree of cure increase in the element starts at various times. Furthermore, it can be noticed that the time separating the end of curing is equivalent to the time separating the the end of injection. This highlights that curing occurs with the same kinetics in the Single-scale model whatever the injection time.

Considering Figures 67 and 68, it can be observed that degree of cure in the channels and in the tows are evolving in different ways especially during the injection phase. In the channels (where flow occurs), the degree of cure exhibits a constant value during injection as for the Single-scale simulation. The explanation is the same as for the Single-scale simulation: an equilibrium is reached between the injected resin and the curing that occurs within the element. In the tows, on the contrary, resin is stored and significant degree of cure increase can be noticed from the first moments after saturation. It can be additionally observed that intra-tow degree of cure increases at the same rate in the tows for the three flow rates until the end of injection. The fact that, for example for the theoretical filling time of 45 s), degree of cure begins to increase faster in the tows after the end of injection highlight the fact that during injection, a mechanism was slowing down cure. This is very likely to be the resin flow that maintained the channel at a temperature close to the injection temperature. During the injection phase, intra-tow cure was therefore generating heat through exothermy but this heat was convected to the flow front by the resin flowing in the channel. Cure was therefore conducted in quasi isothermal conditions in the tows of the entry elements. It can be additionally observed that for the three tested filling times, the duration to reach full cure in the channels and in the tows are close to each other (1-4 s difference).

So, an indicator highlighting the tow channel heat exchanges due to more advanced curing in the tows can be observed in Figure 69. This curve compares the evolution of the degree of cure in the Single-scale configuration and in configuration DS1. At the last times of injection, the entry elements of the Single-scale simulation and the channels of the DS1 simulation are filled with newly mixed resin. It can then be observed that the evolution of degree of cure is different in the two configurations. It can be indeed clearly observed that the degree of cure is increasing faster in configuration DS1 at the first instants after the end of injection. This is due to the resin stored in the tows. It features already a higher value of degree of cure and therefore a higher curing rate. Exothermy in the tows is therefore higher than in the single-scale element. This induced a faster degree of cure increase in the channels. However, at the end of curing, the trends are being inversed (especially for the 90 s long injection). This is due to the fact that along injection, intra-tow resin has cured increasing its degree of cure and generating heat. At the end of curing, tows finish therefore polymerization earlier and stop providing heat to the channels which slows down the final cure of the channels. With these observations, it has been verified that couplings are well reproduced. It has been also established that for the testing conditions of equal mold fiber and injected resin temperature, curing time of the entry elements are similar for single-scale and dual-scale simulations.

It can therefore be concluded that in the considered conditions of equal mold, fiber and resin injection temperature, increasing the injection time increases the curing time in similar proportions for single as well as for dual-scale simulations. Additionally, it has been demonstrated that for the three considered injection times, the prediction of curing times for the entry elements were similar in single and dual scale simulations.

2.3 Process optimization on a part with complex geometry

Former simulations have been conducted on a simple geometry to observe the effects related with single and dual-scale reactive injections. In this section, results of simulations conducted on a more complex geometry will be presented. The shape, dimensions, injection gates and vents of the part are presented in Figure 70. It is meshed with elements measuring 2 cm and injection will be conducted at constant flow rate from the bottom of the part. It contains 954 elements

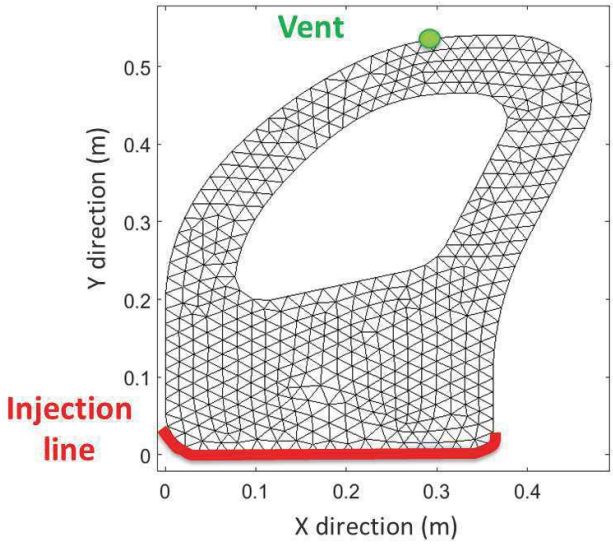

Figure 70: Geometry of the part that will be used for further simulations

Two configurations (Single-scale and DS1) are tested. Optimal injection conditions are investigated. The goals of the optimum injection conditions are to:

- Minimize injection pressure
- Ensure a full curing (degree of cure equal to 1) at any location in the part within 4 minutes (240 s)

Initial mold, fiber and injection temperature are constant and equal to 140° C. The adjustable parameter is the constant injection flow rate (for a sake of simplicity the discussions will be made on theoretical filling times).

Fluid fraction

Due to the fact that the unsaturated area is smaller (9 mm) than the size of the elements (2 cm), no difference of saturation can be noticed in the mappings of fluid fraction in the channel and tow levels in the dual-scale simulation. Therefore Figure 71 presents the saturation of the part with time for a Single-scale simulation with a theoretical injection time equal to 68 s.

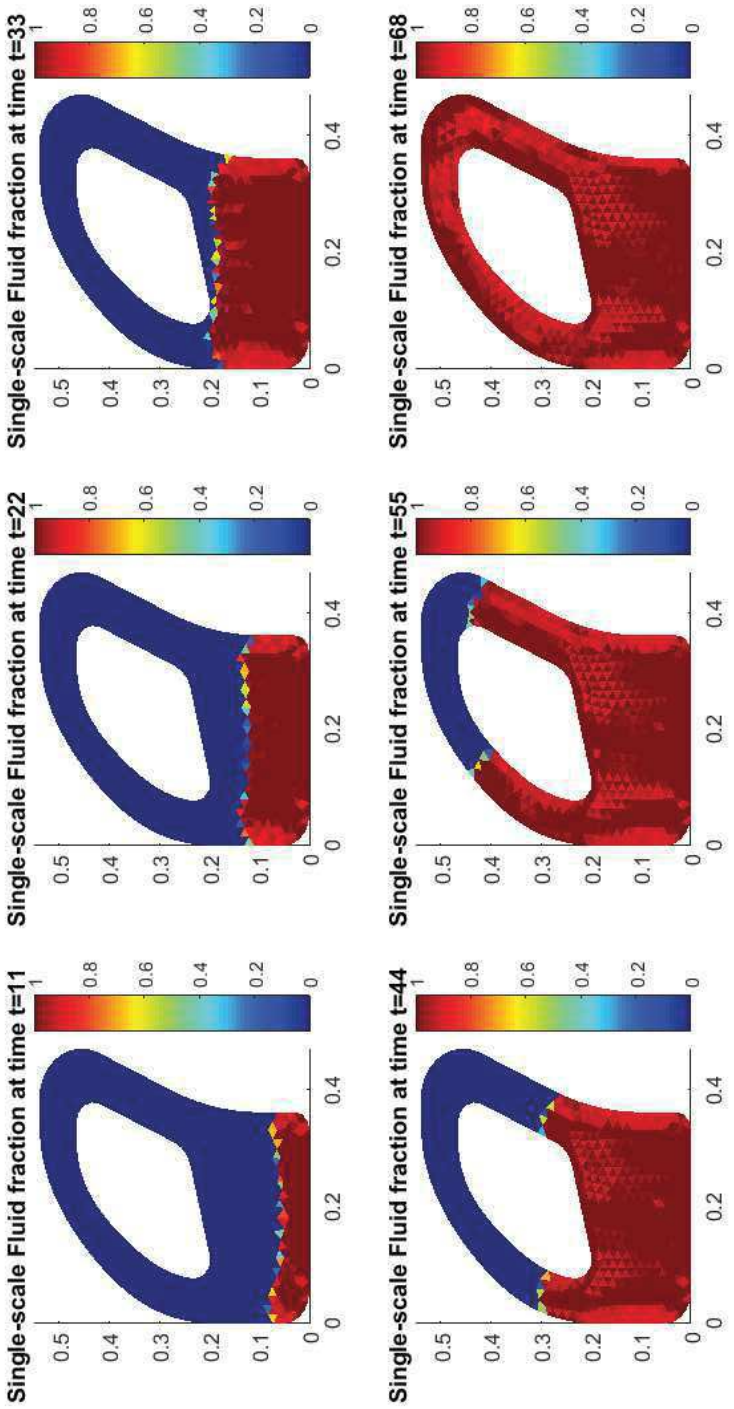

Figure 71: Mappings of the fluid fraction in the part at various times (given in seconds)

It can be observed in Figure 71 that the flow front exhibits a qualitatively good shape along injection and that the part is filled at the end of the theoretical filling time. Therefore, the simulation tool appears to treat the filling problem of a part with a complex shape without major issue and conserving mass.

Injection pressure

As for the UD injection, it is expected that an optimal flow rate can be obtained to minimize injection pressure. Figures 72 and 73 plot the injection pressures for the Single-scale and DS1 configurations.

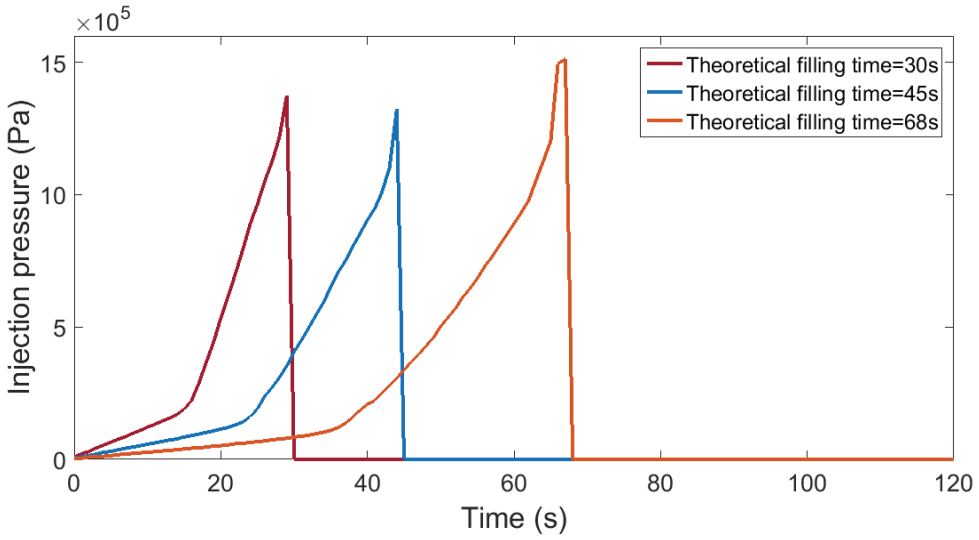

Figure 72: Injection pressures for the Single-scale configuration for various injection flow rates

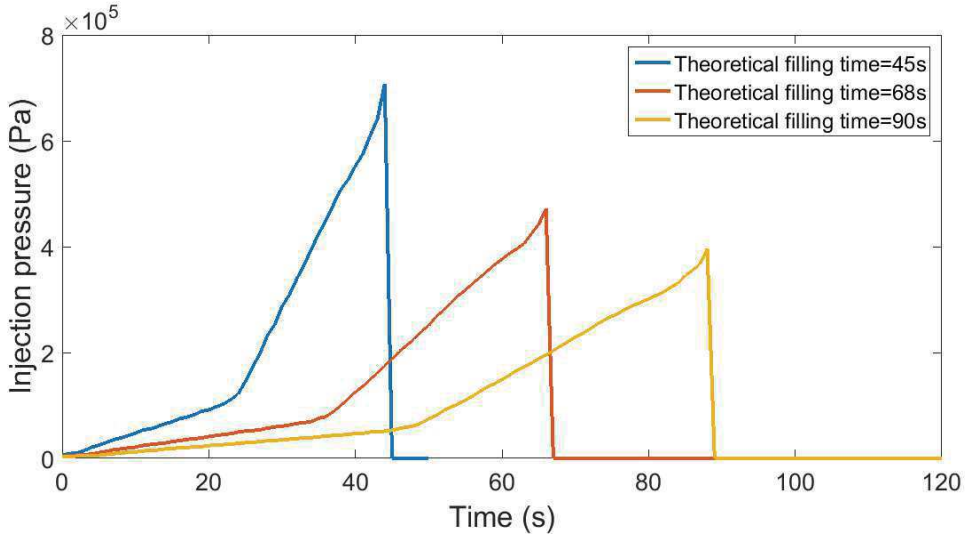

Figure 73: Injection pressures for configuration DS1 and for various injection flow rates

It can be observed from Figures 72 and 73 that injection pressures for the Single-scale configuration are higher than for configuration DS1 for the same filling time. This highlights once again the high influence of viscosity evolution in the Single-scale simulation model. Additionally, it can be observed that as for the simple geometry in section 2.2.3, final injection pressure features a minimum value. This value is achieved for an injection time in the range of 45 s. On the other hand, it does not appear that the global minimal value of final injection pressure is reached for configuration DS1 within 90 s (time of resin gel in stationary conditions). For this reason, the minimal value of final injection pressure that can be reached without risking intra-tow gel is obtained for a filling time of 90 s.

Curing time

It must now be verified that curing time is under 240 s for the two considered theoretical filling times in the two configurations. In Figure 74, the mappings of degree of cure in the Single-scale configuration are presented. Figures 74 and 75 present respectively the mappings of degree of cure in the channels and the tows of configuration DS1.

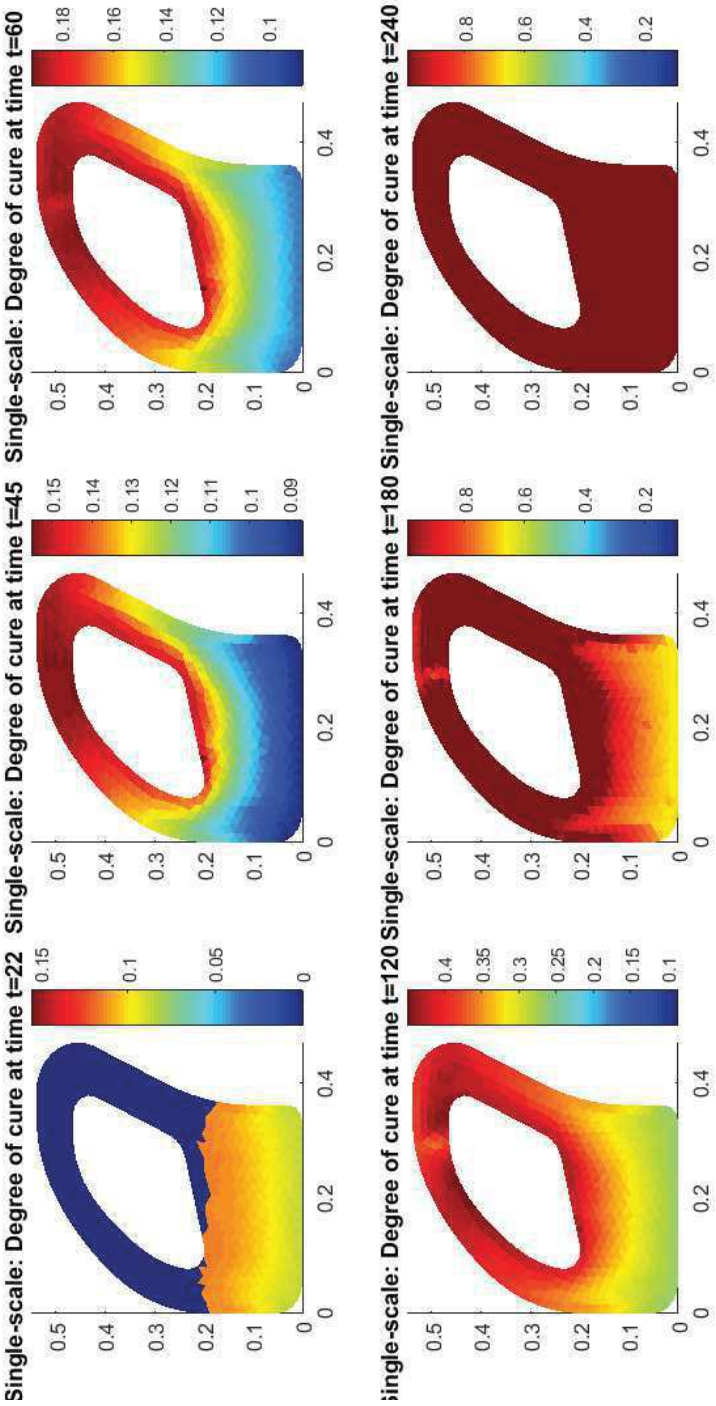

Figure 74: Degree of cure in the part (Single-scale configuration) during injection (t=22 s and t=45 s) and curing (t=60 s, t=120 s, t=180 s, t=240 s)

The trends reported previously are also observed for the more complex shape. The most cured resin is located, during injection near the flow front in the single-scale simulation and in the tows in the dual-scale porous material. This leads to significant differences

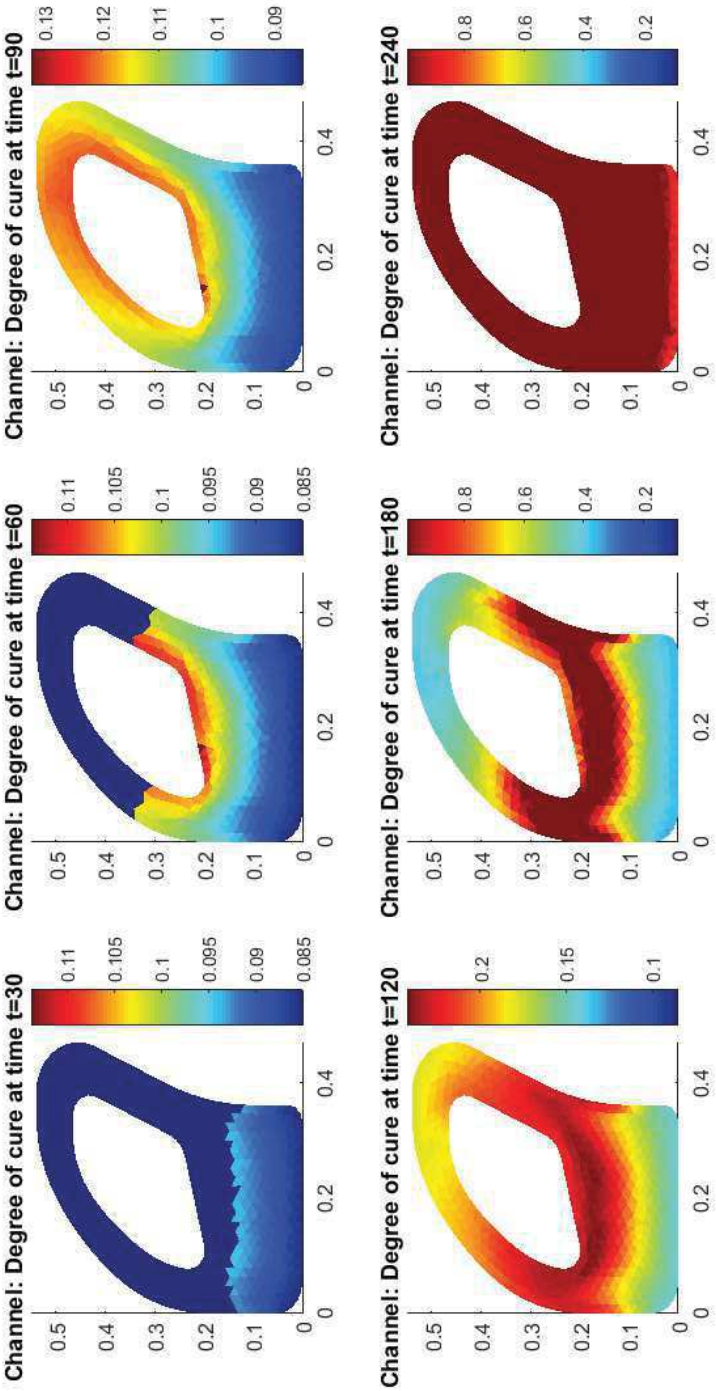

Figure 75: Degree of cure in the channels of configuration DS1 during injection (t=30 s, t=60 s, t=90 s) and curing (t=120 s, t=180 s, t=240 s)

in terms of curing once injection is stopped. Indeed, full curing begin to occur near the flow front in the single-scale simulation, while it occurs in the center of the part in the dual-scale simulation. This result could be of great interest in the prediction of the residual stresses and the induced deformations.

Finally, regarding time to fully cure the part, it can be observed that the single-scale simulation for which injection has been run within 45 s has reached full cure at the end of the 240 s (an investigation in the entry elements reveals that full curing occurs within

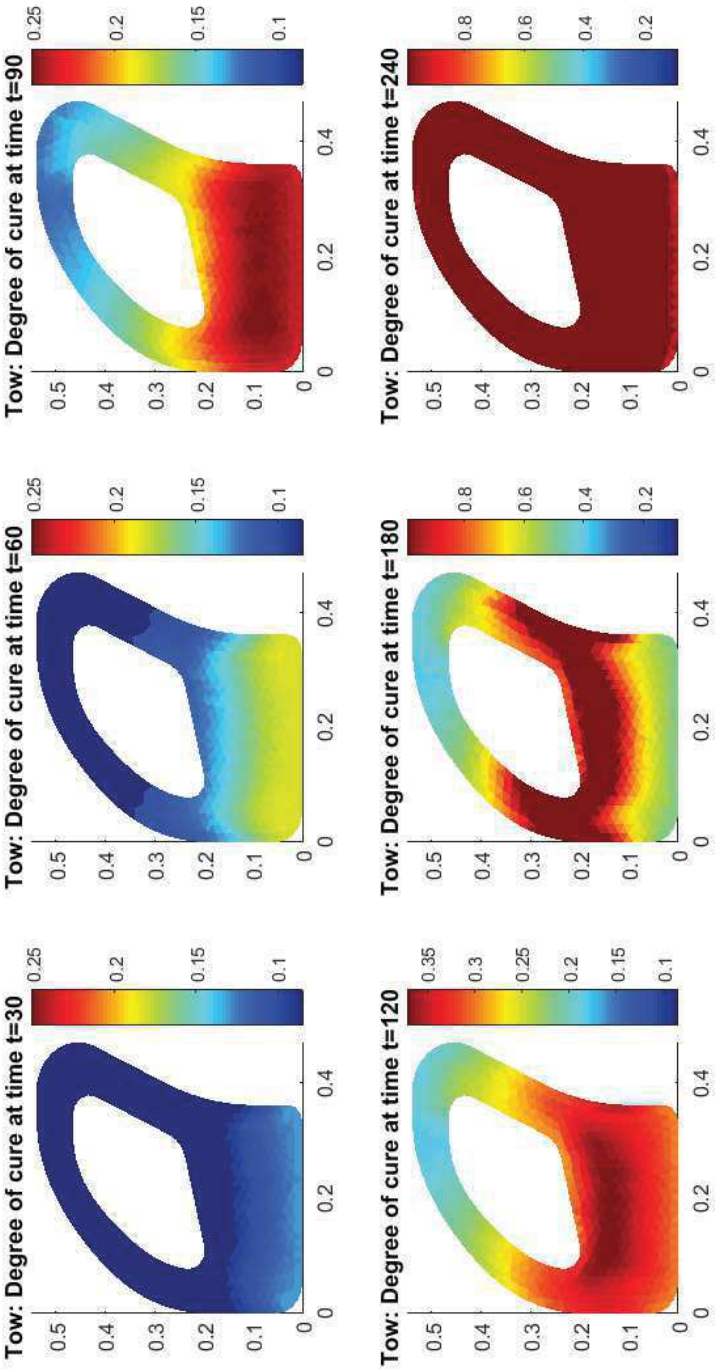

Figure 76: Degree of cure in the tows of configuration DS1 during injection (t=30, t=60, t=90) and curing (t=120, t=180, t=240)

203 s). This not exactly the case for the dual-scale simulation (configuration DS1) for which injection has been run within 90 s. Indeed, the level of cure in the entry elements is not exactly equal to 1 at t=240 s. Degree of cure evolution in these elements reveals that cure occurs within 250 s. Therefore, a reduction of the injection time of 10 s should allow curing the part in the desired time without increasing too much the injection pressure.

Conclusion on process optimization

It can be concluded from this simple optimization case that major differences can be observed in terms of optimal process parameters predicition when dual-scale flow is taken into account or not. Dual-scale flow, and especially intra-tow resin storage affects the distribution of the quantities of interest in the part and therefore the injection pressure and the location of first full cure. For the same specifications, the single-scale simulation predicts optimal parameters to be an injection time of 45 s inducing a final injection pressure of 13.2 bar and a curing time of 203 s. On the other hand, dual-scale simulation recommends an injection time of 80 s inducing a final injection pressure of 4.2 bar and a curing time of 240 s. This highlights the importance of taking the dual-scale effects (and especially intra-tow resin storage) into account.

3 Conclusions

In this chapter, a new numerical model that allows simulating the injection of a reactive resin mixed on-line in single and dual-scale porous materials has been presented. The numerical strategy based on FEM/CV approach for the flow and explicit first order approximation of the time derivative of the advection equations for the transport and update of the quantities of interest (degree of cure and temperature) has been introduced. The two levels of the dual-scale porous materials are treated separately. A macroscopic mesh deals with the flow in the channels of the reinforcement. On the other hand, a microstructure, fitted to its size and shape is associated to each macroscopic element to treat both the delayed saturation (generating the unsaturated area) and the thermal conductive exchanges between the tow and the channel after saturation (intra-tow resin is considered to be stored in a permanent manner). In a view of proposing an efficient and flexible solution, the following new developments have been conducted:

- Implementation of the automatic calculation of the microstructure associated with each macroscopic elements
  Based on purely geometrical considerations, the number and average length of tows in each macroscopic element is calculated automatically to satisfy the overall FVF. This allows conducting simulations with elements larger than a single micro-cell as imposed in the work presented in the literature ([70], [77]) that reduce the computational cost. Furthermore, no constraint is imposed on the mesh avoiding meshing issues.

- Simplification of the micro-scale model to increase flexibility and reduce computational cost
  Under the assumption of high speed injections, tow impregnation is assumed to occur purely transversely in the tows. This reduces the tow saturation problem to a sum of 1D transverse saturation problems that are very fast to conduct. Additionally, the tow is initially meshed only in the transverse direction. Longitudinal meshing is conducted along filling which makes the approach more flexible in terms of meshing and allows treating unsaturated areas smaller or larger than the elements with equivalent degree of accuracy.

A convergence study, conducted on the non-reactive, filling, aspects revealed that significant computational cost reduction could be achieved for equivalent accuracy using the newly developed approach with large elements instead of small elements.
Considering reactive aspects, a convergence study proved the validity of energy balance for all source terms used in the advection equation of temperature as well as equivalence of thermal conductive behaviors for single and dual-scale models featuring the same FVF. Numerical simulations have then be conducted to investigate the influencing parameters o the unsaturated area under non-reactive conditions. It has been highlighted that taking the capillary pressure into account induces a sensibility of the length of the unsaturated area to the pressure gradient: the unsaturated area is larger under higher macroscopic pressure gradients and reaches a maximal value when capillary pressure becomes negligible compared to the channel pressure. When the capillary pressure is not taken into account, the length of the unsaturated area is fully independent from pressure gradient.

Additionally, it has been revealed that the parameter K_c/K_t plays a significant role in the length of the unsaturated area, as well as K_c that affects directly the macroscopic pressure gradient. In a more indirect manner, φ_c plays a role in the length of the unsaturated area since at constant FVF, it imposes a variation of tow geometry and porosity content. However, a parameter that would describe more precisely the microstrucutre would be of

interest in order to estimate if the reinforcement contains a lot of small tows that will be quickly saturated or a small number of large tows inducing a long unsaturated region. Moreover, the influence of the length of the unsaturated area on the injection pressure has been studied for injections at constant flow rate. The non-linearities reported in the literature at the beginning and end of injection have been observed. However, the order of magnitude of the pressure deviation was very limited. Therefore, the interest of reproducing the unsaturated area in an industrial simulation tool for non-reactive injections may be questioned.
Additionally, fully coupled reactive injections with on-line mixing have been conducted to study the reactive related influence of the reinforcement microstructure and process parameters. It has been revealed for single and dual-scale simulations that for a wide range of injection flow rates (leading to short or equivalent injection times compared to the gel time measured in stationnary conditions, final pressure at the end of injection feature a minimal value. This value is comprised between the high values reached at high injection speeds due to Darcean effects and high values due to viscosity increases at the end of long injections due to polymerization.

It has also been demonstrated that significant differences in terms of temperature, degree of cure and viscosity distribution are observed between single and dual-scale simulations, and even between the two tested configurations DS1 (φ_c=8.87%) and DS2 (φ_c=32.7%). Macro-scale viscosity increase is much faster in the single-scale than in the dual-scale simulations due to intra-tow storage that removes the old cured resin from the flow front. For dual-scale simulations, larger channels (DS2) induce higher viscosity evolutions. Therefore, when reaction begins to induce significant viscosity evolutions, injection pressure of the single-scale simulation is higher at the end of injection than for dual-scale simulations.
The influence of the length of the unsaturated area on the process has also be investigated. It has been established that in the considered injection conditions (equal temperature of mold, fibers and injection temperature, the length of the unsaturated area had no influence on the injection pressure. Mappings of the quantities of interest revealed also that the influence of the length of the unsaturated area on the degree of cure or viscosity distribution was negligible.

Additionally, process optimization on a part with complex shape has been conducted leading to significant differences in terms of quantities of interest evolution for single and dual-scale simulations.

Finally, it must be highlighted that the presented simulations have been conducted under some assumptions as the absence of air entrapment in the tows or the permanent intra-tow storage. These mechanisms should however be investigated in the future in order to ensure further refinement in the understanding of the process.

Part III
Experimental determination of the mechanisms influencing reactive RTM

1 Introduction

In the previous section, a review of the published works conducted on dual-scale flow has been presented. The presence of an unsaturated area as well as resin storage inside fiber tows have been identified as the two major phenomena that characterize dual-scale flow. However, only few quantitative experimental studies have been conducted on resin storage even if this aspect appears to be the most influencing mechanism on the reactive injection with online mixing. In this context a full design of experiment based on new techniques has been implemented to enable studying both macroscopically and microscopically intra-tow storage and release mechanisms.
The macroscopic investigation technique is a inspired both from the "two-color experiment" presented by [56] and the principle of spectrophotometry. In this chapter, in a specially developed cavity, a sample is first saturated with a blue colored fluid. The same colorless fluid is then injected in the sample and the evolution of the sample's color along rinsing is tracked by taking pictures while the injected mass is recorded. A calibration of the method is conducted in parallel to enable relating the color recorded on the pictures and the concentration of colorant inside of the sample. The basic principle of the technique is presented in Figure 77. This experiment allows:

- Validating or invalidating the assumption of permanent intra-tow storage
- Quantifying the storage/discoloration tendencies with respect to textile type, fiber orientation and fiber volume fraction (FVF)
- Identifying the colorant storage or evacuation mechanisms

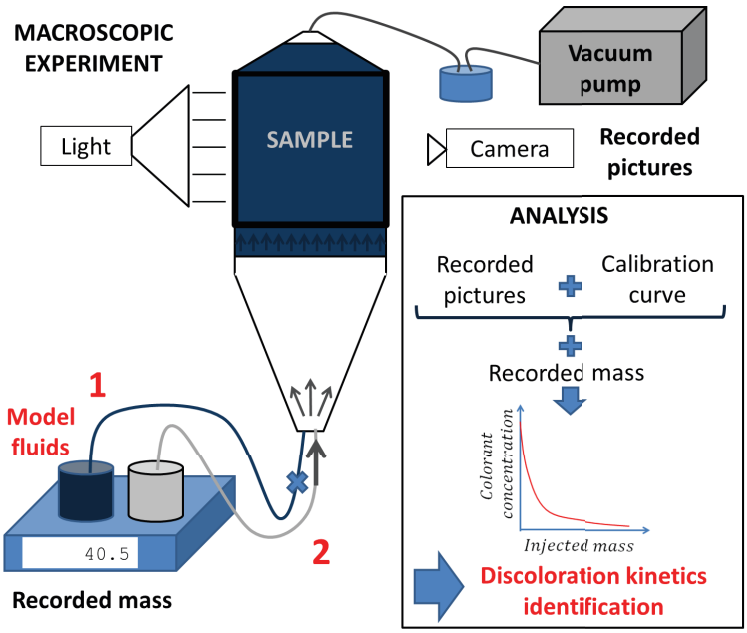

Figure 77: Principle of the macroscopic intra-tow storage investigation experiment

On the other hand, a second experiment has been developed (Figure 78). This experiment aims to reproduce the flow conditions used for the previously presented macroscopic experiment but additionally to enable freezing the resin flow at any moment to allow observing the precise location of the colorant inside of the microstructure during rinsing. This is enabled by using a UV-curing resin whose viscosity does not evolve during injection (as for a model fluid), but which cures within a few minutes when it is exposed to UVs. The cured sample can then be cut and micrographic pictures can be made. This enables:

- The study of the microstructure (channel/overall volume ratio, intra-tow FVF,...) for the various materials and at the various FVF
- The observation of the colorant distribution very locally in the tows as well as at different locations in the samples
- The determination of the origins of the the micro-scale flow mechanisms

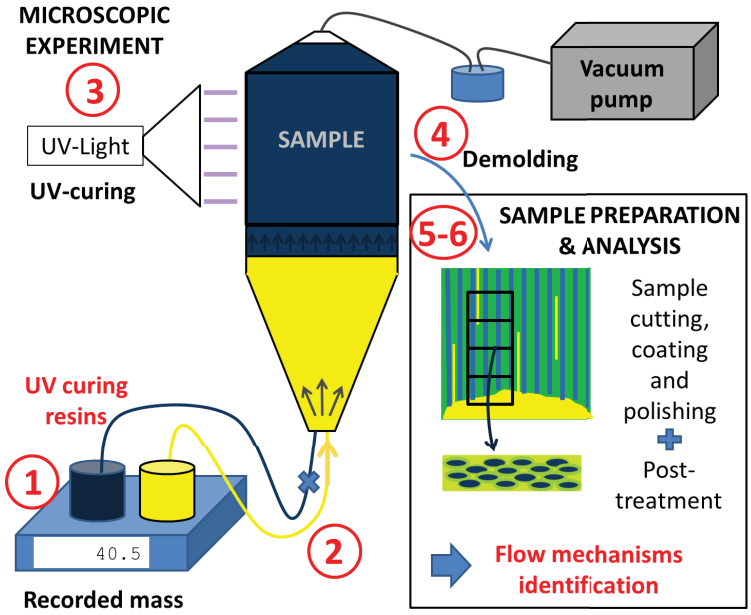

Figure 78: Principle of the microscopic qualitative intra-tow storage investigation experiment

Thus the involved intra-tow storage or release mechanisms can be determined.
The details of the materials, equipment and techniques used as well as the obtained results will be presented in the following sections.

2 Materials

Intra-tow resin storage mechanisms are expected to depend mainly on the microstructure of the impregnated reinforcement. Therefore three types of textiles exhibiting a wide variety of microstructures have been considered in this study: a unidirectionnal, a triaxial and a satin. These materials have been impregnated by several model or curing Newtonian fluids to study the flow mechanisms at the micro-scale. Additionnally, various colorants have been used to track the injected fluid volumes evolution over time. The references and characteristics of these materials are presented hereafter.

2.1 Textiles

2.1.1 Presentation of the textiles

Four types of textiles have been considered in this study, their characteristics and properties will be presented below.

Unidirectional material (UD)

Unidirectional materials are commonly used in the production of structural parts where good mechanical properties induced by the continuity and alignment of the fibers are required. Additionally, they feature interesting flow channels along the UD tows that ease resin flow in the injection processes. This characteristic and the associated dual-scale flow phenomenon, will be deeper investigated, in the case of the unidirectional material produced by Chomarat and referenced *Rovyply UD1135*. This material is made of a heavy warp (1135 g/m^2), stiched, with a PET yarn, to, on the backside, ±45° diagonal and weft (90°) tows (11 g/m^2 for each direction). Its characteristics are summarized in Table 11. Furthermore, Figure 79 gives an overview of this material. Additionally, Tables 12 and 13 give information on the measured areal weight of this material as well as the number of plies and fiber volume fraction, FVF, considered in the experiments. Finally, the permeability of the textile at these FVF are presented in Figure 82.

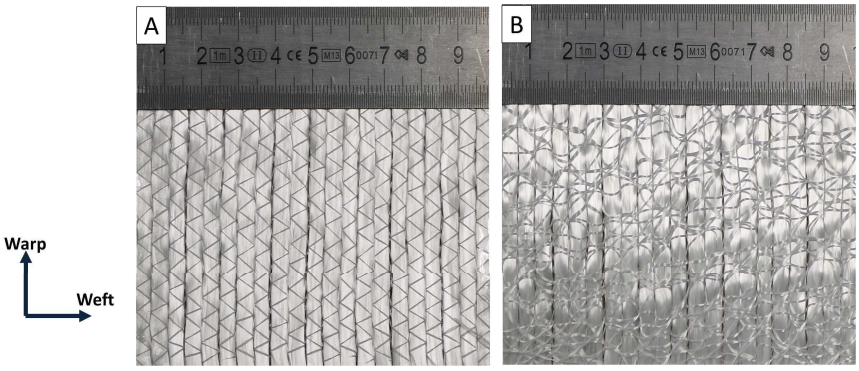

Figure 79: Picture of top side (A) and bottom side (B) of the unidirectionnal textile (UD)

Triaxial material

Multiaxial non crimp fabrics are also widely used in the production of composite materials as they exhibit the good mechanical properties of continuous aligned fiber materials and reduce stacking time by containing plies with several fiber orientations. As unidirectional materials, they feature continuous channels between the tows, but the presence of the various orientations introduces a new geometry in terms of microstructures and tortuosity that make them interesting to study. The triaxial material used in the frame of this study is produced by Chomarat under the reference *Roviply 95/47/00/47/B4T*. It is made of a warp ply with areal weight 943 g/m^2 ±5% and two plies at ± 45° exhibiting both 467 g/m^2 ± 5% areal weight. The characteristics of the triaxial material are summarized in Table 11. Additionally, Figure 80 presents the aspect of the material on both sides and highlights the variability in terms of fiber tow distribution of the diagonal plies on the back side of the textile. Further properties (measured areal weight and considered FVF) of the Triaxial are given in Tables 11 and 12. Figure 82 presents the evolution of permeability of the Triaxial with the FVF.

Satin

Woven materials are another family of textiles used in composite manufacturing. Their microstructure is different from NCFs as the tows are woven. Thus inter-tow channels exhibit more complex geometries and tortuosity than in the NCFs. For this reason, a

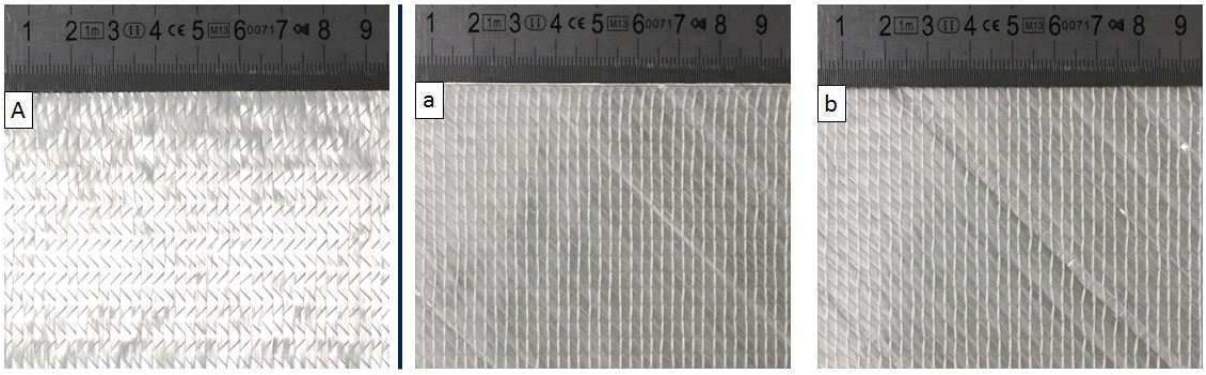

Figure 80: Photographs of top side (A) and bottom side (a and b) of the Triaxial material used in this study. Photographs (a) and (b) show the variety of fiber distributions in the +45° direction

4-harness satin has been chosen to study the flow mechanisms inside this type of textiles. The selected material is produced by Chomarat and referenced *580 SA2*. This textile features an unbalanced areal weight distribution (270 g/m^2 ± 5% in warp and 310 g/m^2 ± 5% in weft). The general characteristics of the textile are summarized in Table 11. Moreover, Figure 81 shows the aspect and characteristic dimensions of the Satin. Finally, the measured areal weight and the FVF considered for this study are presented respectively in Tables 12 and 13. Permeability versus FVF is presented in Figure 82.

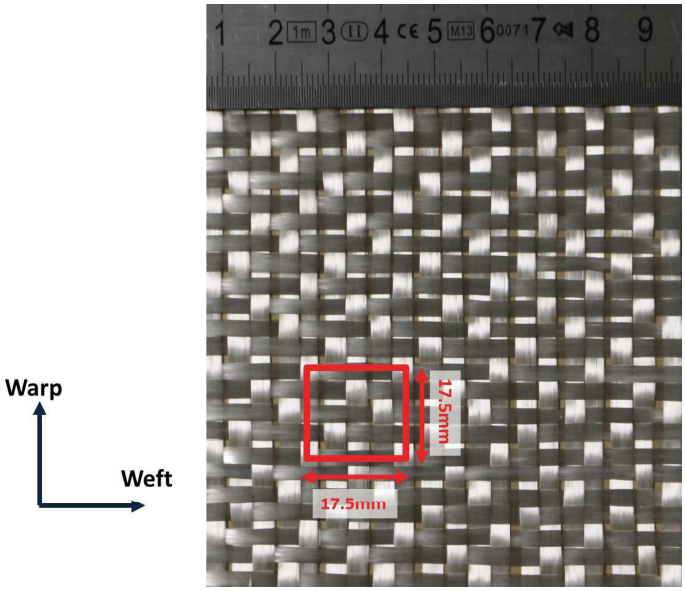

Figure 81: Picture of the Satin material used in this study. The dimension of the unit cell is precised

Breather

During this study, injections has also been made in a breather. This material commercialized by Cytec with reference *RC 3000-10 AB 10* is a felt made of continuous PET fibers. This material has been used both as a reference purely single-scale porous material to study the characteristics of this kind of flow, and also as entry material in the cavity used for the experiments in order to ensure a purely 1D flow in the samples made of the glass fiber textiles presented above. Its characteristics are summarized in Tables 11, 12 and 13.

Nomenclature	**Material**	**Nominal areal weight (g/m^2)**	**Fiber density** (kg/m^3)	**Manufacturer / Reference**
UD	E Glass	1173 ± 5%	2575	Chomarat/ Rovyply UD1135
Triaxial	E Glass	1883 ± 5%	2575	Chomarat/ Roviply 95/47/00/47/B4T
Satin	E Glass	580 ± 5%	2575	1380 kg Chomarat/ 580 SA2
Breather	PET	330 ± 5 %	1380	Cytec/ AB 10

Table 11: Material characteristics of the textiles used for this study

2.1.2 Textile properties characterization

For each textile, areal weight and saturated permeabilities have been measured.

Areal weight measurement
The areal weight ρ_A of the different textiles, required to compute the fiber volume fraction is calculated using the following equation:

$$\rho_A = \frac{m}{A_r} \tag{67}$$

where m is the mass of the considered sample and A_r its area. Ten samples with dimensions 100 mm ×100 mm of each material have been weighed. To realize these weighing, an Adam *CBW-6H* weighing scale has been used (maximal mass: 6 kg, precision: 0.1 g). The values obtained for the several textiles, and the comparison to the nominal values are presented in Table 12. For all further calculations, the measured values will be used.

	UD	**Triaxial**	**Satin**
Nominal areal weight	1173 g/m^2 ± 5%	1883 g/m^2 ± 5%	580 g/m^2 ± 5 %
Measured areal weight	1270 g/m^2 ±2%	1900 g/m^2 ± 1%	572 g/m^2 ± 1%

Table 12: Areal weights of the textiles used in the study

Permeability measurement
The permeabilities of the different textiles have been measured at different fiber volume fractions using an air permeability measurement bench. This unidirectional air permeability bench is based on the technique presented in [30]. Saturated geometric permeability is determined by inverse method, fitting simulation results to the experimental data obtained using rising or dropping air pressure in the sample. Results are presented in Figure 82.

2.2 Model fluids (non-reactive)

2.2.1 Presentation of the fluids

Glycerol / water blends
Glycerol is a colorless fluid consisting of a trialcohol with molecular formula $C_3H_8O_3$ and exhibiting a viscosity of 1.41 Pa.s at 20°C. During this study, Technical Glycerol from VWR has been used in dilution with water in different percentages to obtain the desired viscosities. Figure 84 presents the evolution of the glycerol solution viscosity versus water content. Additionally, the values used for dilution and the associated viscosities will be

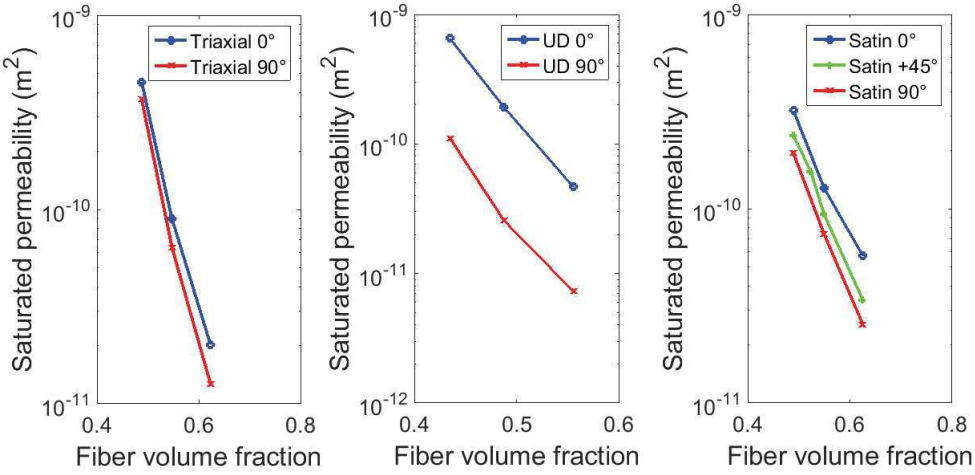

Figure 82: Permeability versus fiber volume fraction for the different textiles considered and for various fiber orientations

presented in Table 14.

Water solutions of Carboxymethyl Cellulose (CMC)

Carboxymethyl Cellulose is a thickener used among other in the food industry. Depending on the degree of substitution of the cellulose chains and the concentration of thickener, a wide range of viscosity can be obtained. The CMC used for this study is provided by Sigma-Aldrich. It features an average molar mass equal to 250 g/mol and 0.7 carboxymethyl groups per anhydroglucose unit. A wide investigation of the properties of CMC solutions (viscosity versus temperature, concentration, shear rate,...) is presented in [81]. It can be noticed (Figure 83) that solutions of CMC can be considered as Newtonian for shear rates up to 1 s^{-1}. This behavior has been confirmed during fluid characterization tests. Additionally, quick calculations show that the shear rate expected in the samples during the injections conducted in this study are in the range of 10^{-6} to 10^{-2} $s^{-}1$ which is low enough to ensure a Newtonian behavior of the CMC solution. Figure 84 presents the evolution of viscosity versus CMC content. The concentration of CMC and the associated viscosities used are reported in Table 14.

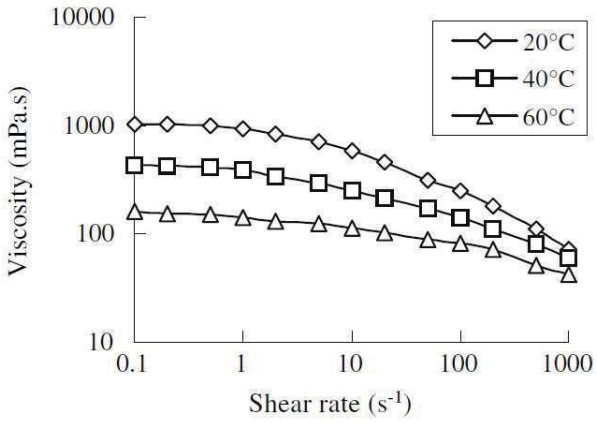

Figure 83: Viscosity evolution of a CMC/water solution with shear rate [81]

2.2.2 Model fluid properties characterization

Model fluid viscosity measurements

Viscosity measurements have been conducted using a Brookfield viscometer referenced "DV1MLVTJ0" and a spindle "ULA" allowing the measurement of viscosities from 1 mPa.s to 500 mPa.s. To realize the measurement, the cylindrical spindle related to the rheometer is immersed in the fluid from which the viscosity wants to be measured. The spindle is brought in rotation by the rheometer that measures the torque necessary to maintain the set rotation speed. The viscosity of the fluid is determined from this torque. In the case of constant viscosity fluids, the measurement is recorded after one minute of spindle rotation. The viscosity of fluids containing various proportions of Glycerol and CMC have been measured. Obtained results are presented in Figure 84. The masses of Glycerol have been measured with the Adam *CBW-6H* weighing scale, while the masses of CMC have been measured using a Mettler Toledo *ML 204*, (maximal mass : 220 g, precision: 0.1 mg).

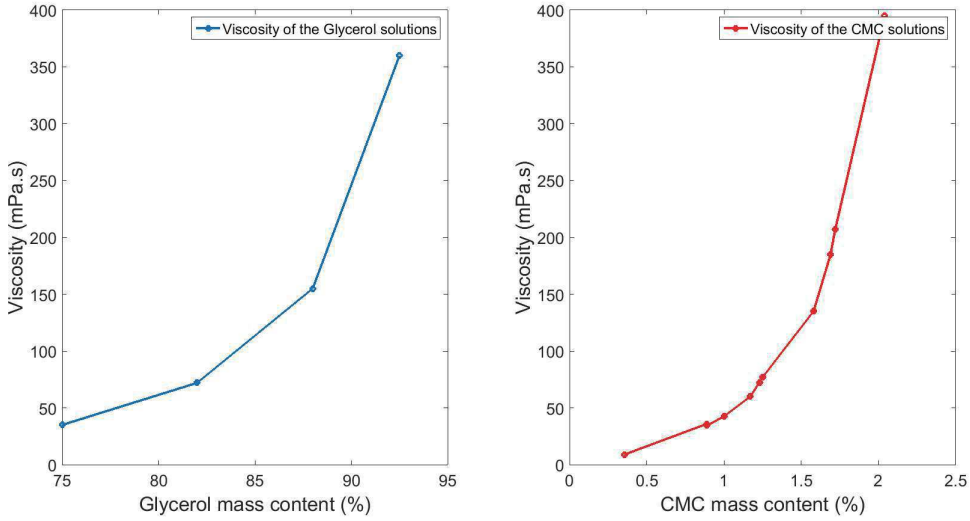

Figure 84: Viscosity versus Glycerol and CMC mass contents in water at 21°C

2.3 Curing resin

2.3.1 Presentation of the curing fluid

The ultra-violet (UV) curing unsaturated polyester resin used for this study is the *SPR-UV CLEAR* polyester resin provided by Shaper. It features an initial viscosity in the range of 1 Pa.s.

2.3.2 Curing fluid properties characterization

Curing time determination of the UV-curing polyester resin

In order to ensure that the UV curing occurs quickly in the part and fixes, as wished, the colorants at the location they occupy at the end of injection, some qualitative tests have been conducted to estimate the gel time of the resin. Samples saturated with blue and fluorescent resins have been placed under the top glass plate used in the setup and exposed to UV-light. Peel-off tests have been made to determine the approximate time required to obtain gel in the center of the part. It has been estimated that the time to gel in the part is in the range of 2 to 3 minutes. Thus, it can be considered that

diffusion phenomena only occur marginally during this time an therefore that the final distribution of the colorant in the part is very close to the distribution when injection is stopped. The experiment will therefore and as wished enable to determine the storage and rinsing mechanisms during dual-scale flow. Additionnally, monitored experiments have highlighted that the exothermic peak in the part is achieved after 20-25 minutes of UV exposition. In these conditions, the time of exposure of the part with UVs is 30 minutes and the side enlightened by the lamp is switched each 5 minutes.

2.4 Colorants

Several types of colorants have been used during the experiments to help studying and quantifying flow mechanisms in the textiles. Quantities of colorant used were in the range of 8.7×10^{-5}% to 4.35×10^{-3}% of mass content (10^{-5} to 5×10^{-4} mol/l) for the macroscopic experiments and 0.05% of mass content for the microscopic mechanisms investigation. Thus, the precision weighing scale Mettler Toledo *ML 204* has been used (precision 0.1 mg).

Blue colorant
The blue colorant used in dilution in glycerol or CMC solutions for the macroscopic experiments is a diazo food dye soluble in water and glycerol with the chemical formula $C_{28}H_{17}N_5Na_4O_{14}S_4$ and the molar mass 867.69 g/mol. It is provided by Colorey under the name *Brilliant Black* and features a colorant percentage of more than 80%.

Yellow colorant
A fluorescent yellow dye is used in solution in the UV-curing polyester resin during the qualitative experiments. It is provided by Colorey under the reference: *Solvent Yellow 98*. It is a Xanthène-type dye with molecular formula: $C_{36}H_{45}NO_2S$ and molar mass: 555.81 g/mol.

Violet colorant
The colorant used in solution in the UV curing polyester resin is provided by Sigma Aldrich (product reference *G2039*) and called Gentian violet. It is a triarmylmethane dye used mainly in inks and in medical applications for its antibacterials and antifungal properties. Its chemical formula is $C_{25}H_{30}ClN_3$ and it features a molar mass of 407.98 g/mol. The used colorant features a colorant percentage of more than 96%

3 Macroscopic trends investigation: Setup and methods

3.1 Principle of the experiment

As introduced in section 1 in this Chapter, the aim of the macroscopic discoloration trends investigation is to determine quantitatively trends in terms discoloration kinetics during a "two-color" like experiments. The developed technique is inspired from spectrophotometry. The sample at the desired FVF is placed in a transparent mold (details in section 3.2.1) and is first saturated with a colored solution containing a known concentration of Blue colorant. Then the same fluid without colorant is injected in the setup. During this rinsing period, the sample is lightened on one side and photographed in grey scale on the other side. The injected mass is also recorded. Additionally and in order to relate the grey level of the recorded pictures and the colorant concentration in the sample, a calibration is conducted: samples with the same FVF as for the real experiments are saturated with fluid containing 5 different colorant concentrations. These samples are then photographed in the lighting conditions as the real experiments. This calibration enable generating a

calibration curve that allows relating grey level and concentration. The principle of the developed method is presented in Figure 85

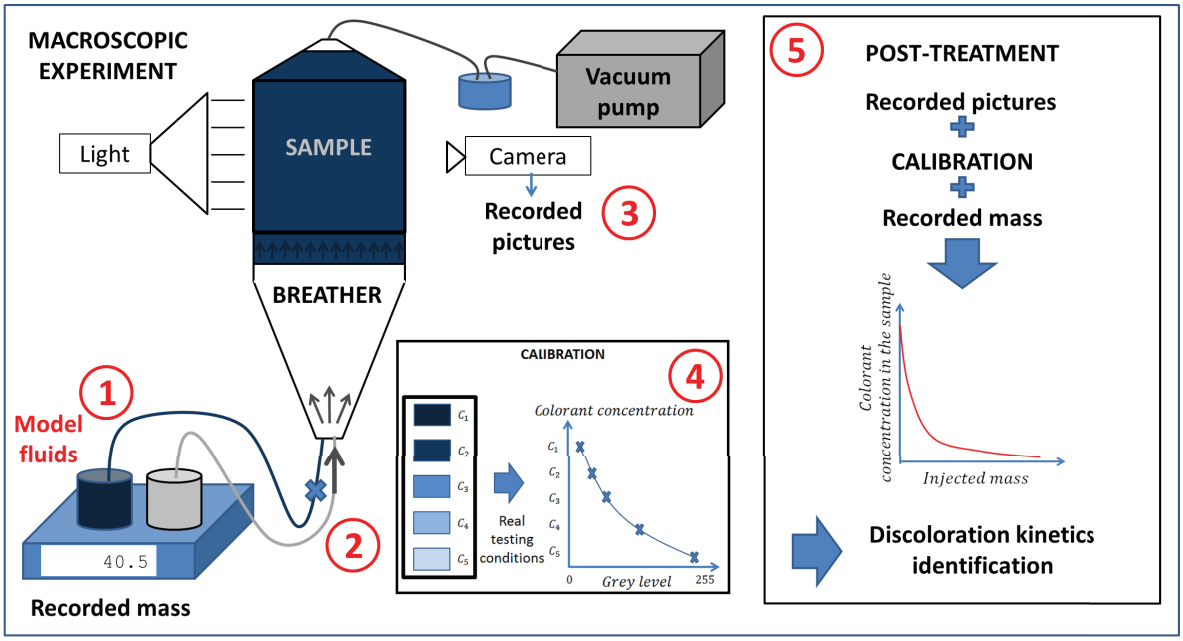

Figure 85: Principle of the developed experiment for macroscopic intra-tow storage investigation

3.2 Setup and equipment

3.2.1 Mold

In order to study the mechanisms influencing intra-tow resin storage during resin injections, a setup has been developed. It has been designed in order to reproduce RTM conditions and to realize several types of experiments within the same cavity (and therefore in the same conditions). Three types of experiments, that will be presented in the following sections, have been conducted using the mold, presented in Figure 86. Figure 87 presents the setup with the textile and the clamping system.

The mold is made of two 10 mm thick Securit glass plates. On the bottom plate (dimension 400 mm×200 mm), a silicon seal is molded and defines the lateral size and shape of the cavity. Injection gates and vents (machined out of PVC plates) are placed at both ends of the cavity. The silicone seal has been tailored for this specific application so that both injection and vent gates are embedded in the seal and avoid leakages. The thickness of the seal is 4.8 mm which allows generating cavities with thicknesses varying from 3.6 to 4.4 mm. The top glass is shorter (dimension 350 mm×200 mm). Calibrated steel plates between the glass plates as well as steel bars on both sides of the glass plates are used to ensure the desired cavity thicknesses.

The cavity is made of a divergent, a rectilinear and a convergent zone. Its aim is to ensure a unidirectional flow in the sample placed at the end of the rectilinear area. The size of the sample is 100 mm×100 mm. Furthermore, for all tests the whole cavity region between the injection gate and the sample is filled with a single-scale porosity Breather in order to avoid any unwanted resin stagnation, as can be observed at the walls of empty cavities.

Three types of experiments have been conducted using this cavity and are presented in the next section.

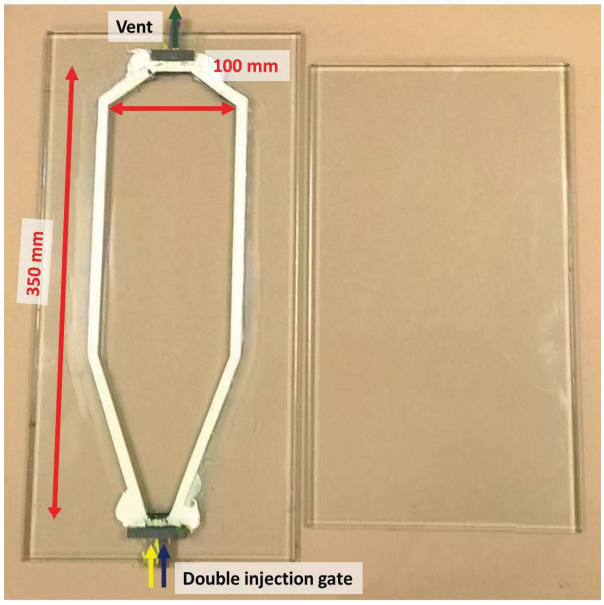

Figure 86: Mold used for the different experiments with top (left) and bottom (right) plate with the silicone seal in white

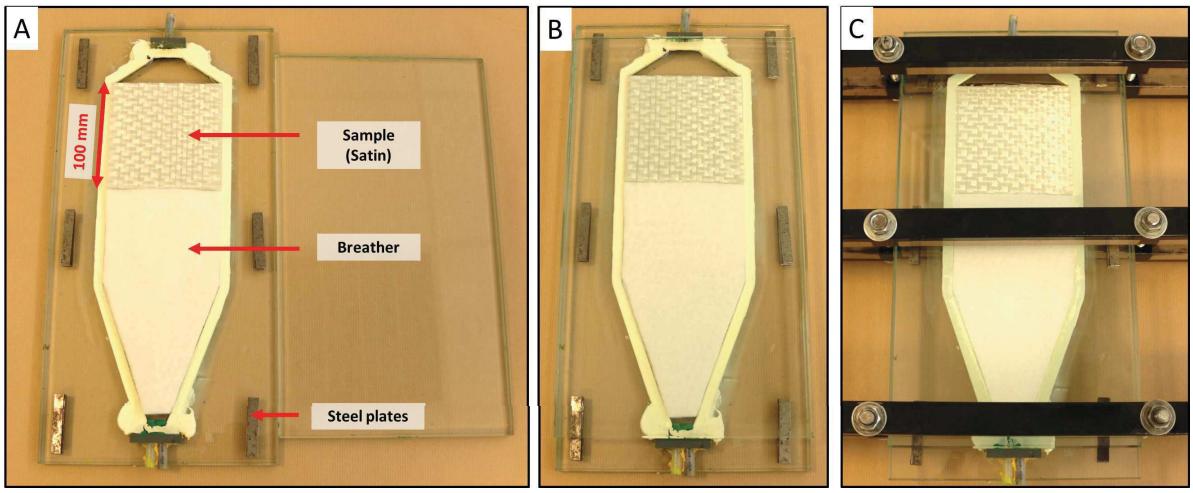

Figure 87: A: Mold with Breather, the fibrous sample and thickness plates, B: Mold closed, C: Mold with the clamping system

3.2.2 Injection equipment

All injections conducted during this research program have been made using vacuum as driving force. The vaccuum pump is a *MPC 052 Z* from Ilmvac GmbH featuring a minimum vacuum value of 8 mbar and a maximal air flow rate of 8 l/min.

3.2.3 Lighting system

A beamer has been used to lighten the samples during injection of the model fluids. The beamer is an Acer *P1341W* with a luminosity of 3000 lumens and a resolution of 1280×800 pixels. The illuminated sample was placed in the center of the projection field to ensure an homogeneous lighting. Projected colors were white or light grey (grey-level: 255, 221 or 160) depending on the experiment.

3.3 Measurement and monitoring equipment

3.3.1 Camera, lenses and acquisition system

The digital camera used during this project was a Canon EOS 70D. The settings used during the different experiments will be detailed in the dedicated sections. For some experiments, the camera has been triggered from a computer using the software EOS Utility enabling the realization of timelaps during quantitative flow experiments investigations. Three types of lenses have been used during this study:

- EFS 18-55 mm for setup photography and flow experiments
- EFS 60 mm for sample photographs
- MP-E 65 mm for photographs of the microstructures

3.3.2 Weighing scale

The weighing scale used for the measurement of the injected mass is the Adam weighing scale introduced in section 2.2.2.

3.4 Post-treatment tools

3.4.1 Software: Matlab

The majority of image and experimental post-treatment has been conducted with the programming Matlab software. The detail of the developed methods will be given in the dedicated sections 3.5.4 and 3.7.

3.4.2 Software: ImageJ

The image analysis software ImageJ has also been used to determine thresholds and realize the analysis on images.

3.5 Experiment calibration

3.5.1 Setup thickness calibration

For each material, considering the areal weight and the minimal and maximal thickness of the seal, test cavity thicknesses and number of plies have been determined for the experiments. The choice of these parameters aims to investigate for each material the evolution of the micro-structure and the intra-tow resin storage on the widest possible range of FVF. Additionally, equivalences in terms of FVF have been organized between the textiles to enable comparing their storage behavior in comparable conditions. The choices of ply number and cavity thickness are summarized in Table 13. Furthermore, in order to use the appropriate calibrated plates so as to ensure that the cavity thickness (and thus the fiber volume fraction) meets the desired value in the sample during injection, calibration tests have been conducted. Clay pellets have been placed in holes made in the samples to measure the thickness of the cavity when it is tightly screwed. The values of the calibration plate thicknesses for the different textiles and fiber volume fractions are presented in Table 13. Due to the use of the glass plates and the screwing system, the error in terms of thickness within the cavity is in the range of $\pm$ 0.1 mm.

UD 4 plies			**Triaxial** 3 plies			**Satin** 10 plies		
FVF	Cavity ± 0.1 mm	Calibrated plates	FVF	Cavity ± 0.1 mm	Calibrated plates	FVF	Cavity ± 0.1 mm	Calibrated plates
0.48	4.2 mm	4.1 mm	0.52	4.3 mm	4.2 mm	0.52	4.3 mm	4.1 mm
0.51	3.9 mm	3.7 mm	0.59	3.8 mm	3.7 mm	0.54	4.15 mm	3.8 mm
0.54	3.7 mm	3.5 mm				0.56	4.0 mm	3.5 mm

Table 13: Thicknesses of the calibration plates to ensure the desired cavity thickness

3.5.2 Selection of fluid viscosities

The goals of this study is to investigate the flow mechanisms involved in the RTM process and especially in short cycle time injections. As stated by Darcy for a given injection pressure, the viscosity of the injected fluid has a direct influence on the flow velocity. In this context, the most appropriate viscosity values should be chosen to ensure injections as quick as possible with respect to the available model and curing fluids, and injection system. Additionally the injection conditions should be similar enough to compare the results obtained with the different fluids. Regarding the injection system, vacuum has been used during this study. Thus, the only possibility to reduce injection time was to reduce the viscosity of the fluid. The range of viscosities that could be achieved with the model fluids was starting from the viscosity of water (approximately 1 mPa.s at 20°C), however the curing resins exhibited initial viscosties in the range of 206 mPa.s for the resin Resimer to approximately 1 Pa.s for the UV-curing resin. These polyester resins could however be diluted with styrene in adequate amounts to reduce their viscosity but maintaining satisfying curing characteristics. Using styrene, the viscosity of both curing resins could be reduced to 100 mPa.s. In this context, a wide range of model fluid viscosities have been investigated. Indeed, the larger versatility of the model fluids allowed to inject lower viscosity fluids to reproduced high speed injections and higher viscosity fluids to ensure that the conditions of UV and reactive injection conditions are comparable to these faster injections. The model fluids used during this study, their composition, density and viscosities are summarized in Table 14.

Glycerol based fluids	**Glycerol content**	**Water content**	**Viscosity**	**Density**
Gly1	75%	25%	35 mPa.s ±2 mPa.s	1.18
Gly2	88%	12%	155 mPa.s ±3 mPa.s	1.20
CMC based fluids	**CMC content**	**Water content**	**Viscosity**	**Density**
CMC0	0.356%	99.64%	9 mPa.s ±2 mPa.s	1
CMC1	0.89%	99.11%	35 mPa.s ±2 mPa.s	1
CMC2	1.69%	98.34%	165 mPa.s ±3 mPa.s	1

Table 14: Composition and viscosities of the several fluids used during this study. Percentages are given in weight

3.5.3 Lighting, camera and concentration selection

As introduced in section 3.1, the quantitative intra-tow resin storage investigation is based on the image analysis of grey scale photographs made along the injection of a transparent fluid in a sample firstly saturated with the same fluid colored with the Blue colorant. The grey values of the pixels from the samples are then converted into colorant concentration

values thanks to a calibration curve. This treatment is also applied to a small region of Breather at the inlet of the sample to enable tracking the concentration of the fluid entering the sample.
So as to ensure a good transcription of pixel grey values into colorant concentrations, the values of pixels are wished to be spread over the whole 0-255 scale for concentration of colorant values ranging from initial concentration to final concentration (potentially 0 mol/l of colorant). In this context, a calibration campaign has been conducted to determine the most appropriate: camera settings, lighting color and colorant concentrations.

- Camera settings
  In order to limit the possible configurations, camera settings have been chosen to stay unmodified for all experiments. Thus the only parameters to spread widely the grey values associated with the reference samples over the 0-255 scale are the choices of the colorant concentrations and the level of grey projected by the beamer. The fixed settings of the camera were:
  - Monochrom picture
  - Focal length: 5.6
  - Exposure time: 1/6 s
  - ISO: 400
- Lighting
  Using a beamer as light source provides the ability to change the projected light from pure white to darker grey. Thus, depending on the fluid and fiber volume fractions considered, the homogeneous values of grey level projected on the samples were: 255, 221 or 160 (on a 0-255 full scale) for a distance between beamer and sample equal to 1.5 m.
- Colorant concentration
  As presented in section 3.1 for each material, each fluid and each fiber volume fraction, a set of sample was saturated with known colorant concentrations to define the pixel-concentration equivalence. Finding appropriate values of concentrations was very important to ensure a good coverage of the 0-255 grey scale. Table 15 summarizes the values of concentration used for the calibration with respect to the fluid used.

	Gly1 and Gly2 Colorant concentrations		**CMC0, CMC1 and CMC2** Colorant concentrations
G_1	5×10^{-4} mol/l	C_1	2×10^{-4} mol/l
G_2	2.5×10^{-4} mol/l	C_2	1×10^{-4} mol/l
G_3	1×10^{-4} mol/l	C_3	5×10^{-5} mol/l
G_4	5×10^{-5} mol/l	C_4	2.5×10^{-5} mol/l
G_5	1×10^{-5} mol/l	C_5	1×10^{-5} mol/l

Table 15: Concentrations of Blue colorant used

3.5.4 Grey level/Concentration calibration curve

Once the settings have been chosen, for each configuration (textile, thickness and test fluid), photographs are made of the calibration set of samples. For each picture of sample, a distribution of pixel grey levels can be represented and studied. From this distribution,

pixel average values so as the standard deviation are then recorded using the software Matlab and the correlation curve pixel value-concentration is established. Figure 88 presents the principle of the calibration technique.

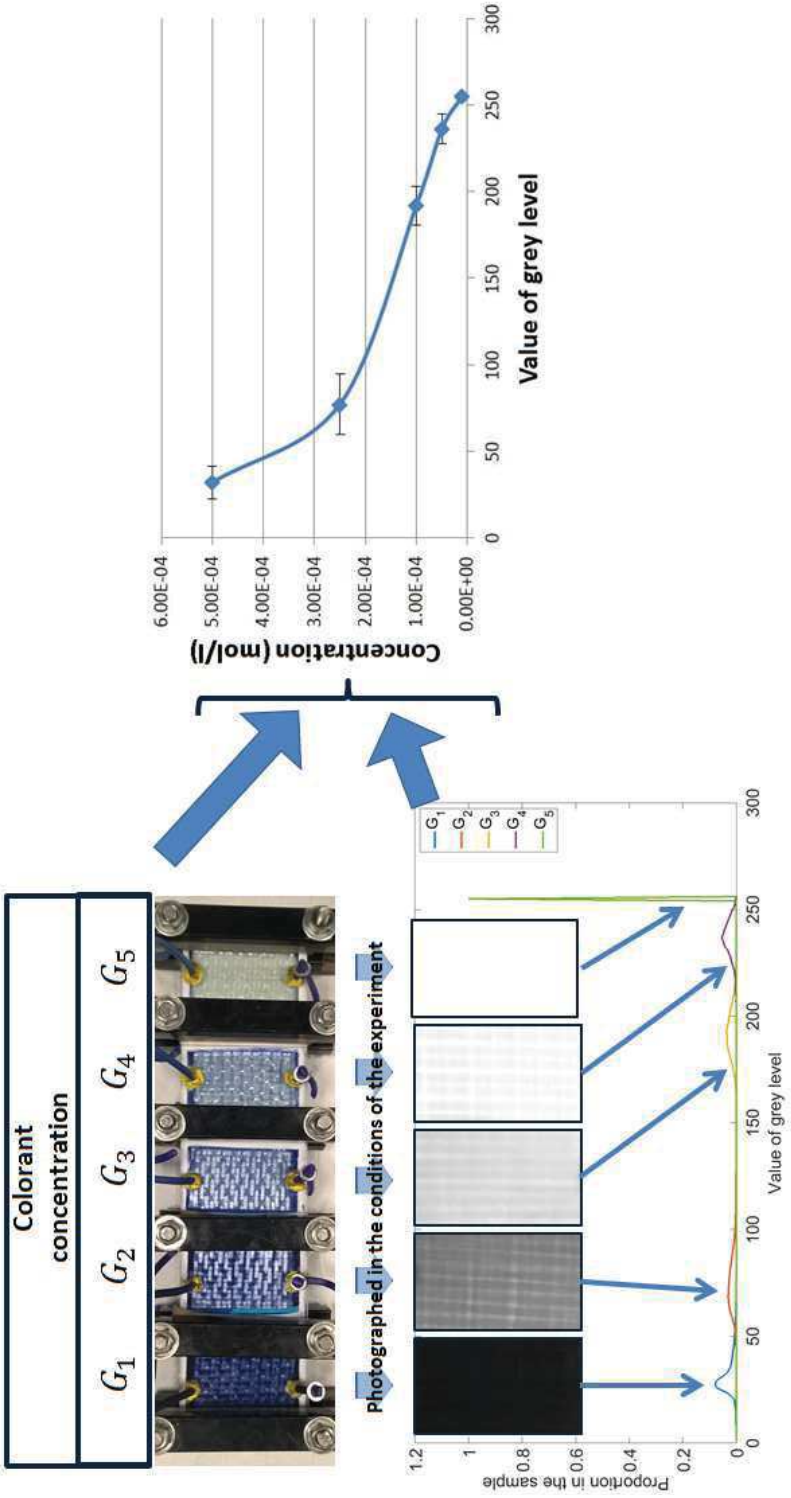

Figure 88: Principle of the calibration technique for the example of the Satin at FVF = 0.52

Additionally, Figures 89, 90 and 91 present the distribution of pixel grey levels for the three materials at a FVF equal to 0.52 for the Satin and the Triaxial and at a FVF equal to 0.51 for the UD.

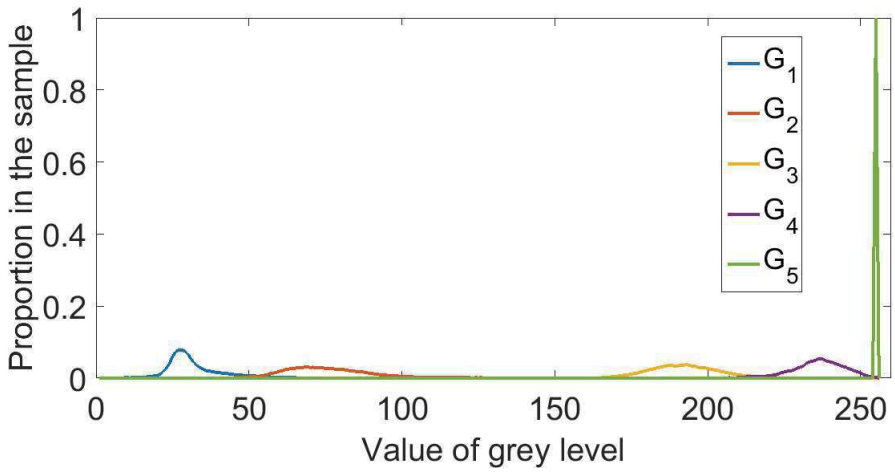

Figure 89: Distribution of grey levels in the calibration samples for the Satin at FVF=0.52

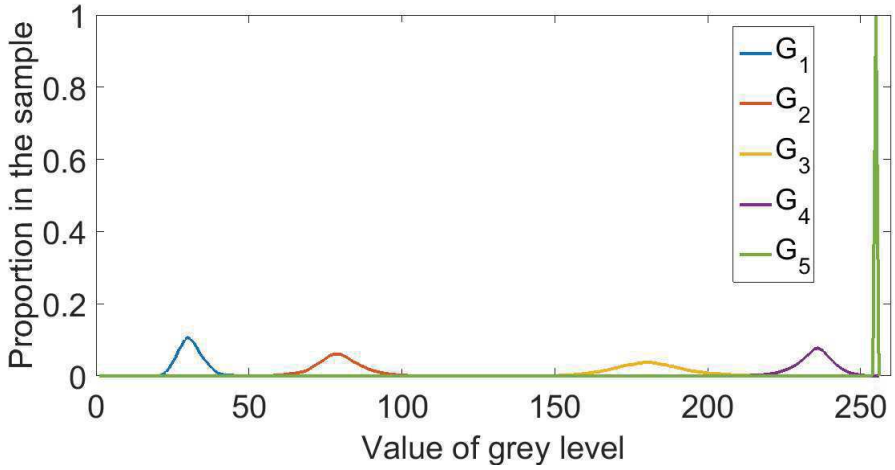

Figure 90: Distribution of grey levels in the calibration samples for the Triaxial at FVF=0.52

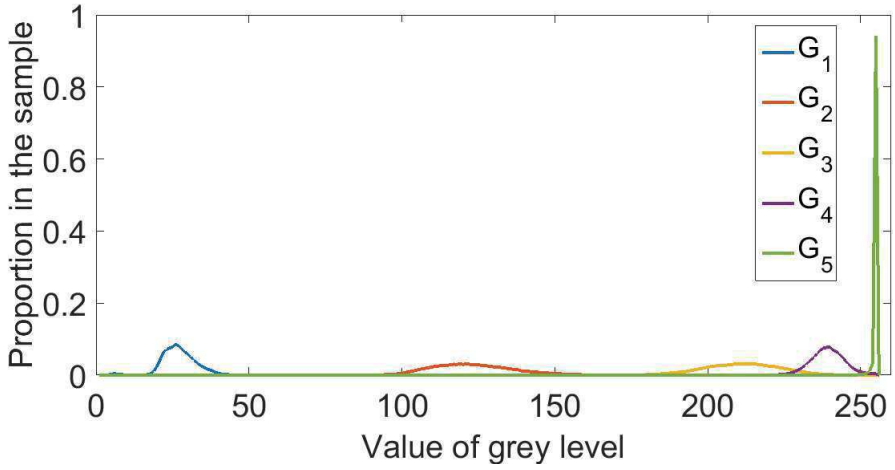

Figure 91: Distribution of grey levels in the calibration samples for the UD at FVF=0.51

It can be observed on these curves that the peaks associated with the grey color of each sample are always separated from the others. This means that the grey value of each sample is representative of its own concentration. There is therefore a unique equivalence between recorded grey level and colorant concentration in the sample. Finally, the calibration curves for the three materials at FVF=0.51-0.52 are presented, as examples in Figure 92. For all curves, logarithmic or linear fitting curves could be established in order to interpolate the grey value-concentration relationship between the measurement points.

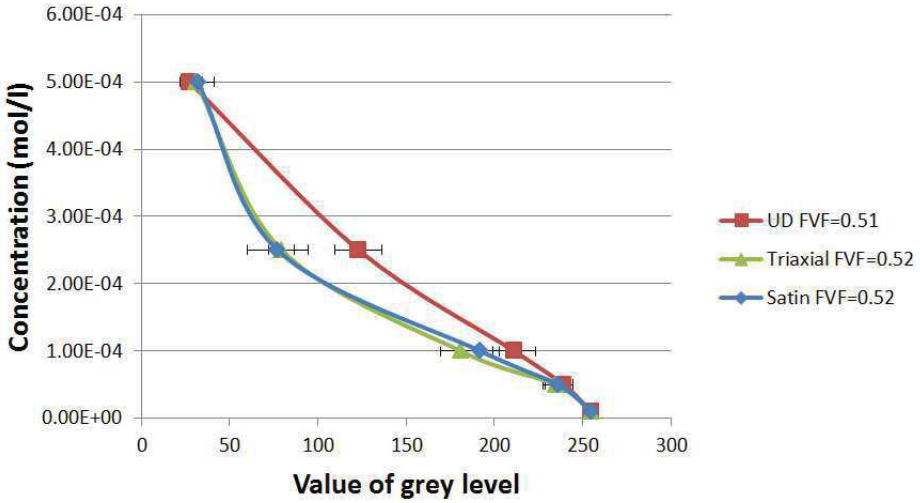

Figure 92: Calibration curves for the three textiles at FVF=0.52 for the Satin and the Triaxial and FVF=0.51 for the UD using fluid Gly1

3.6 Experimental protocol

The experimental protocol follows these steps :

- Setup preparation
  The Breather and the textile are placed in the cavity of the mold and the appropriate thickness plates are placed. The mold is closed and tightly sealed.

- Vacuum check
  Inlet pipes are locked and vacuum is checked by connecting the vacuum pot to the mold. Fluid placed in the pipe between the mold and the vacuum trap allows detecting potential air leakages.

- Mold positioning
  The setup is placed vertically between the lighting source and the camera so that the sample is in the region of lighting generated by the beamer.

- Pipe filling
  Both pipes at the inlet of the mold are filled until the injection gate to avoid any bubble liberation when switching the injected fluids.

- Weighing scale zeroing
  The tare is made on the weighing scale.

- Start of the camera
  From this moment, photographs are taken every 5 or 10 seconds depending on the

experiment duration. The 100 mm×100 mm sample, as well as, the 20 mm×100 mm region of Breather at the inlet of the mold are photographed.

- Fluid injection
  Blue fluid is injected until the beginning of the sample so that the mass injected in the Breather can be recorded. Then, injection of the Blue fluid is continued until reaching the top of the sample and stopped. Then the transparent fluid is injected. Injection of the transparent fluid is stopped when the injected volume of this fluid represents the volume necessary to fill the Breather and 10 to 20 times the volume of the sample.

- Cleaning
  The setup is removed from the experiment location, the mold is opened and the cavity so as the pipes are cleaned and dried.

3.7 Post treatment

- Mass recording
  The weighing scale is placed so that the mass value given on its screen is photographed on each picture. The value of mass is then manually reported in a table until the permanent state is achieved. Then, interpolations are conducted each 30 pictures to track potential non-linearity in flow rate evolution. The recorded mass values can then be used for the different plots.

- Picture post-treatment
  A post-treatment code has been developed with Matlab. First of all, the area of the sample and a strip of Breather (sample and Breather are then treated separately) is selected on each picture. Then, the full image or only parts of it can be treated. The principle of the post-treatment consists in computing for each pixel, the equivalent concentration thanks to the correlation curve. The average value of concentration is then computed by averaging the value over all pixels of the considered area. The principle of this process is presented in Figure 93. After this step, a curve as presented in Figure 94, is obtained.

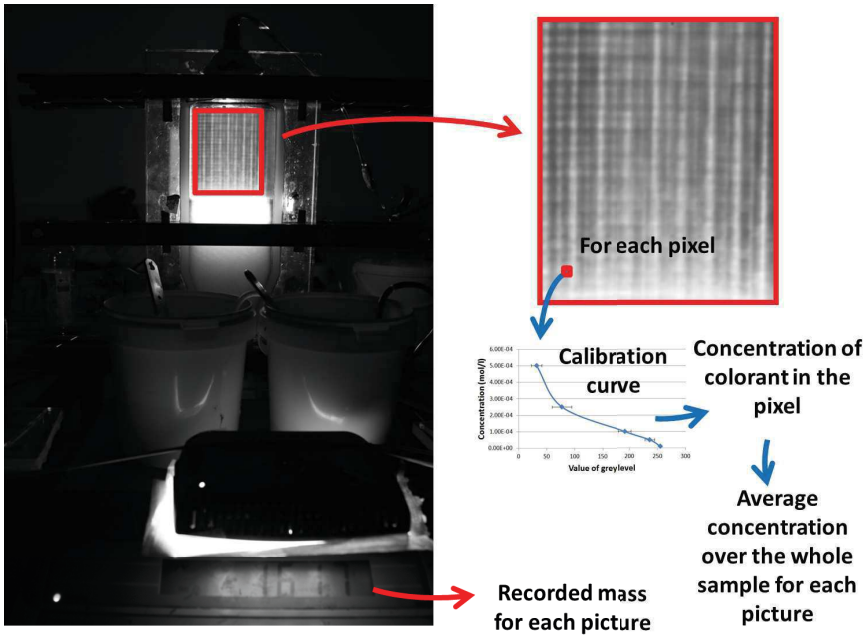

Figure 93: Principle of the quantitative experiment post-treatment

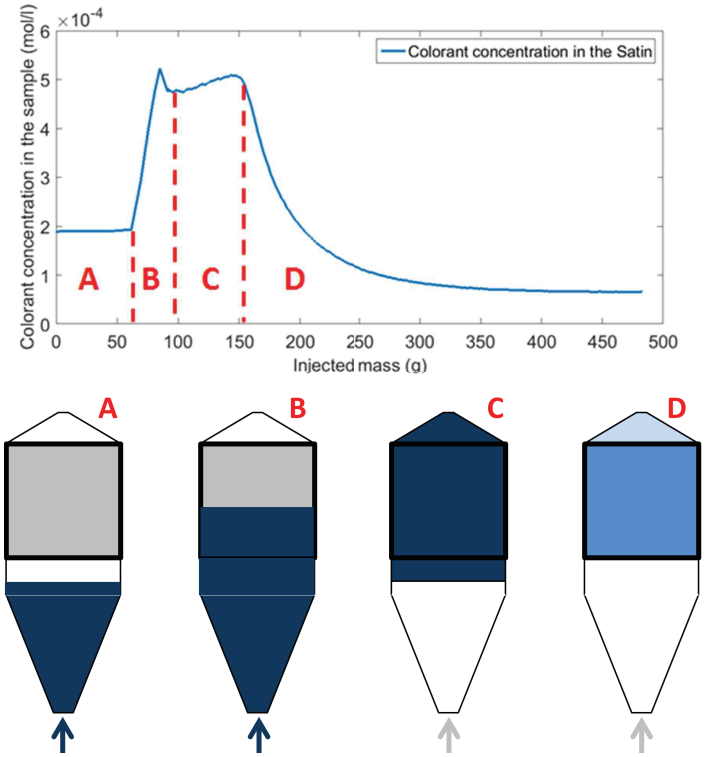

Figure 94: Example of curve obtained by plotting the concentration versus injected mass for the whole experiment, (example of the experiment conducted on the satin at FVF=0.52 with the fluid Gly1)

The concentration of colorant in the sample can be plotted versus the injected mass (Figure 94). The regions of the curves can be separated in four domains. In domain A, the Breather begins to saturate and the sample is dry, the computed value of concentration has no meaning because the sample does not contain fluid. In domain B, the sample is being filled, the peak that can be observed corresponds to the

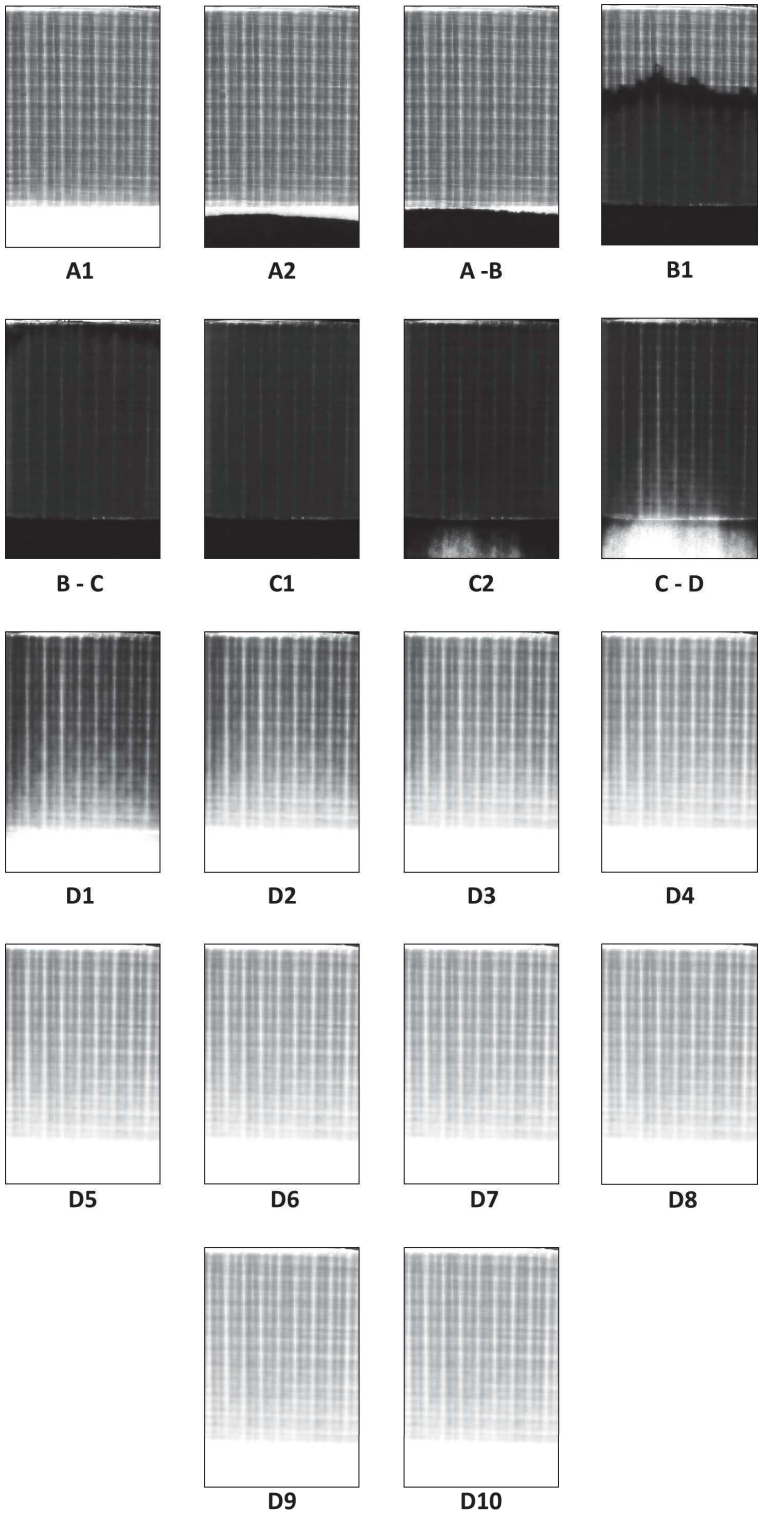

Figure 95: Example of Breather and Satin sample discoloration (FVF=0.52, fluid Gly1)

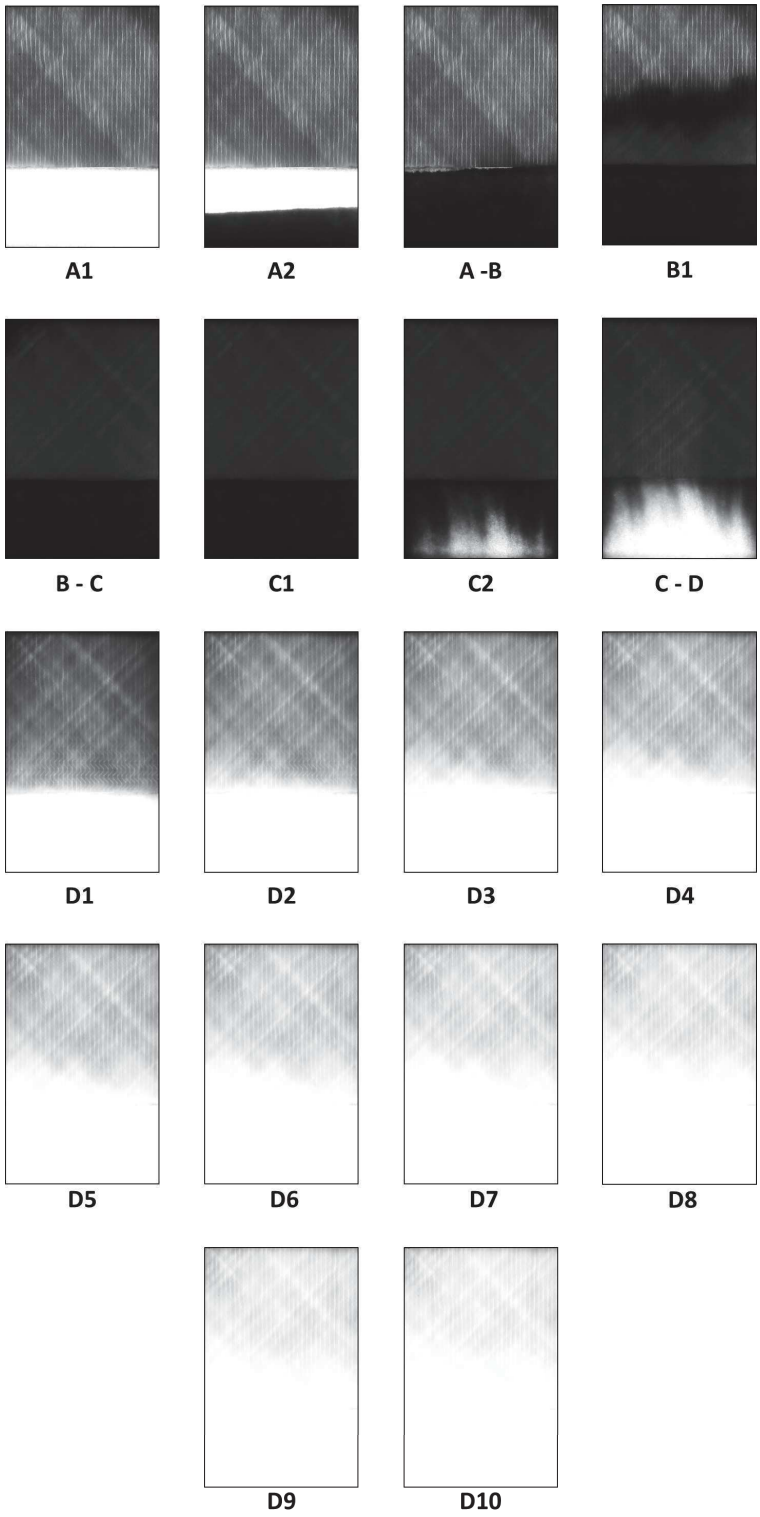

Figure 96: Example of Breather and Triaxial sample discoloration (FVF=0.52, fluid Gly1)

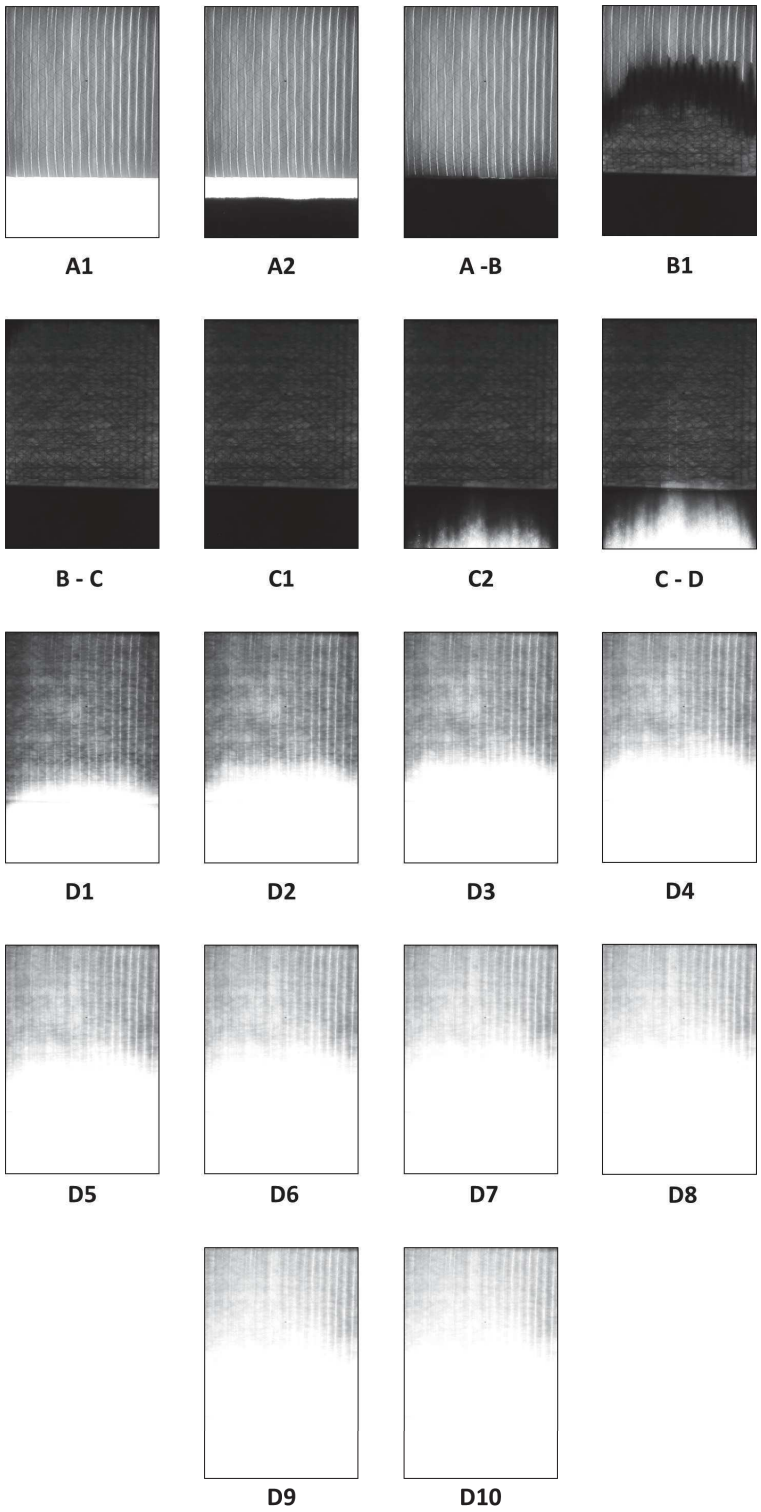

Figure 97: Example of Breather and UD sample discoloration (FVF=0.51, fluid Gly1)

unsaturated area traveling through the sample. In this region, saturated dark regions are overlapping with the area containing air that disperses the light. In domain C, the sample is saturated; this period corresponds to the time for the plain fluid to fill the Breather and reach the bottom side of the sample. Domain D is the domain of interest: the plain fluid flows through the blue saturated sample. It induces colorant evacuation with various kinetics depending on the architecture of the textile. The beginning of domain D is determined during the initial saturation. The domain D begins when the total injected mass is equal to the mass reached when the injection of the blue fluid is stopped (end of B) plus the mass required to saturate initially the Breather (end of A). In order to compare the samples between each other, a normalization of the injected mass and of the concentration can be conducted. The reference mass is measured as the difference between the mass achieved at the end of region B and the mass achieved at the end of A. The reference concentration is measured at the beginning of region D. In the remaining, for discoloration kinetics and storage analysis, only the D region will be plotted. Plotting of discoloration will be made versus the Normalized injected volume. This quantity is the ratio of volume (or mass) of fluid injected in the sample to the volume (or mass) injected initially to saturate the sample. The zero value of Normalized injected volume is fixed at the beginning of region D: when plain fluid begins entering the sample.

Figures 95, 96 and 97 present some of the obtained images of the samples at the different steps of the experiment. The labels Ax, Bx, Cx, and Dx below the images have been taken at consecutive times of regions A, B, and D of Figure 94. For domain D, the images have been made at a constant time laps: exactly one Normalized injected volume has been injected between each picture.

3.8 Designs of experiment

As mentioned in the introduction of this section, no previous study has been conducted on the quantitative investigation of resin storage inside fiber tows. Therefore, a wide experimental plan has been defined and conducted. The influence of the textile type, fiber volume fraction, fiber orientation, fluid velocity and fluid viscosity (the indicated ratio is the ratio of the injected viscosities - 175 mPa.s for the first colored saturation and 35 mPa.s for the rinsing fluid) have been investigated. The three designs of experiment are presented in Tables 16, 17 and 18.

UD					
FVF	**Fiber orientation**	**Fluid type**	**Viscosity** (mPa.s)	**Pressure** (bar)	**Repeats**
0.48	0°	Gly1	35	1	4
0.48	0°	Gly1	35	0.5	1
0.51	0°	Gly1	35	1	2
0.51	90°	Gly1	35	1	1
0.51	0°	CMC1	35	1	1
0.54	0°	Gly1	35	1	2

Table 16: Design of experiment for macroscopic intra-tow investigation in the UD material

Triaxial					
FVF	**Fiber orientation**	**Fluid type**	**Viscosity** (mPa.s)	**Pressure** (bar)	**Repeats**
0.52	0°/-45°/45°	Gly1	35	1	3
0.52	0°/-45°/45°	Gly2	155	1	1
0.52	0°/-45°/45°	CMC0	9	1	1
0.52	0°/-45°/45°	CMC1	35	1	1
0.52	0°/-45°/45°	CMC2	165	1	1
0.52	0°/-45°/45°	CMC1	35	0.3	1
0.52	0°/-45°/45°	CMC1	35	0.2	1
0.59	0°/-45°/45°	Gly1	35	1	3
0.59	0°/-45°/45°	CMC0	9	1	1

Table 17: Design of experiment for macroscopic intra-tow investigation in the Triaxial material

Satin					
FVF	**Fiber orientation**	**Fluid type**	**Viscosity** (mPa.s)	**Pressure** (bar)	**Repeats**
0.52	0°/90°	Gly1	35	1	2
0.52	90°/0°	Gly1	35	1	2
0.52	0°/90°	CMC1	35	1	1
0.54	0°/90°	Gly1	35	1	3
0.54	+45°/ -45°	Gly1	35	1	3
0.56	0°/90°	Gly1	35	1	1

Table 18: Design of experiment for macroscopic intra-tow investigation in the Satin material

4 Macroscopic trends investigation: Results

Using the methods presented in the previous section, the designs of experiments presented in section 3.8 have been realized. First of all, the validity and reliability of the method will be demonstrated. Then the results of the different experiments will be analyzed and combined to exhibit the trends and mechanisms involved in intra-tow storage.

4.1 Validity of the macroscopic intra-tow investigation technique and repeatability

4.1.1 Validity of the technique

In the case of the macroscopic intra-tow storage investigation, the 1D character of the flow in the sample is essential. Moreover, the transition between blue and plain fluid at the inlet of the sample is wished to be as quick as possible. These questions can be answered by analyzing the evolution of the color of the Breather at the inlet of the sample. For the three different materials at FVF=0.51-0.52, the curve of sample and entry Breather normalized concentration versus Normalized injected volume (the injected mass is normalized independently for each region depending on the intrinsic contained mass) are presented in Figures 98, 99 and 100.

It can be observed in the three Figures 98, 99 and 100 that colorant concentration in the breather decreases very quickly compared to the colorant concentration in the samples. This is as expected a consequence of the single-scale character of the Breather compared to the dual-scale character of the textiles. Additionally, the single-scale flow theory pretends that the fluid injected in a single-scale porous material pushes forward the fluid

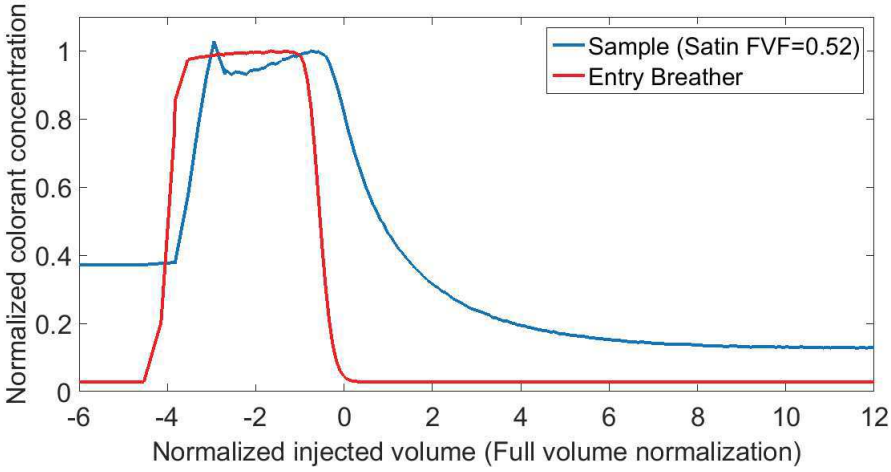

Figure 98: Evolution of the colorant concentration in the entry Breather and the sample (Satin at FVF=0.52) versus Normalized injected volume

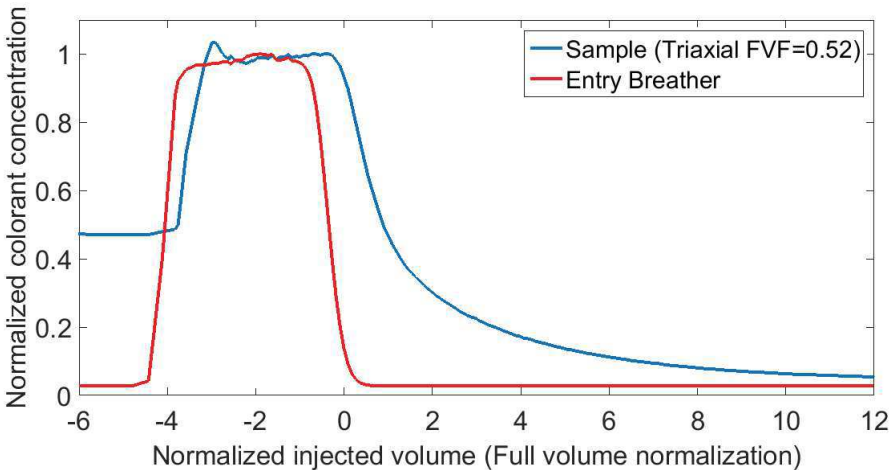

Figure 99: Evolution of the colorant concentration in the entry Breather and the sample (Triaxial at FVF=0.52) versus Normalized injected volume

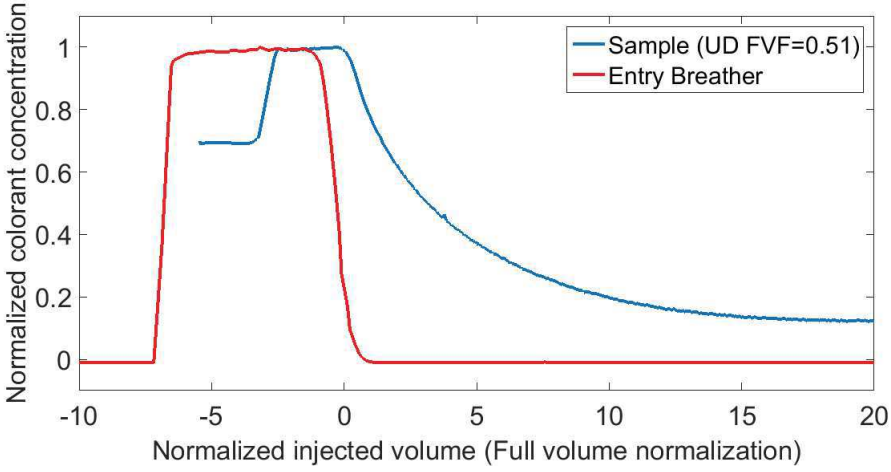

Figure 100: Evolution of the colorant concentration in the entry Breather and the sample (UD at FVF=0.51) versus Normalized injected volume

that already saturates the material. Therefore, it is expected that full evacuation of the colorant contained in the Breather should occur within the time required to inject the mass of fluid contained initially in the considered region. This period corresponds to the -1 to 0 Normalized injected volume in Figures 98, 99 and 100. Quantitative measurements reveal that, during this period, for the satin, the concentration of colorant drops from 96% for the Satin, 88% for the Triaxial and 76% for the UD. Additionally, the injected mass required to reduce the colorant concentration in the entry breather to less than 5% of the initial concentration represents respectively 1.03, 1.26 and 1.4 times the mass initially injected for the Satin, Triaxial and UD experiment. These results validate therefore the single-scale character of the Breather and highlight its ability to evacuate quickly the colored fluid that it contains.

Thus, it can be considered that after a period of about 0.5 Normalized injected volumes, the fluid entering the sample is pure and without colorant. The principle of the discoloration experiment is thus validated.

4.1.2 Repeatability

As presented in the design of experiments in section 3.8, several repetitions of the same experiment have been conducted. It is the case for experiments using the fluid Gly1 with the textile orientation 0°. For each material and each FVF, one to four repeats have been conducted. The first quantity that will be investigated to evaluate the repeatability of the experiments is the injection flow rate: as injections are conducted with imposed pressure, variations in the flow rate would highlight variability within the cavity thickness of the permeability of the textile and thus variability in the microstructure. Figures 101, 102 and 103 summarize the evolution of injected mass during the rinsing period (period starting when the plain fluid reaches the sample) for the different materials and FVF. It can be observed that injection flow rate is almost constant during all injections. This is due to the fact that when the plain fluid enters the entry of the sample, the colored fluid has begun to flow into the vacuum pot: a stationary regime has been reached.

It has been therefore demonstrated that the rinsing period (D) is conducted under stationary flow conditions.

Table 19 summarizes the injection flow rates of all experiments and the associated average value and standard deviations within the same FVF. It can be observed that for the Satin, the standard deviation is smaller than 6% which highlights a good repeatability of experiments in terms of injected mass. On the other hand, for the Triaxial, standard deviation is between 10% and 15%. These higher values might be explained by the heterogeneity of the ±45° plies of the textile which induces potential large flow channels and might increase significantly the injection flow rate. Finally, particular trends are observed on the values obtained from the UD experiments. The average injection flow rate obtained for the experiments at FVF=0.54 and FVF=0.51 are comparable. Additionally, high standard deviation is observed for the FVF=0.54 experiments (24%). This standard deviation is reduced for the FVF=0.51 and FVF=0.48 (respectively 10.9% and 6.50%). This high standard deviation might be due to the large size of the 0° tows. Their respective positions (above each other or between each other through nesting effect) could induce more or less significant channel size reduction (and thus permeability reductions).

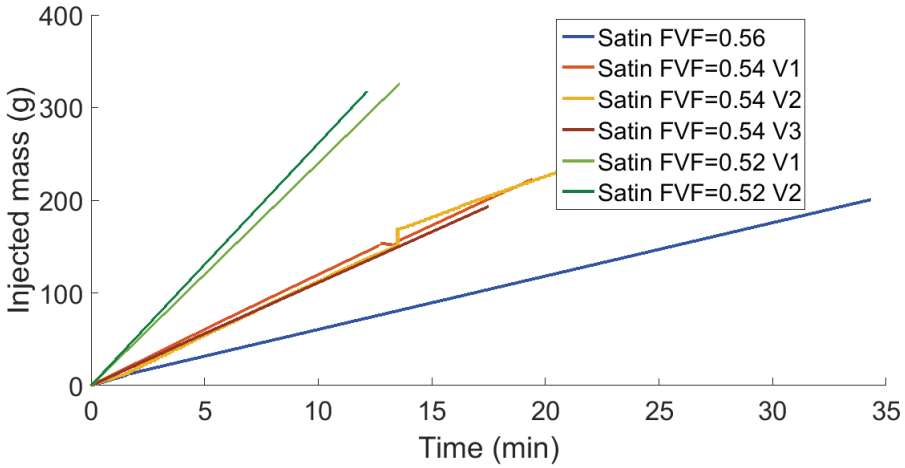

Figure 101: Injected mass versus time for the Satin samples at 0° impregnated with Gly1 at various FVF

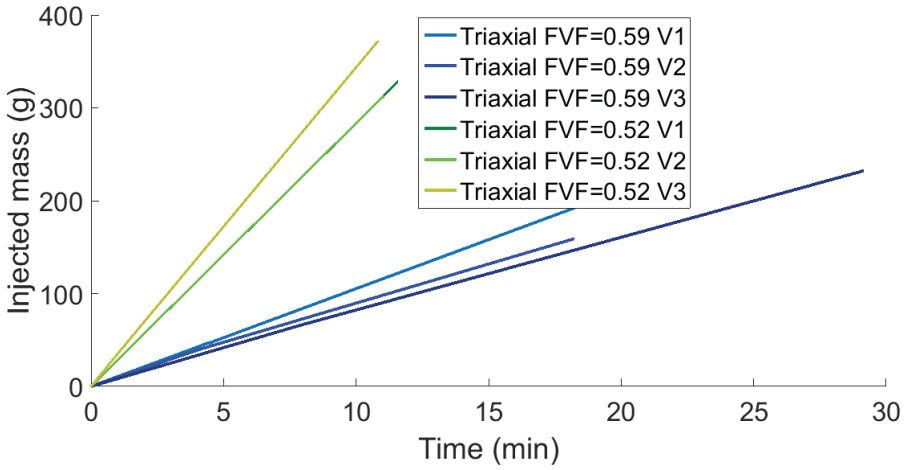

Figure 102: Injected mass versus time for the Triaxial samples at 0° impregnated with Gly1 at various FVF

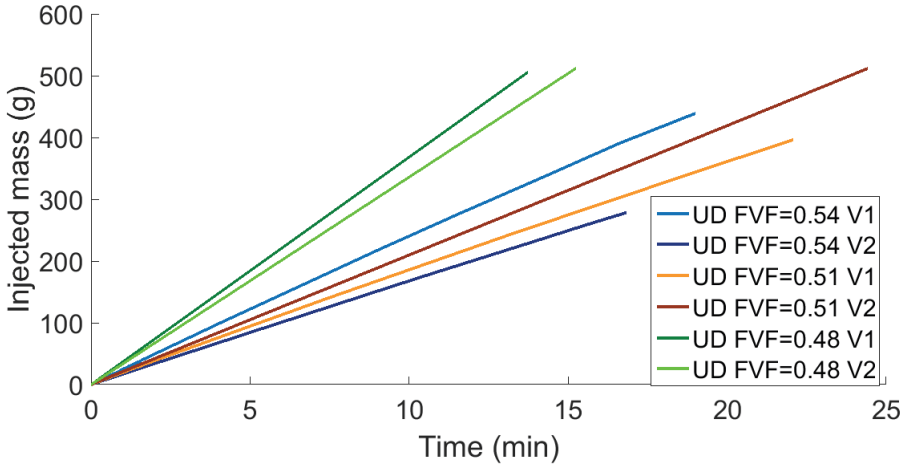

Figure 103: Injected mass versus time for the UD samples at 0° impregnated with Gly1 at various FVF

Therefore a good repeatability in terms of injection flow rates has been observed for the Satin and the Triaxial material for all considered FVFs. However significant varibility has been noticed for the UD, especially at high FVF.

Experiment	Mass flow rate (g/s)	Average mass flow rate (g/s)	Average volume flow rate(cl/s)	Standard deviation
Satin FVF=0.56	0.098	0.098	0.082	–
Satin FVF=0.54 V1	0.199			
Satin FVF=0.54 V2	0.189	0.190	0.158	3.9%
Satin FVF=0.54 V3	0.184			
Satin FVF=0.52 V1	0.400	0.418	0.348	6.0%
Satin FVF=0.52 V2	0.435			
Triaxial FVF=0.59 V1	0.176			
Triaxial FVF=0.59 V2	0.145	0.151	0.126	14.5 %
Triaxial FVF=0.59 V3	0.113			
Triaxial FVF=0.52 V1	0.472			
Triaxial FVF=0.52 V2	0.473	0.505	0.421	11.4%
Triaxial FVF=0.52 V3	0.572			
UD FVF=0.54 V1	0.390	0.333	0.278	24.2%
UD FVF=0.54 V2	0.276			
UD FVF=0.51 V1	0.299	0.324	0.270	10.9%
UD FVF=0.51 V2	0.349			
UD FVF=0.48 V1	0.614	0.587	0.490	6.50%
UD FVF=0.48 V2	0.560			

Table 19: Recorded flow rates for the various experiments

Additionnally, the results of these injections can be represented in terms of discoloration kinetic. Figures 104, 105 and 106 present these results.

It can be observed in Figure 104 that, as for the curves of injected mass, trends on discoloration can be identified depending on the fiber volume fraction. This further highlights the good repeatability of the experiments conducted on the Satin. Considering the Triaxial material, it can be clearly identified that the discoloration curves obtained for FVF=0.59 and FVF=0.52 appear as two distinctly separated families. However, for each FVF, a good repeatability can be observed, which provides the information that deviations of 10 to 15% in terms of injection flow rate does not affect much the results in terms of discoloration. Finally, for the UD, and as expected, trends are not so clear to determine from the repeats of the experiments. The higher the FVF, the less repeatable seem the results. Further investigations should be conducted in order to determine the origin of this heterogeneity in terms of discoloration kinetics and storage mechanisms. Table 20 summarizes the trends identified in this section

	Satin	**Triaxial**	**UD**
Repeatability Injection flow rate	++	+	-
Repeatability Discoloration kinetics	++	++	-

Table 20: Summary of the identified trends on repeatability

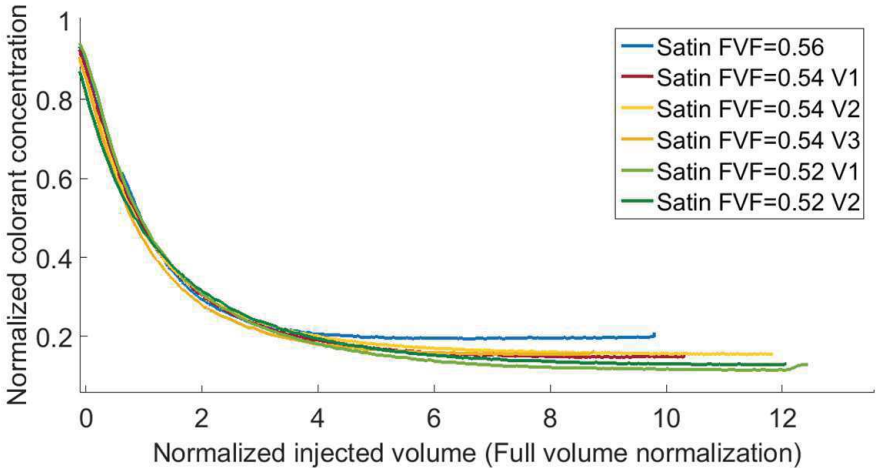

Figure 104: Discoloration kinetic of the Satin samples at 0° impregnated with Gly1 at various FVF

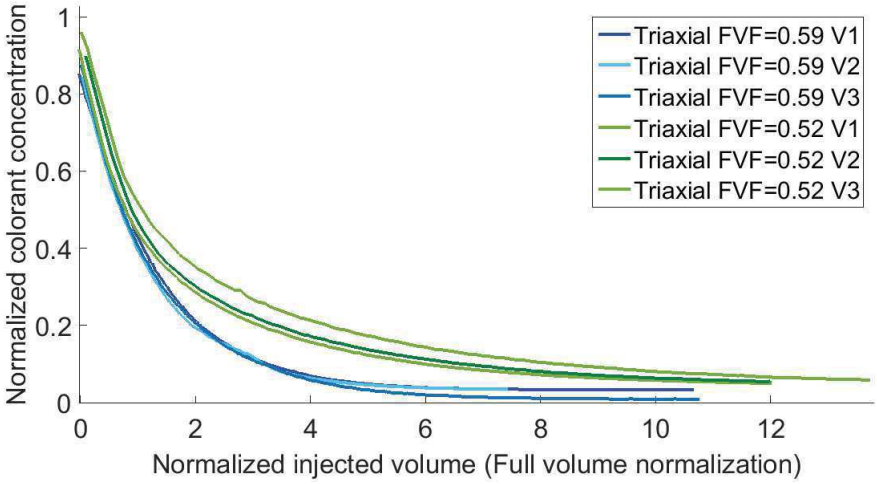

Figure 105: Discoloration kinetic of the Triaxial samples at 0° impregnated with Gly1 at various FVF

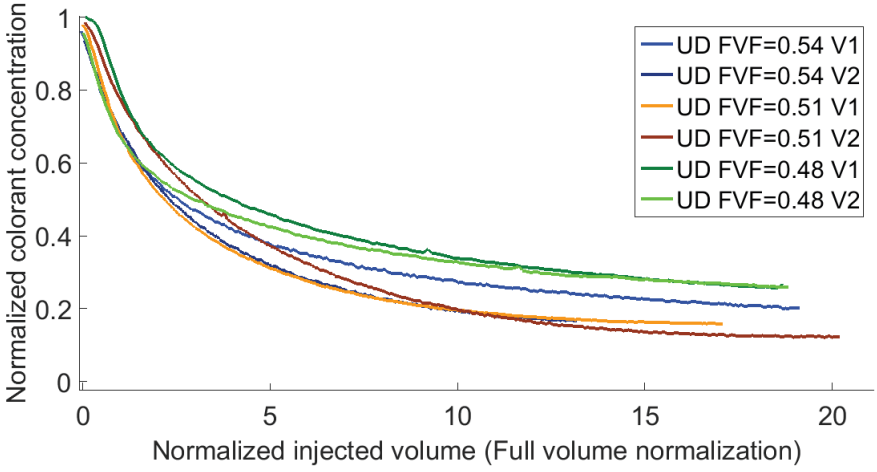

Figure 106: Discoloration kinetic of the UD samples at 0° impregnated with Gly1 at various FVF

Thus, the trends in terms of variability observed on the injection flow rate have been confirmed in terms of discoloration trends. Satin and Triaxial feature a good repeatability of the discoloration curves while UD experiments exhibit more various discoloration kinetics for identical macroscopic parameters. These differences must be therefore due to microscopic characteristics that will be investigated in the following sections.

4.1.3 Influence of viscosity and duration of the injection

An additional question on the topic of repeatability is the question whether the duration of the experiment has an influence on the discoloration kinetics. This aspect might be of great interest with a view to the UV curing injections that will be conducted under slower injection flow rates. Five different fluids (Gly1, Gly2, CMC0, CMC1 and CMC2) have been injected in the same material (Triaxial) at the same fiber volume fraction (FVF=0.52). Figure 107 represents the injected mass versus time during the different injections and Figure 108 shows the discoloration kinetics of these experiments. Additionnally, the injection flow rates of the different experiments are summarized in Table 21.

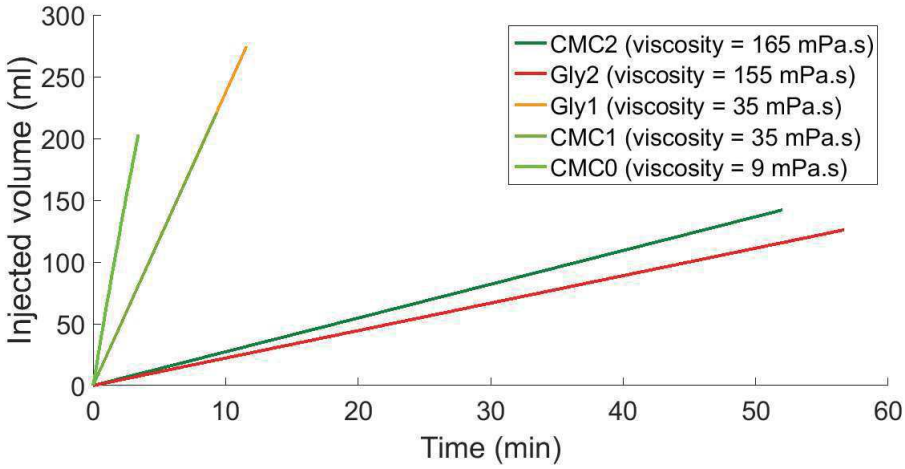

Figure 107: Injected volume of fluid versus time for the different fluids tested for the Triaxial material at FVF=0.52

Experiment	Volume flow rate
CMC2 165 mPa.s	0.046 ml/s
Gly2 155 mPa.s	0.037 ml/s
CMC1 35 mPa.s	0.395 ml/s
Gly1 35 mPa.s	0.395 ml/s
CMC0 9 mPa.s	0.996 ml/s

Table 21: Recorded volume flow rates for the various experiments with the Triaxial at FVF=0.52

Several observations can be made from Figure 107 and Table 21. As expected from the choice of the viscosities, the injection flow rates are multiplied by a factor 20 between the slowest and the fastest experiments. Additionally, the injection flow rates are distributed in three families depending on the range of viscosity. Considering the CMC solution, it can be observed from Figure 108 that the viscosity and/or injection flow rate appears to have a significant influence on the discoloration kinetics. However, for the Glycerol solutions,

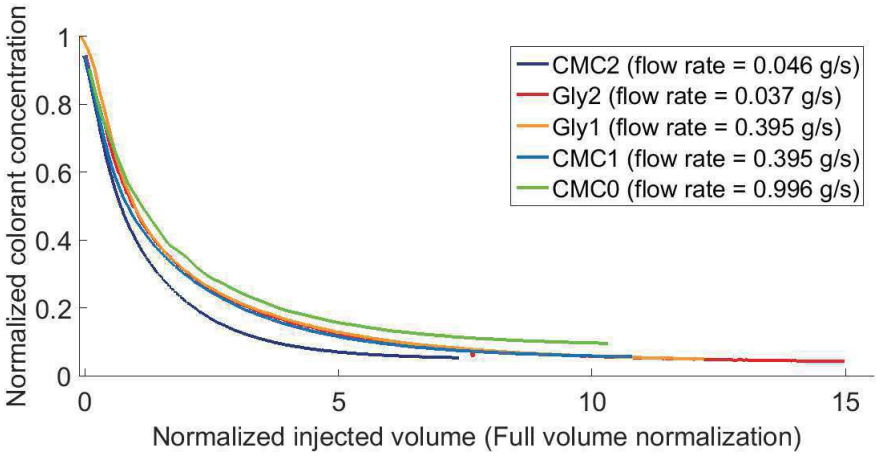

Figure 108: Discoloration kinetic of triaxial samples with FVF=0.52 for several fluid viscosities

the discoloration curves are superposed even if the viscosities exhibit a factor 4.4 and injection time a factor 10. This difference might be due to colorant diffusion mechanisms or filtration/retention of the CMC colorant within the fibrous media. These results may highlight that diffusion occurs more easily in the CMC solution.

Therefore and in order to ensure that diffusion and retention mechanisms are not playing a significant role in the conducted experiments, Glycerol solutions will be used.

4.2 Intra-tow storage: Macroscopic trends investigation

The validity, repeatability and the robustness of the developed technique has been presented in the previous section. The results obtained can now be compared. First, the samples will be considered entirely, afterward, details on local colorant concentration evolution will be investigated and coupled with the qualitative experiments.

4.2.1 Influence of FVF

Figures 104, 105 and 106 have been used to justify the repeatability of the tests. However they also allow to compare the trends in terms of discoloration kinetics for the three textiles at different FVF. It can be highlighted that for the Triaxial textile, increasing the FVF induces a faster discoloration (Figure 105). The same trend is observed for the UD material (Figure 106) even if the trends for fiber volume fractions equal to 0.51 and 0.54 are comparable. On the contrary, for the Satin material (Figure 104), it seems that increasing the FVF increases the ability for the textile to store the colored fluid. Additionally, another difference, observable at the macroscopic scale, between the NCFs and the woven material is the absence or presence of a non-zero asymptotic concentration of colorant. For NCFs, the trends appear to reveal that the asymptotic concentration of colorant in the sample is zero. On the contrary, for the Satin, an asymptotic value of colorant concentration between 10 and 20% of the initial concentration is achieved after the injection of 6 to 8 times the volume of fluid contained in the sample. The trends identified in this section are presented in Table 22. A non-zero asymptotic concentration reveals a permanent residual storage.

	Satin	Triaxial	UD
Discoloration kinetics	-	+	–
Permanent residual storage	++	- -	+
Influence of FVF	-	++	+

Table 22: Summary of the identified trends on discoloration

It has been established that, for NCFs increasing the FVF accelerates the discoloration of the sample. However, the opposite behavior has been observed for the satin: increasing FVF increases slightly the intra-tow storage. Moreover, it has been observed that the Satin features a non-zero colorant concentration discoloration asymptotic behavior as well (in a lesser extent) as the UD while the colorant concentration in the Triaxial tends to zero.

4.2.2 Influence of textile architecture

The repeatability of the tests for the Satin and Triaxial materials enable to compare representative curves obtained with these materials and thus to compare at equivalent FVF the influence of architecture on intra-tow resin storage. Figures 109 and 110 display respectively the discoloration kinetics of the three materials at FVF=0.51-0.52 and the discoloration kinetic of the Satin and UD at 0.54.

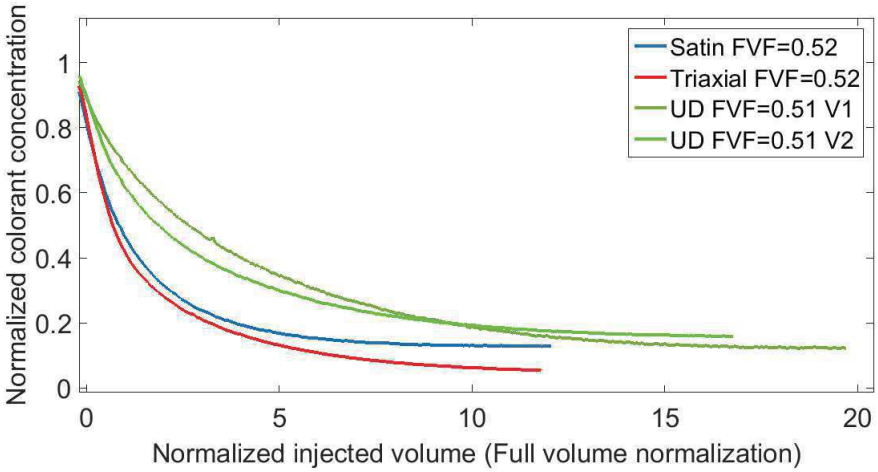

Figure 109: Discoloration kinetic of the three materials at FVF=0.51-0.52 for an injection conducted with fluid Gly1

Some trends can be determined from Figure 109. First of all, the UD material impregnated in the 0° is the material in which storage lasts the longest. It is followed by the Satin that exhibits, as discussed previsously, an asymptotic storage behavior. Finally, the Triaxial appears to enable the fastest evacuation of the colorant with a trend that tends to a final concentration equal to zero.
The trends observed in Figure 109 are confirmed in Figure 110 for higher FVF. The UD, even when it more compacted, has a higher tendency to store fluid than the Satin. The investigation of the microstructre may enable establishing conclusions to explain this phenomenon.

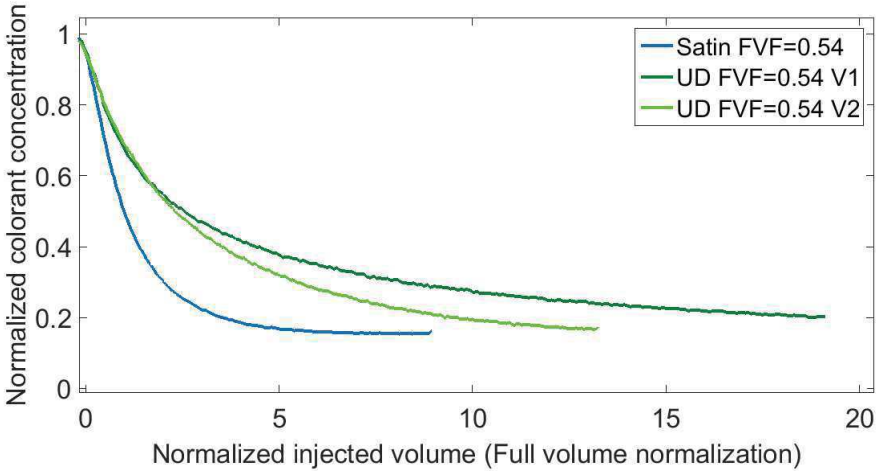

Figure 110: Discoloration kinetic of the Satin and UD at FVF=0.54 for an injection conducted with fluid Gly1

It has been established in this section that at equivalent FVF, UD material stores longer the fluid than the Satin and more than the Triaxial material

4.2.3 Influence of tow orientation

Tests have been conducted to investigate the influence of tow orientation on intra-tow resin storage. Discoloration kinetic curves for the Satin comparing 0° and ±45° are presented in Figures 111 at FVF=0.54. Figure 112 compares the discoloration kinetics of the Satin at 0° and 90° for FVF=0.52. Finally, Figure 113 presents the discoloration kinetics of samples of UD at 0° and 90°. All experiments have been conducted with the fluid Gly1.

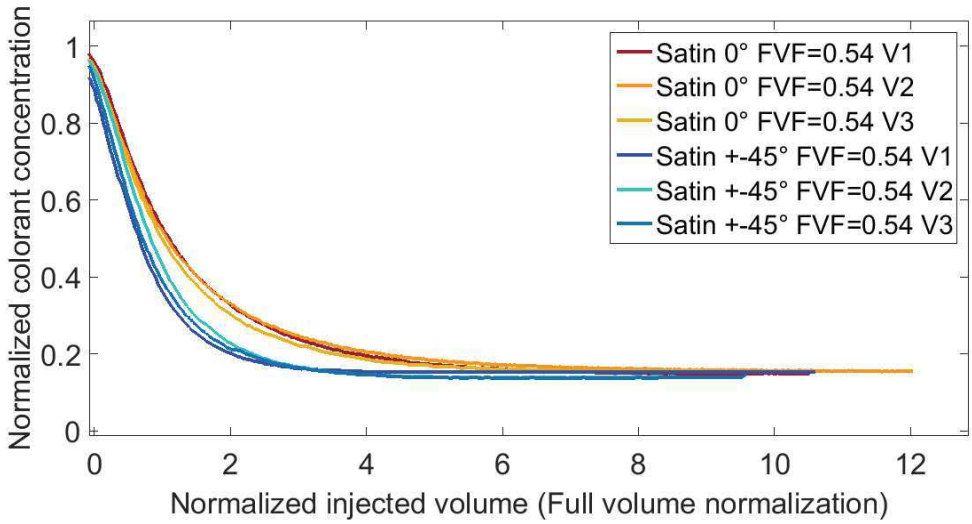

Figure 111: Discoloration kinetic of the Satin samples at at 0° and ±45° impregnated with Gly1 at FVF=0.54

It can be observed in these figures that changing the tow orientation changes the discoloration kinetics of the samples even if the FVF is the same. In the three figures, it can be observed that discoloration is accelerated. In Figures 111 and 112 this accelerated discoloration can be observed for the case of the Satin. Some explanations can be imagined for the faster observed discoloration. As introduced in section 2.1.1, the Satin

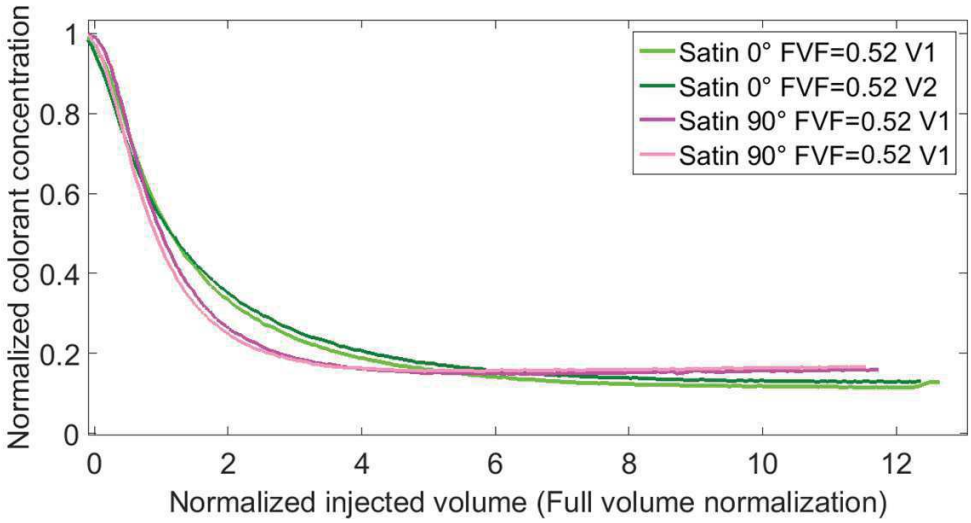

Figure 112: Discoloration kinetic of the Satin samples at 0° and 90° impregnated with Gly1 at FVF=0.52

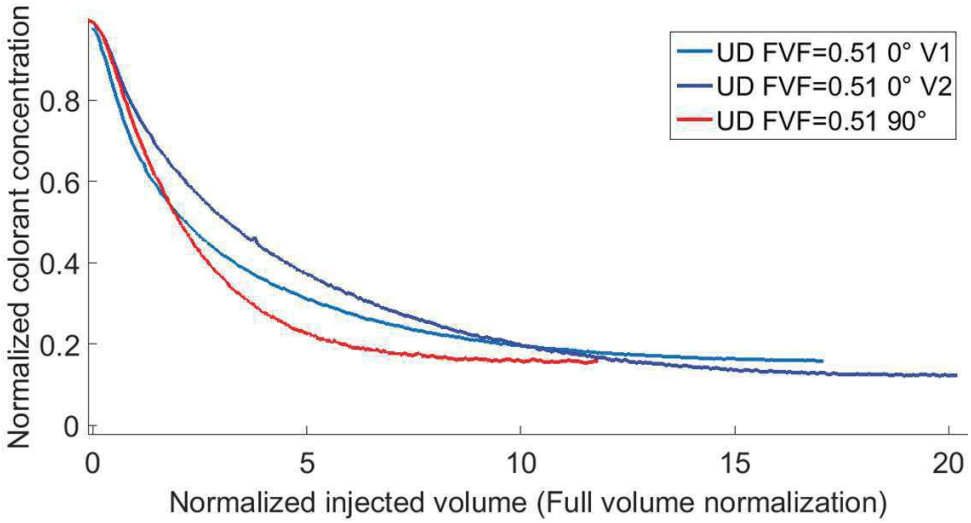

Figure 113: Discoloration kinetic of the UD samples at 0° and 90° impregnated with Gly1 at FVF=0.51

is unbalanced with a higher areal weight in weft than in warp even if the tow size are the same. This means that the textile features less channels in weft (90°) direction than in warp (0°). Therefore, it is expected that the fluid needs to travel through channels exhibiting an increased tortuosity. It can be thus expected that resin will more often flow through the tows and thus evacuate intra-tow stored colored fluid. This assumption is also valid for the 45° injection. In this injection, no channel in the material is aligned with the macroscopic flow direction. This has two consequences: first, the channel tortuosity is increased for the fluid which leads as for the 90° injection to an accelerated discoloration at the edges of these tortuous channels. And second, all tows are exposed to a pressure gradient that is not aligned with their own direction. Transverse intra-tow flow is thus expected to occur and as tows are only some millimeter wide, the intra-tow stored colored fluid is likely to be evacuated quickly out of tow. Due to these two coupled effects, the discoloration is observed to be faster in the 45° injection than in the 90° injection.
However, and even if discoloration trends are different with tow orientations, it can be no-

ticed that, for all orientations, the same asymptotic concentration is reached. This could be explained by the existence in the textile of regions that does not contribute to the flow after saturation, whatever the flow direction. Micro-scale observations should allow to observe these regions and confirm this assumption
On the other hand, the case of the UD is different. The UD material is indeed characterized by its channels in the 0° direction. When the fluid is injected in the 90° direction, the channels are perpendicular to the flow direction and there is no proper flow channel in the direction of the flow in the material. This implies the fluid to flow through the tows and accelerate therefore the evacuation of intra-tow stored colorant. Attention should however be paid to the non-zero asymptotic trend of the colorant concentration in the textile. This characteristic introduces the idea that, as for the satin, permanent intra-tow resin storage occurs inside of the UD sample.

It has been observed in this section that for the Satin, changing the tow orientation to ±45° or 90° compared to flow direction accelerates the discoloration. The same trend is observed for the UD at 90°.

4.2.4 Investigation of concentration variations inside of the sample

Observing the samples during rinsing reveal that significant variations in terms of concentration can be observed along the length of the samples. Figure 114 presents some examples.

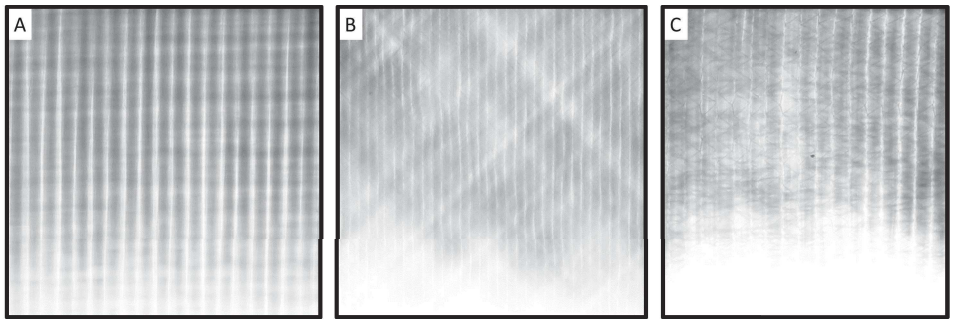

Figure 114: Satin (A), Triaxial (B) and UD (C) at the fiber volume fraction 0.51-0.52 after the injection of 5 times the initially contained volume of fluid

In order to investigate this phenomenon, the analysis area is reduced from the whole sample to five regions distributed along the length of the samples as presented in Figure 115. The evolution of the concentration in these regions is then plotted (as previously) versus the Normalized injected volume. Figures 116, 117 and 118 represent the evolution of the colorant concentration in the five areas of analysis, respectively for the Satin at FVF=0.52, the Triaxial at FVF=0.52 and the UD at FVF=0.51. The testing fluid is Gly1.

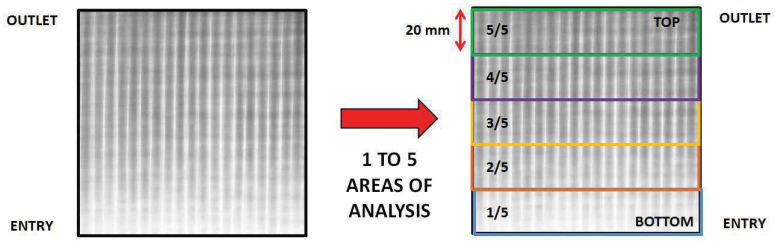

Figure 115: Principle of the new areas of analysis

It can be observed from the different curves that, as expected, the fastest colorant concentration decrease is observed for the bottom fifth (1/5) of sample. Furthermore, for the Triaxial and the UD, the colorant concentration in the first fifth (1/5) drops under 5% of the initial concentration after the injection of 5 Normalized injected volumes. This means that in this region, the colorant has been totally removed from the tows. Moreover, even in the top fifth of the samples of the NCFs, colorant concentration decreases significantly: from 100% to 17% and for the UD from 100% to 54% within the injection of five times of the initial sample fluid content. At the bottom as well as at the top of the sample, flow channels are expected to be cleaned within the first Normalized injected volume of plain fluid. However, the observed further colorant evacuation is not expected from the classical dual-scale flow approach (stating that intra-tow resin storage is permanent). Considering the UD material, fiber tows are aligned in the direction of flow, it can be thus imagined that colorant evacuation at the bottom of the sample is due to intra-tow longitudinal flow. However, at the top of the sample, even if longitudinal intra-tow flow is considered, the top of the fiber tows should be fed with blue fluid flowing in the tows and no further discoloration should be observed until the intra-tow blue-plain interface reaches the considered location. This further discoloration reveals therefore that another rinsing phenomenon is involved in regions of the sample where the intra-tow blue-plain flow front has still not arrived. And this mechanisms appears to be a tow-channel flow exchange as it evacuates colorant from the tows even if these are aligned with the direction of flow. The investigations conducted at the micro-scale fluid flow mechanisms will aim to determine the origin of this out-of-principal flow direction flow mechanism. Finally, a non-zero asymptotic colorant content is observed for the regions 3/5 to 5/5. This could be related to the observation made on the 90° injection conducted in the previous section supposing that permanent storage occurs in some extent in the UD sample.

Thus, it has been established from the study of the UD discoloration curves that three discoloration mechanisms are involved in the process:

- Channel flow
- Principal flow direction intra-tow flow
- Out-of-principal flow direction intra-tow flow (tow-channel exchange flow)

As they occur in one material, they are expected to be observed in the other materials. These three mechanisms are summarized in Figures 119, 120, and 121.

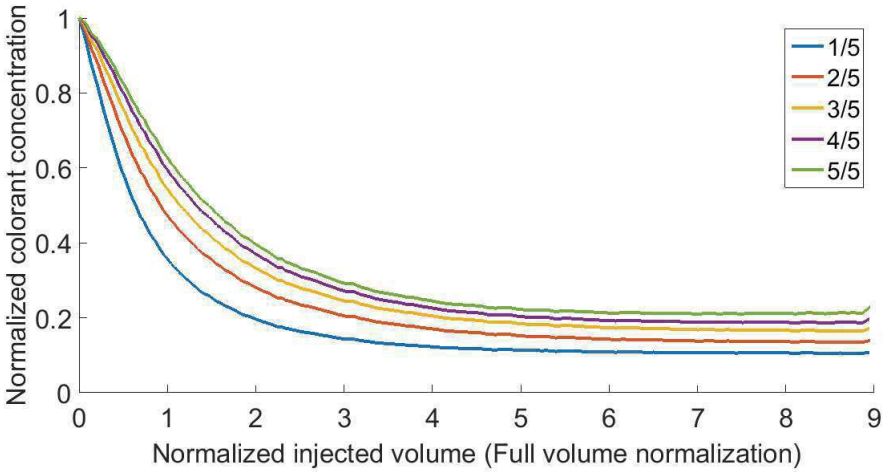

Figure 116: Evolution of the colorant concentration in the 5 areas of analysis versus Normalized injected volume for the Satin at FVF=0.52

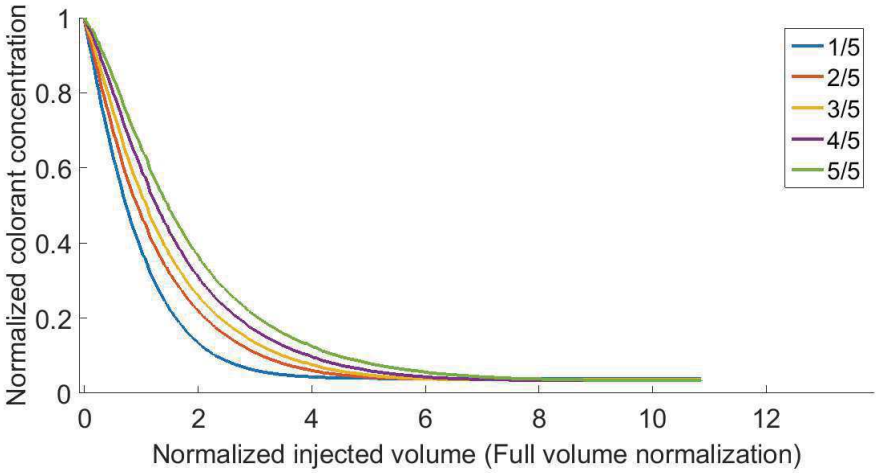

Figure 117: Evolution of the colorant concentration in the 5 areas of analysis versus Normalized injected volume for the Triaxial at FVF=0.52

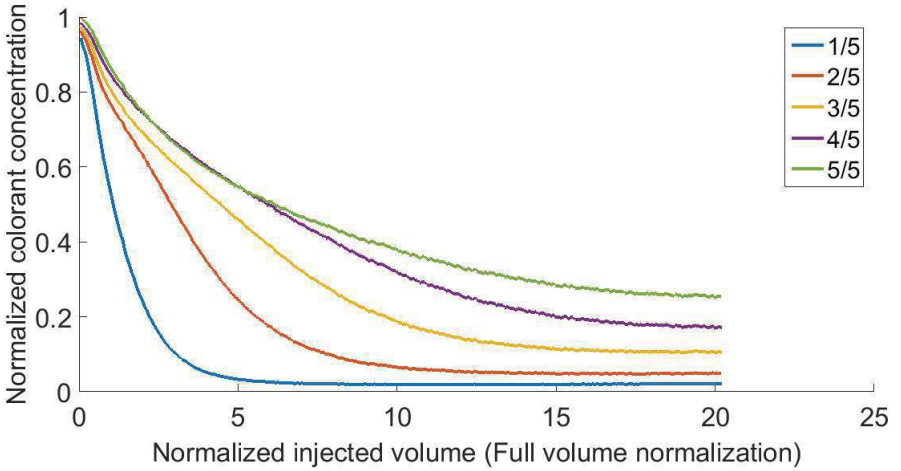

Figure 118: Evolution of the colorant concentration in the 5 areas of analysis versus Normalized injected volume for the UD at FVF=0.51

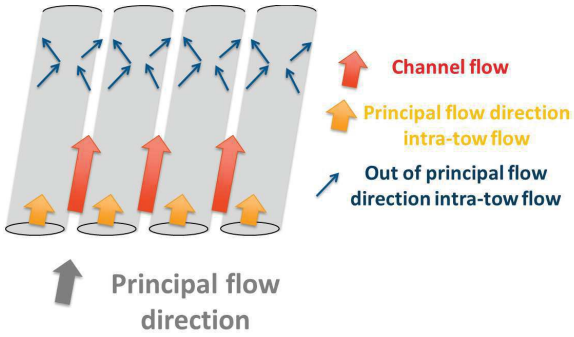

Figure 119: Flow mechanisms in a UD with principal flow direction aligned with the fiber tows

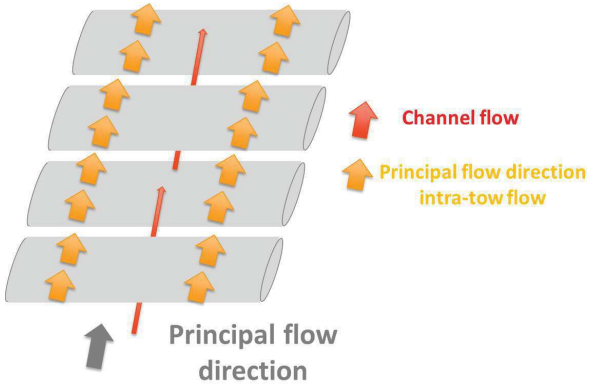

Figure 120: Flow mechanisms in a UD with principal flow direction perpendicular to the fiber tows

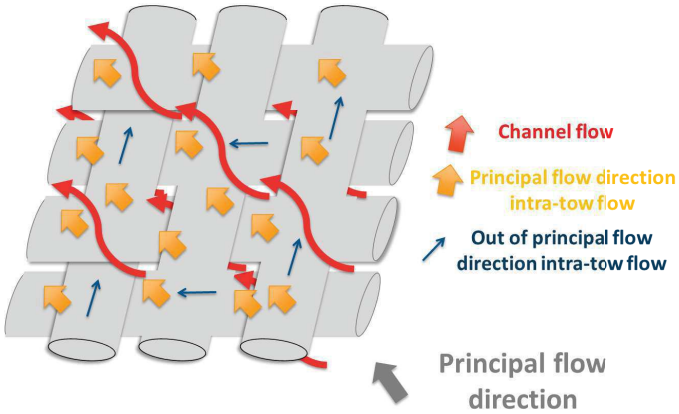

Figure 121: Flow mechanisms in a plain weave with principal flow direction at 45° to the fiber tow orientation

4.3 Conclusions on macroscopic trends investigation

Using the newly developed setup, discoloration experiments have been conducted on three different textiles (UD, Triaxial and Satin) to evaluate the influence of textile architecture, fiber volume fraction and tow orientation on resin storage. Discoloration experiments allowed determining that the UD material, when injected in the direction of the tows features, at the same FVF, the highest and longest storage followed by the Satin and the Triaxial. Regarding textile architecture, a particularity has been noticed for the Satin

contrary to the NCFs: the Satin features a non-zero asymptotic colorant content in the whole sample in the range of 10-20% of the initial content while for the Triaxial, colorant content tends to zero. In the UD samples, entry regions are asymptotically fully discolored but colorant permanent storage occurs downstream in the part.
On the other hand, resin storage has been observed to reduce with the increase of the FVF for the NCFs and sighltly increase with FVF for the Satin. However, giving explanations on the influences of architecture and FVF without proper knowledge of the microstructure, is difficult. Therefore, these aspects will be further investigated after investigation of the microscopic mechanisms in section 6.
Furthermore, analysis of colorant content evolution in the length of the sample and at different fiber orientations allowed identifying the presence of three different flow mechanisms inside of the tested materials during injection: channel flow, intra-tow flow in the direction of the macroscopic flow and intra-tow flow out of the principal direction flow. Indeed, fast discoloration of the channels have been observed experimentally at the first stages of plain fluid injection in the samples (Figures 95, 96 and 97). Additionally, investigation of colorant content in the length of the sample have revealed that full tow discoloration was occurring at the entry of the sample for the Triaxial and UD materials and that the length of the discolored region was increasing with injected volume (further investigation of this aspect will be conducted in section 7.3). This induces that intra-tow flow occurs inside of the tows in the principal flow direction. The consequences of this phenomenon can be also noticed when sample orientation is modified: discoloration is indeed faster when tows are oriented at $\pm 45°$ or $90°$. This is due to the smaller distance to flow through for the resin (the tow width) before reaching the channels and being evacuated. Finally, for the NCF materials, next to the end of the sample, discoloration is also noticed along injection. This discoloration occurs far downstream from the intra-tow colored-plain fluid flow. Therefore, an additional flow mechanism generating local channel-tow flows is expected to be acting in these regions. However its origin cannot be determined only from a macroscopic analysis. Therefore, this phenomenon will be deeper investigated in section 6 dedicated to the mircoscopic mechanism investigation.
Finally, it must be emphasized that intra-tow flow mechanisms induce major colorant evacuation as colorant content in the tested samples has been measured to be reduced by 2 to 5 for a Normalized injected volume equal to 5 (50-20% of remaining colorant in the 10 first centimeters of a part measuring 60 cm). And the colorant content has been observed to tend to zero for the NCF materials for longer injections. These results are not in agreement with the classically made assumption of permanent intra-tow resin storage in dual-scale simulations. Therefore, when micro-scale flow mechanisms will have been identified and quantified, a new simulation approaches taking these flow mechanisms into account should be proposed.

5 Microscopic mechanisms investigation: Setup and methods

5.1 Principle of the experiment

The experiment presented in the previous section delivers average information on intra-tow resin storage during fluid injection. It provides however neither information on the location of the dark colored fluid in the microstructure nor on the micro-scale mechanisms generating quick or slow discoloration. Therefore, the aim of the technique presented in this section is to observe the location of the colorant rich regions within the microstructure during injection to identify the flow mechanisms. In order to achieve this goal, UV curing resin is injected instead of the model fluid in the previously presented setup, using the same

injection protocol (mold, materials, cavity thicknesses,...). This resin features no viscosity evolution without UV exposition and a curing time of a few minutes when exposed to UVs. Thus, the injection conditions of the previous quantitative experiments can be reproduced with the advantage that colorant location in the part can be fixed at any time by stopping injection and quickly exposing the part to UVs. This allows observing precisely the location of the colored resin inside the microstructure at the different times during rinsing. The principle of the technique as well as the methods of post-treatment are summarized in Figure 122.

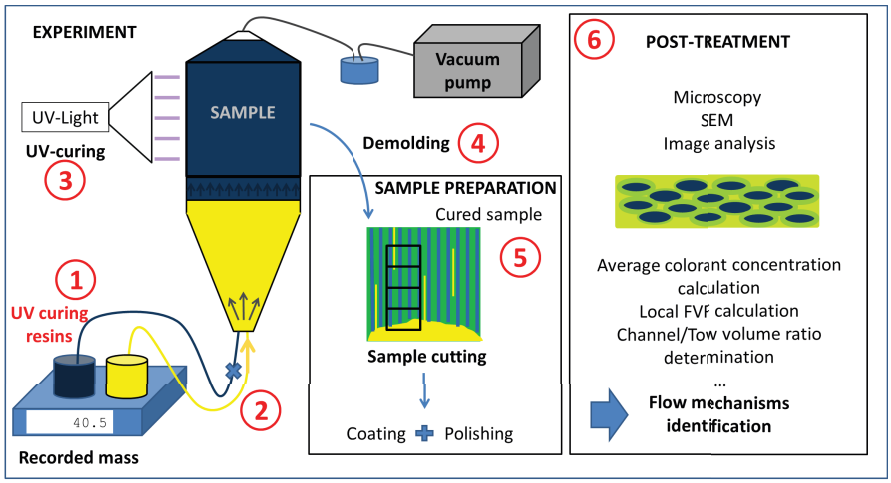

Figure 122: Principle of the experiments and post-treatment for micro-scale flow mechanism investigation

5.2 Setup and equipment

5.2.1 Mold and injection system

The same mold and injection system as for the quantitative experiment has been used (sections 3.2.1 and 3.2.2).

5.2.2 UV-curing equipment

In order to cure the UV curing resin, a UV lamp with a power of 36 W and wave length spectrum between 320 and 400 nm has been used.

5.3 Measurement and monitoring equipment

5.3.1 Camera, lenses and acquisition system

Weighing scale screen picture taking during the experiment as well as sample photographs were made using the Canon digital camera presented in section 3.3.1, the lense EFS 18-55 mm was used for setup photography and the lense MP-E 65 mm for photographs of the microstructures.

5.3.2 Weighing scale

In order to determine the moment to stop the experiments (regarding the equivalent volumes of yellow resin injected in the sample) the Adam weighing scale presented in section 2.2.2 has been used.

5.3.3 Scanning Electronic Microscope

For microstructure analysis of the samples, a JEOL JSM 6060LA Scanning electron microscope has been used.

5.3.4 Micro-tomograph

For micro-tomography imaging of the samples, an Xradia micro tomograph with a maximal X-ray voltage of 150 keV at 10 W has been used.

5.4 Post-treatment tools

As for the quantitative experiments, the software Matlab and ImageJ were used to conduct post treatment on the sample pictures.

5.5 Experiment calibration

The same thickness calibration has been used as for the qualitative experiments in order to obtain UV cured parts that exhibit the same microstucture as the samples used in the qualitative experiment (Table 13).

5.5.1 Selection of fluid viscosity

As discussed previously, macroscopic and microscopic experiments are wanted to be realized in comparable flow conditions and with injection times as short as possible. In the case of reactive resins, viscosity could not be reduced below 100 mPa.s without affecting the curing properties of the resin. Therefore, this viscosity has been chosen. Table 23 summarizes the additional polyester weight content and initial viscosity of the UV-curing resin.

Curing fluid	**Polyester content** (%)	**Additionnal styrene content** (%)	**Viscosity**
UV-curing polyester	80	20	100 mPa.s ±10 mPa.s

Table 23: Composition (in weight) and viscosity of UV-curing resin used during this study

5.5.2 Resin curing characterization

As presented in section 2.3.2, the UV curing characteristics of the resin have been determined. Gel occurs within 2-3 minutes of exposure on each side of the sample.

5.6 Experimental protocol

5.6.1 Injection and curing

The first steps of the protocol are the following:

- Setup preparation
  A demolding (release) agent is spread in the mold prior to the placement of the Breather and the fibrous reinforcement.
- Vacuum check
- Placement of the mold in position (horizontal position is used in the case of the UV curing experiment).

- Pipe filling to avoid air bubbles
- Weighing scale zeroing
- Start of the camera
- Fluid injection
  Violet colored UV-curing resin is first injected to saturate the sample. Then the Yellow colored resin is injected. Once the desired mass of fluorescent resin has been injected, the injection is stopped.
- UV-curing
  Just after stopping the injection, a UV light is positioned on the sample to quickly cure the resin and fix the colorant at its location. The curing sequence is 2 minutes on each side at the beginning and then 30 minutes with side changing each 5 minutes to fully cure and allow demolding.
- Demolding
  After 30 minutes of UV exposure, the resin is cured. The mold is opened and the part is removed.

5.6.2 Sample preparation

Post treatment begins with the cut of samples out of the cured part. This step is realised on a 3-axes trimming machine *Charly 2U T6* (from the company Charly Robot) with a 3 mm diameter drill. Samples with dimensions 22 mm×17 mm are presented in Figure 123. For each part, 4 samples are trimmed starting at 10 mm from the bottom side of the UV-cured part. The observations will be conducted on the bottom side of the samples. Therefore, the sections that will be analyzed are located respectively at 10 mm, 30 mm, 50 mm and 70 mm from the bottom side of the part (which corresponds to the center of the windows considered in the macroscopic investigations).

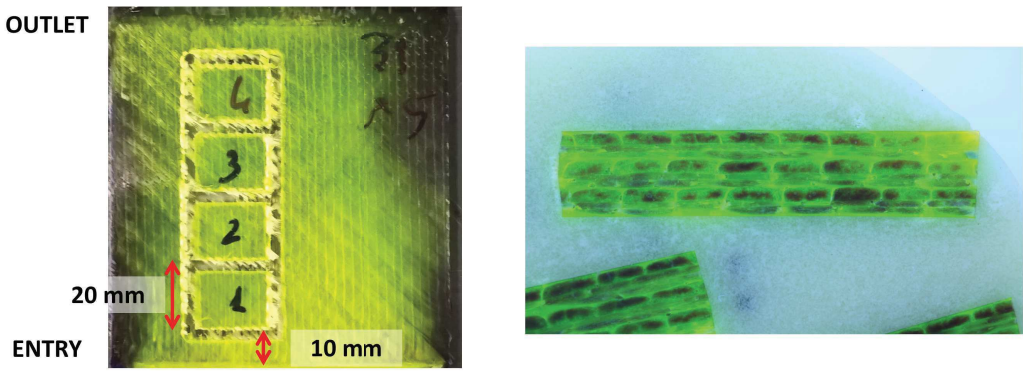

Figure 123: Example of a part after the trimming (left) and polishing (right) of the samples for micrography

The samples are then prepolished, coated and polished with Struers SiC polishing papers from 320 to 4000.

5.6.3 Imaging the samples

Four types of pictures have been taken from the polished samples:

- Colored macro pictures of the samples
  In order to study the storage in the microstructure.

- SEM macro images of the samples
  In order to estimate the channel/tow volume ratio in the parts.
- Colored micro pictures of the tows
  In order to determine the location of storage within the fiber tows.
- SEM micro images of the tows
  In order to determine the intra-tow local fiber volume fraction and fiber distribution.

5.7 Post-treatment: Image analysis methods

5.7.1 Determination of the storage location

After polishing, pictures are taken of each sample and some areas of interest using the camera and respectively the EFS or MP-E65 lense. These pictures are taken in color. They are then cropped to only keep the area of the sample and converted to grey levels. Then a threshold is applied to define the limit in terms of grey level that separates regions saturated with the initial colorant concentration and regions where violet colorant has been evacuated. This threshold step is manual and therefore induces some extent of error in terms of area distribution between the violet and yellow regions. This error is estimated to be in the range of ±5%. An illustration of the steps of this processing chain are presented in Figure 124.

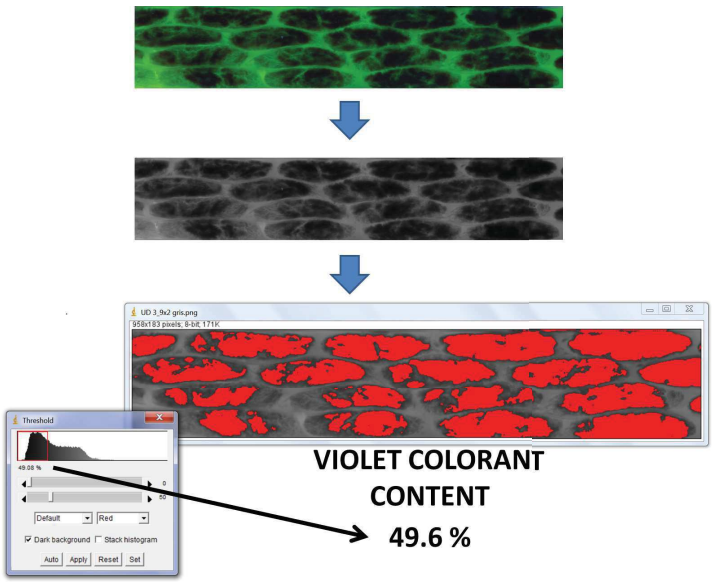

Figure 124: Steps of the processing chain for the estimation of the area occupied by the initially injected violet resin

5.7.2 Channel/tow volume distribution

Studying the microstructure (and especially the channel/tow volume distribution and the local FVF) of the part for different textiles and different macroscopic fiber volume fractions may help defining the origin of the trends observed on the rinsing mechanisms. Images based on retroscattered electrons (to enhance the contrast between the glass fibers and the resin) have been made for the different samples. Moreover, post-treatment has been conducted in order to determine the channel/tow volume distribution and the local FVF. Using the software ImageJ, the images are first transformed into 8-bit images. Then, a

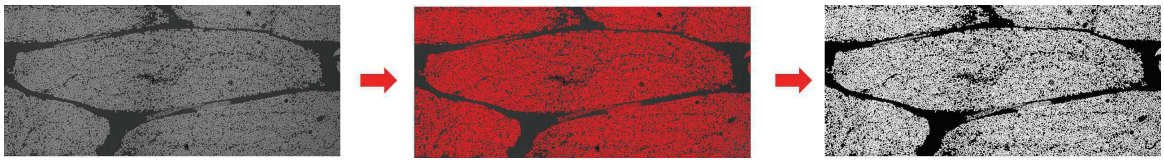

Figure 125: Steps of the binarization

threshold is determined to separate the grey levels corresponding to the fibers and the grey levels corresponding to the resin. Figure 125 presents this binarization step.

For channel/tow volume distribution, the image is then eroded once and a particle treatment is applied to fill the resin regions inside the tows. The remaining black area of each image represents then the section of the channels at the position of the cut in the sample. Figure 126 gives an overview of a micrographic image after this treatment. Results of the observations are reported in Table 26.

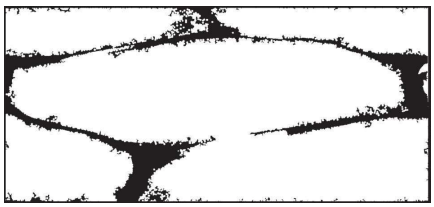

Figure 126: Image after deletion of resin rich areas inside the fiber tows

5.7.3 Microscopic local FVF measurement methods

The local FVF inside the fiber tows may have a significant influence on the resin flow pattern. Therefore, micro-scale FVF mappings have been conducted. Starting from the binarized image of the microstructure, the average pixel value, representing directly the FVF has been computed over window sizes from 5 pixels×5 pixels to 30 pixels×30 pixels for images exhibiting a resolution of 0.47 pixel/μm. Figures 127 and 128 presents the obtained results for the sample of Figures 125 and 126.

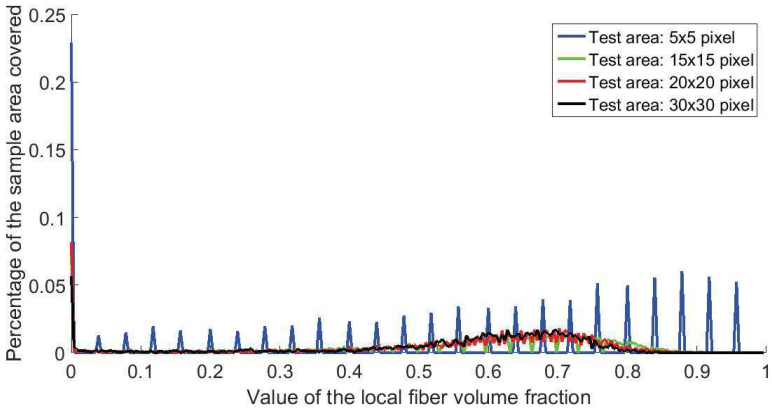

Figure 127: Distribution of the local fiber volume fraction of the UD sample shown in Figure 126

It can be observed from Figure 128 that the distribution of FVF in the considered sample converges for window sizes equal or larger than 20×20 pixels (42 μm×42 μm). Therefore, this value of window size has been used for all samples. The mapping of FVF obtained with the presented technique is presented in Figure 129.

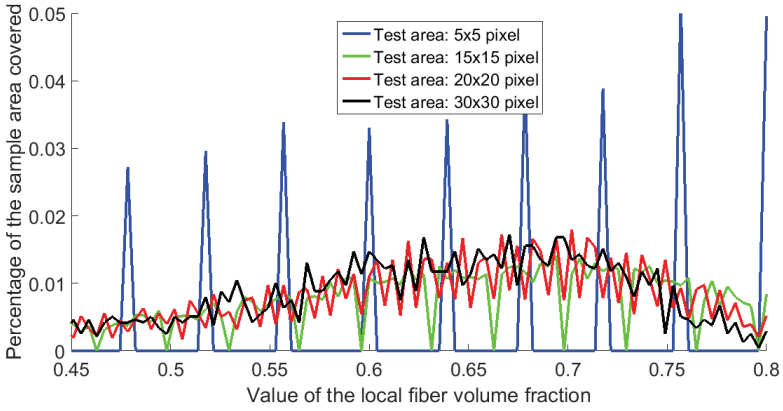

Figure 128: Detail of the fiber volume fraction distribution curve for $0.45 < \text{FVF} < 0.8$ of the UD sample shown in Figure 126

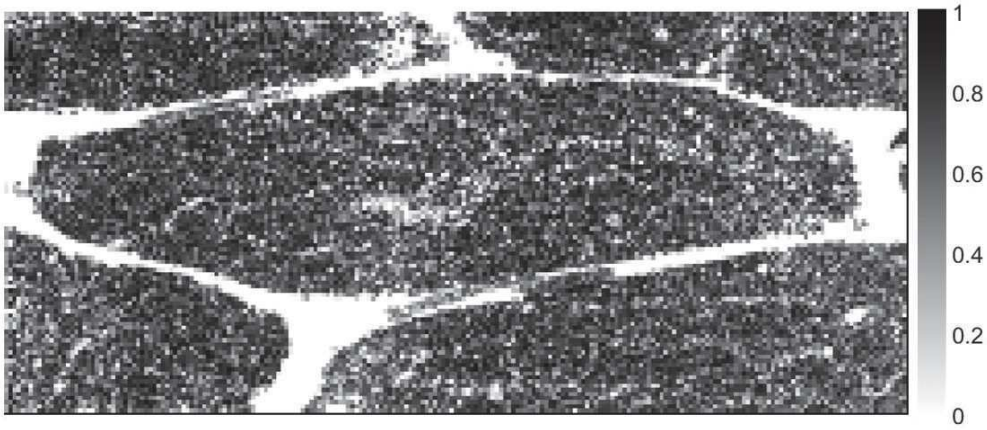

Figure 129: Mapping of the local fiber volume fraction of the UD sample shown in Figure 126 for a window size equal to 20×20 pixels

5.8 Design of experiment

The aims of these experiments are multiple:

- Corroborate the trends evolution observed in the quantitative intra-tow storage investigation
- Study the influence of compaction (FVF increase) on the channel/tow volume ratio
- Study the intra-tow local FVF characteristics of the different textiles at the different FVF
- Relate the microscopic analyses with the colorant distribution in the microstructure to define the origins of the trends observed in section 4.

Therefore, all textiles and FVF configurations studied previously have been reproduced for the UV-curing experiments. Moreover, for some configurations, the experiment has been frozen at several values of yellow injected mass of resin. Table 24 summarizes the realized design of experiments. Results are given hereafter. The Normalized injected volume is ratio of volume of yellow resin injected in the sample to the volume of resin required initially to saturate the sample. For example, a Normalized injected volume equal to 5 corresponds to the impregnation of the part (10 cm) with blue resin followed by the injection a volume of resin required to saturate 50 additional centimeters of reinforcement. The studied 10×10 cm sample can then be considered as the 10 first centimeters of a part measuring 60 cm.

UD				
FVF	**Fiber orientation**	**Direction of observation**	**Pressure**	**Normalized injected volume**
0.48	0°	0°	0.5 bar	5
0.51	0°	0°	0.5 bar	2
0.51	0°	0°	0.5 bar	5
0.51	0°	0°	0.5 bar	10
0.54	0°	0°	0.5 bar	5
Triaxial				
FVF	**Fiber orientation**	**Direction of observation**	**Pressure**	**Normalized injected volume**
0.52	0°/-45°/45°	0°	0.5 bar	2
0.52	0°/-45°/45°	0°	0.5 bar	5
0.52	0°/-45°/45°	0°	0.5 bar	10
0.59	0°/-45°/45°	0°	0.5 bar	2
0.52	0°/-45°/45°	0°	0.5 bar	5
Satin				
FVF	**Fiber orientation**	**Direction of observation**	**Pressure**	**Normalized injected volume**
0.52	0°/90°	0°	0.5 bar	2
0.52	0°/90°	0°	0.5 bar	5
0.56	0°/90°	0°	0.5 bar	5
0.56	0°/90°	90°	0.5 bar	5

Table 24: Design of experiment for micro-flow mechanisms investigation

6 Microscopic mechanisms investigation: Results

6.1 Validation of the macroscopic trends

Before investigating further the micro-scale flow mechanisms, the equivalence between the experiment presented in section 3 and the UV-curing experiments needs to be verified. Therefore, the proportion of each sample's area occupied by the violet resin has been measured and compared to the colorant concentration measured in the macroscopic experiment. Figure 130 presents the principle of this comparison.

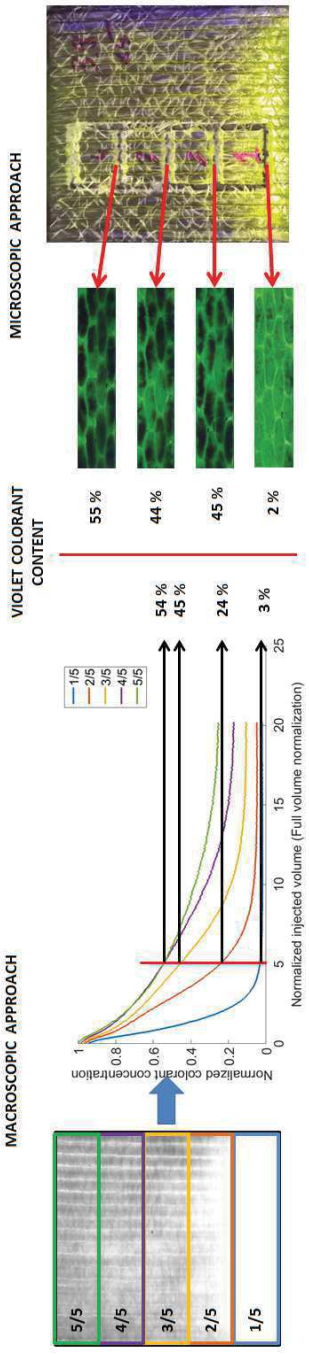

Figure 130: Principle of the comparison of the results of the macroscopic and microscopic trends investigation experiments

As in section 4.2.4, the sample of the macroscopic investigations is divided in five areas of analysis. The length of each area measures 20 mm starting form the bottom of the sample. On the other hand, the UV-cured samples have been cut at locations equal to 10, 30, 50 and 70 mm from the bottom of the sample. Thus, the value of colorant content in the samples of the UV-cured parts should be equivalent to the ones obtained from the discoloration curved of the four bottom areas of analysis for equivalent injected volumes. Results of the comparison are presented in Table 25.

Injected Normalized Volume	2	2	5	5	10	10
UD FVF=0.48			Macro	UV		
Location 1			24%	0%		
Location 2			45%	47%		
Location 3			52%	53%		
Location 4			53%	52%		
UD FVF=0.51	Macro	UV	Macro	UV	Macro	UV
Location 1	24%	50%	2%	0%	0%	0%
Location 2	62%	70%	24%	45%	19%	40%
Location 3	69%	71%	45%	44%	19%	40%
Location 4	75%	70%	55%	54%	31%	23%
UD FVF=0.54 (Nested)			Macro	UV		
Location 1			0%	0 %		
Location 2			15%	17%		
Location 3			32%	42%		
Location 4			39%	37%		
UD FVF=0.54 (Superposed)			Macro	UV		
Location 1			5%	2%		
Location 2			33%	58%		
Location 3			41%	57%		
Location 4			42%	62%		
Triaxial FVF=0.52	Macro	UV	Macro	UV	Macro	UV
Location 1	15%	21%	5%	1.5%	0%	0%
Location 2	25%	41%	11%	11%	0%	0%
Location 3	29%	45%	14%	21%	0%	0%
Location 4	31%	60%	15%	25%	0%	0%
Triaxial FVF=0.59	Macro	UV	Macro	UV		
Location 1	10%	3%	0%	0%		
Location 2	18%	26%	0%	0%		
Location 3	22%	31%	0%	0%		
Location 4	27%	36%	0%	0%		
Satin FVF=0.52	Macro	UV	Macro	UV		
Location 1	14%	25%	8%	0%		
Location 2	26%	29%	14%	12%		
Location 3	27%	34%	18%	16%		
Location 4	39%	35%	20%	33%		
Satin FVF=0.56			Macro	UV		
Location 1			12%	15%		
Location 2			18%	30%		
Location 3			23%	40%		
Location 4			26.5%	42%		

Table 25: Compared results of colorant content in the samples during macroscopic and microscopic (UV) experiments

It can be observed in Table 25 that for the majority of tested configurations, results of the macroscopic and UV experiments exhibit similar results. For all configurations (except for the Triaxial with FVF=0.52 and Normalized injected volume equal to 2, the UD with superposed tows at FVF=0.54 and Normalized injected volume equal to 5 and the Satin at FVF=0.56 and Normalized injected volume equal to 5), colorant content computed from the macroscopic investigations and observed in the microstructure exhibit maximal difference of 10%. Insofar as sample observation is a very local observation while the macroscopic investigation averages the value of concentration over 1/5 of the part, as threshold determination is a manual process, the obtained results can be considered as equivalent for the two experiments. This validates the equivalence of the experimental condition for the injection of model fluids and UV-curing resin. Therefore, the results obtained with the UV-cured parts will enable to study at the micro-scale the origins of the discoloration trends observed at the macro-scale in section 4.

The equivalence of experimental conditions between the macroscopic discoloration trends investigation experiment and the UV-curing experiments has been demonstrated. Thus, observations made at the micro-scale will enable to explain the trends observed in section 4.

6.2 Microstructure evolution versus FVF

Studying the evolution of the microstructure versus FVF for all materials could enable to determine the origins of the discoloration trends observed in section 4. Indeed, it has been observed in this former section, that for the NCF (Triaxial), increasing the FVF (reducing the thickness of the setup) induce a faster discoloration, but that it is the contrary for the Satin. In order to explain these phenomena, the evolution of the channel/tow volume distribution and intra-tow fiber volume fraction will be investigated.

6.2.1 Channel/tow volume distribution versus FVF

Using the technique presented in section 5.7.2, the SEM macro images of the different samples have been post-treated. Figures 131, 132 and 133 present the aspect of the microstructure with channels in black and tows in white.

Figure 131 presents the samples made of the UD reinforcement. It can be clearly noticed from these cuts that two types of tow distribution can be obtained during stacking: nested tows or tows above each other. However, no clear trend can be observed in terms of channel size evolution with compaction (thickness reduction between the maximal and minimal thicknesses is only 6% which leads to limited microstructure geometrical modifications that cannot be observed easily at first sight).

Figure 132 presents the cut samples made of the Triaxial reinforcement. The most noticeable difference between the sample at FVF=0.52 and the sample at FVF=0.59 is the reduction of the channels between the plies. Therefore, a reduction of the channel/overall area ratio is expected.

Figure 133 presents some of the images obtained by microtomography from the Satin samples observed at different thicknesses. It can be clearly seen from these images that the channel pattern is very complex and three-dimensional as no continuity can be observed from plane cuts.

Numerical values obtained from the analysis of the images presented in Figures 131, 132 and 133 are reported in Table 26. In this table, φ_c is reported for the UD and the Satin at various FVF. For the UD, cuts are made perpendicular to the channels so that the channel/overall area ratio is equal to the channel/overall volume ratio. For the Satin, the

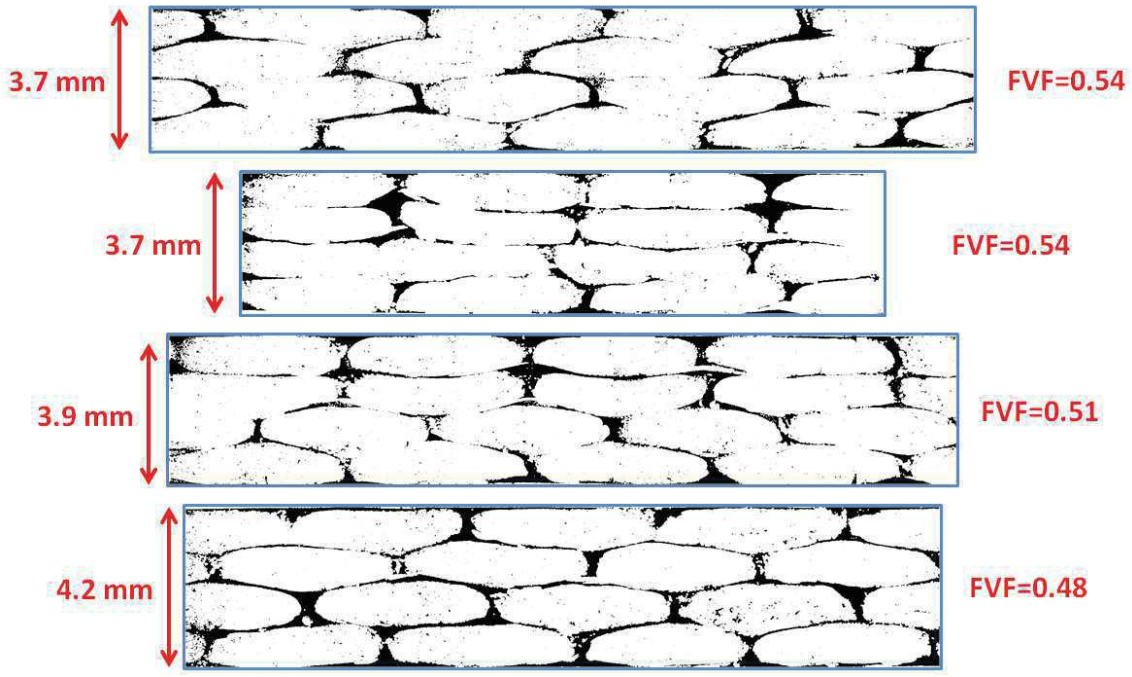

Figure 131: Channel/tow distribution in the UD samples at various macroscopic FVF obtained by SEM

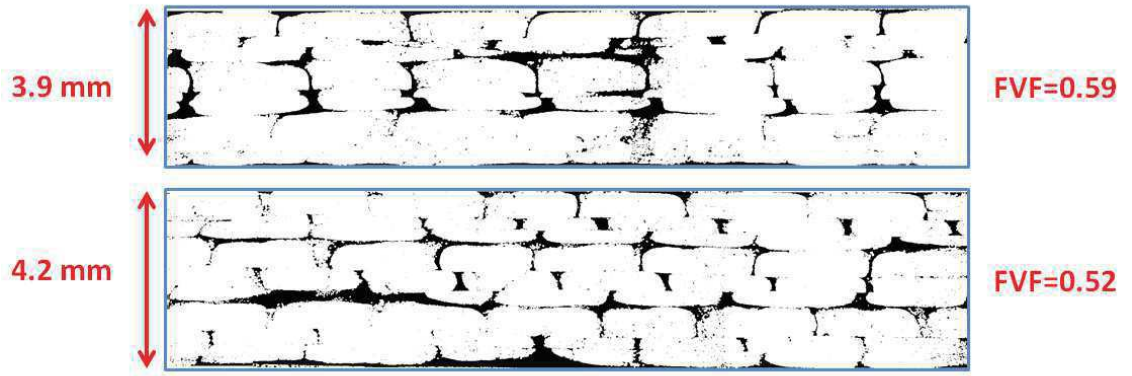

Figure 132: Channel/tow distribution in the Triaxial samples at various macroscopic FVF obtained by SEM

average value of channel/overall area ratio in the 190 images made in the thickness of the sample are averaged to obtain the value of φ_c. In the case of the Triaxial, however, tomography images have not been done. Therefore the reported values are the channel/overall area ratio in the cuts. This value differs from φ_c due to the + and - 45° channels that the material contains and whose cross section is overestimated by the observation of the cut. These values are not be comparable with the values of φ_c determined for the the other materials, however, they are comparable between each other for the two FVF values.

A clear trend can be noticed from Table 26, the cross section of the channels is reduced when the fiber volume fraction is increased. This observation can be done for all materials. The case of the UD is particular in the sense that when tows are superposed, the volume of channels is slightly higher than when nesting occurs for an equal average FVF. Additionally, it can be noticed that, values of φ_c are very similar for macroscopic FVF

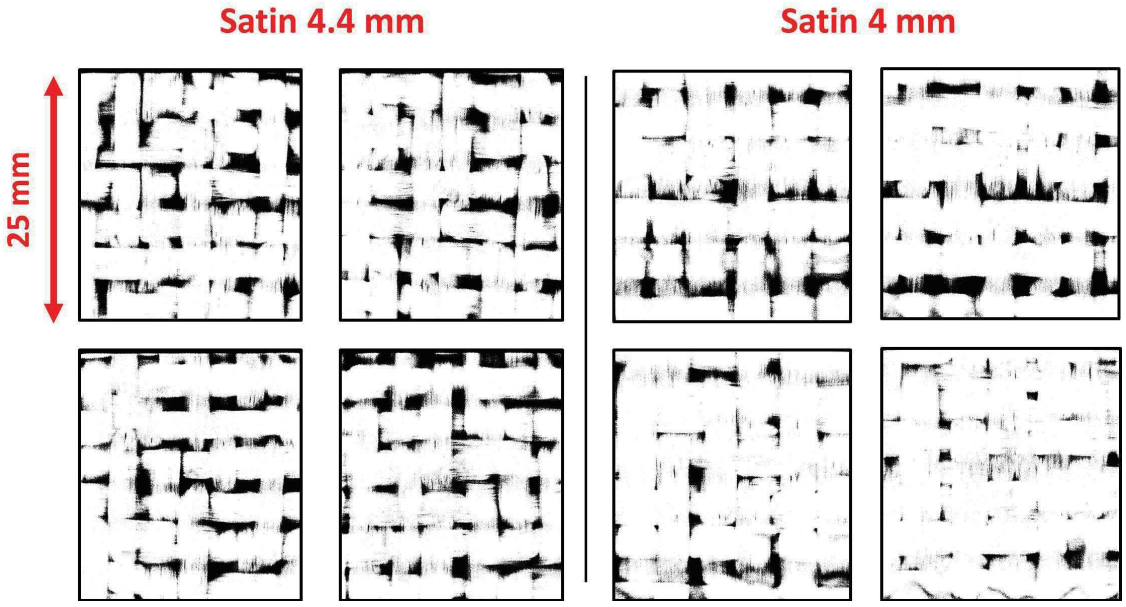

Figure 133: Channel/tow distribution in the Satin samples at various macroscopic FVF. Images obtained by micro-tomography obtained by micro-tompgraphy

UD	FVF=0.48	FVF=0.51	FVF=0.54 Nested
Channel/overall volume ratio (φ_c)	13%	10%	9%
Error	±1%	±1%	±1%
			Superposed
Channel/overall volume ratio (φ_c)			10%
Error			±1%
Triaxial		FVF=0.52	FVF=0.59
Channel/overall area ratio		10.5%	8%
Error		±1%	±1%
Satin		FVF=0.52	FVF=0.56
Channel/overall volume ratio (φ_c)		9%	8%
Error		±2%	±2%

Table 26: Channel to overall volume ratio (φ_c) for the various materials at the various FVF

values equal to 0.51 and 0.54. This could be a part of the explanation for the observations made in section 4.2.1 dealing with the discoloration kinetics where similar discoloration kinetics had been observed at these two FVF.
It can be finally noticed that the channel cross section reduction is limited to 1.5-4% which enduces FVF increases in the range of +1.5-4%. However, the macroscopic FVF increases are expected to be in the range of 4-7%. Therefore, intra-tow FVF is also expected to increase with compaction in order to match the macroscopic FVF.

The channel/overall volume ratio reduces with the reduction of the sample thickness (and thus the increase of the FVF). However this reduction is not the only mechanism inducing the increase of the macroscopic FVF. The evolution of intra-tow FVF needs also to be investigated.

6.2.2 Intra-tow FVF versus macroscopic FVF

Using the technique presented in section 5.7.3, the intra-tow local FVF can be calculated for the tows perpendicular to the cut direction of the samples. For all samples, the local intra-tow FVF of four to ten tows have been investigated. The values of average intra-tow FVF versus macroscopic FVF for these tows are presented in Table 27, as well as the standard deviation whithin each tow and between the tows of the same sample.

UD	FVF=0.48	FVF=0.51	FVF=0.54 Nested
Average intra-tow FVF	0.58	0.62	0.62
Standard deviation within the tows	11%	11%	11%
Standard deviation between the tows of the same sample	3.5%	3.6%	3.7%
			Superposed
Average intra-tow FVF			0.64
Standard deviation within the tows			11%
Standard deviation between the tows of the same sample			3.6%
Triaxial		FVF=0.52	FVF=0.59
Average intra-tow FVF		0.58	0.64
Standard deviation within the tows		10%	10%
Standard deviation between the tows of the same sample		6.5%	3.5%
Satin		FVF=0.52	FVF=0.56
Average intra-tow FVF		0.62	0.66
Standard deviation within the tows		10%	10%
Standard deviation between the tows of the same sample		4.7%	4.8%

Table 27: Intra-tow fiber volume fraction for the tows perendicular of the cutting direction of the samples for the different FVF

A clear trend can be noticed from Table 27: when the macroscopic FVF is increased, the intra-tow FVF increases too. This trend can be observed for all materials, the only exception being for the UD for which, similar average values of intra-tow FVF are observed for macroscopic FVF equal to 0.51 and 0.54. This highlights once again the issue of the respective locations of the tows in the UD stacking: for the same macroscopic FVF=0.54, when tows are superposed, the intra-tow locally recorded FVF is higher (equal to 0.64) than when tows are nested, (intra-tow FVF equal to 0.62). The phenomenon of higher intra-tow FVF values for the superposed tows of the UD are presented in Figure 134.

It can be seen in Figure 134 that the region of the tow located under an other tow features a high FVF while a region of the same tow present lower FVF values where it is not compacted. When tows are superposed, the regions of higher FVF are larger than when nesting occurs, which leads to higher intra-tow FVF in average. Similar cases of over-compaction are recorded in the Satin sample at macroscopic FVF=0.56. In some cases, tows can exhibit FVF values in the range of 0.70-0.75 at the location where multiple tow crossings are superposed. Figure 135 presents the typical FVF distribution in the tows of the Satin sample at FVF=0.56.

This phenomenon could explain the permanent storage observed in the Satin material. Indeed, in these over-compacted regions, local permeability could be so low that the flow velocity could become negligible once saturation is achieved.

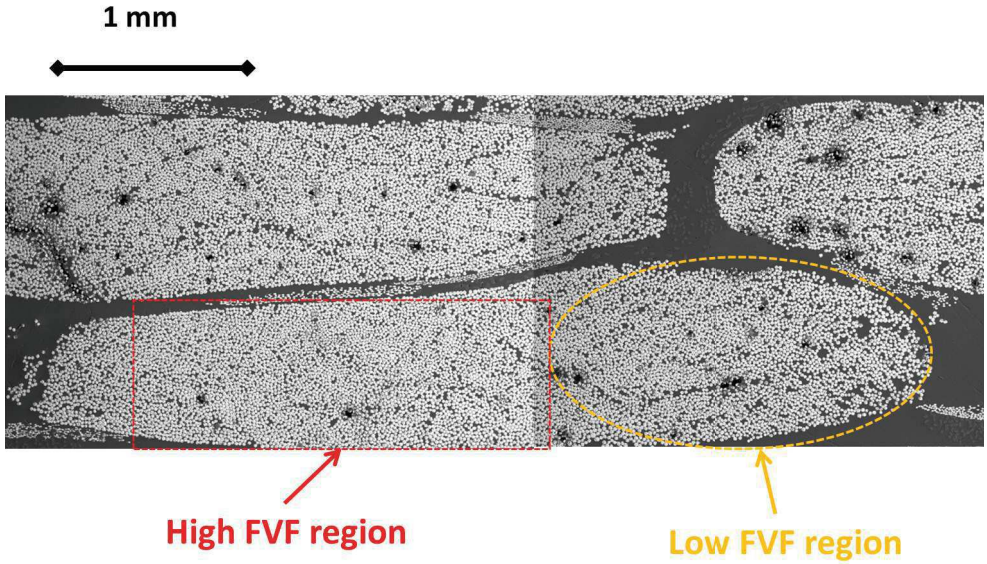

Figure 134: Example of a tow in a sample of UD at FVF=0.54. One side of the tow is squeezed by the above located tow generating a high FVF region while the free other side exhibits a lower FVF

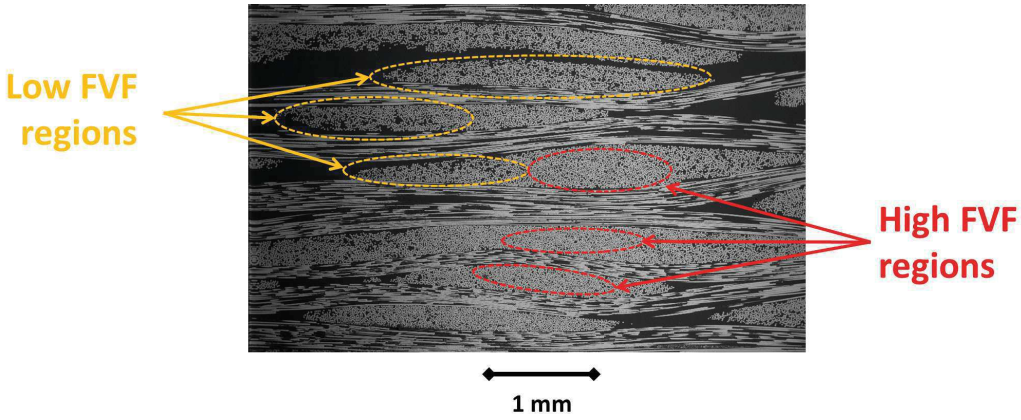

Figure 135: Cross section of a Satin sample at FVF=0.56. Some regions that are not compacted feature low intra-tow FVF while others compacted tows feature high FVF values

Furthermore, the study of the standard deviation within the tows reveals that its values is in the same range of ± 10% for all experiments. This value highlights the fact that the intra-tow FVF is not constant and that inside a fiber tows cohabit locally high and low FVF regions. These variations are small compared to the difference of porosity between the intra-tow region and the channel, and are not questionning the dual-scale porous character of the considered reinforcements, however, these variations could play a role in the micro-scale flow phenomena. It can be indeed expected that non-negligible flow occurs in the lowest FVF (high permeability) intra-tow regions.

The local intra-tow FVF has been reported to increase with the macroscopic FVF. However, the value of intra-tow FVF is not homogeneously distributed in the tows. Depending on the surrounding microstructure, the tows can feature higher of lower FVF values. Moreover, inside of the one single tow, standard deviation on the value of FVF is in the range of ± 10%. Therefore, faster or slower local microscopic flow velocities and thus higher or lower evacuation or storage are expected within the same tow. In order to investigate this aspect, a correlation between the observed location of violet resin and the local intra-tow FVF will be conducted.

6.3 Identification of micro-scale flow mechanisms

6.3.1 Correlation between violet resin location and local intra-tow FVF

At the end of section 4, the hypothesis has been formulated, that longitudinal intra-tow flow may occur during injection. In order to validate this assumption, mappings of intra-tow colorant locations and mappings of local FVF have been made for the same tows. The aim of this approach is to compare the colorant rich regions and the high FVF regions. If a longitudinal intra-tow flow occurs, it is expected that Violet colorant will be evacuated first from low FVF regions. In Figure 136, the comparison is conducted on a UD sample at FVF=0.48 and for a Normalized injected volume equal to 5. In order to reduce the potential influence of the upstream microstructure on the observed colorant concentration distribution, the studied sample is extracted from the part at location 1 (10 mm from the entry of the sample). Figure 136 compares the colorant distribution in 3 tows and the local FVF mapping in these same tows. The color scale has been adjusted to highlight in dark violet the high FVF regions that are more likely to store the resin. It can be thus noticed that the limit of FVF=0.6 has been chosen as it appears to be the limit between colorant rich and colorant poor regions.

Figure 137 presents the same comparison for a tow of the Triaxial material at macroscopic FVF=0.56 and for a Normalized injected volume equal to 2. As the tows at 10 mm from the sample entry are fully discolored, the observation is conducted on the cut made at 30 mm from the entry. Limit between Violet and Yellow on the scale has been placed at FVF=0.66.

It can be seen in Figure 136 that the colorant location in the tows exhibit complex patterns. Darker and lighter areas are spread heterogeneously within the fiber tows. The dark violet colored regions as well as the yellow colored regions can be located at any position in the tows, in the center or at the border. It can only be noticed that dark violet regions are more often located next to the region of contact between two tows. However, no trivial explanation can be given on this heterogeneous distribution when considering only the colorant distribution. But, when comparing the colorant rich regions and the high FVF regions, clear similarities appear. The colorant rich regions correspond approximately to the areas where the local FVF is greater than 0.6. The same observations can be made for the tow of the Triaxial material (Figure 137) with a limit of FVF at 0.66. In this context, the complex colorant distribution pattern and especially the fact that yellow resin is observed, surrounded by violet resin, in the center of some tows can only be explained by longitudinal intra-tow flow. The yellow resin observed in the center of the tows has flown inside of the tow through the lower FVF regions to reach the observation area. Thus flow does really occur longitudinally in the tows. It can be also added that the mechanisms inducing a higher violet colorant storage in the regions next to contact areas between tows is due to locally higher FVF (due to local compaction) and not to a longer distance to the channels.

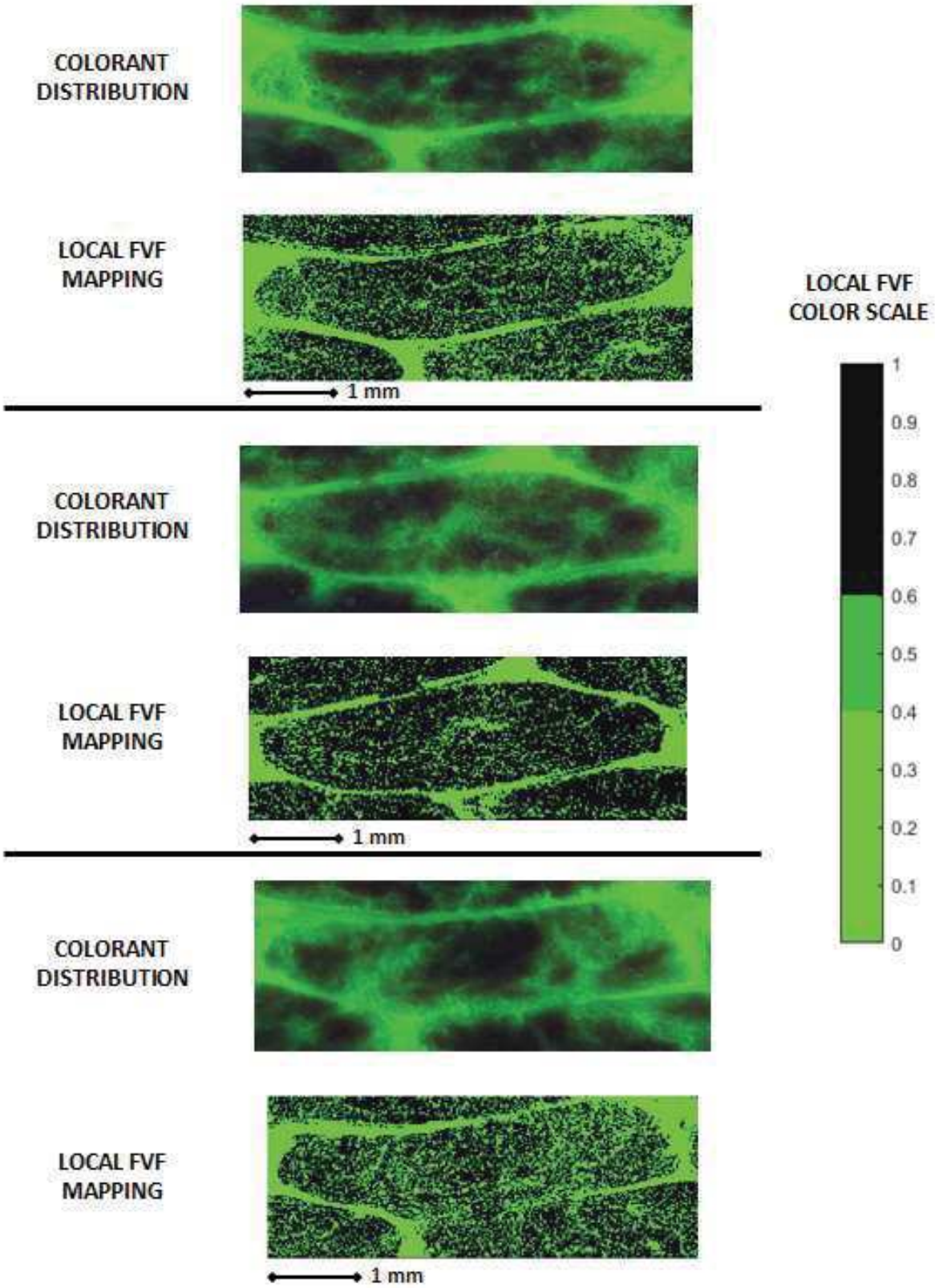

Figure 136: Comparison between intra-tow colorant distribution in the UD at FVF=0.48 at location 1 after 5 Normalized injected volumes and the intra-tow FVF

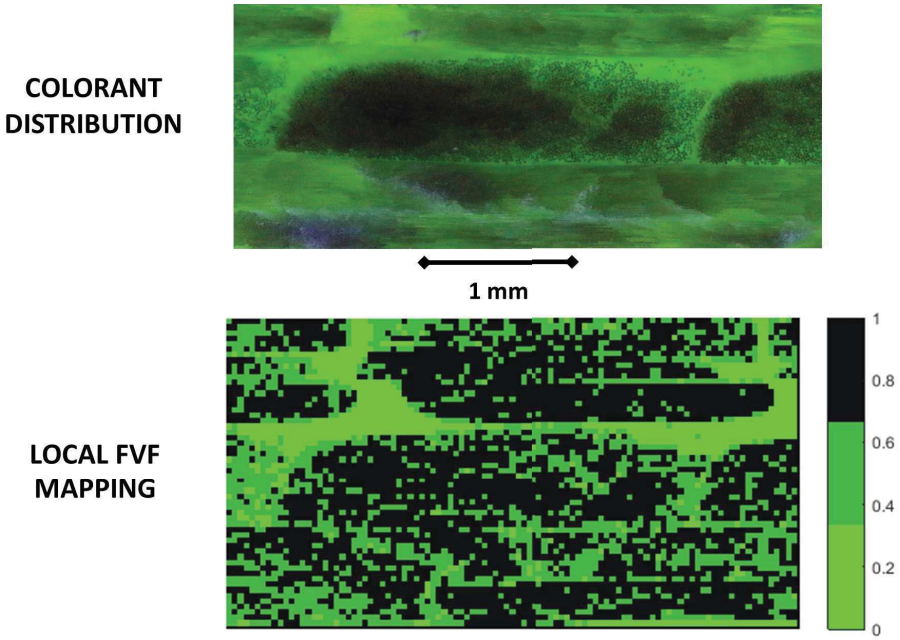

Figure 137: Comparison between intra-tow colorant distribution in the Triaxial at FVF=0.56 at location 2 after 2 Normalized injected volumes and the intra-tow FVF

Intra-tow discolorations at the entry of the samples can be considered as mainly driven by intra-tow longitudinal flow. The influence of other flow mechanisms (channel-tow fluid exchanges) will be investigated in the following sections.

6.3.2 Evolution of the intra-tow violet colorant content with distance from entry

The previous section aimed to determine relationships between intra-tow local FVF and violet colorant storage associated with the longitudinal intra-tow flow. In this section, the mechanism of out-of-principal flow direction colorant evacuation will be investigated. To do so, the violet colorant content and location will be studied inside of a single tow along the direction of flow (Figure 138). As tows are perpendicular to the observation direction, the same fiber tow has been cut at several distances from the entry, which allows evaluating its colorant content and distribution with increasing distance from the entry. Intra-tow discolorations observed away from the area of violet-yellow intra-tow front will be due to out-of-principal direction flow.

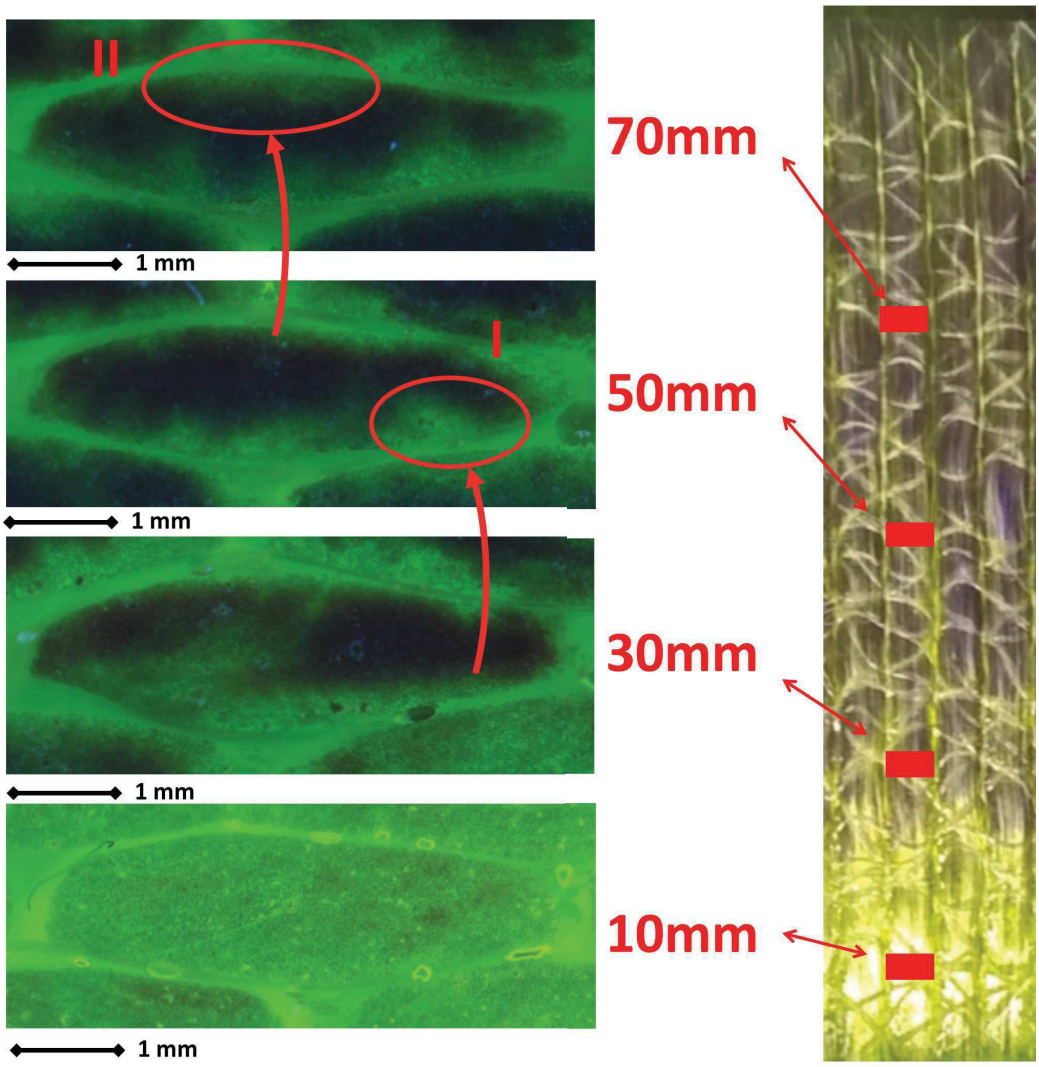

Figure 138: Micrographs of a single tow of the UD material at several distances from the entry of the sample (FVF=0.48 and Normalized injected volume = 5)

Figure 138 presents the aspect of the cross section of the same tow at 10, 30, 50 and 70 mm from the entry of a UD sample at FVF=0.48 after 5 Normalized injected volumes. It can be observed in Figure 138 that the tow is totally discolored at a distance of 10 mm from the entry of the sample. At 30 mm, yellow resin can be seen in the center of the tow. This location corresponds therefore to the region of yellow/violet intra-tow front. Beyond 30 mm, the intra-tow is still fully violet however, discolored area can be observed

at the periphery of the tow. These regions are distributed over the whole periphery of the tows. In a general manner, for the samples positioned at more than 30 mm from entry, if a location has been discolored, the same location in the downstream tow cross section are discolored. This is in good agreement with the observations made in the previous section: it has been indeed proven that intra-tow flow depends on the local FVF. Therefore, flow in the low FVF regions is faster. It is thus expected to find locations in the tow, downstream from the major Yellow/Violet front, where Yellow resin has already arrived through intra-tow flow. However, particular discolored regions (I, II, III and IV in Figures 138, 139 and 140) can also be identified. Their particularity lays in the fact that they seem to "appear" respectively at 50 and 70 mm from entry even if no particular discoloration is noticeable at 30 and 50 mm in these regions. This seems to mean that the discoloration of these regions is due to streamlines that locally do not follow the channel but interact with the tows. This mechanism is likely to be due to locally lower FVF regions. It can indeed be seen in Figure 139 that the discolored areas that "appear" in regions of the tow where upstream resin is still Violet correspond to lower FVF areas. Similar observation can be made for a tow of the Triaxial material at FVF=0.59 after the injection of 2 Normalized injected volumes in Figure 140.

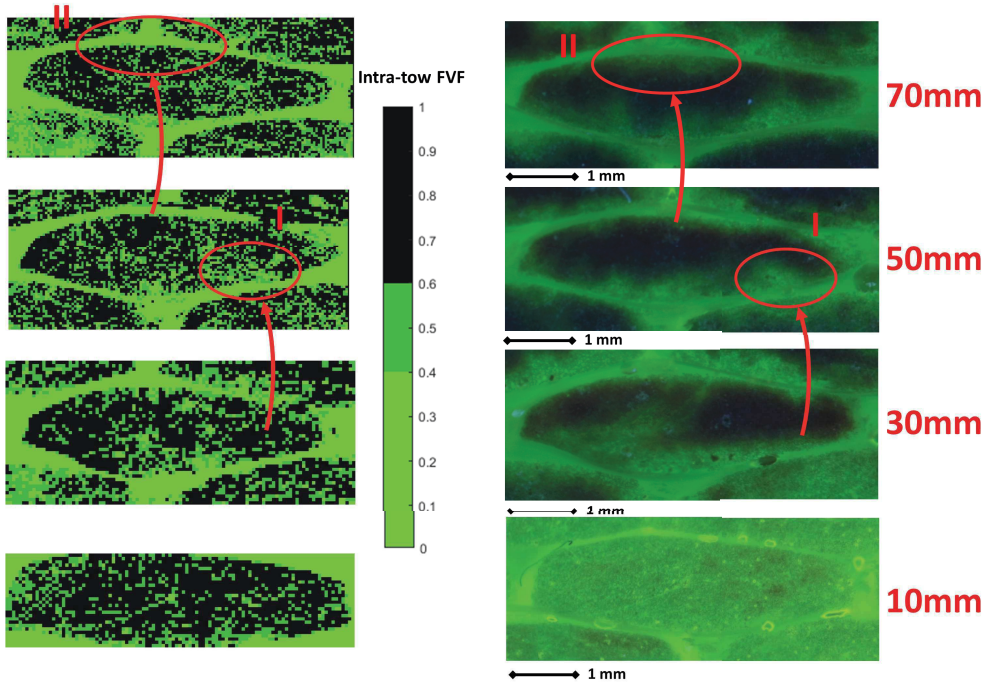

Figure 139: Micrographs of a single tow of the UD material at several distances from the entry of the sample (FVF=0.48 and Normalized injected volume = 5) and comparison with the local intra-tow FVF distribution

These two mechanisms (intra-tow flow in low FVF regions and local streamline deviations due to lower FVF regions) corroborates therefore the observation made in section 4 and explain the mechanisms inducing tow discoloration away from the major violet-yellow intra-tow. Figure 141 illustrates the principle of these two mechanisms.

Thus, the mechanisms inducing tow discoloration downstream from the major intra-tow yellow/violet front can be explained both by the intra-tow flow in the low FVF regions and by local FVF low regions that induce channel/tow flow. Further intra-tow longitudinal flow then contributes to evacuate the colorant downstream from the low FVF regions.

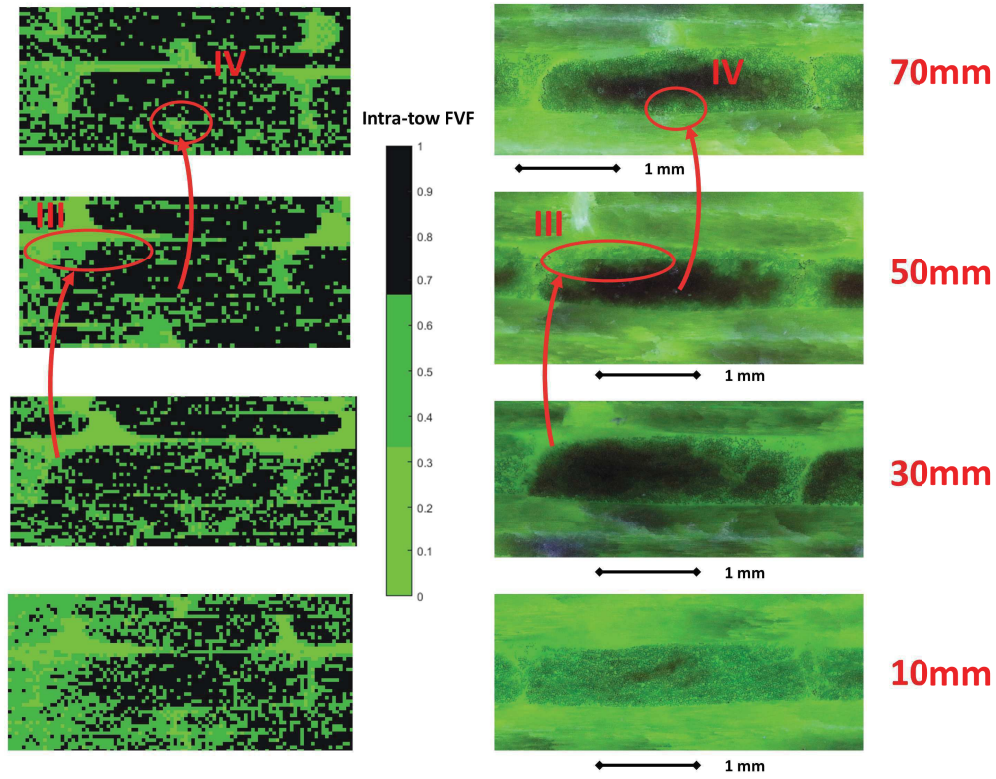

Figure 140: Micrographs of a single tow of the Triaxial material at several distances from the entry of the sample (FVF=0.59 and Normalized injected volume = 2) and comparison with intra-tow FVF distribution

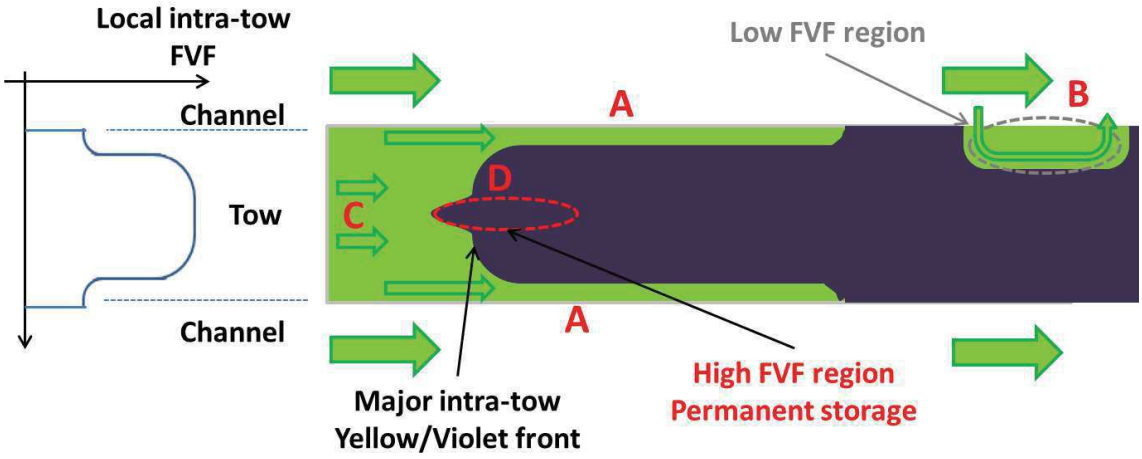

Figure 141: Micro-scale mechanisms involved in tow discoloration downstream from the major Yellow/Violet intra-tow front

6.4 Conclusions on micro-scale mechanisms investigation

In this section, the microstructural properties of the various materials have been investigated for various FVF values. It has been observed as expected that part thickness reduction (overall FVF increase) led to the reduction of the channel cross section but also an increase of the average intra-tow FVF. Additionally, a clear relationship has been established between the colorant location in the tows during rinsing and the local FVF distribution. Lower FVF regions are discolored faster that higher FVF regions. Moreover,

near the entry, discoloration occurs not only at the border of the tow but also in the center implying the presence of a longitudinal intra-tow flow. This mechanism is the most influencing mechanism of intra-tow colorant evacuation. It has been also observed, for tows aligned with the principal flow direction, that discolored region may "appear" at certain positions in the tows even if upstream region are still colored with the violet resin. This is related to locally lower FVF regions that might induce local channel-tow flow even in the saturated region. To conclude, it has been identified that intra-tow flow does occur. The majority of this flow occurs in the direction of the macroscopic however, local out of principal flow may occur due to local intra-tow FVF fluctuations. Therefore, in order to reproduce accurately the dual-scale flow, the assumption of permanent resin storage inside the tows should no longer be used and models featuring tows with a distribution of FVF values should be implemented in order to take the intra-tow flow accurately into account.

7 Macro and micro-scale analysis

In the previous sections, the flow mechanisms have been investigated separately at the macroscopic and microscopic levels. This allowed, on one hand, comparing the discoloration kinetics of several reinforcements for various textile architectures, FVF and fiber orientations highlighting the presence of three different flow mechanisms. On the other hand, the investigation of the microstructural properties of the samples highlighting the evolution of the microstructure with compaction (as well for the channels as for the tows). Additionally, a clear relationship between the intra-tow FVF distribution and the storage properties have been demonstrated. These observations highlight that saturated flow in a dual-scale porous material does not only occur in the channels but also in the tows. In this section, the trends observed in sections 4.2 and 6.2 will be coupled to the microstructure analysis to determine parameters characterizing the higher or lower intra-tow resin storage.

7.1 Average FVF calculated from micro-scale analysis

In order to validate the measured quantities, the average FVF calculated from the microscopic observations are compared with the theoretical values. Only the case of the UD is considered as it is the case for which the value of φ_c provides the greatest confidence. Equation 68 is used for this calculation. The calculated values are reported in Table 28.

$$FVF = 1 - (\varphi_c + (1 - \varphi_c)(1 - FVF_{micro})) \tag{68}$$

UD	FVF=0.48	FVF=0.51	FVF=0.54 Nested	FVF=0.54 Superposed
Calculated FVF from micro-scale analysis	0.50	0.56	0.56	0.58

Table 28: macroscopic fiber volume fraction calculated from φ_c and the intra-tow measure FVF

It can be observed in Table 28 that the FVF calculated from the microscopic observations features higher values than the theoretical values. An explanation can be given to explain this tendency. The intra-tow FVF has been measured in the center of the tows and did therefore not include in its calculation the lower FVF regions located at the border of the tows. These border regions where however considered as tow region in the calculation of φ_c. Thus, they contribute to reduce φ_c and are assumed to be filled with a FVF equal to the average value in the calculation. Also the FVF micro values have been obtained using

thresholding which induces potential deviations. For these reasons, the difference between theoretical and estimated FVF values from the micro-scale analyses can be considered as acceptable.

7.2 Dual-scale character of the samples

Using the results presented in section 6.2.2, it is possible to calculate the channel/tow permeability ratio as well as the pore volume ratio that are classically used to estimate the dual-scale character of a reinforcement. Gebart model [24] (hexagonal model with a fiber radius equal to 7 μm) is used to calculate intra-tow longitudinal and transverse permeabilities. Table 29 summarizes the values obtained for the various materials and configurations. The reported channel permeability K_c is the permeability in the 0° direction.

It can be noticed from Table 29 that channel/tow permeability ratio are in the range of 44 to 246 for the longitudinal direction and 120 to 650 in the transverse direction. Additionally, it can be observed that this ratio decreases with compaction. This result is physically correct as compaction tends to press tows against each other and reduce the size of the macroscopic gaps to the size of the microscopic gaps. The dual-scale feature tends to be reduced as compaction increases. Additionally, it can be observed that the UD is the material that features the highest $\frac{K_c}{K_t}$ ratio even at high compaction levels. This can be directly related to the observed trends of section 4. Indeed, the higher the permeability ratio, the hardest it will be for the fluid to be evacuated from the tows. In the same way, Triaxial and Satin feature comparable permeability ratios at FVF=0.52 with a slightly higer value for the Satin. This can be related to Figure 109 in which similar discoloration trends had been observed for these two materials at this FVF. Finally, a similar analysis can be conducted for the injection in the UD at 90° compared in Figure 113 to injections in UD samples at 0°. For the UD at 90°, K_c=3.42×10$^-$11m^2 while $K_{t\perp}$=4.52×10$^-$13 ^{2} leading to a permeability ratio of 76. This ratio is much smaller than any other ratio obtained for injections at 0° and it is observed that the discoloration is also the fastest in the 90° sample. It appears therefore that the permeability ratio is a good indicator of intra-tow storage. However, the geometric aspect of the microstructure is also likely to play a role in the storage or evacuation effects.

A good correlation between the channel/tow permeability ratio and intra-tow resin storage has been identified. Permanent storage is increasing with the $\frac{K_c}{K_t}$ ratio.

7.3 Local intra-tow FVF and longitudinal intra-tow front propagation

As presented in Table 25 and Figures 95, 96 and 97, total discoloration occurs at the entry of the UD and Triaxial samples. Using the results of the macroscopic trends investigation, it is possible to determine the velocity of the colored-plain fluid front inside of the tows. In this section the measured colored-plain fluid flow front velocity will be compared to the theoretical flow front velocity that would be observed in the tows considering an intra-tow permeability calculated using relationships derived by Gebart [24] (for hexagonal fiber distribution). The goal of this investigation is to confirm the assumption that longitudinal intra-tow flow is driven and can be modeled by a Darcy flow.

Experimental colored-plain fluid front velocity measurement

Using the picture obtained from the macroscopic trends investigations, the following treat-

UD	FVF=0.48	FVF=0.51	FVF=0.54 Nested	FVF=0.54 Superposed
Channel permeability K_c (m^2)	4.6×10^{-10}	2.16×10^{-10}	1.22×10^{-10}	1.22×10^{-10}
φ_c	13%	10%	9%	10%
Average intra-tow FVF	0.58	0.62	0.62	0.64
Pore volume ratio [51] (Equation11 in Part I)	3.88	5.58	6.27	5.76
Average longitudinal intra-tow permeability $K_{t\parallel}$ (m^2)	1.87×10^{-12}	1.20×10^{-12}	1.20×10^{-12}	9.7×10^{-13}
$\frac{K_c}{K_{t\parallel}}$	246	180	102	126
Average transverse intra-tow permeability $K_{t\perp}$ (m^2)	7.07×10^{-13}	4.52×10^{-13}	4.52×10^{-13}	3.56×10^{-13}
$\frac{K_c}{K_{t\perp}}$	650	478	270	344
Triaxial		FVF=0.52	FVF=0.59	
Channel permeability K_c (m^2)		1.42×10^{-10}	3.04×10^{-11}	
Average intra-tow FVF		0.58	0.64	
Average longitudinal intra-tow permeability $K_{t\parallel}$ (m^2)		1.87×10^{-12}	9.67×10^{-13}	
$\frac{K_c}{K_{t\parallel}}$		75	31	
Average transverse intra-tow permeability $K_{t\perp}$ (m^2)		7.06×10^{-13}	3.56×10^{-13}	
$\frac{K_c}{K_{t\perp}}$		202	85	
Satin		FVF=0.52	FVF=0.56	
Channel permeability K_c (m^2)		8.94×10^{-11}	5.20×10^{-11}	
φ_c		9%	8%	
Average intra-tow FVF		0.62	0.66	
Pore volume ratio [51] (Equation11 in Part I)		6.27	7.59	
Average longitudinal intra-tow permeability $K_{t\parallel}$ (m^2)		1.21×10^{-12}	7.66×10^{-13}	
$\frac{K_c}{K_{t\parallel}}$		74	44	
Average transverse intra-tow permeability $K_{t\perp}$ (m^2)		4.52×10^{-13}	2.77×10^{-13}	
$\frac{K_c}{K_{t\perp}}$		198	120	

Table 29: Permeability ratio and pore volume ratio for the considered textile configurations

ment is applied. The central area of the samples is selected and for each picture, the length (given by the arrow in Figure 142) from the sample entry over which the average concentration is below 1.2×10^{-5} mol/l (for fluid Gly1) is recorded and plotted versus Normalized injected volume. The principle of the treatment is presented in Figure 142.

Figure 143 and 144 summarizes the results obtained with fluid Gly1 respectively for the UD material at FVF=0.48, 0.51 and 0.54 and the Triaxial material at FVF=0.52 and 0.59.

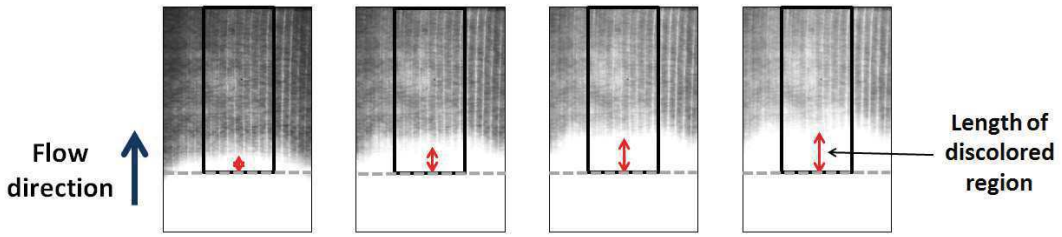

Figure 142: Principle of the measurement of the length of the discolored (white) area

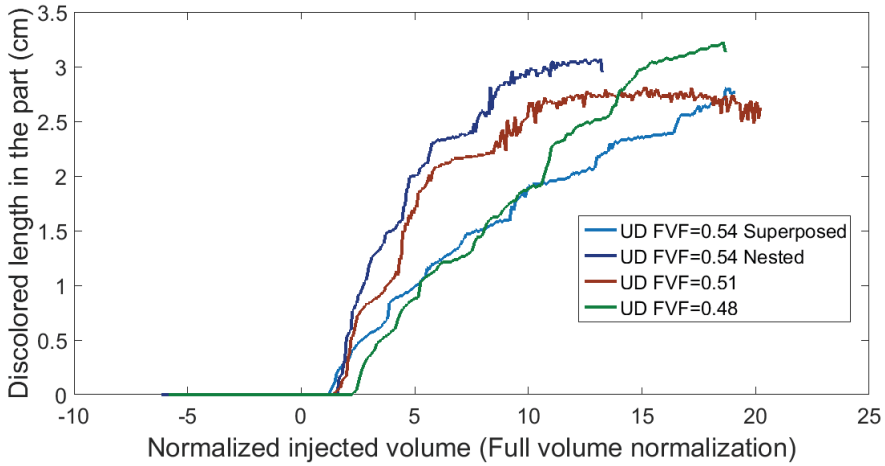

Figure 143: Evolution of the position of the colored-white interface in the fiber tows of the UD material

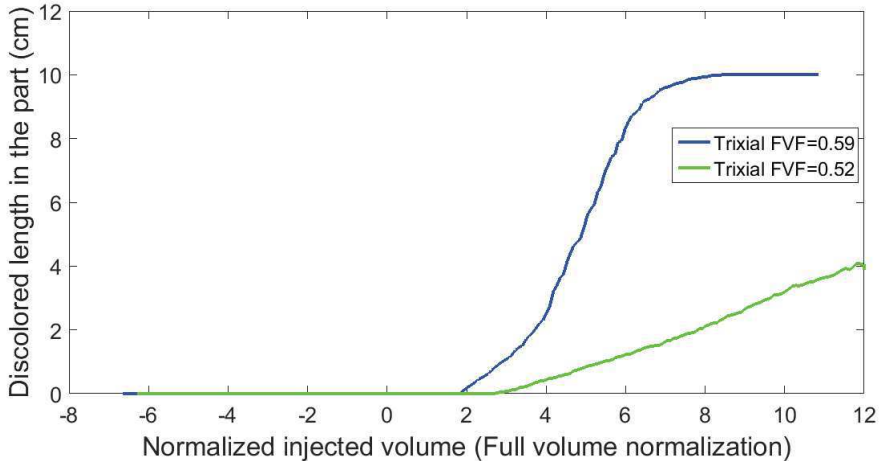

Figure 144: Evolution of the position of the colored-white interface in the fiber tows of the Triaxial material

Various trends can be observed. In Figure 143 (UD material), a two phase front propagation can be observed for all curves: during the first phase (below a discolored length equal to 2.5 cm), the length of the discolored area grows following an almost linear but irregular evolution. After 2.5 cm, the front propagation appears to slow down. This slowing down is principally observed for the high FVF materials (FVF=0.51 and FVF=0.54). For FVF=0.48 the length of the discolored area does not seem to have reached a steady value after 18 Normalized injected volumes.

On the other hand, the trends observed for Triaxial material (Figure 144) are different. For FVF=0.52, an almost linear increase of the length of the discolored area can be observed while for FVF=0.59, a two-slope curve has been obtained. Additionally for this FVF the length of the discolored area reaches 10 cm (the length of the sample), which means that the part is fully discolored after 8 Normalized injected volumes.

Intra-tow theoretical flow velocity calculation
The theoretical values of longitudinal intra-tow flow is calculated as follows:

$$\overrightarrow{v_{intra}} = \frac{K_{t_{\parallel}}}{K_c \times \phi_t} \times \frac{Q_{macro}}{A_{macro}} \tag{69}$$

In equation 69, $\overrightarrow{v_{intra}}$ is the intra-tow pore flow velocity, $K_{t_{\parallel}}$ is the longitudinal intra-tow permeability computed from Gebart equation (hexagonal fiber distribution) [24] using the measured value of intra-tow FVF. K_c is the macroscopic permeability determined from results presented in section 6.2.2 ϕ_t is the intra-tow porosity, Q_{macro} is the macroscopic flow rate and A_{macro} the cavity cross section. Table 30 summarizes the values of FVF, permeability, flow rates and cross section used for the calculations and Table 31 compares the values of front velocity measured from the experiments and the values expected from theoretical intra-tow flow with the applied conditions.

UD	FVF=0.54 V1 Nested	FVF=0.54 V2 Superposed	FVF=0.51	FVF=0.48
Intra-tow average FVF	0.62	0.64	0.62	0.58
Intra-tow average porosity ϕ_c	0.38	0.36	0.38	0.42
Macroscopic permeability K_c (m^2)	1.22×10^{-10}	1.22×10^{-10}	2.16×10^{-10}	4.6×10^{-10}
Intra-tow average longitudinal permeability $K_{t_{\parallel}}$(m^2)	1.2×10^{-12}	9.7×10^{-13}	1.2×10^{-12}	1.87×10^{-12}
$K_c/K_{t_{\parallel}}$	100	126	178	246
Volumic flow rate Q_{macro} (m^3/s)	3.31×10^{-6}	2.34×10^{-6}	2.96×10^{-6}	5.20×10^{-6}
Cavity cross section A_{macro} (m^2)	3.7×10^{-4}	3.7×10^{-4}	3.9×10^{-4}	4.2×10^{-4}
Triaxial	FVF=0.59	FV=0.52		
Intra-tow average FVF	0.64	0.58		
Intra-tow average porosity ϕ_c	0.36	0.42		
Macroscopic permeability K_c (m^2)	3.04×10^{-11}	1.42×10^{-10}		
Intra-tow average longitudinal permeability $K_{t_{\parallel}}$ (m^2)	9.67×10^{-13}	1.87×10^{-12}		
$K_c/K_{t_{\parallel}}$	31	75		
Volumic flow rate Q_{macro} (m^3/s)	1.49×10^{-6}	4.01×10^{-6}		
Cavity cross section A_{macro}(m^2)	3.7×10^{-4}	4.4×10^{-4}		

Table 30: Values used for the calculation of the theoretical intra-tow flow velocities in the UD and 0° tows of the Triaxial material

In Table 31, two scenarios have been envisaged for the calculation of the theoretical intra-tow longitudinal flow. Indeed, plain/blue or yellow/violet front in the tows will move forward with the speed corresponding to the lowest permeability regions. Therefore, the case of a flow moving forward in a tow exhibiting the homogeneous average FVF has been envisaged as well as the case of regions exhibiting the average FVF +10% (corresponding to the value of FVF plus the standard deviation).

It can be observed in Table 31 that the values of measured intra-tow flow velocities are in four cases out of six between the two theoretical values corresponding to FVF and FVF

UD	FVF=0.54 Nested	FVF=0.54 Superposed	FVF=0.51	FVF=0.48
Average intra-tow FVF	0.62	0.64	0.62	0.58
Theoretical intra-tow flow velocity v_{intra}^{theo}(FVF) (mm/s)	0.214	0.107	0.072	0.066
Average intra-tow FVF +10%	0.68	0.70	0.68	0.64
Theoretical intra-tow flow velocity v_{intra}^{theo}(FVF +10%) (mm/s)	0.098	0.047	0.033	0.039
Measured intra-tow front velocity v_{intra}^{meas} (mm/s)	0.033	0.053	0.049	0.069
Triaxial	FVF=0.59	FVF=0.52		
Average intra-tow FVF	0.64	0.58		
Theoretical intra-tow flow velocity v_{intra}^{theo}(mm/s)	0.253	0.219		
Average intra-tow FVF +10%	0.70	0.64		
Theoretical intra-tow flow velocity v_{intra}^{theo}(FVF+10%) (mm/s)	0.147	0.132		
Measured intra-tow front velocity (mm/s) v_{intra}^{meas}	0.160	0.081		

Table 31: Comparisons of measured intra-tow front velocities and theoretical intra-tow flow velocities

+10%. This result highlights the fact that the principle of considering an intra-tow flow governed by Darcy flow and the intra-tow longitudinal permeability is acceptable. Some explanations can be given for differences noticed between theoretical and measured values in the two other cases. First of all, the value FVF +10% does not, by definition of the standard deviation, correspond to the maximal intra-tow FVF. For this reason, locally higher FVF regions can generate a slower moving plain/blue fluid front. Moreover and as highlighted several times previously, the properties of the UD exhibit a certain variability. For this reason, the value of K_c that has been measured for a nested configuration is likely to underestimate the permeability for the superposed-tow case leading to an overestimated intra-tow flow velocity. In this context, the fact that four out of six comparisons feature agreeing results between calculation and measurement, provides some confidence and let think that the expected trend has been obtained. Figures 145 and 146 present some examples of experimental flow front propagation curves compared to the theoretical flow front propagation.

Close to the inlet and in the early times, intra-tow flow seems to be a Darcean flow.

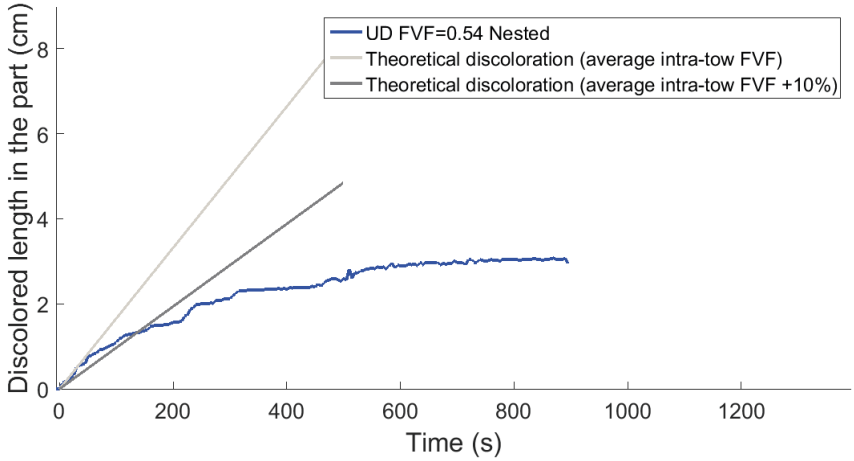

Figure 145: Comparison between measured and theoretical plain/blue fluid flow front progression in the UD at FVF=0.54

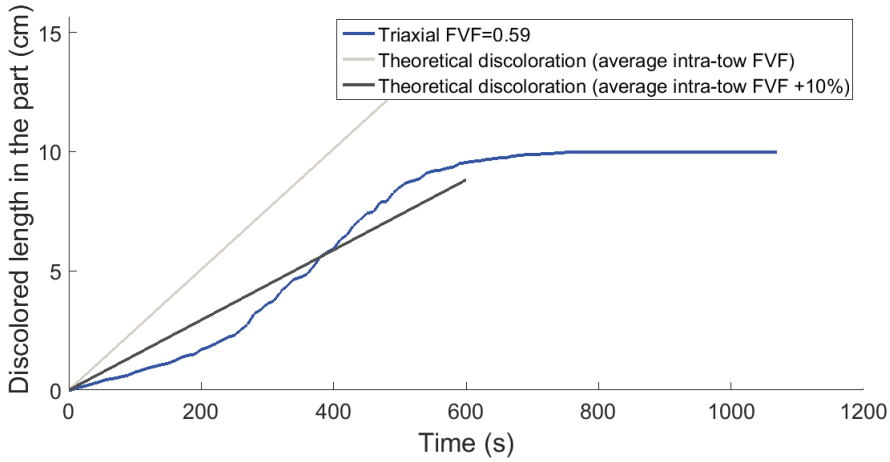

Figure 146: Comparison between measured and theoretical plain/blue fluid flow front progression in the Triaxial at FVF=0.59

8 Conclusions

In this chapter, a full experimental program based both on macroscopic and microscopic investigations have been conducted to understand and quantify the mechanisms involved in a fluid flow inside dual-scale porous materials. Starting from the principle of studying quantitatively and qualitatively the discoloration of a sample initially saturated with a colored fluid, two types of experiments have been conducted.

On one side, macroscopic observations have been made using model fluids in an experimental setup developed especially for this work. The colorant content of a sample initially saturated with a colored fluid has been tracked along the injection of a plain fluid. These macroscopic investigation allowed to compare the discoloration trends for three different textiles (an UD, a Triaxial and a Satin), at various FVF and for various fiber orientations. It has been established from these observations that the UD material was storing longer the colorant than the two other materials at the same FVF. Additionally, the storage capacity of the NCF textiles have been shown to reduce with increasing FVF, while for the Satin, similar discoloration trends have been observed for the considered FVF. Fi-

nally, fiber orientation and analysis of the discoloration of the samples over their length allowed to establish that three main flow mechanisms are involved in the discoloration of the samples:

- Channel flow
- Intra-tow flow in the direction of the macrocopic flow
- Channel/tow flow out of the direction of macroscopic flow

On the other hand, micro-scale flow mechanisms investigations have been conducted. Using the same setup and experimental conditions as for the macroscopic trends investigations, discolorations experiments have been run using a UV-curing resin. This allowed to stop the injection and freeze the resin and the colorant at its location at various times during injection. Good accuracy between the colorant contents obtained from this experiment and the macroscopic investigation has been obtained. Therefore, further investigation on the micro-scale flow mechanisms have been conducted. Evolution of the microstructure with compaction has been investigated to determine the evolution of the size of the channels and intra-tow FVF with increasing overall FVF. Channels have been shown to reduce in size with compaction and tows to exhibit higher internal FVF. Additionally, colorant concentration and intra-tow FVF has been compared exhibiting a clear relationship between the colorant rich and the high local intra-tow FVF regions. Intra-tow flow driven by the intra-tow FVF has thus been identified as the significant intra-tow flow mechanism. Additionally, and in a lower extent, local intra-tow lower FVF regions have been shown to generate channel-tow flow with a flow direction different of the macroscopic flow direction. Finally, macroscopic and microscopic investigations have been coupled to determine some trends. The channel/tow permeability ratio has been demonstrated to play a significant role in storage/evacuation of the colorant. Additionally, experimental intra-tow plain/colored fluid front velocity has been sucessfully compared with a theoretical Darcy flow inside of the tows using the longitudinal intra-tow permeability calculated from the intra-tow FVF.

To conclude, it has been observed in this chapter that intra-tow flow does occur in dual-scale porous materials. Macroscopic as well as microscopic investigations allowed to establish that three flow mechanisms are involved: channel flow, intra-tow flow in the direction of the macroscopic flow and channel-tow flow out of the macroscopic flow direction. These mechanisms are significant as colorant contents in the various experiments was reduced by 2 to 5 within the injection of 5 times the volume of the area of analysis. It appears therefore that classical dual-scale simulations that consider intra-tow storage as permanent are making significant errors in neglecting the intra-tow flow. It is therefore recommended to consider a simulation approach that would take the aspects of intra-tow flow and non permanent storage into account.

Conclusion and Perspectives

Conclusion

In the current context of growing introduction of the composite in the automotive industry, a deep look has been taken on the reactive RTM process with on-line mixing. The goal of this research program has been to investigate the mechanisms involved in this process when short cycle times are wished to be reached. This investigation has been conducted first through a literature review and then through numerical simulation and through experimental works.

Literature review revealed that only few studies have been conducted on the topic of RTM reactive injections in dual-scale porous materials. On the numerical aspects, the proposed solutions were very complex and CPU time consuming and therefore not suited for direct industrial applications. Considering experimental approaches, despite a certain number of works on single-scale reactive injections, only very few and qualitative experiments had been conducted on dual-scale reactive aspects. In this context, it had been decided to conduct both the development of a numerical tool allowing to simulate accurately, efficiently and in a flexible manner the dual-scale reactive RTM process with on-line mixing and to develop an experimental setup to conduct experimental investigations. The aim of this double investigation program was to investigate, with each tool, aspects that could not be carried out by the other. Thus, parameters influencing the length of the unsaturated area, and very local (intra-tow and channel) property distribution during a reactive injection with on-line mixing have been studied with the simulation tool while the micro and macro-scale flow mechanisms involved in dual-scale porous material has been investigated through experiments.
Regarding numerical aspects, a flexible numerical tool has been developed allowing the simulation of reactive injection with on-line mixing in single or dual-scale porous materials. New features making simulation more flexible and efficient have been developed in a view of an integration in the module PAM-RTM of the software ESI PAM-COMPOSITES.
The simulations conducted on this tool allowed to determine the following major conclusions:

- In isothermal injection conditions with constant injection flow rate, the influence of the unsaturated area on the injection pressure is negligible as soon as it is smaller than 1/5 of the length of the part
- In reactive conditions with a resin injected at the temperature of the mold and the fibers, the length of the unsaturated area has no significant influence on the injection pressure nor on the distribution of the quantities of interest in the part
- Reactive injections simulated in a single-scale or a dual-scale route feature very different results in terms of temperature, degree of cure and viscosity distribution, due to intra-tow resin storage
- The parameter φ_c (channel/overall volume ratio) has been shown to play a significant role in reactive injections. Indeed, viscosity increases have been reported to be higher in large channels than in small channels for materials featuring the same overall FVF.

Regarding experimental aspects, a new setup has been developed to allow the quantitative investigation of intra-tow resin storage during RTM injections in dual-scale porous materials. These macro-scale investigations have been coupled with micro-scales investigations conducted on UV-cured parts realized in the same experimental conditions. Once coupled, the results of the macroscopic and microscopic investigations allowed determining

the mechanisms involved in intra-tow resin storage or evacuation.
The major results obtained from the experimental investigations are listed below:

- Intra-tow resin storage is non permanent contrary to the classical assumption formulated in the literature
- For all materials, increasing the FVF reduces the size of the channels and increases the intra-tow FVF. This induces for NCF a decrease and for woven materials a increase of the intra-tow storage.
- Intra-tow resin storage depends significantly on fiber orientation regarding flow direction
- Intra-tow resin storage is clearly linked to the K_c/K_t ratio associated to the considered flow direction
- Three mechanisms generate resin evacuation of a saturated sample:
  - Channel flow
  - Intra-tow flow in the direction of the principal flow
  - Channel-tow flow out of the principal flow direction
- Intra-tow flow is a Darcean flow

These investigations have provided new knowledge and quantification of the mechanisms involved in the RTM process with on-line mixing but also raised new questions and needs. These will be discussed in the following section.

Perspectives

The conclusion formulated in this work have provided, thanks to experiments numerical simulations, knowledge on mechanisms influencing the high speed reactive RTM process with on-line mixing. These results should now be either used or deeper investigated. Several perspectives can be given as well on the numerical as on the experimental aspects. Numerical perspectives are listed below:

- As revealed by the experiments, intra-tow storage is not permanent. A numerical solution should therefore be proposed in order to treat this release.
  This implementation would require to introduce tow-tow resin exchange between neighbor elements but also channel-tow and tow-channel fluid exchange in the saturated area. The respective influence of tow-tow versus channel-tow and tow-channel volume exchange should be governed by the direction of the principal flow regarding the direction of the tows.
- The necessity of simulating the unsaturated area should be accurately considered. This transient micro-scale mechanism is computationally expensive and the unsaturated area has been shown to play only a minor role as well in isothermal as in reactive conditions.
  This conclusion has been made considering isothermal and reactive conditions without the formation of air bubbles. In order to go further into the details of the process, the aspect of air entrapment could be considered. However, for high flow velocities, porosities have been reported to be in the range of some percents ([38]) which would still be acceptable for automotive applications.

- In order to provide a simple to implement solution for dual-scale flow, a simplified single-scale model including the influencing sink and source terms could be developed in a first time.
- Taking these aspects into account, implementation of the dual-scale flow with on-line mixing should be conducted in the industrial PAM-RTM solver.

Experimental perspectives are listed below:

- Temperature and pressure monitored reactive injections with on-line mixing should be conducted in order to validate the numerical model.
  These experimental experiments could be compared to simulations assuming permanent intra-tow storage or taking intra-tow flow into account.
- Using the macrosopic technique presented in section 3 of part III, discolorations of one single ply could be studied to to observe flow mechanisms. Reducing the number of plies to one could allow a better observation compared to the 3- to 10-plies stacks used in this study.
- A simple testing methodology should be proposed to characterize the reinforcements and detemine its storage capacity in order to perform the appropriate simulation of the process

Appendix

Calculation of numbers and equivalent length of tows in the elements

One of the claims of the developed method is its ability to calculate automatically the number and average length of tows contained in each element depending on the size and shape of the element but also on the geometrical characteristics of the textile. The calculation steps of these determinations will be presented here.

For this demonstration, the reinforcement is a unidirectional material (the same approach needs to be conducted on each layer if the material is mutliaxial). The width of a repetitive cell has value b and tows are oriented with an angle γ to the x axis. The position of the nodes of the element are assumed known (Figure 147).

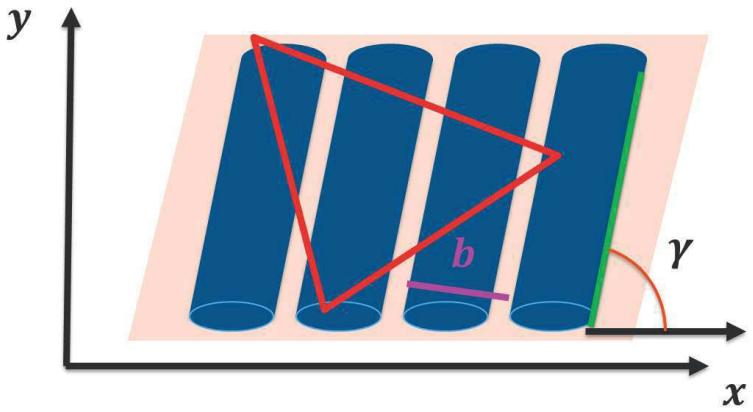

Figure 147: Considered element and characteristics of the unidirectional material

Two quantities must be determined for the further calculations: the average length of the tows in the element and the number of tows in the element.

The calculation of the average length of the tows in the element is made by calculating the length L in Figure 148. This length is the longest distance from a node to the opposite segment in the direction parallel to the tows and is determined thanks to trigonometric analysis. The average length of the tows in the element is simply $\frac{L}{2}$.

The technique to calculate the number of tows in the element is presented in Figure 149. Supposing the width b of the repetitive cell of the material known from experimental measurement, the length B is calculated from the known position of the nodes of the element. B represent the width of the element projected on the direction perpendicular to the tows. Dividing B by b allows therefore to determine the number of unit cells contained in the element. This value is however a real number. Therefore, a short calculation is made to estimate the closest number of tows or half tows to the ratio $\frac{B}{b}$. If the number of tows is slightly higher than the real ratio $\frac{B}{b}$, the length of the tows is reduced to ensure the appropriate FVF in the element. If the number of tows is smaller that the ratio $\frac{B}{b}$, the length of the tows is slightly increased.

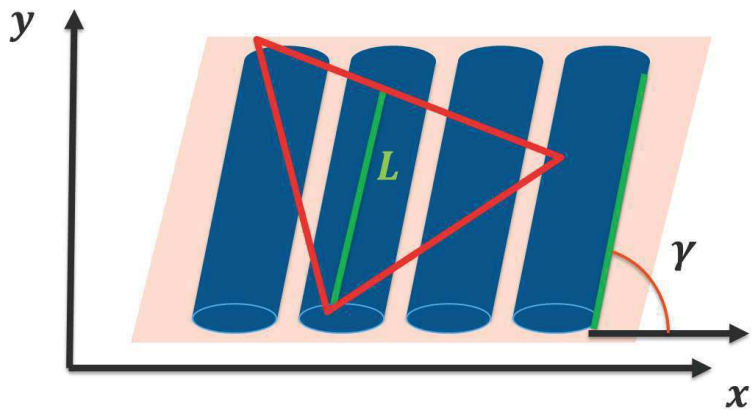

Figure 148: Determination of the average length $\frac{L}{2}$ of the tows

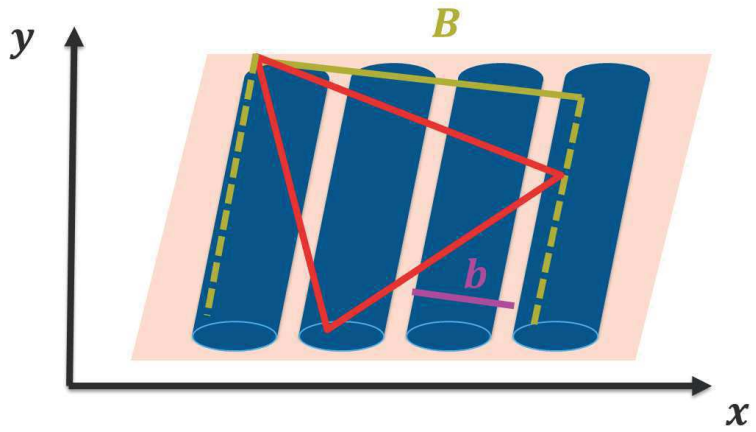

Figure 149: Determination of the number of tows in the element

With this technique it is therefore possible to determine the number and average length of tows in each element, whatever fiber orientation or the size of the element. The method can be extended to multiaxial materials by treating each direction after the other.

Nomenclature

The various notations used in this work are summarized in the following Table 32.

a, b	Major, minor semi axis of ellipse	K_t,$K_\perp$	Tow transverse permeability
A_i	Cross section of region i	L_{imp},S_{imp},V_{imp}	Impregnated tow length, surf., vol.
α	Degree of cure	l_ϵ	Characteristic pore dimension pore
α_g	Degree of cure at gel point	L_{tow}, S_{tow}	Length and surface of the tow
Bc	Boundary source term	m and n	Parameters of the Kamal model
C	Coefficient advection equations	mu	Viscosity of the fluid
c	Parametre model Gebart	mu_g	Viscosity at the glass transition
C_a	Capillary number	$n1$, $n2$	Nb of tows in directions 1 and 2
C_p	Heat capacity	P	Pressure
C_1,C_2	Coefficients of the WLF model	P_{av}	Average pressure in an element
C_I	Parameter for Gebarts model	ϵ	Porosity
D	Constant for Pusatcioglus model	phi^*	Shape function
Δt	Time step	φ_c	Channel/overall volume ratio
δ	Test function saturated elements	ψ	Sink index
ds	subscript for dual-scale quantity	Q	Flow rate
E, F	Constants Castro-Macoscko model	Q_{abs}	Flow rate of tow absorption
e	Considered element	R	Constant of ideal gases
E_a,E_μ	Energies of activation	rf	Radius of the fiber
γ_{st}	Surface tension	ρ_i	Density of the medium i
γ	Pore volume ratio	S^T, S^α	Sink-source for Temp./Deg. of cure
H	Enthalpy	S_I	Flow sink term
H_t	Enthalpy of the reaction	ss	Subscript for single scale quantity
I	Fluid filing factor	S_{tot1}, S_{tot2}	Surface of 1 tow in dir. 1 and 2
I_{th}	Limit for filled elements	T	Temperature
k	Heat conductivity	T_g0	Glass transition temperature
k_{KC}	Kozeny Carman constant	θ	Fiber-resin contact angle
K	Permeability	v	Fluid velocity
K_{mu}	Pre exponential factor	V_i	Considered volume
$K_\parallel$	Tow longitudinal permeability	v_{pore}	Pore fluid velocity
k_1,k_2	Arrhenius rate coefficients	V_1, V_2	Volumes of fluid
K_c	Channel permeability	V_{alpha}	Parameters for Gutowskis model
k_{ii}	Parameters for Gutowskis model	Vf	Fiber volume fraction
K_{ii}	Permeability in Gutowskis model	Vf_{max}	Maximal FVF

Table 32: List of notations used in this work

The various subscripts used in this work are summarized in Table 33.

c	Channel	out	For fluid exiting an element
ds	Dual-scale	r	Resin
f	Fiber	ss	Single-scale
in	For fluid entering an element	t	Tow

Table 33: List of subscripts used in this work

References

[1] Emmanuelle Abisset-Chavanne and Francisco Chinesta. Toward an optimisation of the reactive resin transfer molding process: thermo-chemico-mechanical coupled simulations. *International Journal of Material Forming*, 7(2):249–258, 2014.

[2] KJ Ahn, JC Seferis, and JC Berg. Simultaneous measurements of permeability and capillary pressure of thermosetting matrices in woven fabric reinforcements. *Polymer composites*, 12(3):146–152, 1991.

[3] Vincenza Antonucci, Michele Giordano, Kuang-Ting Hsiao, and Suresh G Advani. A methodology to reduce thermal gradients due to the exothermic reactions in composites processing. *International journal of heat and mass transfer*, 45(8):1675–1684, 2002.

[4] Eric Arquis. Ecoulements capillaires et chargés dans les procédés d'élaboration de composites par aps et rmi. *S01 Modélisation avancée en mécanique des solides et des fluides*, 2015.

[5] Arthur Babeau, Sébastien Comas-Cardona, Christophe Binetruy, and Gilles Orange. Modeling of heat transfer and unsaturated flow in woven fiber reinforcements during direct injection-pultrusion process of thermoplastic composites. *Composites Part A: Applied Science and Manufacturing*, 77:310–318, 2015.

[6] Baiju Z Babu and Krishna M Pillai. Experimental investigation of the effect of fiber-mat architecture on the unsaturated flow in liquid composite molding. *Journal of Composite Materials*, 38(1):57–79, 2004.

[7] Simon Bickerton, Hubert C Stadtfeld, Karl V Steiner, and Suresh G Advani. Design and application of actively controlled injection schemes for resin-transfer molding. *Composites Science and Technology*, 61(11):1625–1637, 2001.

[8] Francois Boinot and Alain Gurliat. Moulage par injection de résine à basse pression ou procédé rtm. *Techniques de l'ingénieur. Plastiques et composites*, (A3728):A3728–1, 1991.

[9] Poulikakos D Boomsma, K. The effects of compression and pore size variations on the liquid flow characteristics in metal foams. *Journal of fluids engineering*, 124:263–272, 2002.

[10] Joel Breard, Abdelghani Saouab, and Guy Bouquet. Numerical simulation of void formation in lcm. *Composites Part A: Applied Science and Manufacturing*, 34(6):517–523, 2003.

[11] MV Bruschke and Suresh G Advani. A finite element/control volume approach to mold filling in anisotropic porous media. *Polymer composites*, 11(6):398–405, 1990.

[12] Phillip C Carman. Fluid flow through granular beds. *Transactions-Institution of Chemical Engineers*, 15:150–166, 1937.

[13] JM Castro and CW Macosko. Studies of mold filling and curing in the reaction injection molding process. *AIChE Journal*, 28(2):250–260, 1982.

[14] Albert W Chan and Sun-Tak Hwang. Modeling nonisothermal impregnation of fibrous media with reactive polymer resin. *Polymer Engineering & Science*, 32(5):310–318, 1992.

[15] Mourad Chohra, Suresh G Advani, Ali Gokce, and Shridhar Yarlagadda. Modeling of filtration through multiple layers of dual scale fibrous porous media. *Polymer composites*, 27(5):570–581, 2006.

[16] Sébastien Comas-Cardona, Christophe Binetruy, and P Krawczak. Unidirectional compression of fibre reinforcements. part 2: A continuous permeability tensor measurement. *Composites Science and Technology*, 67(3):638–645, 2007.

[17] Sébastien Comas-Cardona, Saeed Ziaee, and Suresh G Advani. Spatially homogeneous gelation in liquid composite molding. *Polymer engineering and science*, 42(8):1667, 2002.

[18] Raymond Comolet and Jean BONNIN. Mécanique expérimentale des fluides. 1964.

[19] TR Cuadrado, J Borrajo, RJJ Williams, and FM Clara. On the curing kinetics of unsaturated polyesters with styrene. *Journal of Applied Polymer Science*, 28(2):485–499, 1983.

[20] M Deléglise, P Le Grognec, C Binetruy, P Krawczak, and B Claude. Modeling of high speed rtm injection with highly reactive resin with on-line mixing. *Composites Part A: Applied Science and Manufacturing*, 42(10):1390–1397, 2011.

[21] Mathieu Devillard, Antoine Laut, and Suresh G Advani. On-line mixing during injection and simultaneous curing in liquid composite molding processes. *Polymer composites*, 26(1):74–83, 2005.

[22] JA García, Ll Gascón, Francisco Chinesta, E Ruiz, and F Trochu. An efficient solver of the saturation equation in liquid composite molding processes. *International journal of material forming*, 3(2):1295–1302, 2010.

[23] L Gascón, JA García, F LeBel, E Ruiz, and F Trochu. A two-phase flow model to simulate mold filling and saturation in resin transfer molding. *International Journal of Material Forming*, 9(2):229–239, 2016.

[24] BR Gebart. Permeability of unidirectional reinforcements for rtm. *Journal of composite materials*, 26(8):1100–1133, 1992.

[25] B Gourichon, C Binetruy, and P Krawczak. Experimental investigation of high fiber tow count fabric unsaturation during rtm. *Composites Science and Technology*, 66(7):976–982, 2006.

[26] B Gourichon, C Binetruy, and P Krawczak. A new numerical procedure to predict dynamic void content in liquid composite molding. *Composites Part A: applied science and manufacturing*, 37(11):1961–1969, 2006.

[27] T G Gutowski, Z Cai, S Bauer, D Boucher, J Kingery, and S Wineman. Consolidation experiments for laminate composites. *Journal of Composite Materials*, 21(7):650–669, 1987.

[28] M. Healey and R. Johnsen. Non-crimp fabrics, June 17 2004. US Patent App. 10/466,673.

[29] Yann Henzel, Joël Bréard, Patrick Faitout, David Cayeux, and Raymond Gauvin. Dynamique des écoulements en milieux poreux double échelle. *Comptes Rendus de l'Académie des Sciences-Series IIB-Mechanics-Physics-Astronomy*, 327(11):1171–1177, 1999.

[30] Yi Hou, Sébastien Comas-Cardona, C Binetruy, and Sylvain Drapier. Gas transport in fibrous media: Application to in-plane permeability measurement using transient flow. *Journal of Composite Materials*, 47(18):2237–2247, 2013.

[31] M Ivankovic, Loredana Incarnato, Jose Maria Kenny, and Luigi Nicolais. Curing kinetics and chemorheology of epoxy/anhydride system. *Journal of Applied Polymer Science*, 90(11):3012–3019, 2003.

[32] MR Kamal and S Sourour. Kinetics and thermal characterization of thermoset cure. *Polymer Engineering & Science*, 13(1):59–64, 1973.

[33] KN Kendall and CD Rudd. Flow and cure phenomena in liquid composite molding. *Polymer composites*, 15(5):334–348, 1994.

[34] JM Kenny, A Maffezzoli, and L Nicolais. A model for the thermal and chemorheological behavior of thermoset processing:(ii) unsaturated polyester based composites. *Composites Science and Technology*, 38(4):339–358, 1990.

[35] Jeffrey M Lawrence, Valentin Neacsu, and Suresh G Advani. Modeling the impact of capillary pressure and air entrapment on fiber tow saturation during resin infusion in lcm. *Composites Part A: Applied Science and Manufacturing*, 40(8):1053–1064, 2009.

[36] François LeBel, Amir Ershad Fanaei, Eduardo Ruiz, and François Trochu. Experimental characterization by fluorescence of capillary flows in dual-scale engineering fabrics. *Textile Research Journal*, 83(15):1634–1659, 2013.

[37] G Lebrun, R Gauvin, and KN Kendall. Experimental investigation of resin temperature and pressure during filling and curring in a flat steel rtm mould. *Composites Part A: Applied Science and Manufacturing*, 27(5):347–356, 1996.

[38] Jean Sébastien Leclerc and Edu Ruiz. Porosity reduction using optimized flow velocity in resin transfer molding. *Composites Part A: Applied Science and Manufacturing*, 39(12):1859–1868, 2008.

[39] L James Lee, WB Young, and RJ Lin. Mold filling and cure modeling of rtm and srim processes. *Composite Structures*, 27(1-2):109–120, 1994.

[40] Yongjing Lee, Shilin Yan, Dequan Lee, and Fei Yan. The sink term to different kinds of fibrous mat during the unsaturated filling process. *Applied Composite Materials*, 23(3):239–253, 2016.

[41] Raounak Loudad. *Modélisation du couplage hydromécanique lors de la mise en oeuvre des composites par infusion.* PhD thesis, Université du Havre, 2016.

[42] TS Lundström. The permeability of non-crimp stitched fabrics. *Composites part A: applied science and manufacturing*, 31(12):1345–1353, 2000.

[43] Adil Mamoune, Abdelghani Saouab, Tariq Ouahbi, and Chung Hae Park. Simple models and optimization of compression resin transfer molding process. *Journal of Reinforced Plastics and Composites*, 30(19):1629–1648, 2011.

[44] Jovan Mijovic and Chee Hung Lee. Modeling of chemorheology of thermoset cure by modified wlf equation. *Journal of applied polymer science*, 37(4):889–900, 1989.

[45] Markus Nordlund, TS Lundström, Vilnis Frishfelds, and Andris Jakovics. Permeability network model for non-crimp fabrics. *Composites Part A: Applied Science and Manufacturing*, 37(6):826–835, 2006.

[46] Markus Nordlund and Véronique Michaud. Dynamic saturation curve measurement for resin flow in glass fibre reinforcement. *Composites Part A: Applied Science and Manufacturing*, 43(3):333–343, 2012.

[47] Richard S Parnas, J Grant Howard, Thomas L Luce, and Suresh G Advani. Permeability characterization. part 1: A proposed standard reference fabric for permeability. *Polymer Composites*, 16(6):429–445, 1995.

[48] Y De Parseval, KM Pillai, and SG Advani. A simple model for the variation of permeability due to partial saturation in dual scale porous media. *Transport in porous media*, 27(3):243–264, 1997.

[49] N Patel, V Rohatgi, and L James Lee. Micro scale flow behavior and void formation mechanism during impregnation through a unidirectional stitched fiberglass mat. *Polymer Engineering & Science*, 35(10):837–851, 1995.

[50] P Peyser and WD Bascom. Kinetics of epoxy resin polymerization using differential scanning calorimetry. *Journal of Applied Polymer Science*, 21(9):2359–2373, 1977.

[51] KM Pillai and SG Advani. A model for unsaturated flow in woven fiber preforms during mold filling in resin transfer molding. *Journal of Composite Materials*, 32(19):1753–1783, 1998.

[52] KM Pillai and SG Advani. Numerical simulation of unsaturated flow in woven fiber preforms during the resin transfer molding process. *Polymer Composites*, 19(1):71–80, 1998.

[53] Krishna M Pillai and Rajendra S Jadhav. A numerical study of nonisothermal reactive flow in a dual-scale porous medium under partial saturation. *Numerical Heat Transfer*, 47(2):109–136, 2004.

[54] SY Pusatcioglu, AL Fricke, and JC Hassler. Heats of reaction and kinetics of a thermoset polyester. *Journal of Applied Polymer Science*, 24(4):937–946, 1979.

[55] Sridhar Ranganathan, Frederick R Phelan, and Suresh G Advani. A generalized model for the transverse fluid permeability in unidirectional fibrous media. *Polymer Composites*, 17(2):222–230, 1996.

[56] Tonmoy Roy, Charity Dulmes, and Krishna M Pillai. Experimental investigations of the unsaturated flow in liquid composite molding. In *Proceedings of the 5th Canadian international composites conference, Vancouver, Canada*, 2005.

[57] Edu Ruiz, V Achim, S Soukane, F Trochu, and J Bréard. Optimization of injection flow rate to minimize micro/macro-voids formation in resin transfer molded composites. *Composites science and technology*, 66(3):475–486, 2006.

[58] F Sánchez, JA García, Ll Gascón, and Francisco Chinesta. Towards an efficient numerical treatment of the transport problems in the resin transfer molding simulation. *Computer Methods in applied mechanics and engineering*, 196(21):2300–2312, 2007.

[59] JSU Schell, M Deleglise, C Binetruy, P Krawczak, and P Ermanni. Numerical prediction and experimental characterisation of meso-scale-voids in liquid composite moulding. *Composites Part A: applied science and manufacturing*, 38(12):2460–2470, 2007.

[60] JSU Schell, M Renggli, GH Van Lenthe, R Müller, and P Ermanni. Micro-computed tomography determination of glass fibre reinforced polymer meso-structure. *Composites Science and Technology*, 66(13):2016–2022, 2006.

[61] Sanjay Sharma and Dennis A Siginer. Permeability measurement methods in porous media: A review. In *ASME 2008 International Mechanical Engineering Congress and Exposition*, pages 179–200. American Society of Mechanical Engineers, 2008.

[62] Chih-Hsin Shih and L James Lee. Effect of fiber architecture on permeability in liquid composite molding. *Polymer Composites*, 19(5):626–639, 1998.

[63] Pavel Simacek and Suresh G Advani. A numerical model to predict fiber tow saturation during liquid composite molding. *Composites Science and Technology*, 63(12):1725–1736, 2003.

[64] Pavel Šimáček and Suresh G Advani. Desirable features in mold filling simulations for liquid composite molding processes. *Polymer Composites*, 25(4):355–367, 2004.

[65] Pavel Simacek, Valentin Neacsu, and Suresh G Advani. A phenomenological model for fiber tow saturation of dual scale fabrics in liquid composite molding. *Polymer Composites*, 31(11):1881–1889, 2010.

[66] J Slade, KM Pillai, and SG Advani. Investigation of unsaturated flow in woven, braided and stitched fiber mats during mold-filling in resin transfer molding. *Polymer Composites*, 22(4):491–505, 2001.

[67] S Soukane and F Trochu. Application of the level set method to the simulation of resin transfer molding. *Composites Science and Technology*, 66(7):1067–1080, 2006.

[68] Hua Tan and Krishna M Pillai. Fast liquid composite molding simulation of unsaturated flow in dual-scale fiber mats using the imbibition characteristics of a fabric-based unit cell. *Polymer Composites*, 31(10):1790–1807, 2010.

[69] Hua Tan and Krishna M Pillai. Numerical simulation of reactive flow in liquid composite molding using flux-corrected transport (fct) based finite element/control volume (fe/cv) method. *International Journal of Heat and Mass Transfer*, 53(9):2256–2271, 2010.

[70] Hua Tan and Krishna M Pillai. Multiscale modeling of unsaturated flow in dual-scale fiber preforms of liquid composite molding i: isothermal flows. *Composites Part A: Applied Science and Manufacturing*, 43(1):1–13, 2012.

[71] Hua Tan and Krishna M Pillai. Multiscale modeling of unsaturated flow in dual-scale fiber preforms of liquid composite molding iii: reactive flows. *Composites Part A: Applied Science and Manufacturing*, 43(1):29–44, 2012.

[72] Hua Tan, Tonmoy Roy, and Krishna M Pillai. Variations in unsaturated flow with flow direction in resin transfer molding: An experimental investigation. *Composites Part A: Applied science and manufacturing*, 38(8):1872–1892, 2007.

[73] F Trochu, R Gauvin, and D-M Gao. Numerical analysis of the resin transfer molding process by the finite element method. *Advances in Polymer Technology*, 12(4):329–342, 1993.

[74] CL Tucker, Richard B Dessenberger, et al. Governing equations for flow and heat transfer in stationary fiber beds. *Composite Materials Series*, pages 257–257, 1994.

[75] Moon-Kwang Um and Woo Il Lee. A study on the mold filling process in resin transfer molding. *Polymer Engineering & Science*, 31(11):765–771, 1991.

[76] Joseph Walther, Pavel Simacek, and Suresh G Advani. The effect of fabric and fiber tow shear on dual scale flow and fiber bundle saturation during liquid molding of textile composites. *International journal of material forming*, 5(1):83–97, 2012.

[77] Y Wang and SM Grove. Modelling microscopic flow in woven fabric reinforcements and its application in dual-scale resin infusion modelling. *Composites Part A: Applied Science and Manufacturing*, 39(5):843–855, 2008.

[78] JR Weitzenböck, RA Shenoi, and PA Wilson. Radial flow permeability measurement. part a: Theory. *Composites Part A: Applied Science and Manufacturing*, 30(6):781–796, 1999.

[79] Malcolm L Williams, Robert F Landel, John D Ferry, et al. The temperature dependence of relaxation mechanisms in amorphous polymers and other glass-forming liquids. *J. Am. Chem. Soc*, 77(14):3701–3707, 1955.

[80] Fei Yan, Shilin Yan, Yongjing Li, and Dequan Li. Experimental measurements of sink terms for unsaturated flow during liquid composite molding. *Journal of Residuals Science & Technology*, 13(6), 2016.

[81] Xiao Hong Yang and Wei Ling Zhu. Viscosity properties of sodium carboxymethylcellulose solutions. *Cellulose*, 14(5):409–417, 2007.

[82] Yeong-Eun Yoo and Woo Il Lee. Numerical simulation of the resin transfer mold filling process using the boundary element method. *Polymer Composites*, 17(3):368–374, 1996.

UNIVERSITE BRETAGNE LOIRE

CENTRALE NANTES

Thèse de Doctorat

Mathieu IMBERT

Titre de la thèse : RTM réactif haute cadence avec mélange en tête dans des renforts fibreux à double-échelle de porosité : Développements et investigations expérimentaux et numériques

Title of thesis: High speed reactive RTM with on-line mixing in dual-scale fibrous reinforcements: Experimental and numerical developments and investigations

Résumé

Le moulage RTM à haute cadence est un procédé de fabrication composite prometteur qui satisfait les exigences de l'industrie automobile pour produire des pièces structurelles complexes avec un temps de cycle court. Cependant, les réductions de temps de cycle sont un véritable défi. Dans ce procédé, une résine est injectée avec mélange en dans la cavité d'un moule contenant un renfort fibreux. Ce flux de résine réactive génère des schémas d'écoulement complexes et des couplages thermo-chimio-rhéologiques forts. En raison de la grande sensibilité de la résine et des temps de cycle serrés, la prédiction de la stratégie d'injection optimale est très difficile et très coûteuse à mener expérimentalement. Le travail réalisé a donc poursuivi deux objectifs: 1. Identifier et quantifier expérimentalement les mécanismes influençant le procédé RTM réactif avec mélange en tête et 2. Développer une méthode de simulation numérique en vue d'introduire les mécanismes identifiés dans le logiciel industriel PAM COMPOSITE développé par ESI Group. L'identification et la quantification des mécanismes ont été réalisées grâce à des investigations expérimentales et numériques. Un nouveau montage expérimental a été développé pour l'étude du mécanisme de stockage de résines intra-mèche grâce à des observations aux échelles macro- et microscopiques. De plus, une méthode numérique a été développée pour simuler l'écoulement réactif de la résine dans des matériaux à simple et à double échelle de porosité. Cette méthode a permis d'étudier les mécanismes locaux difficiles à mesurer expérimentalement et de préparer le transfert vers le logiciel industriel d'ESI.

Mots clés
RTM réactif haute cadence, Mélange en tête, Double-échelle de porosité, Renfort fibreux, Expérimental, Numérique

Abstract

High Speed Resin Transfer Molding (RTM) is a promising composite manufacturing process fitting automotive industry requirements to produce complex structural parts with a perspective of short cycle times. However, cycle time reductions are a real challenge. In this process, a resin mixed on-line with curing agents is injected in the cavity of a mold containing a fibrous reinforcement. This flow of reactive resin generates a complex flow pattern and strong thermo-chemo-rheological couplings. Due to the high sensitivity of the resin cure, and the tight cycle times, prediction of the optimal injection strategy is very difficult and very expensive to conduct experimentally. In this context, two goals where followed in this work: 1. Identify and quantify experimentally the mechanisms, related to the process or to the reinforcement, influencing the reactive RTM process with on-line mixing and 2. Develop a numerical simulation method in a view of introducing the identified mechanisms in the industrial software PAM COMPOSITE developed by ESI Group. Identification and quantification of the mechanisms were realized thanks to experimental investigations and numerical simulations. A new experimental setup has been developed for the investigation of the mechanism of intra-tow resin storage through macro-scale and micro-scale observations. Additionally, a numerical method has been developed to simulate the reactive flow of a resin in single and dual-scale porous materials. This method allowed both to investigate local mechanisms difficult to study experimentally and prepare the transfer to the industrial software of ESI.

Key Words
High speed reactive RTM, On-line mixing, Dual-scale porosity, Fibrous reinforcement, Experimental, Numerical